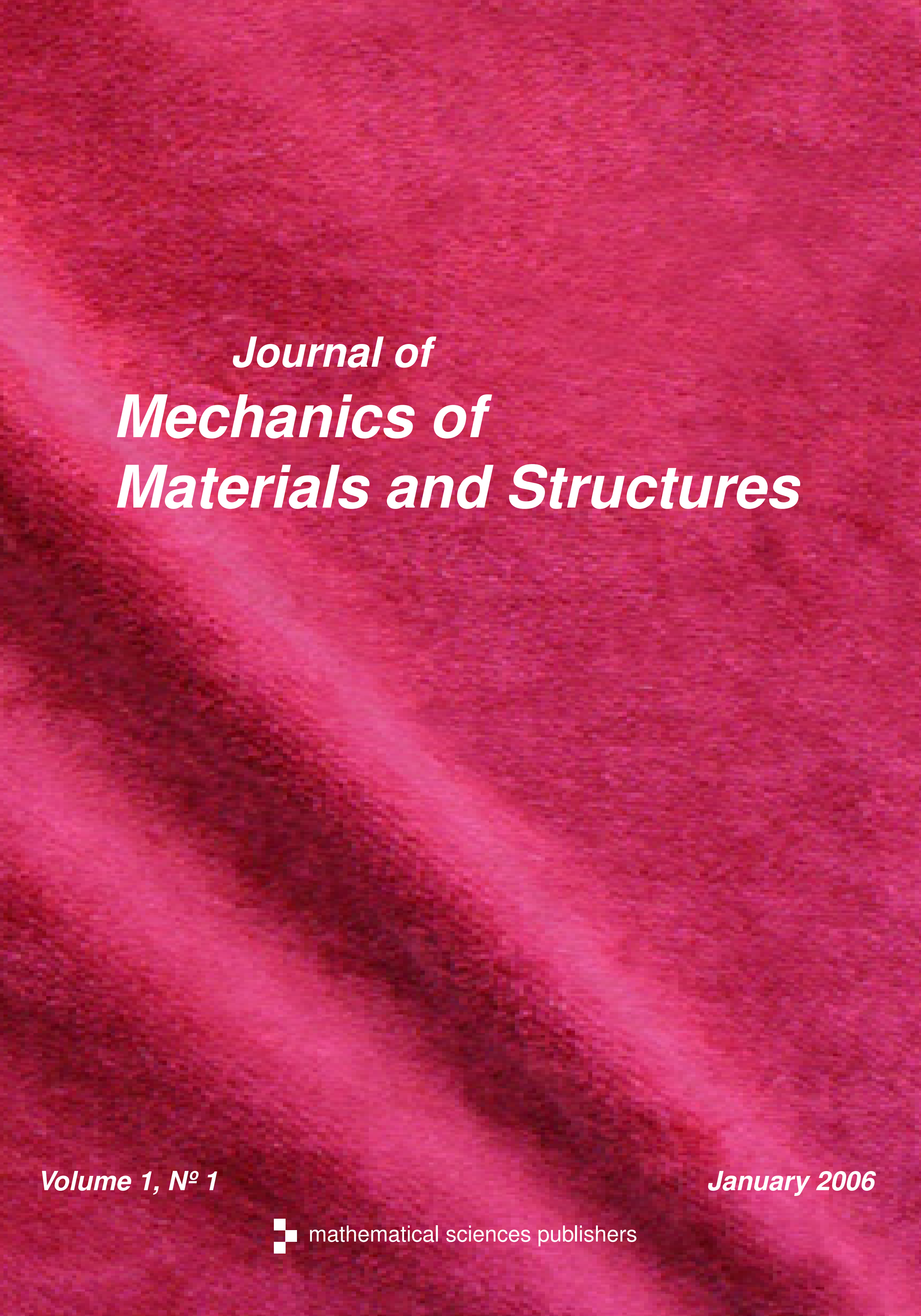

Journal of Mechanics of Materials and Structures

Volume 1, № 1

January 2006

mathematical sciences publishers

JOURNAL OF MECHANICS OF MATERIALS AND STRUCTURES

http://www.jomms.org

EDITOR-IN-CHIEF	Charles R. Steele
ASSOCIATE EDITOR	Marie-Louise Steele Division of Mechanics and Computation Stanford University Stanford, CA 94305 USA
SENIOR CONSULTING EDITOR	Georg Herrmann Ortstrasse 7 CH–7270 Davos Platz Switzerland

BOARD OF EDITORS

D. BIGONI	University of Trento, Italy
H. D. BUI	École Polytechnique, France
J. P. CARTER	University of Sydney, Australia
R. M. CHRISTENSEN	Stanford University, U.S.A.
G. M. L. GLADWELL	University of Waterloo, Canada
D. H. HODGES	Georgia Institute of Technology, U.S.A.
J. HUTCHINSON	Harvard University, U.S.A.
C. HWU	National Cheng Kung University, R.O. China
IWONA JASIUK	University of Illinois at Urbana-Champaign
B. L. KARIHALOO	University of Wales, U.K.
Y. Y. KIM	Seoul National University, Republic of Korea
Z. MROZ	Academy of Science, Poland
D. PAMPLONA	Universidade Católica do Rio de Janeiro, Brazil
M. B. RUBIN	Technion, Haifa, Israel
Y. SHINDO	Tohoku University, Japan
A. N. SHUPIKOV	Ukrainian Academy of Sciences, Ukraine
T. TARNAI	University Budapest, Hungary
F. Y. M. WAN	University of California, Irvine, U.S.A.
P. WRIGGERS	Universität Hannover, Germany
W. YANG	Tsinghua University, P.R. China
F. ZIEGLER	Tech Universität Wien, Austria

PRODUCTION

PAULO NEY DE SOUZA	Production Manager
SILVIO LEVY	Senior Production Editor
NICHOLAS JACKSON	Production Editor

mathematical sciences publishers

©Copyright 2007. Journal of Mechanics of Materials and Structures. All rights reserved.

JOURNAL OF MECHANICS OF MATERIALS AND STRUCTURES
Vol. 1, No. 1, 2006

TO OUR READERS AND AUTHORS

CHARLES STEELE AND MARIE-LOUISE STEELE

The new journal which you are reading, known as JoMMS to its already large circle of friends, is the fruit of a collaboration between an experienced Editorial Board, our authors and referees, and the staff of MSP, an innovative nonprofit publisher. George Herrmann serves as Senior Editorial Advisor, and the journal follows his philosophy of broad coverage and stringent peer review.

As we proudly present this first issue to the world, we can say with confidence that this publication will set a standard for technical publications in the twenty-first century and will provide a wealth of services to readers and libraries. In choosing to publish with MSP, the editoral board acknowledges that while commercial publishers have helped satisfy a need that technical societies were slow to recognize, it is now time for a change. The sole goal of MSP is to keep research publications in the hands of researchers for the benefit of the scientific community, using the full panoply of modern software and networking tools to produce high quality at an affordable price. JoMMS's features include:

- the option of color figures without page charges;
- free universal access after a year of publication, and right away for Volume 1;
- convenient subscriber access by IP range;
- indexing on major search engines and on the journal web site, jomms.org;
- support for optional nonprint material such as sound, movies, animations, source software, and embedded data behind plots and tables;
- downloadable PDF files with full links for cross-references and bibliographical items, including frequently updated links to other publications;
- careful typesetting, copy editing, and figure handling;
- a license-to-publish model rather than a transfer-of-copyright model, so that authors keep control of their creation;
- a low subscription price that will not grow faster than the number of pages and indeed may drop as the subscriber base expands.

Few journals even approach this in terms of benefits to you and the community. We hope you will submit your best work to JoMMS and encourage your library to subscribe. Please feel free to ask questions and offer suggestions and ideas.

Charles and Marie-Louise Steele
Stanford, January 2006

CHARLES STEELE: *Division of Mechanics and Computation, Stanford University,
Stanford, CA 94305, USA*
chasst@stanford.edu

MARIE-LOUISE STEELE: *Division of Mechanics and Computation, Stanford University,
Stanford, CA 94305, USA*
jomms.steele@stanford.edu

JOURNAL OF MECHANICS OF MATERIALS AND STRUCTURES
Vol. 1, No. 1, 2006

WRINKLED MEMBRANES
PART I: EXPERIMENTS

Y. WESLEY WONG AND SERGIO PELLEGRINO

This paper presents a detailed experimental study of the evolution and shape of reversible corrugations, or *wrinkles*, in initially flat, linear-elastic and isotropic thin foils subject to in-plane loads. Two sets of experiments were carried out, on a rectangular membrane under simple shear and on a square membrane subjected to two pairs of equal and opposite diagonal forces at the corners. Salient findings are that: the wrinkle profile is generally well approximated by a half sine wave in the longitudinal direction, with constant or linearly-varying transverse wavelength; sudden changes in the shape of the membrane, accompanied by changes in the number of wrinkles, occur in both cases; in the sheared membrane the wrinkle pattern remains essentially unchanged for increasing shear displacement, whereas in the square membrane a large diagonal wrinkle appears when the corner load ratio is around 3.

1. Introduction

Thin, prestressed membranes are a key element of the next generation of spacecraft, to provide deployable mirror surfaces, solar collectors, sunshields, solar sails, etc. While some of these applications demand very smooth surfaces, and hence membranes that are biaxially prestressed, for several other applications slightly nonsmooth membranes are acceptable, provided that the size and shape of the deviation from the nominal shape are sufficiently small. The realization of wrinkled or partially wrinkled membrane structures, as opposed to structures with totally smooth surfaces is often much simpler and cheaper [Jenkins 2001], and therefore, for those applications in which a slightly wavy surface may be acceptable, engineers are now faced with the task of estimating the extent and amount of waviness.

This paper, the first in a series of three, aims to observe the formation, evolution, and shape of reversible corrugations, or *wrinkles* that form in initially flat, linear-elastic and isotropic thin foils, or *membranes*, under the action of in-plane loads. Initial imperfections, arising say from the presence of permanent creases due to previous folding of the membrane, are not considered. The experimental observations made in the present paper form the basis for an analytical model that will explain

---

Keywords: plate buckling, membrane structures, wrinkling.

and identify the key characteristics of wrinkles and provide simple predictions for the wavelength and amplitude of the wrinkles; see [Wong and Pellegrino 2006a]. Detailed numerical simulations will appear in [Wong and Pellegrino 2006b].

Previous work on wrinkled membranes has focussed mainly on the load transfer characteristics of wrinkled membranes and the associated, nonlinear constitutive relationships. Wrinkled shear webs were first investigated by Wagner [1929] and later by Reissner [1938] and Mansfield [Mansfield 1968; 1989], and these studies established wrinkled membranes as a very useful and efficient structural element for lightweight structures. Stein and Hedgepeth [1961], followed by many others, investigated the nonlinear load-displacement or moment-rotation relationship of partially wrinkled membrane structures.

Only recently have the wrinkle details, such as wrinkle pattern, wavelength and amplitude, been of interest to researchers [Cerda et al. 2002; Wong and Pellegrino 2002; Epstein 2003], so it is appropriate to begin with an experimental characterization of the way in which wrinkles form and develop in simple, thin membrane structures. Particular aims of the present study will be to examine how wrinkles change in response to the applied loads and also how repeatable any particular pattern of wrinkles is when the loads are removed and then reapplied, in order to establish particular features of their behaviour that one needs to be aware of when setting out to develop appropriate analytical or computational models.

Hence, this paper will present experiments that were carried out first on a rectangular membrane whose long edges are sheared uniformly, thus forming a series of approximately uniform diagonal wrinkles, and secondly on a square membrane subjected to two pairs of equal and opposite diagonal forces at the corners, where the ratio between the magnitude of the forces had different values. In each experiment the wrinkle pattern was carefully measured, and the wrinkle wavelength and amplitude were obtained from the measurements.

The layout of the paper is as follows. Section 2 presents a brief review of previous experimental work on wrinkled membranes. Section 3 describes the apparatus for the two sets of experiments. Sections 4 and 5 present the experimental results obtained from the membrane in shear and from the square membrane, respectively. Section 6 concludes the paper.

2. Review of previous work

Early experiments on wrinkled membranes mainly focussed on the measurement of overall response parameters, such as the end rotation of a pressurized cylinder in pure bending [Stein and Hedgepeth 1961] or the torque-rotation relationship of a stretched circular membrane attached to a central hub [Stein and Hedgepeth 1961; Mikulas 1964]. These particular experimental studies were carried out to validate wrinkling theories developed specifically to analyse partially wrinkled membranes. They also intended to confirm that the membrane retained most of its stiffness after wrinkling had first occurred, although a notable softening was in fact observed with the growth in the extent of the wrinkled regions.

In another classical study, Mansfield [1968; 1970] determined the orientation of the wrinkle lines in membranes with different shapes, for different boundary conditions. Only qualitative correlations between theory and the experimental observations were attempted.

Performing detailed measurements on thin membranes is not easy, mainly because high accuracy noncontact measurement apparatus is needed. A set of carefully planned experiments, including accurate measurements of wrinkle details by using a capacitance proximity sensor, were carried out by Jenkins et al. [1998] on a square Mylar membrane subjected to different combinations of shear and tension forces. These experiments showed that both the wrinkle amplitude and the number of wrinkles increase with the applied shear force, but decrease with the tension force. The reverse relationship was found between the wrinkle wavelength and the applied forces.

The same measurement technique was later extended by Blandino et al. [2001] to measure the surface profile of a thin, aluminized 0.5 m square Kapton® membrane subjected to four corner forces, to include the effects of thermal gradients within the membrane. Blandino et al. [2001] also produced a complete out-of-plane displacement contour plot for the membrane using photogrammetry, and compared the two sets of measurements in the region near a corner of the membrane. Good agreement was observed, with an accuracy of up to ±0.02 mm on the wrinkle amplitudes.

The main disadvantage of capacitance sensors is that they need a metallic surface target and the sensor must be in electrical contact with the membrane. As for photogrammetry, a large number of target points is required in order to capture fine wrinkle details and the postprocessing of the images can be time-consuming [Blandino et al. 2002a]. However, the latest applications of this technique, based on the commercial software package Photomodeler 4.0 [Blandino et al. 2003], have shown that this technique is making very rapid advances.

All of the work mentioned above was carried out on initially flat films. The effect of preexisting creases on the constitutive behaviour of thin foils has been investigated by Murphey [2000] and Papa and Pellegrino [2005].

3. Experimental techniques

In the present study we are interested in measuring the out-of-plane displacement/amplitude of wrinkles formed in a nominally flat membrane. The particular membrane that was used is a polyimide film made by DuPont, known as Kapton HN®. This film is already widely used for various spacecraft applications, because of its optical properties (e.g. excellent adhesion to metal films), electrical and thermal conductivity, and environmental compatibility and survivability. Some of these foils were supplied with a mirror surface finish, which made the selection of a suitable measurement device particularly challenging.

A Charge Coupled Device (CCD) laser displacement sensor, model LK-081 supplied by Keyence, was used for all experiments presented in this paper. Unlike conventional laser sensors, which use the whole light distribution in the beam spot and hence tend to be affected by the surface finish of the target surface, this particular device detects the pixel with the peak light intensity and uses triangulation to measure the distance from the laser to the reflecting surface. The device is positioned at a reference distance of 80 mm from the surface and has a measurement range of ±15 mm, corresponding to a full output of ±5 V (amounting to 3 mm/V), with a resolution of 3 μm.

The voltage output from the laser was logged to a Schlumberger SI 3531P data acquisition system set at 2 readings per second, and the position of the laser corresponding to each measurement was worked out by assuming that the laser travels at a uniform speed.

3.1. ***Laser scanning frame.*** The laser was mounted on a supporting unit attached via two linear guides to an Al-alloy frame; see Figure 1(a). The position of the supporting unit is controlled by a 10 mm diameter brass threaded rod, held by two end bearings and driven by a geared DC motor, whose speed is such that the laser is moved at a rate of 0.5 mm/s. The connection is through a floating nut, to avoid jamming. Although a small vibration is induced in the frame by the movement of the laser, it was found that the noise on the laser output was negligible.

The maximum travel of the laser, in the x-direction, defined in Figure 1(b), is approximately 400 mm.

3.2. ***Shear test apparatus.*** An apparatus to subject rectangular membranes to a state of simple shear was designed and constructed, in order to measure the profile of different sections of the membrane by means of the laser scanning frame described in Section 3.1.

This shear rig comprises a stiff base plate and two parallel blocks holding the longer edges of the membrane. One block is fixed and the other, which holds the upper edge of the membrane, can be moved along the x-axis, in either sense, to apply shear displacements. Movement in the y-direction is not allowed.

Four linear bearings support the movable edge of the membrane, whose position can be precision controlled by means of a threaded rod, and monitored with a digital displacement gauge with an accuracy of ±0.05 mm.

First, the membrane is attached to the moving edge. Then, before clamping the fixed edge, a small initial stress is applied in the y-direction by means of a system of counterweights, connected to the membrane by Kapton® tabs through Kevlar® cords running over closely spaced pulleys. The surplus membrane, cords, counterweights, etc. are removed after tightening the fixed edge clamping strip. The complete experiment set-up is shown in Figure 1(b).

The overall dimensions of the base plate are 430 mm × 440 mm. The whole rig was constructed of steel and its parts were sized on the basis that the maximum deflection should be less than 0.1 mm under a maximum load of 1.7 N/mm from the membrane (corresponding to the ultimate stress of Kapton HN®, which is 69 N/mm^2, and considering 0.025 mm thick membranes [DuPont 2001]). The maximum normal stress in any test described in this paper will be less than half this ultimate value, to stay well within the linear range of the material. Wong [2003] has measured an average Young's Modulus of 3500 N/mm^2 and an average Poisson's ratio of 0.31 in Kapton HN®, over a range of three film thicknesses (0.0125, 0.025, and 0.05 mm) and for strains up to 0.8%.

3.3. ***Square membrane apparatus.*** A 650 mm square frame was designed to hold a 500 mm square membrane and apply point loads at the four corners. This frame was built by welding four 25 mm × 1.5 mm steel square hollow sections, with a diagonal bracing member welded at the back. Four 12 mm square bars were welded across the four corners of the frame. These provide end attachments for the membrane, through 4 mm holes drilled through each bar.

Corner attachments, able to withstand a maximum tension of 20 N without inducing any plastic deformation of the membrane, were made as follows. The corners of the membranes were cut at 45° to the sides, to a width of 25 mm; 1.5 mm diameter steel pins were attached to the cut edges, with a 25 mm wide by 40 mm long strip of Kapton® adhesive tape doubled back over the membrane (thus, each pin forms a 25 mm wide spreader bar, which distributes the applied load as surface tractions on either sides of the membrane, over a patch of 25 mm × 20 mm); a 0.9 mm diameter Kevlar® cord was used to connect the centre of the pin to a strain gauged turn-buckle. The connection between the turn-buckle and the cord was designed such that minimum distortions were introduced during tensioning and the cord length could be adjusted at any stage of the experiment.

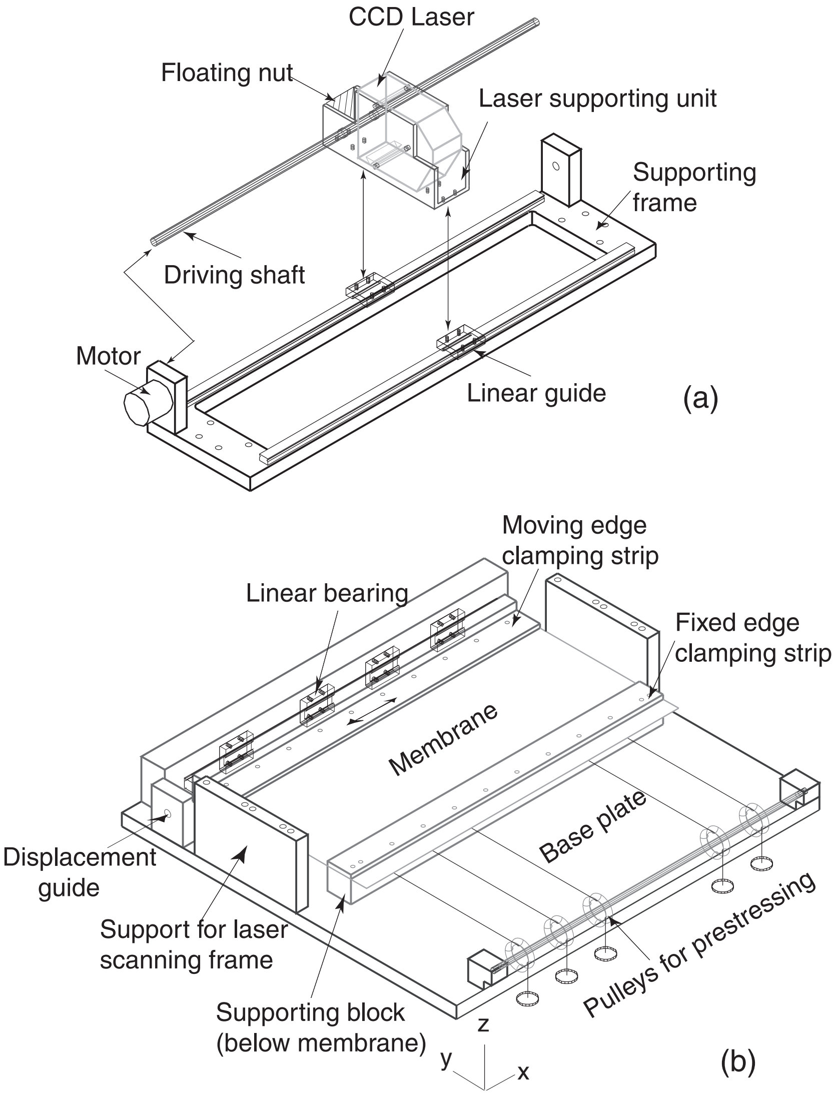

Figure 1. (a) Laser scanning frame, (b) Shear-rig.

The same type of connection was used for all four corners of the membrane. Thus, the tension force applied at each corner could be varied to produce different load ratios, T_1/T_2. Note that, for equilibrium, only two forces can be varied independently. Hence, two strain meters were used to monitor the load levels.

The load frame was designed such that the effect of gravity on the wrinkles formed in the membrane could be compared, for any chosen load condition, by holding the membrane either vertical or horizontal.

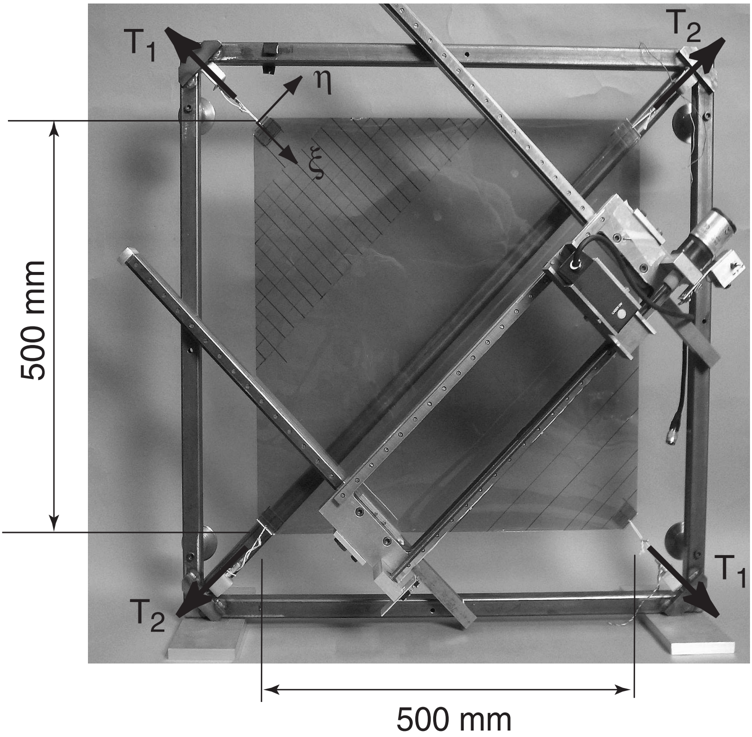

Figure 2. Square frame experimental set-up, in vertical configuration.

The laser scanning frame described in Section 3.1 was attached to the square frame through linear bearings running on guide rails at 45° to the sides of the frame. The complete experimental set-up is shown in Figure 2. (An additional local coordinate system, ξ, η, is defined in this figure.) The use of the linear guides enables the laser to scan, in the η direction, profiles of the membrane with different values of ξ. Two pairs of corner tension forces, T_1 and T_2, are also indicated in the figure.

4. Membrane in shear

The main purpose of subjecting rectangular membranes to simple shear was to investigate the variation of the wrinkle parameters — that is, the relationship between out-of-plane displacement and wavelength — with the magnitude of the applied shear displacement. The boundary conditions are relatively simple in this case; the two long edges of the membrane are held at a fixed distance while the two side edges are unrestrained, and so the wrinkles arrange themselves to form a repeating pattern. All test results presented in this section were obtained on 380 mm wide membranes with a height, between the supports, of 128 mm.

4.1. ***Wrinkle pattern.*** The overall wrinkle pattern (see Figure 3) shows that, apart from two "fan" regions near the short edges of the membrane, the wrinkles are inclined at an angle of 45° to the upper and bottom edges of the shear-rig. They are also parallel to each other, of course.

As the shear displacement was gradually increased, the wrinkle pattern remained essentially unchanged, all the wrinkles in the middle being inclined at approximately 45° to the edges, as before, and the two side fans becoming more distorted. The size of the central wrinkled region, bounded by the two fan regions, remained almost unchanged, although the number of wrinkles increased when the shear displacement was increased. Figure 3 shows the wrinkle patterns corresponding to shear displacements of 0.5 mm, 1.0 mm, 2.0 mm and 3.0 mm (for which the maximum normal strain is 1.2%, and so Kapton® begins to behave nonlinearly), for a 0.025 mm thick film.

Repeating this test on foils of different thickness showed that *the number of wrinkles decreases when the thickness of the membrane is increased*, the shear displacement being equal. An extensive set of photographs of these wrinkle patterns can be found in Wong [2003].

4.2. ***Wrinkle profile.*** The wrinkle details were further investigated by scanning the membranes across the middle (section A-A in Figure 3) with the CCD laser.

The laser measurements provide the out-of-plane displacement of the membrane, w. Plotting this height vs. the position of the laser is a useful tool for studying the characteristics of the wrinkles. Figure 4 shows four plots of this kind, based on measurements taken half-way between the two long edges of the membrane ($y = 64$ mm) on a 0.025 mm thick Kapton® film. The four plots, for shear displacements of $\delta = 0.5$ mm, $\delta = 1.0$ mm, $\delta = 2.0$ mm, and $\delta = 3.0$ mm, which correspond one by one to the wrinkle patterns shown in Figure 3.

A common feature of the plots shown in Figure 4, see for example Figure 4(b), is the presence of three distinct regions, as follows. Regions (i) and (iii) consist of two high peaks each, close to the free edges on the sides of the membrane. Region (ii), in the middle, is characterised by fairly uniform wrinkles and it will be shown in Part 2 of this paper series that the key characteristics of the wrinkles in Region (ii) can be captured with a simple analytical model.

In Figure 4 it can be noticed that the number of wrinkles increases with the applied shear displacement. More precisely, if each crest in these plots is counted as a wrinkle, the plots show that there are 15 wrinkles for $\delta = 0.5$ mm, 17 for $\delta = 1.0$ mm, 18 for $\delta = 2.0$ mm, and 19 for $\delta = 3.0$ mm. Also, it was observed during the experiments that when δ was increased gradually and monotonically, changes in the numbers of wrinkles occur *suddenly*. A detailed numerical simulation, described in the third paper in this series [Wong and Pellegrino 2006b], shows that any change

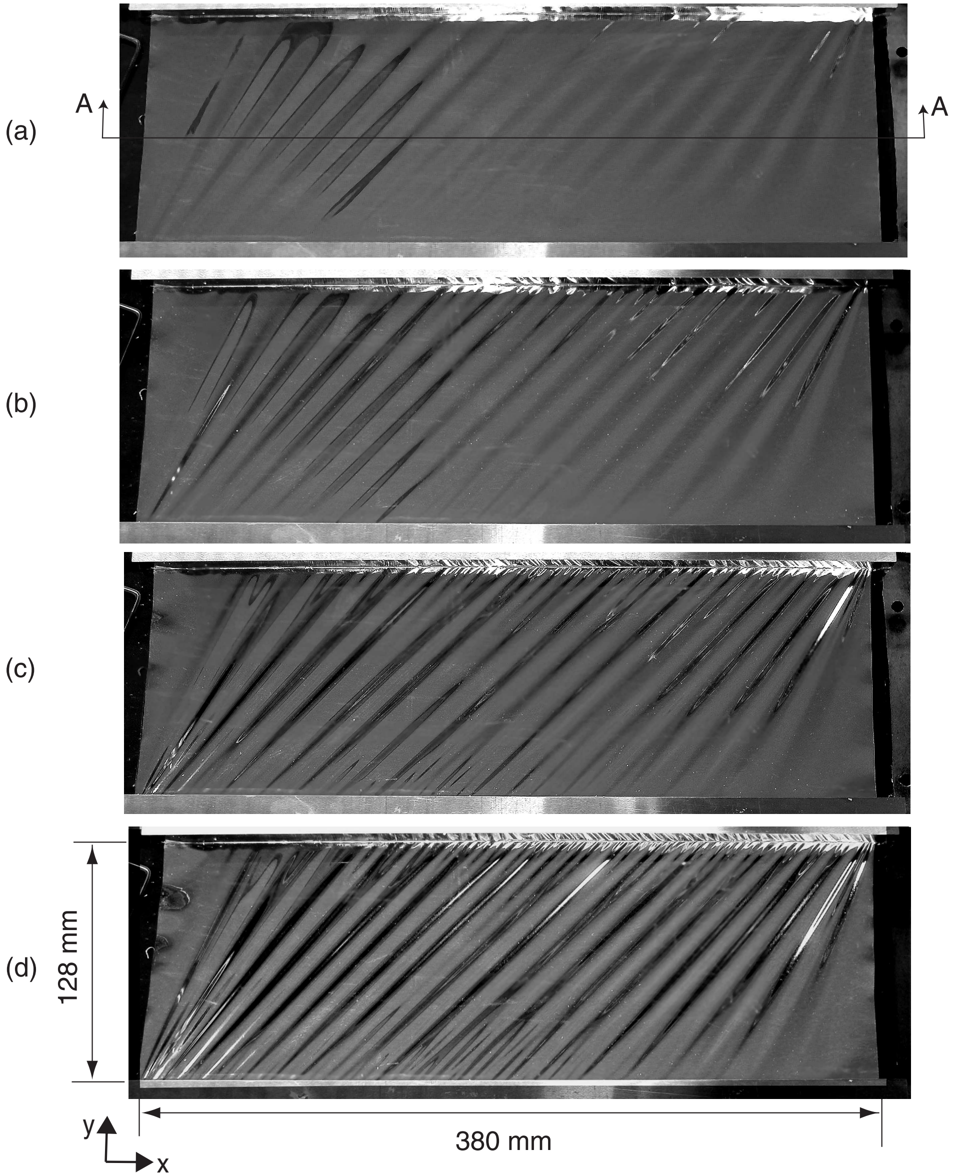

Figure 3. Wrinkle patterns for a 0.025 mm thick Kapton® film under shear displacements of (a) $\delta = 0.5$ mm, (b) $\delta = 1.0$ mm, (c) $\delta = 2.0$ mm, and (d) $\delta = 3.0$ mm.

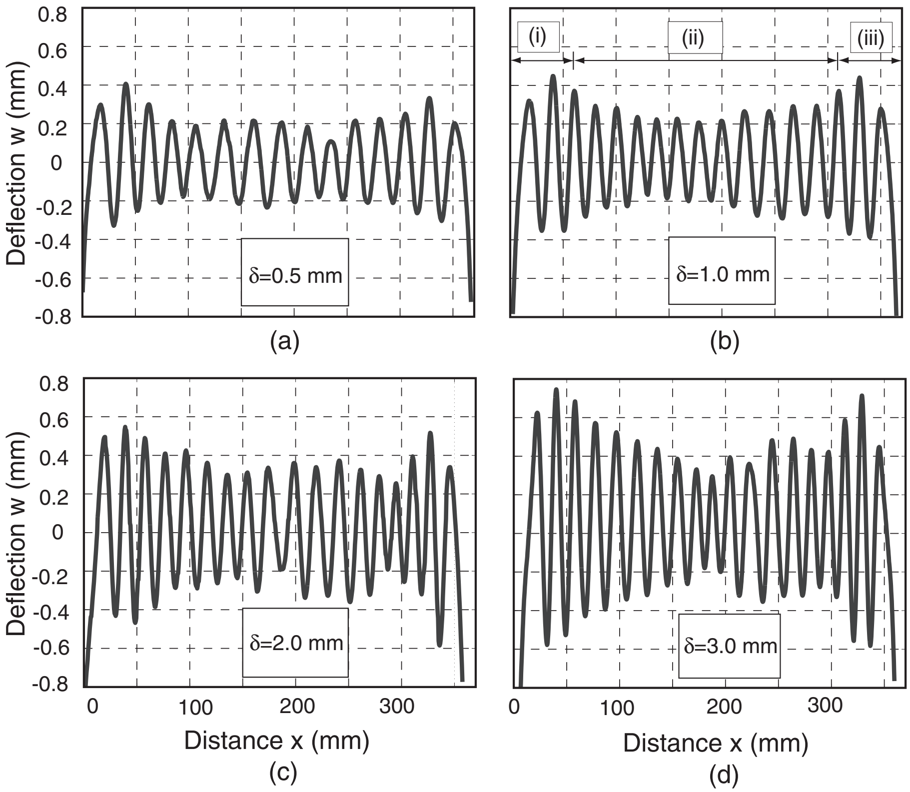

Figure 4. Section A-A of 0.025 mm thick Kapton® film for shear displacements of (a) $\delta = 0.5$ mm, (b) $\delta = 1.0$ mm, (c) $\delta = 2.0$ mm, and (d) $\delta = 3.0$ mm.

in the number of wrinkles is the effect of an instability (mode jumping) that usually occurs near the edge of the membrane.

Another important observation that can be made from Figure 4 is that both the wrinkle amplitudes and the number of wrinkles increase, whereas their corresponding wavelengths decrease when δ is increased.

Figure 5 shows the evolution in the profile of the membrane during an unload–reload cycle, beginning immediately after the load cycle depicted in Figure 4. It is interesting to compare the membrane profiles that correspond to the same value of the shear displacement, but at different stages of the loading cycle. For example, for $\delta = 2.0$ mm the number of wrinkles is 18 when δ is increasing — see Figure 4(c) — but it is 19 when δ is decreasing — see Figure 5(b). Similarly, for $\delta = 0.5$ mm their numbers are 15 and 19, respectively.

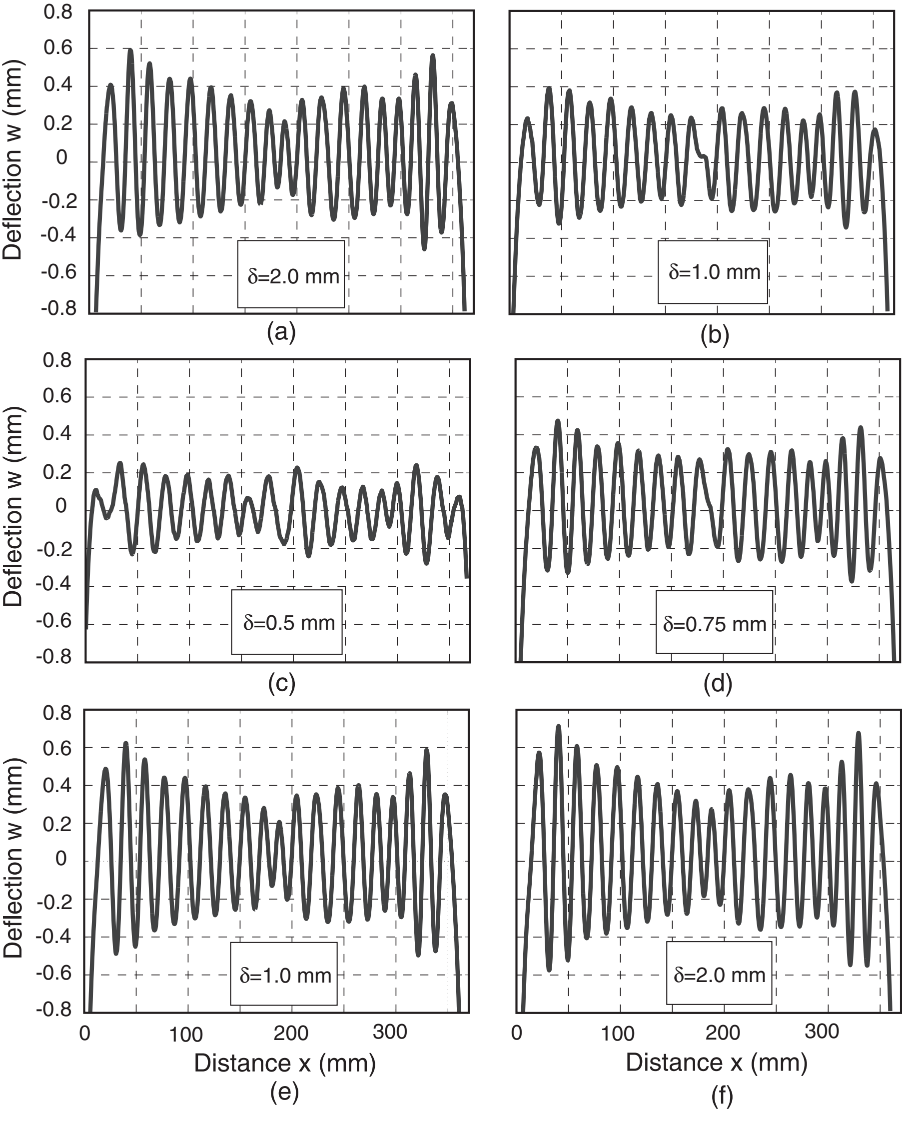

Figure 5. Section A-A of 0.025 mm thick Kapton® film under shear, during (a–c) unloading and (d–f) reloading.

After the first unloading small residual imperfections were noted, resulting from slippage/yielding of the material near the clamped edges. Upon reloading, these imperfections have the effect of driving the membrane more rapidly towards its final configuration (with 19 wrinkles) much earlier, compared to the nearly perfect membrane used in the first loading cycle.

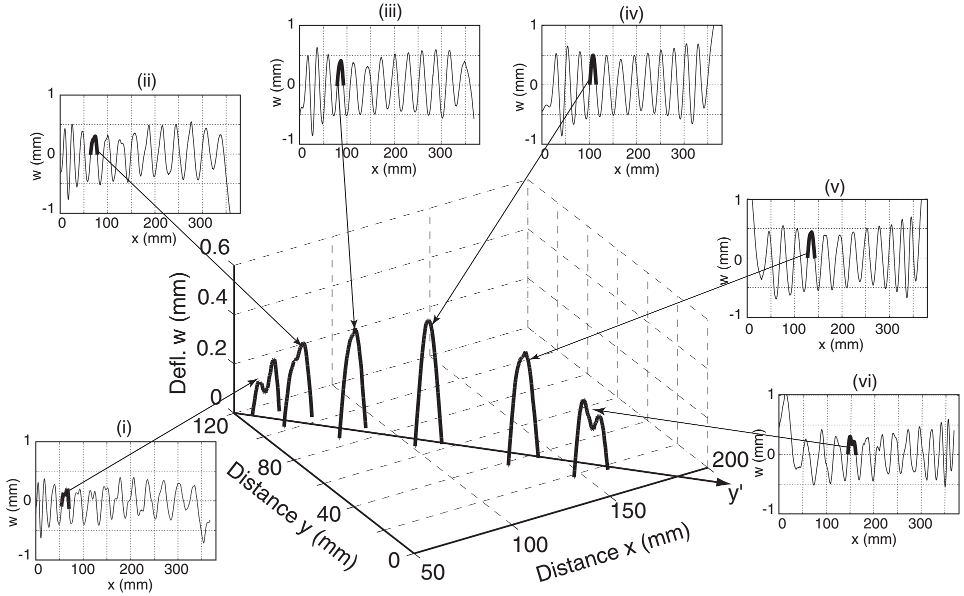

Figure 6. Three-dimensional view of half-wrinkle in sheared membrane.

4.3. ***Wrinkle shape.*** The maximum wrinkle amplitude can be expected to occur half-way between the two clamped edges of the membrane. In order to verify this, and to measure the longitudinal shape of a wrinkle, additional profiles of the membrane were measured at the following distances from the fixed edge, $y = 15$ mm, $y = 30$ mm, $y = 64$ mm, $y = 85$ mm, $y = 105$ mm and $y = 110$ mm, for the same shear displacement. These profiles, labelled (i) to (vi), are shown in Figure 6. The central part of this figure shows a three-dimensional reconstruction of the shape of a particular half-wrinkle, based on corresponding segments of the six profiles. Then, having defined a new axis y' at 45° to x and y, as shown in Figure 6, the amplitudes of the six selected crests have been plotted in Figure 7 together with a half sine wave whose amplitude has been scaled to match the wrinkle amplitude at point (iv). The shape of the wrinkle can be described quite accurately by this simple mode-shape.

In addition to obtaining information on the amplitude of a wrinkle, the half-wavelength of this particular wrinkle — given by the base width of the six crests in Figure 6 — can be seen to remain approximately constant, except when it approaches the end supports; see Figure 6(i) and (vi). This particular effect may be due to localised deformation imposed by the clamping strips; additional small wrinkles appear in these end regions. Also note that large displacements occur at the free side edges.

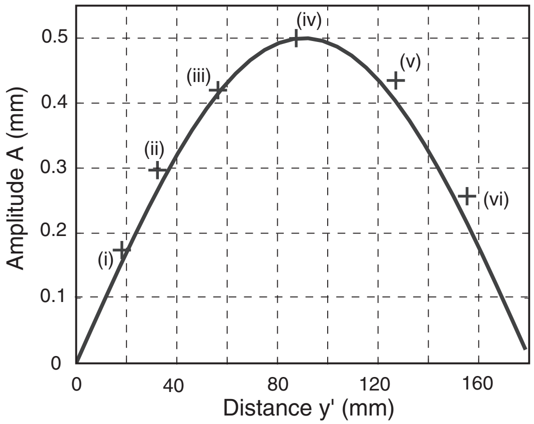

Figure 7. Comparison of longitudinal wrinkle profile with a sinusoidal mode shape, for sheared membrane.

4.4. ***Discussion.*** This study has revealed a number of important characteristics of wrinkles in thin rectangular membranes under simple shear.

It was already observed in [Mansfield 1989], and it has been confirmed, that the wrinkle pattern comprises a general "parallelogram" of wrinkles in the central region, containing approximately uniform wrinkles at 45°, plus two triangular fan regions which include a small highly stressed corner region and a triangular slack region, near the side edges. The extent of these fan regions remains approximately unchanged when the magnitude of the shear displacement δ is varied.

It has been established that in the uniformly wrinkled region the wrinkle amplitude and wavelength vary with δ. More precisely, the wrinkle wavelength decreased with increasing δ, although the rate of change was found to decrease as δ grew larger. Conversely, both the amplitude and the number of the wrinkles were found to initially increase with δ. For $\delta > 1.5$ mm (corresponding to a normal strain of 0.6% along the wrinkles) the wrinkle pattern was found to have become stable: only one more wrinkle could be formed, and only by increasing δ to almost 3 mm.

The average wrinkle wavelength and average amplitude (taken as the average wrinkle height in the central region, discarding the higher peaks at the corners) for Kapton® membranes of three different thicknesses have been plotted against the shear displacement in Figure 8.

5. Membrane under corner loads

In the case of the square membrane subject to corner loads, two load cases were investigated. First, the membrane was subjected to a series of gradually increasing symmetrical tension loads $T (= T_1 = T_2)$ at its four corners. Second, one pair of

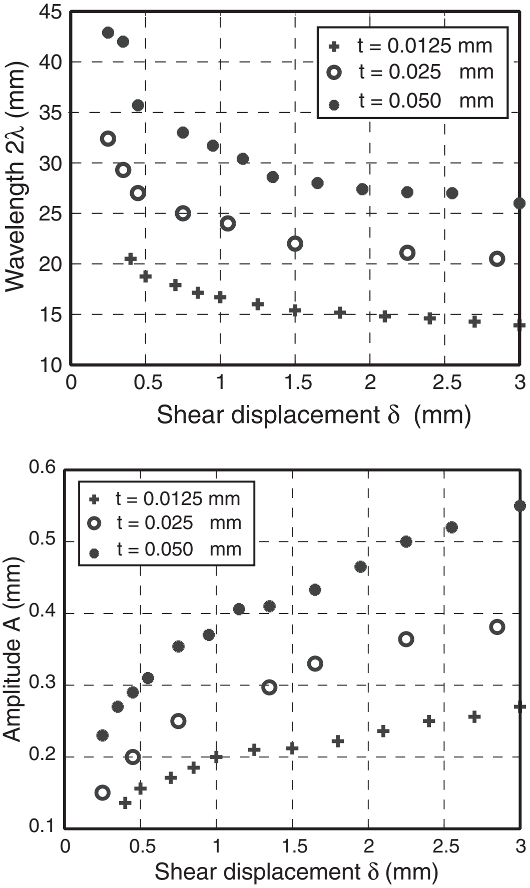

Figure 8. Average wrinkle wavelengths measured in the x-direction (top) and average wrinkle amplitudes (bottom) in sheared membranes of different thicknesses.

loads, T_2, was kept constant while the other pair, T_1, was increased, to study the effects of different load ratios. The associated wrinkle details were measured for every load case and for different membrane thicknesses. Here we present results from a set of experiments on a 0.025 mm thick, 500 mm by 500 mm Kapton® membrane.

5.1. ***Symmetric loading ($T_1 = T_2$).*** The membrane was first loaded up to 5 N at all four corners and the wrinkle profile was scanned with the CCD laser at six different locations, corresponding to the following values of the coordinate ξ (measured from a corner of the membrane loaded by one of the forces T_1): $\xi = 35$ mm, $\xi = 53$ mm, $\xi = 70$ mm, $\xi = 105$ mm, $\xi = 141$ mm, and $\xi = 177$ mm. (The coordinate system ξ, η is defined in Figure 2.) After all six profiles had been scanned, one pair of loads, T_1, was increased to 10 N and finally to 20 N, and all scans were repeated.

Wrinkle profiles were produced by plotting the membrane out-of-plane displacement, w, against the distance η across the membrane (measured from the edge of the membrane) for two load levels, $T = T_1 = T_2 = 5$ N and $T = T_1 = T_2 = 20$ N. The results are presented in Figure 9. Note that the membrane slopes down from left to right, by about 0.5 mm, and this effect needs to be discounted when measuring the wrinkle amplitudes. Blandino et al. [2002a] carried out an almost identical experiment, but using triangular tabs at the corners of the membrane.

Examining the plots in Figure 9 shows that for increasing distance from the corner of the membrane, first the amplitude of the wrinkles increases, reaching a maximum at $\xi \approx 105$ mm, and then starts decreasing. The wrinkles become vanishingly small when $\xi \approx 180$ mm; the central part of the membrane is unwrinkled. Also note that, if edge effects are neglected, the wrinkle amplitudes for symmetrical loading are quite small, and indeed much smaller than will be observed under asymmetric loading, in the next section.

An interesting observation is that the extent of the wrinkled regions in the membrane remains essentially the same, despite a four-fold increase in the load level, and wrinkle amplitude and wavelength are reasonably uniform, apart from the edges of the membrane. However, the number of wrinkles increased when the load was increased, as already observed by Blandino et al. [2002b], and did so suddenly, thus showing mode-jumping as already observed in the shear experiment presented in Section 4.2. Figure 9(d) shows that the number of wrinkles increased from four when $T = 5$ N, to five when $T = 20$ N. The wrinkle wavelength decreases correspondingly, and the wrinkle amplitude is also observed to have decreased with the higher loads.

Figure 9 also shows that the wrinkle profiles at the smaller load, $T = 5$ N, are less uniform than at the higher load, $T = 20$ N. Therefore, rather than considering individual wrinkles, average values will be used to study general trends.

A photograph showing the overall wrinkle pattern for $T = T_1 = T_2 = 5$ N is shown in Figure 10(a). It can be seen that there are four, symmetric wrinkled regions, radiating from each corner, plus a large central region which is visibly free of wrinkles. These visual observations agree with the earlier discussion of the wrinkle profiles.

5.2. ***Asymmetric loading.*** Under symmetric loading the wrinkle amplitudes had been found to be small. In the second load case, a diagonal wrinkle with larger features was formed by increasing the load ratio, T_1/T_2. T_2 was kept fixed at 5 N, and T_1 was gradually increased from 5 N to 20 N.

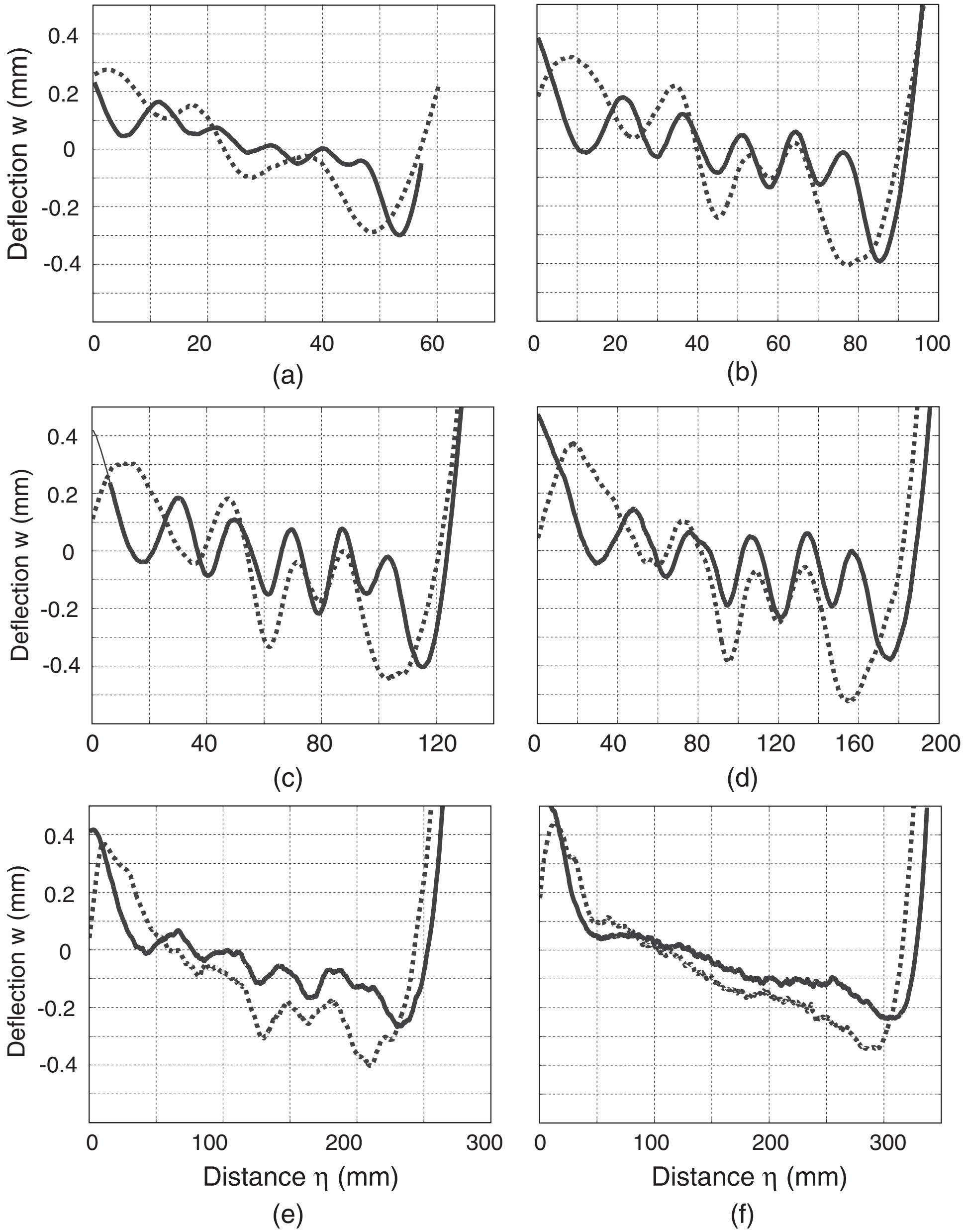

Figure 9. Wrinkle profiles in 0.025 mm thick, square Kapton® membrane, for $T = T_1 = T_2 = 5$ N (dashed) and $T = T_1 = T_2 = 20$ N (solid), at following distances from corner (a) $\xi = 35$ mm, (b) $\xi = 53$ mm, (c) $\xi = 70$ mm, (d) $\xi = 105$ mm, (e) $\xi = 141$ mm and (f) $\xi = 177$ mm.

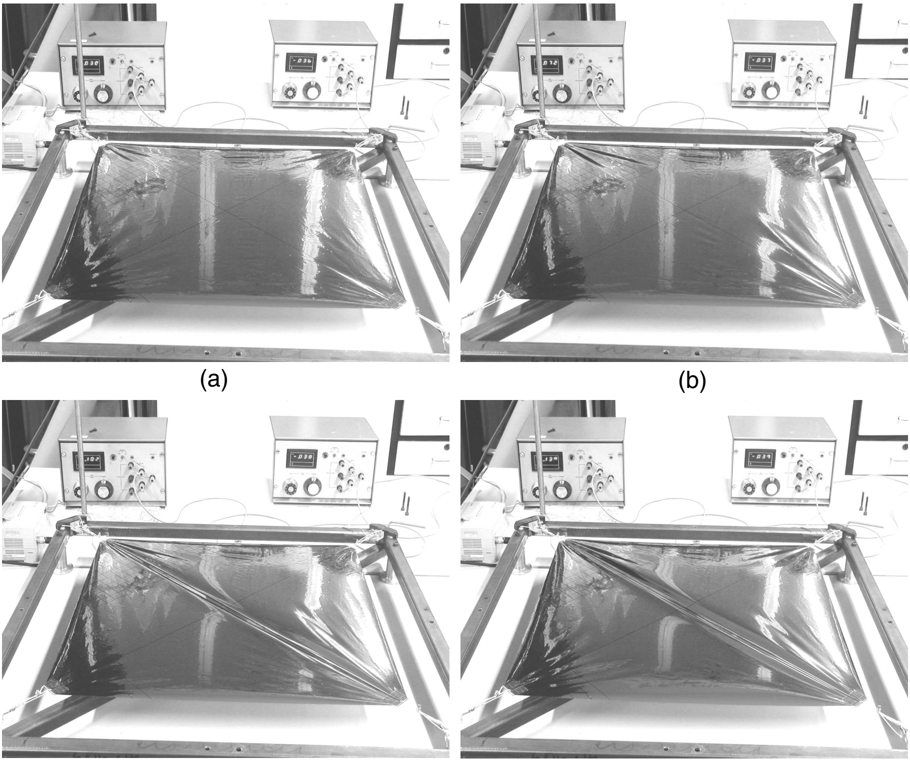

(a) (b) (c) (d)

Figure 10. Wrinkle pattern in 0.025 mm thick square Kapton® membrane for (a) $T_1/T_2 = 1$, (b) $T_1/T_2 = 2$, (c) $T_1/T_2 = 3$ and (d) $T_1/T_2 = 4$.

Figure 10 shows the overall wrinkle pattern in the membrane, for different load ratios. The wrinkle pattern was generally unchanged for T_1/T_2 up to 2, again with wrinkles radiating from the corners and the central wrinkle-free region gradually becoming smaller as the load ratio increased. The appearance of the membrane changed when T_1/T_2 was increased from 2 to 3; a diagonal wrinkle formed between the more heavily loaded corners and this diagonal wrinkle became more dominant, with a larger amplitude and wavelength when the maximum load ratio of $T_1/T_2 = 4$ was applied, as shown in Figure 10(d).

To monitor the growth of this diagonal wrinkle the profile of the membrane was measured at three cross-sections, $\xi = 105$ mm, $\xi = 177$ mm and $\xi = 355$ mm, for each load ratio. These profiles are plotted in Figure 11.

The most noticeable feature in these figures is a very large central wrinkle at $T_1/T_2 = 4$, with correspondingly large edge displacements, but not in Figure 11(c)

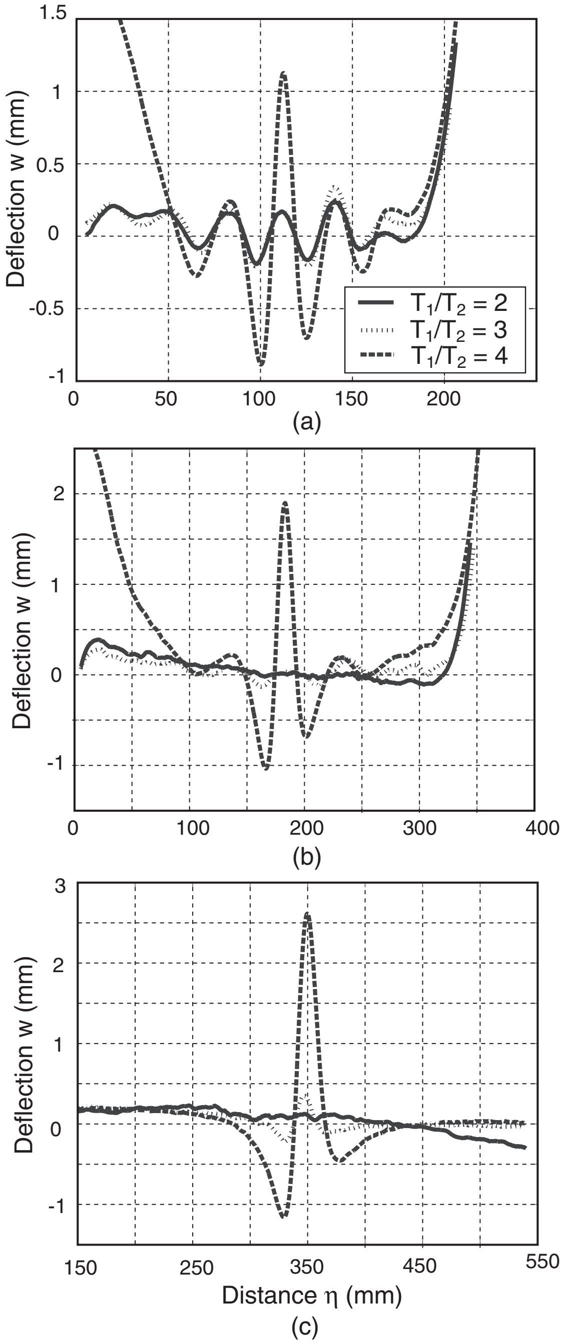

Figure 11. Wrinkle profiles for 0.025 mm thick, square Kapton® membrane at (a) $\xi = 105$, (b) $\xi = 177$ and (c) $\xi = 355$ mm for different load ratios.

which corresponds to a section of the membrane containing the other two corners of the membrane. The figure also shows that there are still no wrinkles beyond $\xi = 177$ mm for $T_1/T_2 = 2$. But at $T_1/T_2 = 3$, a wrinkle has started to form across the centre of the membrane, at $\xi = 355$ mm.

Similar experiments were conducted on two more Kapton® films, one thinner (0.0125 mm thick) and one thicker (0.05 mm). Both films exhibited the same behaviour as that described above for the 0.025 mm thick film. Photographs showing the wrinkle patterns observed in these films, under different load ratios can be found in [Wong 2003].

The situation can be summarised as follows. For load ratios up to 2, only corner wrinkles form in any of these membranes. These wrinkles are more obviously visible in the thinnest film, where many more wrinkles were observed, and are hardly noticeable in the thickest film. At $T_1/T_2 = 3$ a diagonal wrinkle was noticed in the central region of all films, and this wrinkle dominates the wrinkle pattern at the maximum load ratio of 4. In all cases, there were two small wrinkled regions in the other two corners of the membrane. The magnitudes of these smaller wrinkles were not measured.

5.3. ***Discussion.*** Average wrinkle wavelengths and amplitudes were obtained from the plots in Figure 9, and also from analogous plots for membranes of two other thicknesses; they are shown in Figure 12. These average values were computed over the central portion of the membranes, where “more uniform” wrinkle profiles are observed, and thus disregarding the side edges. Because the wrinkle profiles at lower stress levels had been found to be less uniform, the average wavelengths and amplitudes were computed from the wrinkle profiles measured at the highest load levels, which were $T = 10$ N for the 0.0125 mm thick film and $T = 20$ N for the 0.025 mm and 0.05 mm thick films.

The wrinkle wavelengths for all three membranes were found to increase approximately linearly with the distance from the corner, see Figure 12. This observation is consistent with the radial wrinkle pattern pointed out in Figure 10.

Figure 13 shows the longitudinal profile of an average wrinkle, obtained by plotting the average wrinkle amplitudes versus distance from the corner of the membrane. For the two thinner films these amplitudes first increase and then decrease, after attaining a maximum value approximately in the middle of the wrinkle profile, and generally both the wavelength and amplitude increase with the thickness of the membrane.

However, the thickest membrane did not follow these trends; it attained its maximum wrinkle amplitude much closer to the corner, at $\xi = 70$ mm. This difference is probably because the load-to-thickness ratio, which was kept constant in the 0.0125 mm and 0.025 mm thick membranes, was halved in the 0.05 mm thick

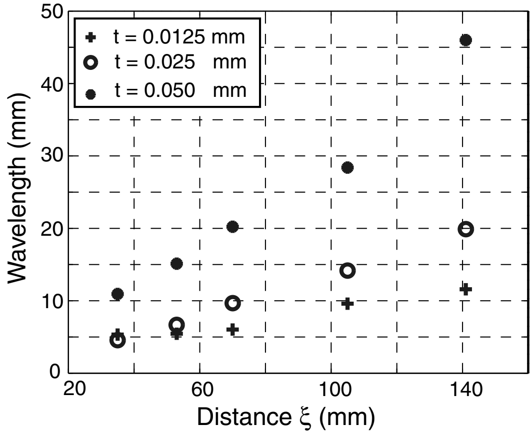

Figure 12. Average wrinkle wavelength in corner region of square membrane, vs. distance from corner, for $T_1/T_2 = 1$.

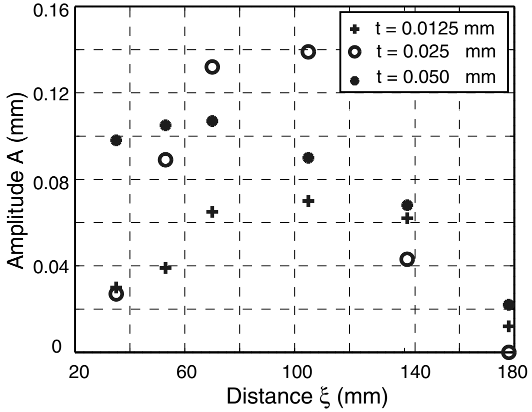

Figure 13. Longitudinal profile of corner wrinkles in square membrane, for $T_1/T_2 = 1$.

membrane, because the corner attachments could only carry a maximum load of only 20 N.

Thus, the profiles of the wrinkles in the thinner membranes can, again, be described quite accurately by a half sine wave, but this approximation becomes less accurate for thicker membranes under low stress.

For the asymmetric load case, the cross-sectional plots shown in Figure 11 have provided insight into the interaction between the large diagonal wrinkle and the (much smaller) corner wrinkles. Several other interesting details can be noted in these plots. For example, the wrinkle profile can be seen to have become (almost) anti-symmetric about a central diagonal line. Also, at the highest load ratio, $T_1/T_2 = 4$, both the width and the amplitude of the central diagonal wrinkle were found to increase with the distance from the corner. A detailed study by Wong [2003] has confirmed that for all three membrane thicknesses both of these parameters reach their maximum magnitude at the centre of the membrane, at $\xi = 355$ mm. The wrinkle profiles beyond this point are the mirror image of the profile in the first half membrane.

6. Conclusion

In addition to the points made in the detailed discussion presented at the end of each experiment, in Sections 4.4 and 5.3, there are some general features of the problems studied that should also be noted.

First, the two experiments presented in this paper share a number of common features, as follows.

- Wrinkle profile; well approximated by a half sine wave in the longitudinal direction with linearly-varying transverse wavelength in the transverse direction. Indeed, there is no wavelength variation at all in the sheared membrane problem.
- Mode jumping, that is, a sudden change in the number of wrinkles, occurs both in the central, uniformly wrinkled, part of the sheared membrane and in the corner regions of the square membrane. In both cases, this is due to the fact that only an integral number of wrinkles is allowed by the boundaries.

Second, on the other hand, some important differences have become apparent, as follows.

- Wrinkle pattern: its evolution is different in the two cases. Whereas in the sheared membrane the wrinkle pattern remains essentially unchanged for increasing shear displacement, in the square membrane a large diagonal wrinkle appears when the corner load ratio is around 3.
- Average stress: due to the presence of stress concentrations at the corners of the tabs, wrinkles appear in this membrane even though the average stress is rather low. One effect is that the wrinkle characteristics in the square membrane experiments appear to be more repeatable than in the sheared membrane, where slippage/yielding is prone to occur along the edges.

Although none of the features noted is particularly surprising, these are useful points to come back to in the following two papers in this series.

Acknowledgements

The authors thank Professor C. R. Calladine, FRS, for useful discussions and suggestions. Helpful suggestions by an anonymous reviewer are acknowledged. Financial support from NASA Langley Research Center (research grant NAG-1-02009, technical monitor Dr. K. Belvin) and the Cambridge Commonwealth Trust is gratefully acknowledged.

References

[Blandino et al. 2001] J. R. Blandino, J. D. Johnston, J. J. Miles, and J. S. Soplop, "Thin film membrane wrinkling due to mechanical and thermal loads", in *42th AIAA/ASME/ASCE/AHS/ASC Structures, Structural Dynamics and Material Conference and Exhibit*, 2001. AIAA-2001-1345.

[Blandino et al. 2002a] J. R. Blandino, J. D. Johnston, and U. K. Dharamsi, "Corner wrinkling of a square membrane due to symmetric mechanical loads", *J. Spacecraft Rockets* **39** (2002), 717–724.

[Blandino et al. 2002b] J. R. Blandino, J. D. Johnston, J. J. Miles, and U. K. Dharamsi, "The effect of asymmetric mechanical and thermal loading on membrane wrinkling", in *43rd AIAA/ASME/ASCE/AHS/ASC Structures, Structural Dynamics and Material Conference and Exhibit*, 2002. AIAA-2002-1369.

[Blandino et al. 2003] J. R. Blandino, R. Pappa, and J. Black, "Model identification of membrane structures with videogrammetry and laser vibrometry", in *44th AIAA/ASME/ASCE/AHS/ASC Structures, Structural Dynamics, and Material Conference and Exhibit*, 2003. AIAA-2003-1745.

[Cerda et al. 2002] E. Cerda, K. Ravi-Chandar, and L. Mahadevan, "Wrinkling of an elastic sheet under tension", *Nature* **419** (2002), 579–580.

[DuPont 2001] DuPont, "Summary of properties for Kapton polyimide film", 2001, Available at http://www.dupont.com/kapton.

[Epstein 2003] M. Epstein, "Differential equation for the amplitude of wrinkles", *AIAA Journal* **41** (2003), 327–329.

[Jenkins 2001] C. H. Jenkins, *Membrane and inflatable structures technology for space applications*, AIAA, Reston, VA, 2001.

[Jenkins et al. 1998] C. H. Jenkins, F. Haugen, and W. H. Spicher, "Experimental measurement of wrinkling in membranes undergoing planar deformation", *Experimental Mechanics* **38** (1998), 147–152.

[Mansfield 1968] E. H. Mansfield (editor), *Tension field theory a new approach which shows its duality with inextensional theory*, 1968.

[Mansfield 1970] E. H. Mansfield, "Load transfer via a wrinkled membrane", *Proc. R. Soc. Lond. A.* **316** (1970), 269–289.

[Mansfield 1989] E. H. Mansfield, *The bending and stretching of plates*, 2nd ed., Cambridge University Press, 1989.

[Mikulas 1964] M. M. Mikulas, "Behavior of a flat stretched membrane wrinkled by the rotation of an attached hub", NASA, 1964.

[Murphey 2000] T. W. Murphey, *A nonlinear elastic constitutive model for wrinkled thin films*, Ph.D. thesis, Department of Mechanical Engineering, University of Colorado at Boulder, 2000.

[Papa and Pellegrino 2005] A. Papa and S. Pellegrino, "Mechanics of systematically creased thin-film membrane structures", pp. 18–21 in *46th AIAA/ASME/ASCE/AHS/ASC Structures, Structural Dynamics and Materials Conference*, Austin, TX, April 2005 2005. AIAA 2005-1975.

[Reissner 1938] E. Reissner, "On tension field theory", pp. 88–92 in *Proc. 5th Int. Cong. Appl. Mech.*, 1938.

[Stein and Hedgepeth 1961] M. Stein and J. M. Hedgepeth, *Analysis of partly wrinkled membranes*, NASA Langley Research Center, 1961.

[Wagner 1929] H. Wagner, "Flat sheet metal girder with very thin metal web", *Zeitschrift für Flugtechnik Motorluftschiffahrt* **20** (1929), 200–207, 227–233, 256–262, 279–284.

[Wong 2003] Y. W. Wong, *Wrinkling of thin membranes*, Ph.D. thesis, University of Cambridge, 2003.

[Wong and Pellegrino 2002] Y. W. Wong and S. Pellegrino, "Amplitude of wrinkles in thin membrane", pp. 257–270 in *New approaches to structural mechanics, shells and biological structures*, edited by H. Drew and S. Pellegrino, Kluwer, 2002.

[Wong and Pellegrino 2006a] Y. W. Wong and S. Pellegrino, "Wrinkled membranes II: analytical models", *J. Mech. Materials Struct.* **1** (2006), 27–61.

[Wong and Pellegrino 2006b] Y. W. Wong and S. Pellegrino, "Wrinkled membranes III: numerical simulations", *J. Mech. Materials Struct.* **1** (2006), 63–95.

Received 3 Mar 2005. Revised 10 Oct 2005.

Y. WESLEY WONG: `wesleywong@cantab.net`

SERGIO PELLEGRINO: `pellegrino@eng.cam.ac.uk`
Department of Engineering, University of Cambridge, Trumpington Street, Cambridge, CB2 1PZ, United Kingdom

JOURNAL OF MECHANICS OF MATERIALS AND STRUCTURES
Vol. 1, No. 1, 2006

WRINKLED MEMBRANES
PART II: ANALYTICAL MODELS

Y. WESLEY WONG AND SERGIO PELLEGRINO

We present a general analytical model for determining the location and pattern of wrinkles in thin membranes and for making preliminary estimates of their wavelength and amplitude. A rectangular membrane under simple shear and a square membrane subject to corner loads are analysed. In the first problem, our model predicts the wavelength and the wrinkle amplitude to be respectively inversely proportional and directly proportional to the fourth root of the shear angle. Both values are directly proportional to the square root of the height and thickness of the membrane, and are independent of the Young's modulus. In the second problem two wrinkling regimes are identified. The first regime is characterised by radial corner wrinkles and occurs for load ratios less than $1/(\sqrt{2}-1)$; the number of wrinkles is proportional to the fourth root of the radius of the wrinkled region and the magnitude of the corner force, and inversely proportional to the Young's modulus and thickness cubed. The amplitude of these wrinkles is inversely proportional to their number, directly proportional to the square root of the radius of the wrinkled region and the magnitude of the corner force, and inversely proportional to the square root of the Young's modulus and thickness. The second regime occurs for load ratios larger than $1/(\sqrt{2}-1)$, and is characterised by a large diagonal wrinkle, plus small radial wrinkles at all four corners. Analytical expressions for the variation of the width and amplitude of the large wrinkle with the load ratio are obtained for this case also. All analytical predictions are compared with experimental and computational results from the other two papers in this series.

1. Introduction

This is the second paper in a three-part series that deals with estimating wrinkle details, i.e. shape, wavelength, and amplitude, in thin, initially flat and stress-free membranes subject to certain prescribed in-plane load and boundary conditions.

The first paper [Wong and Pellegrino 2006a] presented an experimental study of two different problems. First, a rectangular membrane whose longer edges are sheared uniformly, and thus forms a "parallelogram" of approximately uniform wrinkles at 45° to the edges. Second, a square membrane loaded by two pairs

---

Keywords: complementary strain energy bounds, membrane structures, wrinkling.

of equal and opposite diagonal forces applied at the corners, which forms fans of uniform corner wrinkles if the ratio between the larger pair of forces and the smaller ones is less than about 2.5, but forms a large diagonal wrinkle aligned with the pair of larger forces if the ratio is higher than 2.5. A particularly interesting feature of the second problem is the change in the wrinkle pattern in response to changes in the force ratio. Detailed measurements of the shape of the wrinkles were made, and trends in the variation of the wavelength and amplitude were observed in each case.

The present paper presents a simple analytical model for heavily wrinkled membranes. This model is able to explain many features of the behaviour observed in the experiments and leads to a general method for making approximate estimates of both the overall wrinkle pattern and the average wrinkle amplitude and wavelength. This method is then applied to the sheared membrane and the square membrane problems, and analytical expressions are obtained in each case for the wrinkle wavelength and amplitude. Finally, the predictions made from these expressions are compared with the experimental results from [Wong and Pellegrino 2006a] and computational results from [Wong and Pellegrino 2006b], and are found to be remarkably accurate.

The layout of the paper is as follows. Section 2 presents a brief review of the literature on analytical methods for determining the extent of the wrinkle region and, within it, the direction of the wrinkles. Here the classical assumption is that the bending stiffness of the membrane is negligible, and hence an infinitely large number of vanishingly small wrinkles should form. A more detailed review of the recent literature; in which the bending stiffness of the membrane is no longer neglected, is then presented. Solutions for uniform, parallel wrinkle amplitudes have been published. Section 3 outlines the key ideas of our simple analytical model. Section 4 applies this model to the sheared membrane; here the wrinkles are known to be at 45° to the edges and so the implementation of our analytical model is rather straightforward. Section 5 implements the model for the square membrane. Here no analytical characterization of the wrinkle region exists, and so a range of simple, approximate equilibrium stress fields are proposed; a criterion for selecting the best approximation (which depends on the ratio of corner loads) is suggested. The derivation of the wrinkle wavelength and amplitude then follows along similar lines to Section 4. Section 6 compares the analytical predictions obtained in Sections 4 and 5 with results from the other two papers in this series. Section 7 concludes the paper.

2. Review of previous analytical models

Membrane wrinkling has attracted much interest in the past, starting from the observation that the web of a thin-walled beam can carry loads well above the initial buckling value, which prompted the development of tension field theory by Wagner [1929]. Simpler and yet more general formulations of this theory were proposed by Reissner [1938] and Mansfield [1968; 1970; 1989].

Reissner explained this theory by considering a thin strip under shear. He noted that up to a certain intensity of the shear load a uniform state of shear stress is induced in the sheet. If the load is increased beyond this intensity buckling occurs; however, if the distance of the longer edges of the sheet is kept constant, the shear load can be increased without failure to an intensity much greater than that at which buckling first took place. The out-of-plane deformation of the sheet after wrinkles are formed has been characterised in the first paper in the present series.

Reissner noted that once wrinkles are formed, the strip is mainly stressed in tension along the wrinkles, while the compressive stress perpendicular to the wrinkles — which is the cause for the wrinkles — is small compared with the tensile stress. At this point the fundamental assumption of tension field theory is that this compressive stress, and also the bending stresses induced by the out-of-plane deformation, are negligible in comparison with the tensile stress. Therefore, the theory searches for plane stress solutions such that one principal stress is positive and the other is zero. This is done by considering an elastic, anisotropic material (whose material directions depend on the stress field) with modulus of elasticity $E_\eta = 0$, where η is the principal stress direction transverse to the wrinkles. Reissner showed that the line $\eta =$ constant is straight, and went on to derive expressions for the rotationally symmetric stress field in a sheet forming a circular annulus whose edges are sheared.

A generalization of this theory was later proposed by Mansfield [1968; 1970], who introduced the concept of a tension ray, defined by the trajectories of tensile principal stress (the wrinkle directions), which again must be straight. He showed that, given a wrinkled membrane whose boundaries are in part free and in part subjected to given planar displacements, the direction of the tension rays is such that the (stretching) strain energy is *maximised*. This results in a powerful variational technique with which Mansfield determined the tension rays in, among others, semi-infinite and finite length rectangular strips clamped to rigid tie rods (Figure 1). A comprehensive presentation of this work can be found in [Mansfield 1989].

With the same fundamental assumptions of the tension field theory, but allowing for finite strains, an alternative approach [Pipkin 1986] is to construct a *relaxed strain energy* such that if at a point both principal stretches are less than 1 (i.e.

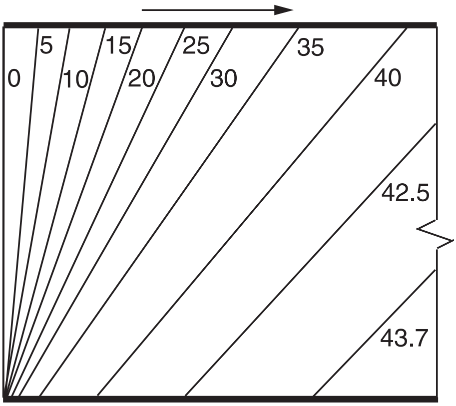

Figure 1. Tension rays in a semi-infinite membrane under simple shear, from [Mansfield 1989].

the membrane is slack) the relaxed strain energy is defined to be zero; if one principal stretch is greater than 1 the relaxed strain is defined on the basis of the larger stretch, and if both principal stretches are greater than 1 then a standard strain energy function is used. This formulation implicitly gets rid of compressive stresses, and has the advantage that it fits within a standard variational formulation. This approach was further developed and formalised by Steigmann [1990] and implemented numerically by Haseganu and Steigmann [1994] and Ligaro and Valvo [2000]. A generalization of the relaxed strain energy approach [Epstein and Forcinito 2001] in terms of a hyperelastic material which saturates when wrinkles form makes it easier to derive consistent expressions for the strain energy variations in the wrinkled state. Wu [1978], Wu and Canfield [1981], and Roddeman et al. [1987] have proposed to deal with wrinkling by modifying the deformation tensor such that the principal stress directions are either unchanged, in the case of isotropic membranes, or rotated appropriately in the case of anisotropic membranes.

Stein and Hedgepeth [1961] tackled the analysis of a partially wrinkled membrane, which can be divided into taut regions and wrinkled regions, by introducing the concept of a variable Poisson's ratio, which accounts for the geometric strains induced by wrinkling. These authors were able to obtain analytical solutions for, e.g., the moment-curvature relationship of a stretched rectangular membrane loaded by axial forces and bending moments at the ends. Here the wrinkles begin to form along the tension edge of the membrane, and propagate towards the neutral axis when the moment is increased.

A premise common to all of the above work is that a membrane is modelled as a *two-dimensional continuum unable to carry compression and with negligible bending stiffness*. Hence, it is implicitly assumed that an infinite number of wrinkles of

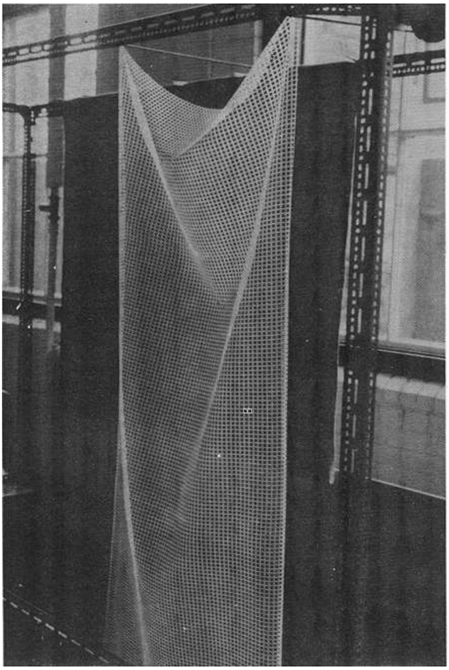

Figure 2. Wrinkles in a hanging "blanket", from [Rimrott and Cvercko 1986].

infinitesimally small amplitude would form; it is generally believed that the stress fields produced by these theories are a good approximation to the stress fields in real membranes, when they are heavily wrinkled [Steigmann 1990]. Analytical solutions for the onset of wrinkles in rectangular membranes subject to uniaxial tension plus simple shear were obtained by Lin and Mote [1996]; these solutions incorporate, of course, the bending stiffness of the membrane.

The first study of the shape of a heavily wrinkled membrane (as opposed to the lightly corrugated shape that occurs soon after the onset of wrinkles) which also took into account the role played by the membrane bending stiffness was the "hanging blanket" solution by Rimrott and Cvercko [1986]. Consider a membrane held at two corner points at the same height. A number of curved wrinkles form under the action of gravity (Figure 2). The tension-line field, i.e., the stress distribution that occurs in the membrane if out-of-plane displacements are neglected and yet no compressive stress is allowed anywhere in the membrane, had previously been determined by Mansfield [1981] for the case of a rectangular blanket. Rimrott and Cvercko [1986] considered a membrane with sinusoidal, instead of straight boundaries, and for this particular case obtained a solution for the *post-wrinkling*

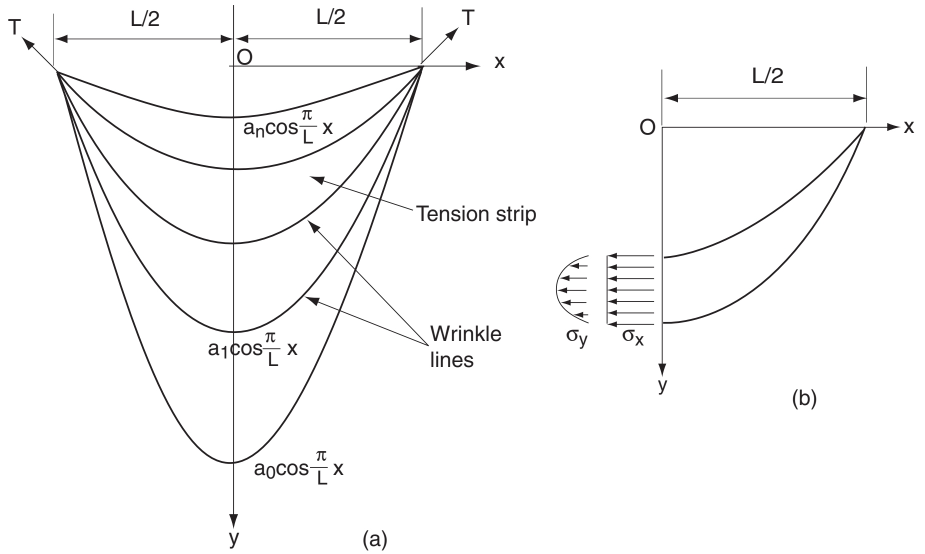

Figure 3. (a) Tension strips in hanging blanket and (b) detail of third tension strip, showing stress distribution along centre line, from Rimrott and Cvercko [1986].

tension-line field, where the membrane deforms out of plane while forming a number of wrinkles.

Rimrott and Cvercko noted that equilibrium of the membrane in the out-of-plane distorted configuration requires each finite-size wrinkle to carry a uniform horizontal force component; this horizontal force is equal in each wrinkle. Hence, having shown that the boundaries of the wrinkle lines (Figure 3) have amplitudes $a_n, \ldots, a_0$ that form a geometric progression ($a_i/a_{i+1} = \text{constant}$) it follows that the horizontal stress component, σ_x, at the centre of the wrinkle is largest in the more closely spaced wrinkles at the top of the membrane. Associated with σ_x, there is a compressive stress σ_y that vanishes at the edges of each finite-size wrinkle and reaches a maximum along the centre line of the wrinkle; see Figure 3(b). Rimrott and Cvercko assumed that the critical value, σ_{cr}, of this compressive stress is a characteristic of the blanket material and showed that for any chosen value of σ_{cr} there is corresponding number of finite-sized tension strips in the membrane.

Instead of Rimrott and Cvercko's "material constant", we have used for σ_{cr} the Euler buckling stress of an infinitely long, thin plate of thickness t, Young's modulus E, and Poisson's ratio ν [Wong and Pellegrino 2002]. Hence,

$$\sigma_{\text{cr}} = -\frac{\pi^2 E t^2}{12(1-\nu^2)\lambda^2}, \tag{1}$$

where the width of the plate, λ, matches the unknown half-wavelength of the wrinkle. We derived expressions for the wrinkle wavelength and amplitude in a long, rectangular membrane in simple shear. This approach, which forms the basis for the methodology presented in this paper, was extended in [Wong et al. 2003] to square membranes loaded by corner forces.

Epstein [2003] set up an approximate strain-energy analysis of a field of uniform, parallel wrinkles. Having assumed the wrinkles to be of sinusoidal shape longitudinally and to form circular arcs transversally (the same assumption had also been made by Murphey et al. [2002]), Epstein showed that, given a longitudinal strain ϵ_ξ and wrinkling strain (transverse) ϵ_η, the wrinkle amplitude is

$$A = \sqrt{2kL(\bar{\xi} - \bar{\xi}^2)}, \tag{2}$$

where $k = \sqrt{3\epsilon_\eta^2 t^2 / 2\epsilon_\xi (1 - \nu^2)}$ and $\bar{\xi} = \xi / L$ is a nondimensional length variable along the wrinkle (where L is the length of the wrinkle).

For the case of a square membrane of side length H, we have $\epsilon_\xi = \gamma/2$ and $\epsilon_\eta = \gamma(\nu - 1)/2$, and Epstein obtained

$$A = \sqrt{\sqrt{\frac{3\gamma}{4(1-\nu^2)}}(1 - \nu)\frac{\sqrt{2}Ht}{2}}. \tag{3}$$

Energy-based derivations of the amplitude and wavelength of uniform, parallel wrinkles in a rectangular sheet under tension were obtained by Cerda and Mahadevan [2003].

The model presented in the next sections unifies our previous solutions [Wong and Pellegrino 2002; 2003] and can be used to tackle other nonparallel, nonuniform wrinkle fields.

3. Analytical model: general features

Our analytical approach is in four parts, as follows.

First, we propose a two-dimensional stress field that involves no compression anywhere in the membrane; the regions where the minor principal stress is zero are then assumed to be wrinkled and the wrinkles are assumed to be aligned with the major principal stress directions. Ideally, both equilibrium and compatibility should be satisfied everywhere by this stress field, but analytical solutions in closed form (obtained by tension field theory, for example) exist only for simple boundary conditions. However, we will show in Section 6 that a carefully chosen, simple stress field that satisfies only equilibrium can provide quick solutions that are useful for preliminary design. When several such stress fields have been identified, an estimate of the complementary strain energy associated with each field is used to select the most accurate one. More accurate stress fields, leading to better estimates of the wrinkle details, can be obtained, of course, from a two-dimensional finite element stress analysis using membrane elements.

Second, we note that the bending stiffness of the membrane is finite, although small, and hence a compressive stress will exist in the direction perpendicular to the wrinkles. Because of its comparatively small magnitude, this stress was neglected in the first part of the analysis. We assume that this compressive stress varies only with the half-wavelength, λ, of the wrinkles and set it equal to the critical buckling stress of a thin plate in uniaxial compression. By Euler's formula applied to a plate of unit width [Calladine 1983], we have

$$\sigma_{\mathrm{cr}} = -\frac{\pi^2 E t^2}{12(1-\nu^2)\lambda^2} \tag{4}$$

Thus, the stress across the wrinkles is a known function of the wrinkle wavelength.

Third, in each wrinkled region we describe the out-of-plane displacement of the membrane, w, in terms of an unknown magnitude, A, and sinusoidal shape functions in a ξ, η coordinate system. The ξ and η-axes are aligned with the principal curvature directions, i.e. tangent and transverse to the wrinkles, respectively, and the half-wavelengths of these shape functions correspond to the length and width of the wrinkles. Thus, w automatically vanishes along the boundaries of the wrinkled zone.

The equation of equilibrium in the out-of-plane direction for a membrane that is not subject to any out-of-plane loading can be written in the form

$$\sigma_\xi \kappa_\xi + \sigma_\eta \kappa_\eta = 0 \tag{5}$$

(see [Calladine 1983]), where κ_ξ and κ_η are the principal curvatures, which can be obtained by differentiation of w. Since the stress distribution along the wrinkles is known, from the stress field determined during the first part of the analysis, in the transverse direction it can be assumed that

$$\sigma_\eta = \sigma_{\mathrm{cr}} \tag{6}$$

Enforcing Equation (5) at a single point, the midpoint of a wrinkle will be chosen, provides an equation from which λ can be determined.

Fourth, the wrinkle amplitudes are estimated by considering the total transverse strain ϵ_η as the sum of two components, a material strain (due to Poisson's ratio effects) and a wrinkling strain (due to in-plane geometric contraction associated with out-of-plane displacement). The sum of these two strains must match the boundary conditions imposed, e.g. by the wrinkle-free regions of the membrane.

Next, this general wrinkle model will be employed to predict the wrinkle details in two specific examples.

4. Analysis of membrane in shear

Consider a flat rectangular membrane of length L, height H, and thickness t, with clamped long edges and short free edges. The upper edge is translated by an amount δ in the direction of the edge itself, thus subjecting the membrane to a state of simple shear that causes the formation of a series of wrinkles, as seen in Figure 4. A full explanation of the resulting wrinkle pattern was presented in [Wong and Pellegrino 2006a], but here we will focus on the uniform wrinkles at 45° to the edges, in the central part of the membrane.

Consider one of these uniform wrinkles in the central, uniformly wrinkled part of the membrane, depicted in Figure 5.

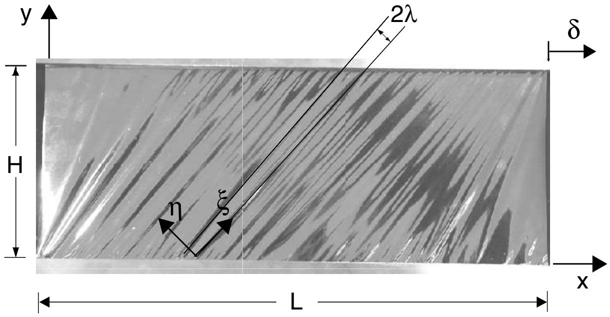

Figure 4. Rectangular Kapton sheet under simple shear.

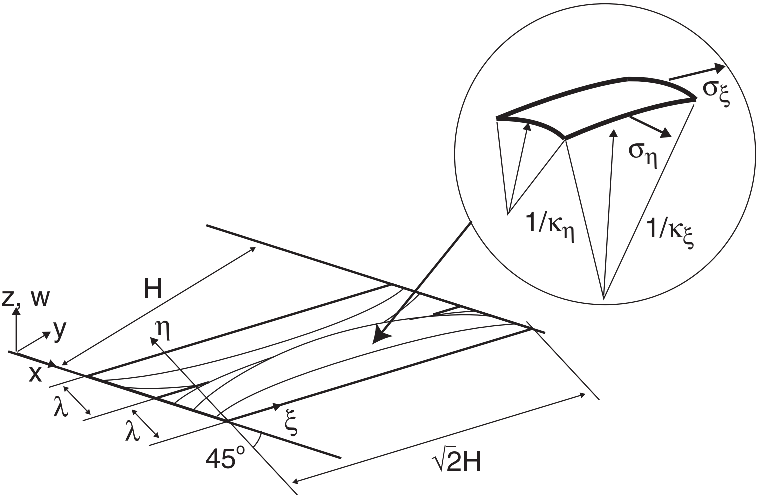

Figure 5. Perspective view of a single wrinkle.

Note that the initially flat membrane has deformed into a doubly-curved surface, alternately above and below the original xy plane of the membrane. This wrinkled surface intersects the xy plane at a regular spacing λ, defined as the half-wavelength of the wrinkle; neglecting edge effects, it can be assumed that these intersections occur along straight lines.

A simple mode-shape describing the wrinkled surface can be readily set up using the coordinate system ξ, η shown in Figure 5, where ξ is along the said intersection line, i.e. parallel to the wrinkle direction, and η is perpendicular to it. The boundary conditions on the out-of-plane displacement w are satisfied if we assume the mode shape

$$w = A \sin \frac{\pi(\xi + \eta)}{\sqrt{2}H} \sin \frac{\pi \eta}{\lambda} \tag{7}$$

Nothing is said at this stage about in-plane deflection. Since the wrinkles are long and narrow, $\eta \ll \xi$ apart from a small region near the origin. Hence, the mode shape can be simplified to

$$w \approx A \sin \frac{\pi \xi}{\sqrt{2}H} \sin \frac{\pi \eta}{\lambda} \tag{8}$$

The stress field consists of tension rays at 45° to the edges, and the stress along the wrinkles, σ_ξ, is much larger than the transverse stress, σ_η. Hence, neglecting σ_η when writing the stress-strain relationship in the ξ-direction, we obtain

$$\sigma_\xi = E\epsilon_\xi \tag{9}$$

For simple shear

$$\epsilon_\xi = \gamma/2 \tag{10}$$

where $\gamma = \delta/H$ and, substituting into Equation (9) we obtain

$$\sigma_\xi = E\gamma/2 \tag{11}$$

Recall that, although σ_η is relatively small in comparison with σ_ξ, in order for the wrinkle to have formed, the transverse stress must have reached the critical buckling stress given in (4).

The principal curvatures that appear in the equilibrium equation (5) can be determined as in [Calladine 1983] by differentiating (8):

$$\kappa_\xi = -\frac{\partial^2 w}{\partial \xi^2} = \frac{\pi^2 A}{2H^2} \sin \frac{\pi \xi}{\sqrt{2}H} \sin \frac{\pi \eta}{\lambda}, \tag{12}$$

$$\kappa_\eta = -\frac{\partial^2 w}{\partial \eta^2} = \frac{\pi^2 A}{\lambda^2} \sin \frac{\pi \xi}{\sqrt{2}H} \sin \frac{\pi \eta}{\lambda}. \tag{13}$$

These expressions are only exact where $\partial w/\partial \xi \approx 0$ and $\partial w/\partial \eta \approx 0$, which is indeed the case at a wrinkle mid point. Substituting Equations (4), (11), (12) and

(13) into (5), simplifying and rearranging yields for the wrinkle half-wavelength the expression

$$\lambda = \sqrt{\frac{\pi H t}{\sqrt{3(1-\nu^2)\gamma}}}. \tag{14}$$

To find an expression for the amplitude, A, of the wrinkle we note that the imposed strain ϵ_η, given by

$$\epsilon_\eta = -\gamma/2, \tag{15}$$

(as can be seen from Mohr's circle), has to be equal to the sum of the material strain

$$\epsilon_{\eta \mathrm{M}} = -\frac{\nu}{E}\sigma_\xi \tag{16}$$

with the average geometric strain, $\epsilon_{\eta \mathrm{G}}$, produced by wrinkling. This wrinkling strain is obtained by taking the difference between the projected width of a wrinkle and its actual width, and dividing by the actual width. Hence

$$\epsilon_{\eta \mathrm{G}} = \frac{\lambda - \displaystyle\int_0^\lambda \left(1 + \frac{1}{2}\left(\frac{\partial w}{\partial \eta}\right)^2\right) d\eta}{\displaystyle\int_0^\lambda \left(1 + \frac{1}{2}\left(\frac{\partial w}{\partial \eta}\right)^2\right) d\eta}. \tag{17}$$

Here, assuming the slope $\partial w/\partial \eta$ to be small, the term $(\partial w/\partial \xi)^2$ in the denominator can be neglected.

Next, consider the centre line across a wrinkle, and hence substitute $\xi = H/\sqrt{2}$ into (8). Substituting the resulting expression for w into (17) and working out the in integral gives

$$\epsilon_{\eta \mathrm{G}} = -\frac{\pi^2 A^2}{4\lambda^2}. \tag{18}$$

Finally, setting

$$\epsilon_\eta = \epsilon_{\eta \mathrm{M}} + \epsilon_{\eta \mathrm{G}} \tag{19}$$

as explained, we obtain

$$-\frac{\gamma}{2} = -\frac{\nu}{E}\sigma_\xi - \frac{\pi^2 A^2}{4\lambda^2}. \tag{20}$$

Substituting (11) into (20) and solving for A gives

$$A = \frac{\sqrt{2(1-\nu)\gamma}}{\pi}\lambda, \tag{21}$$

from which λ can be eliminated using Equation (14), to find

$$A = \sqrt{\frac{2Ht}{\pi}\sqrt{\frac{(1-\nu)\gamma}{3(1+\nu)}}}. \tag{22}$$

It can be readily verified that this expression is equivalent to that obtained by Epstein [2003], apart from a factor of 0.77. This discrepancy is mainly due to the fact that Epstein assumed circular arcs as the wrinkle mode shape, instead of a double sinusoid.

4.1. ***An energy approach.*** An alternative approach to find λ for the present, simple boundary conditions, is to set up an expression for the strain energy in a wrinkled thin plate, including the second-order strain due to out-of-plane deflection, and to minimize with respect to λ. The membrane is modelled as a thin plate stretched in the ξ-direction and wrinkled in the η-direction.

The general expression for the bending strain energy per unit area of an initially flat plate that is bent into a cylindrical shape of curvature κ_η is

$$U_b = \frac{1}{2}\frac{Et^3}{12(1-\nu^2)}\kappa_\eta^2. \tag{23}$$

As κ_η is not constant — see Equation (13) — the average strain energy per unit area, $\overline{U}_b$, is obtained from

$$\overline{U}_b = \frac{1}{2}\frac{Et^3}{12(1-\nu^2)}\left(\frac{1}{\sqrt{2}H\lambda}\int_0^\lambda\int_0^{\sqrt{2}H}\kappa_\eta^2\,d\xi\,d\eta\right) = \frac{1}{2}\frac{Et^3}{12(1-\nu^2)}\frac{\pi^4A^2}{4\lambda^4}. \tag{24}$$

The stretching strain energy per unit area can be obtained, neglecting stretching in the η-direction, from

$$U_s = \tfrac{1}{2}Et\epsilon_\xi^2. \tag{25}$$

Here, ϵ_ξ is the sum of the strain due to the in-plane shear, Equation (10), plus that due to the out-of-plane deflection due to wrinkling:

$$\epsilon_\xi = \frac{\gamma}{2} + \frac{1}{2}\left(\frac{\partial w}{\partial \xi}\right)^2. \tag{26}$$

Thus ϵ_ξ is also not constant. Hence, consider the average strain energy per unit area over a wrinkle, $\overline{U}_s$, given by

$$\overline{U}_s = \frac{1}{2}Et\left(\frac{1}{\sqrt{2}H\lambda}\int_0^\lambda\int_0^{\sqrt{2}H}\epsilon_\xi^2\,d\xi\,d\eta\right) \approx \frac{Et}{2}\frac{\gamma^2}{4} + \frac{Et}{2}\frac{\pi^2A^2\gamma}{16H^2}. \tag{27}$$

The first of these terms is independent of the wrinkle amplitude, A; therefore it will not be carried through to the next stage of the analysis.

The total mean strain energy per unit area (neglecting the term without A) is given by

$$\overline{U} = \overline{U}_b + \overline{U}_s = \frac{1}{2}\frac{Et^3}{12(1-\nu^2)}\frac{\pi^4A^2}{4\lambda^4} + \frac{Et}{2}\frac{\gamma^2}{4} + \frac{Et}{2}\frac{\pi^2A^2\gamma}{16H^2}. \tag{28}$$

Next, expressing A in terms of λ, Equation (21), we obtain

$$\overline{U} = \frac{(1-\nu)Et\gamma}{2}\left(\frac{\pi^2 t^2}{24(1-\nu^2)\lambda^2} + \frac{\gamma\lambda^2}{8H^2}\right). \tag{29}$$

Differentiating with respect to λ and setting $d\overline{U}/d\lambda = 0$ gives an expression equivalent to Equation (14). This result shows that the simple equilibrium formulation with an assumed stress σ_η, presented in Section 4, captures the same effects as the analytically more elaborate energy formulation.

5. Analysis of membrane under corner loads

The second problem considered in this paper is an initially flat, square membrane of side length $L+2a$ and thickness t, subjected to two pairs of equal and opposite corner forces, T_1 and T_2, as shown in Figure 6. Note that the actual corners of the membrane have been removed, and it is assumed that the concentrated loads are applied to the membrane through rigid beams of length d. We are interested in determining the wrinkle pattern for different values of the ratio T_1/T_2. This problem was investigated experimentally in [Wong and Pellegrino 2006a, Section 5].

A key difficulty in extending the approach of Section 3 to the present problem is that no tension field solution is known for this problem and so an approximate solution will be sought. We propose four different, no-compression "equilibrium" stress fields, some of which are only valid if the ratio of the corner forces is in a particular range. For each stress distribution an upper-bound estimate of the corner displacements will be obtained, and so, when for a given load ratio and membrane dimensions there is more than one potential stress distribution, the best

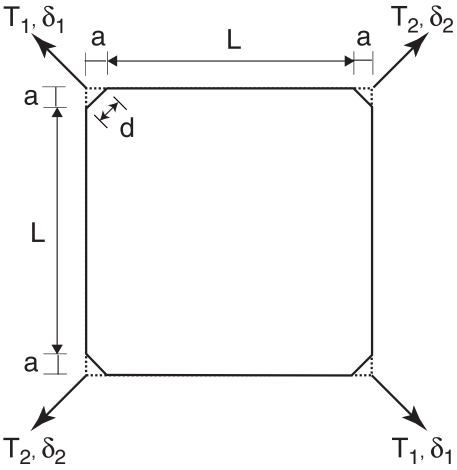

Figure 6. Square membrane subject to corner loads.

approximation to the actual stress field in the membrane will be obtained by choosing the particular distribution that produces the lowest upper bound for the corner deflections.

5.1. ***Stress fields.*** Figure 7 shows four possible stress fields, all of which satisfy equilibrium everywhere and involve no compressive stress at any point. In each case the membrane has been divided into regions that are either unloaded or subject to a simple state of stress. The stress field in Figure 7(b) is valid only for $T_1 = T_2$,

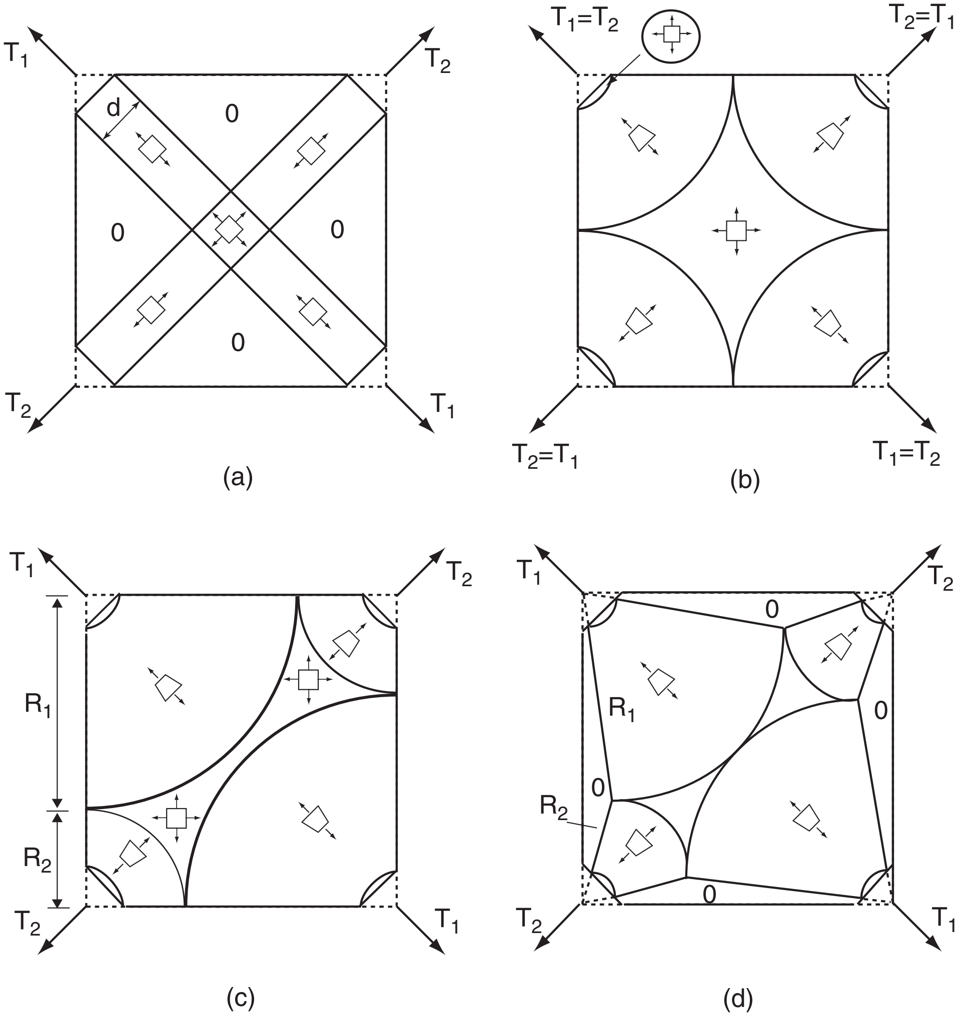

Figure 7. Equilibrium stress fields: (a) diagonal strip field; (b, c) wedge fields; (d) variable angle wedge field. A trapezium denotes a purely radial stress field.

while the others are more general, although still subject to some restrictions to be explained later.

Although equilibrium is satisfied, there is no guarantee that the elastic strains associated with these fields are compatible; indeed obvious compatibility violations can be easily detected for the simpler fields.

For each stress field it is possible to produce an estimate of the corresponding corner displacements, δ_1 and δ_2, defined in Figure 6. These displacements are computed using an upper-bound approach based on the complementary strain energy in the membrane.

The theorem of minimum complementary energy [Calladine 1983] states that the total complementary energy in a linear-elastic structure is minimum for the actual stress distribution. Hence, for an assumed stress field satisfying equilibrium but not necessarily compatibility, the complementary energy will be higher than for the actual stress distribution; thus

$$U \leqslant U^*, \tag{30}$$

where U and U^* are the actual and the estimated complementary energies. Hence, given a set of stress fields, we will define the "best" to be the stress field that produces the smallest estimate of U^*.

U^* can be calculated from

$$U^* = \frac{1}{2} \int_V (\epsilon_1 \sigma_1 + \epsilon_2 \sigma_2)\, dV, \tag{31}$$

where σ_i and ϵ_i denote the principal stresses and strains.

By conservation of energy, U is given for two given sets of corner forces, T_i, and corresponding corner displacements δ_i by

$$U = \frac{1}{2} \sum_{i=1}^{2} 2T_i \delta_i = T_1 \delta_1 + T_2 \delta_2. \tag{32}$$

Hence, from Equation (30), the average of the corner displacements, each weighted by the corresponding applied forces, determined by means of this method, is always an upper bound to the correct value.

Diagonal strip field. Figure 7(a) shows a simple stress field, consisting of four diagonal tension strips of width d, each under uniform uniaxial stress, plus a biaxially stressed centre region. The remaining parts of the membrane are unstressed.

For the case of symmetric loading, $T_1 = T_2 = T$ and $\delta_1 = \delta_2 = \delta$, the uniaxial stress in the tension strips is

$$\sigma_t = \frac{T}{dt} \tag{33}$$

and the complementary energy in each diagonal region is

$$U_1^* = \frac{1}{2}\int_V \frac{\sigma_t^2}{E} dV = \frac{T^2 L}{2\sqrt{2} d E t}, \tag{34}$$

whereas the complementary energy in the central biaxially stressed region is

$$U_2^* = \int_V \frac{\sigma_t^2(1-\nu)}{E} dV = \frac{T^2(1-\nu)}{Et}. \tag{35}$$

Hence, considering the four diagonal regions plus the central region, the total complementary energy for this stress field is

$$U^* = \frac{T^2}{Et}\left(\frac{\sqrt{2}L}{d} + (1-\nu)\right). \tag{36}$$

Therefore, the corner displacement, δ, can be determined from (30), (32), and (36) which give

$$\delta \leqslant \frac{T}{2Et}\left(\frac{\sqrt{2}L}{d} + (1-\nu)\right). \tag{37}$$

Wedge field. The second stress field, shown in Figure 7(b), is for symmetric load cases, $T_1 = T_2 = T$ and $\delta_1 = \delta_2 = \delta$. This field is based around four identical wedges subject to purely radial stress, joined by a central region under uniform biaxial stress, and with small corner lunes also under uniform biaxial stress. Detailed views are shown in Figure 8.

The stress distribution in the wedge region, ABCD, is assumed to be purely radial and inversely proportional to the distance r from the apex O:

$$\sigma_r = \frac{T}{\sqrt{2}rt}, \tag{38}$$

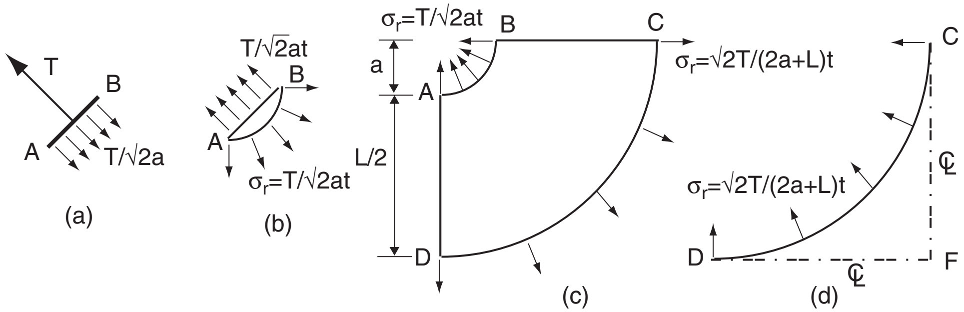

Figure 8. Components of wedge field: (a) free body diagram of edge beam; (b) biaxially stressed corner lune; (c) radially stressed wedge region; (d) one quarter of biaxially stressed centre region.

where $a < r < a + L/2$. Hence, the radial stress is uniform on any circular arc and all other stress components are zero. It can be readily shown that this distribution satisfies equilibrium, indeed this distribution was inspired from the classical plane-stress solution for a wedge-shaped thin plate [Timoshenko and Goodier 1970].

The radial stress along the curved edges of this wedge are equilibrated by two regions of uniform, biaxial stress: the lune AB and the central region defined by the arc CD and the symmetry lines CF and DF. The stress magnitudes in these two regions are obtained by substituting $r = a$ and $r = a + L/2$, respectively, into (38).

The complementary energy for each of these regions can be found by an approach analogous to that described in Section 5.1, although now the derivation is much lengthier as the integration of the complementary strain energy has to be carried out over several regions. Thus we obtain for the corner displacement the upper bound

$$\delta \leqslant \frac{T}{4Et}\left(\pi \ln\left(1 + \frac{L}{2a}\right) + 2(1 - \nu)\right). \tag{39}$$

This type of stress field can be extended to asymmetric loading. Starting from the symmetric case described above, consider increasing T_1. For equilibrium to be still satisfied, the key requirement is that the radial stress along the four arcs bounding the central region should be uniform. Since now σ_r in each wedge region is proportional to T_i/r, we can compensate for the increase in T_1 by increasing correspondingly the outer radius of this wedge, or by decreasing the outer radius of the wedge corresponding to T_2, or both; see Figure 7(c). For the stress along the edges of the centre region to be uniform, clearly we require that $R_1/R_2 \propto T_1/T_2$.

This approach is valid until the two arcs of larger radius touch at the centre of the membrane, which happens when

$$\frac{R_1}{R_2} = \frac{T_1}{T_2} = \frac{1}{\sqrt{2} - 1} \approx 2.41. \tag{40}$$

When $T_1 \neq T_2$ the corner displacements δ_1 and δ_2 are also different. Hence, computing the overall complementary energy does not lead to a bound on a particular corner displacement. A useful estimate of the radial corner displacements can be obtained by dividing the membrane into two parts, each associated with the displacements of a pair of opposite corners; the split is illustrated in Figure 9. For example, the corners loaded by T_1 are associated with the larger two wedges, plus the two areas labelled A_1.

The areas labelled A_1 and A_2 needed for the complementary strain energy calculation are given by

$$A_1 = \frac{(R_1 + R_2)^2}{2} - \frac{\pi R_1^2}{4} - R_2^2 = \frac{1}{2}\left(1 - \frac{\pi}{2}\right) R_1^2 + R_1 R_2 - \frac{R_2^2}{2}$$

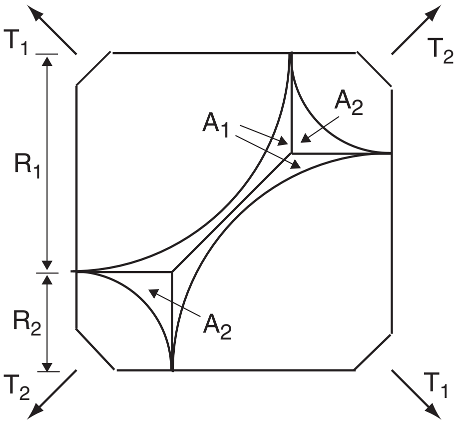

Figure 9. Partitioning of membrane for energy calculation.

and

$$A_2 = R_2^2 - \frac{\pi R_2^2}{4}.$$

Thus, after computing the complementary strain energy associated with each corner, we obtain

$$\delta_1 \leqslant \frac{T_1}{4Et}\left(\pi \ln \frac{R_1}{a} + \frac{1-v}{R_1^2}(4R_1R_2 - 2R_2^2)\right), \tag{41}$$

$$\delta_2 \leqslant \frac{T_2}{4Et}\left(\pi \ln \frac{R_2}{a} + 2(1-\nu)\right). \tag{42}$$

Note that, although Equations (41) and (42) are useful tools for design, they are not rigorous expressions, since their validity is not underpinned by the complementary energy theorem.

Variable angle wedge field. As stated earlier, the wedge stress field presented in Section 5.1 is only valid up to $T_1/T_2 \approx 2.41$. At this point the edges of the larger two wedges come into contact, thus forming a single region (continuous between the two most heavily loaded corners of the membrane) without tensile stress in the transverse direction. Note that the limit of 2.41 closely corresponds to the load ratio at which a diagonal wrinkle was first observed experimentally [Wong and Pellegrino 2006a].

A more general stress field, which allows us to consider larger values of T_1/T_2, has been shown in Figure 7(d). Here, the outer radius of the wedges corresponding to the larger loads is kept equal to the value at which the wedges meet at the centre of the membrane

$$R_1 = a + L/\sqrt{2} \tag{43}$$

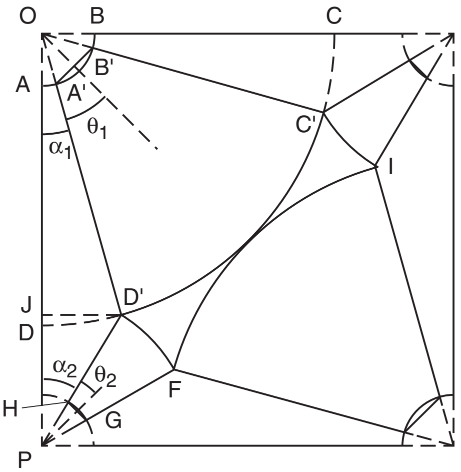

Figure 10. Geometry of variable angle wedge field.

but the angle subtended by these wedges, $2\theta_1$, is allowed to vary, depending on T_1/T_2. This has the effect that the outer radius of the remaining two wedges also varies.

Thus, this stress field consists of: four wedges subject to purely radial stress (A′B′C′D′, D′FGH, etc.); a central region under uniform biaxial stress (C′D′FI); and four corner lunes also under biaxial stress. This leaves four triangular edge regions that are unstressed. The acute angles of these triangles are related to the wedge half-angles by

$$\alpha_i = \frac{\pi}{4} - \theta_i. \tag{44}$$

The stress distribution in each of the four wedge regions is given by a generalization of (38) to a wedge subtending an angle of $2\theta_i$

$$\sigma_r = \frac{T_i}{2rt\sin\theta_i}. \tag{45}$$

Hence, the normal stress along the edges of C′D′FI is obtained by substituting $r = R_1$ and $r = R_2$ into (45), and for the two magnitudes to be equal we require

$$\frac{T_1}{2R_1 t\sin\theta_1} = \frac{T_2}{2R_2 t\sin\theta_2}. \tag{46}$$

Rearranging (46) we obtain the general condition

$$\frac{R_2\sin\theta_2}{\sin\theta_1} = \frac{R_1 T_2}{T_1}. \tag{47}$$

For any given T_1 and T_2, and since R_1 is known, R_2, θ_1, and θ_2 have to satisfy this condition.

Two additional conditions on R_2, θ_1, and θ_2 are obtained as follows. For the first condition, note that

$$\overline{JD'} = \overline{OD'} \sin\alpha_1 = R_1 \sin\left(\frac{\pi}{4} - \theta_1\right) \tag{48}$$

and also

$$\overline{JD'} = \overline{PD'} \sin\alpha_2 = R_2 \sin\left(\frac{\pi}{4} - \theta_2\right). \tag{49}$$

Equating these expressions for $\overline{JD'}$ and rearranging

$$R_2 = R_1\left(\sin\frac{\pi}{4} - \theta_1\right)\Big/\left(\sin\frac{\pi}{4} - \theta_2\right). \tag{50}$$

For the second condition, apply the sine rule to D′OP to obtain

$$\frac{R_1}{\sin\alpha_2} = \frac{2a + L}{\sin(\pi - \alpha_1 - \alpha_2)} \tag{51}$$

Substituting Equation (44) and grouping all unknowns on the right-hand side gives

$$\frac{\cos(\theta_1 + \theta_2)}{\sin\left(\frac{\pi}{4} - \theta_2\right)} = \frac{2a + L}{R_1}. \tag{52}$$

Equations (47), (50), and (52) can be solved for any given value of $T_1/T_2 > 1/(\sqrt{2} - 1)$ to determine the corresponding parameters of the stress field.

Figure 11 is a plot of the variation with T_1/T_2 of the angles that determine the four wedges, θ_1 and θ_2. Note that, since the wedge angles become smaller as T_1/T_2 increases, the slack regions along the edges of the membrane, denoted by a “0” in Figure 7(d), get bigger.

The complementary strain energy associated with each of the corner displacements is then calculated, splitting the central, biaxially stressed region into areas A_1 and A_2, which now have the expressions

$$\begin{aligned} A_1 &= \frac{(2a + L)^2}{2} - R_1^2(\theta_1 + \sin\alpha_1\cos\alpha_1) - R_2^2\cos^2\alpha_2, \\ A_2 &= R_2^2(\cos^2\alpha_2 - \theta_2 - \sin\alpha_2\cos\alpha_2). \end{aligned}$$

Thus, following the same approach as in Section 5.1, we obtain

$$\delta_i \le \frac{T_i}{4Et\sin^2\theta_i}\left(2\theta_i \ln\frac{R_i}{a} + (1 - \nu)(\theta_i - \sin\theta_i\cos\theta_i) + \frac{A_i}{R_i^2}\right), \tag{53}$$

where i takes the values 1 or 2, depending on the corner of interest.

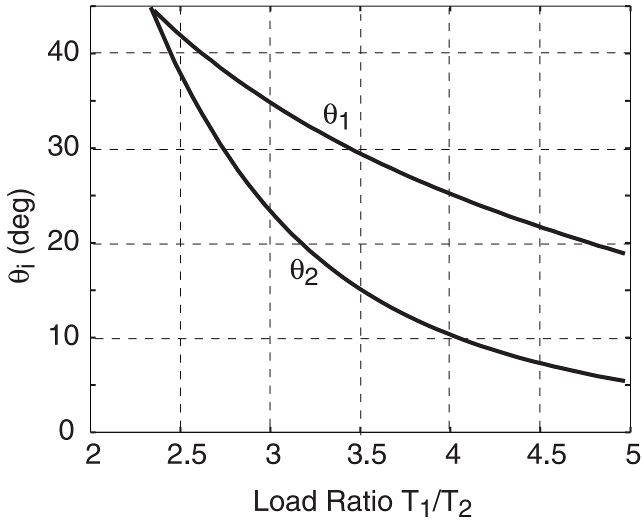

Figure 11. Geometric parameters of variable angle wedge field.

5.2. ***Wrinkle details.*** Based on the no-compression stress fields that have been proposed in Section 5.1, two different kinds of wrinkle patterns can be expected. Note that the diagonal strip stress field was included only for the sake of explanation but, as it does not lead to accurate estimates, it will not be used for any further analysis.

If $T_1/T_2 < 1/(\sqrt{2}-1)$, there is a biaxially stressed region at the centre of the membrane, separating four uniaxially stressed corner regions. Hence, four separate fans of wrinkles will form near the corners, but they cannot go through the centre. If $T_1/T_2 \geq 1/(\sqrt{2}-1)$, the two larger uniaxial stress regions join up at the centre of the membrane. Hence, there is a continuous, narrow diagonal region that is uniaxially stressed, and so in this case a small number of wrinkles can go all the way from one highly loaded corner to the other.

In the first case, we will assume each fan to consist of identical, radial wrinkles that start right at the edge of a biaxially stressed corner lune and extend as far as an unknown radius, R_w. This analysis can be more easily explained for the case of symmetric loading. In the second case, although fans of wrinkles will also form, we will focus on the much larger, diagonal wrinkle parallel to the loads T_1.

Corner wrinkles. Figure 12 shows a corner of a symmetrically loaded membrane. Here, R_w denotes the outer radius of the wrinkled zone, and it is assumed that the wrinkles start right at the edge of the biaxially stressed lune, AB. Note that in the region between R_w and R the formation of wrinkles is possible, because the stress is still uniaxial, but there isn't enough spare material for the wrinkles to actually

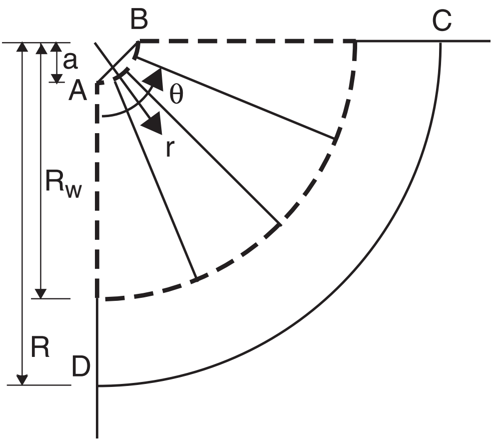

Figure 12. Region affected by fan of $n = 4$ half-wrinkles.

show. R denotes the outer radius of the wedge stress field, hence $R = a + L/2$ for symmetric loading. However, we will keep the more general notation.

The profile of the membrane in the wrinkled zone is assumed to be given by

$$w = A \sin \frac{\pi(r - a)}{R_w - a} \sin 2n\theta, \tag{54}$$

where the angle θ is measured from an edge of the membrane, A is an unknown amplitude, and n is the total number of half-wrinkles, each subtending an angle of $\pi/2n$. Note that the particular mode shape sketched in Figure 12 and assumed in Equation (54) sets the out-of-plane displacement of the membrane to zero along the edges, and assumes an integer number of half-wrinkles, for simplicity.

The value of n can be determined by considering out-of-plane equilibrium in the middle of a wrinkle. At such a point the principal directions of curvature are r and θ, and hence the equilibrium equation is

$$\sigma_r \kappa_r + \sigma_\theta \kappa_\theta = 0, \tag{55}$$

where κ_r and κ_θ are the radial and hoop curvatures obtained by differentiation of Equation (54). Hence,

$$\kappa_r = -\frac{\partial^2 w}{\partial r^2} = \frac{A\pi^2}{(R_w - a)^2} \sin \frac{\pi(r - a)}{R_w - a} \sin 2n\theta,$$

$$\kappa_\theta = -\frac{1}{r^2}\frac{\partial^2 w}{\partial \theta^2} = \frac{4An^2}{r^2} \sin \frac{\pi(r - a)}{R_w - a} \sin 2n\theta.$$

The centre of a wrinkle is the point where the curvatures are maximum, hence it is located at

$$\tilde{r} = \frac{R_w + a}{2} \tag{56}$$

The maximum curvatures are therefore

$$\tilde{\kappa_r} = \frac{A\pi^2}{(R_w - a)^2}, \qquad \tilde{\kappa_\theta} = \frac{16An^2}{(R_w + a)^2}. \tag{57}$$

The radial stress at the centre of the wrinkle is obtained by substituting Equation (56) into the general expression for the wedge field, Equation (38). Hence

$$\sigma_r = \frac{\sqrt{2}T}{(R_w + a)t}. \tag{58}$$

The hoop stress will be set equal to the critical buckling stress, Equation (4), with λ set equal to the central wrinkle half-wavelength, $\tilde{\lambda}$. Hence,

$$\tilde{\lambda} = \frac{\pi\tilde{r}}{2n} = \frac{\pi(R_w + a)}{4n}$$

and so

$$\sigma_\theta = -\frac{4Et^2n^2}{3(1-\nu^2)(R_w + a)^2}. \tag{59}$$

Substituting Equations (57), (58) and (59) into (55) and simplifying gives

$$\frac{\sqrt{2}\pi^2 T}{(R_w + a)(R_w - a)^2 t} - \frac{64Et^2n^4}{3(1-\nu^2)(R_w + a)^3} = 0,$$

from which, solving for n,

$$n = \sqrt[4]{\frac{3\sqrt{2}\pi^2(1-\nu^2)(R_w + a)^3}{64Et^3(R_w - a)^2}T}. \tag{60}$$

To find the amplitude, A, we equate the total hoop strain, obtained from the in-plane displacement field, to the sum of the material strain and the geometric strain due to the wrinkles.

The displacement field is assumed to be purely radial. Hence, denoting by $u(r)$ the radial displacement, defined to be positive in the positive r direction, we have

$$u = \int_R^r \epsilon_r dr = \int_R^r \frac{\sigma_r}{E} dr = \frac{T}{\sqrt{2}Et} \ln \frac{r}{R},$$

where it has been assumed that $u(R) \approx 0$. The hoop strain at the centre of a wrinkle is therefore

$$\tilde{\epsilon_\theta} = \frac{\tilde{u}}{\tilde{r}} = \frac{\sqrt{2}T}{Et(R_w + a)} \ln \frac{R_w + a}{2R}. \tag{61}$$

On the other hand, the material hoop strain and the geometric hoop strain due to the out-of-plane deformation associated with wrinkling, at the centre of a wrinkle, are respectively

$$\tilde{\epsilon}_{\theta\mathrm{M}} = -\nu\frac{\sigma_r}{E} = -\frac{\nu}{E}\frac{\sqrt{2}T}{(R_w+a)t}, \qquad \tilde{\epsilon}_{\theta\mathrm{G}} = -\frac{\pi^2A^2}{4\tilde{\lambda}^2} = -\frac{4A^2n^2}{(R_w+a)^2}. \tag{62}$$

Hence, substituting Equations (61) and (62) into

$$\tilde{\epsilon}_{\theta} = \tilde{\epsilon}_{\theta\mathrm{M}} + \tilde{\epsilon}_{\theta\mathrm{G}}$$

and simplifying, we obtain

$$\frac{\sqrt{2}T}{Et}\ln\frac{R_w+a}{2R} = -\frac{\sqrt{2}\nu T}{Et} - \frac{4A^2n^2}{R_w+a}.$$

Solving for A we find

$$A = \frac{1}{n}\sqrt{\frac{R_w+a}{2\sqrt{2}Et}\left(\ln\frac{2R}{R_w+a} - \nu\right)T} \tag{63}$$

Finally, we can determine the value of the outer radius of the wrinkled region, R_w, by looking for the value of r at which the material hoop strain is the total hoop strain, and so $\epsilon_{\theta\mathrm{G}} = 0$. Hence, we substitute $r = R_w$ into general expressions for ϵ_θ and $\epsilon_{\theta\mathrm{M}}$, and then set $\epsilon_\theta = \epsilon_{\theta\mathrm{M}}$ to find

$$\frac{T}{\sqrt{2}EtR_w}\ln\frac{R_w}{R} = -\frac{\nu T}{\sqrt{2}EtR_w}, \tag{64}$$

from which, solving for R_w,

$$R_w = e^{-\nu}R. \tag{65}$$

Asymmetric loading. The analysis presented in the previous section can be generalised to cover the case of nonsymmetric loading with $1 < T_1/T_2 < 1/(\sqrt{2}-1)$, and can also be used to characterize the fans of corner wrinkles that occur when $T_1/T_2 > 1/(\sqrt{2}-1)$.

In the latter case, though, we are mainly interested in the largest wrinkle, which runs along the diagonal parallel to the loads T_1, as depicted in Figure 13. Incidentally, due to the narrowness of the region of contact between the two larger wedge stress fields, it is reasonable to assume that only a single large wrinkle will be able to form.

Consider the coordinate system ξ, η shown in the figure, with axes parallel and orthogonal to the wrinkle direction, and the simple mode shape

$$w = A\sin\frac{\pi\xi}{\sqrt{2}(L+a)}\sin\frac{\pi\eta}{\lambda} \tag{66}$$

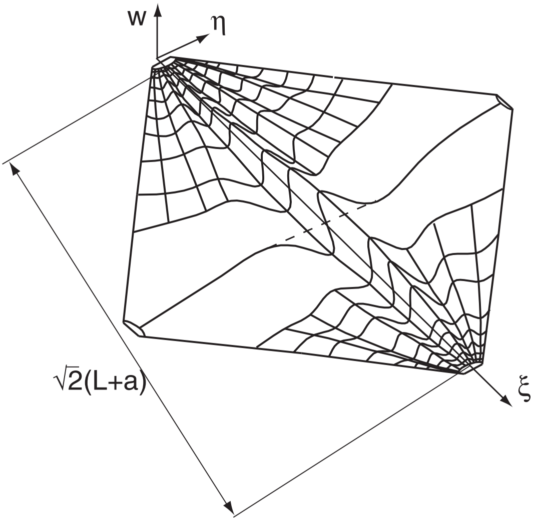

Figure 13. Wrinkle pattern for $T_1/T_2 \geq 1/(\sqrt{2}-1)$.

where λ is the half-wavelength, and A the maximum amplitude. We will follow the same procedure of Section 5.2 to estimate the wavelength of this wrinkle.

The longitudinal and transverse curvatures, obtained by differentiating Equation (66), are

$$\kappa_\xi = -\frac{\partial^2 w}{\partial \xi^2} = \frac{A\pi^2}{2(L+a)^2} \sin\frac{\pi\xi}{\sqrt{2}(L+a)} \sin\frac{\pi\eta}{\lambda},$$

$$\kappa_\eta = -\frac{\partial^2 w}{\partial \eta^2} = \frac{A\pi^2}{\lambda^2} \sin\frac{\pi\xi}{\sqrt{2}(L+a)} \sin\frac{\pi\eta}{\lambda},$$

and the corresponding maximum values, at the centre of the membrane, are

$$\tilde{\kappa}_\xi = \frac{A\pi^2}{2(L+a)^2}, \qquad \tilde{\kappa}_\eta = \frac{A\pi^2}{\lambda^2}. \tag{67}$$

The longitudinal stress at the centre of the wrinkle is obtained by determining the wedge angle θ_1, as explained in Section 5.1, and then noting that at the centre of the membrane ξ and r are parallel. Hence,

$$\sigma_\xi = \frac{T_1}{\sqrt{2}(L+2a)t\sin\theta_1}. \tag{68}$$

The transverse stress, σ_η, at the centre of the wrinkle is given by Equation (4), as usual. Substituting Equations (67), (68) and (4) into Equation (5), and then solving for λ gives

$$\lambda = \sqrt[4]{\frac{\pi^2 E t^3 (L+2a)(L+a)^2 \sin\theta_1}{3\sqrt{2}(1-\nu^2)T_1}}. \tag{69}$$

The calculation of the wrinkle amplitude is different from the earlier case, as now we are dealing with a localised wrinkle. Hence, instead of working in terms of strains, we will consider the total extensions along the diagonals of the membrane.

We begin by noting that the variable angle wedge stress field involves slack regions along all four edges of the membrane. Hence, neglecting the effects of any out-of-plane deformation, we can think of the edges of the membrane simply as four rigid links connected by pin-joints, and hence forming a square four-bar linkage. Therefore, since the corners of the membrane subjected to the loads T_1 move outwards, each by δ_1 (whose value can be estimated with (53), for $i = 1$), the corners subjected to the loads T_2 move *inwards* by δ_1. Therefore, the extension of the diagonal parallel to the loads T_2 is $-2\delta_1$.

This extension includes a component due to elastic stretching, found by integrating the elastic strains along the diagonal, and hence given by $2\delta_2$. The value of δ_2 can be estimated with Equation (53), for $i = 2$. It also includes a component due to the geometric strain induced by the single wrinkle, which can be found by multiplying the wave-length, 2λ, by the wrinkling strain, Equation (18); this gives $-\pi^2 A^2/2\lambda$. Therefore, we obtain

$$-2\delta_1 = 2\delta_2 - \frac{A^2\pi^2}{2\lambda}$$

and, solving for A,

$$A = \frac{2\sqrt{\lambda(\delta_1+\delta_2)}}{\pi} \tag{70}$$

where λ is given by (69) and δ_1, δ_2 are given by (53).

6. Validation of analytical results

The analytical predictions of the wrinkle details, developed in Sections 4 and 5.2 will now be compared against a variety of “reference” results obtained experimentally or numerically, on Kapton HN® membranes with measured Young’s modulus $E = 3500$ N/mm^2 and Poisson ratio $\nu = 0.31$ [Wong and Pellegrino 2006a].

6.1. ***Membrane in shear.*** The dimensions of the membranes were $H = 128$ mm by $L = 380$ mm.

To begin with, we consider the average magnitude of the midsurface minor principal stress, i.e., the compressive stress across the wrinkles, acting at midheight. This stress would be difficult to measure experimentally, but can be readily obtained

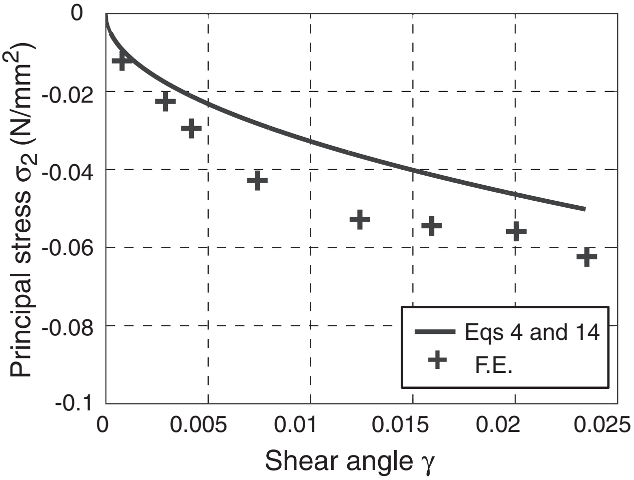

Figure 14. Minor principal stress at midheight, for 0.025 mm thick Kapton membrane in shear.

from a detailed finite-element simulation where the membrane is represented by thin-shell elements.

Figure 14 compares, for different values of the shear angle, the average stress obtained in [Wong and Pellegrino 2006b] with analytical predictions obtained by substituting (14) into (4). The largest discrepancy between the analytical predictions, which do not take into account the fans of wrinkles at either end of the membrane, and a very detailed finite element simulation is never more than 30%.

Next, we consider the relationships between the wrinkle wavelength, 2λ, and the amplitude, A, with the angle of shear, γ, provided by (14) and (22), respectively. Figures 15 and 16 show plots of these relationships, together with a large set of experimental results obtained from Kapton membranes of three different thicknesses, and a set of finite-element simulation results, obtained in [Wong and Pellegrino 2006b]. Both sets of results bunch closely along the analytical predictions.

6.2. ***Membrane under corner loads.*** The geometrical parameters of the membrane were $L = 472$ mm, $a = 17$ mm, and $t = 0.025$ mm.

First, we consider the membrane loaded by four equal forces. For this case we will focus on the corner load-displacement relationship and the details of the corner wrinkles.

Figure 17 compares the predictions of the corner displacements from Equations (37) and (39) (both of which are known to provide upper-bound estimates on the correct displacement) with two sets of reference values, obtained from two different types of finite element models [Wong and Pellegrino 2006b].

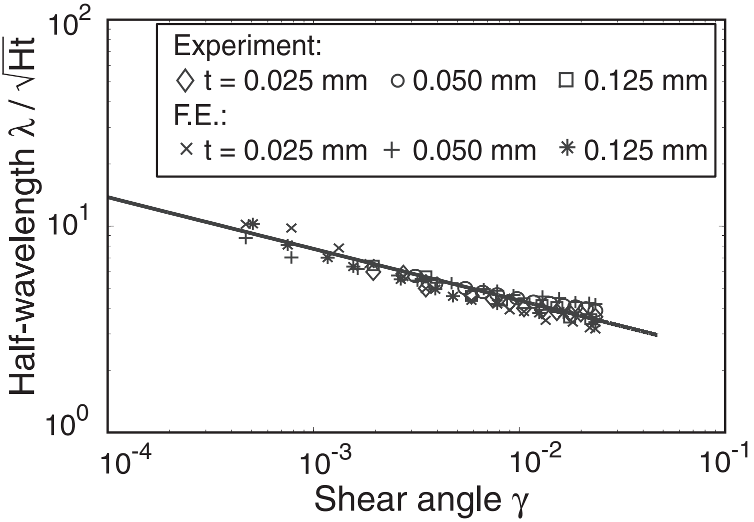

Figure 15. Comparison between nondimensional wrinkle half-wavelength from Equation (14) (solid line) and two sets of reference results, for membrane in shear.

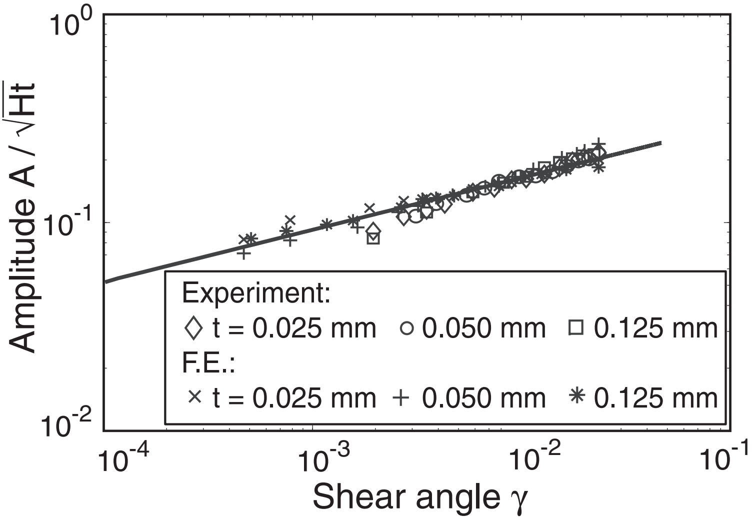

Figure 16. Comparison between nondimensional wrinkle amplitude from Figure 16 (solid line) with two sets of reference results, for membrane in shear.

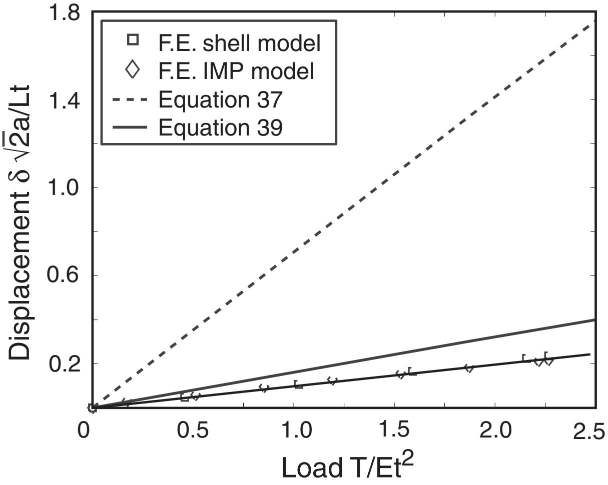

Figure 17. Relationship between nondimensional corner displacement and load, for symmetric loading of square membrane.

The two sets of finite-element results fit almost exactly on a straight line, and both analytical predictions are also linear. Equation (39), based on the wedge field, gives much closer predictions than (37), based on the diagonal strip field. This suggests that, among these two, the wedge field provides a much more accurate approximation to the actual stress distribution in the membrane when equal corner loads are applied.

Table 1 compares the number of corner wrinkles and their maximum amplitude, predicted using Equations (60) and (63), with direct experimental measurements [Wong and Pellegrino 2006a] and results from finite-element simulations using a thin-shell model [Wong and Pellegrino 2006b], for two different load levels, $T =$ 5 N and 20 N.

	n			A (mm)		
	Equation (60)	Exp.	F.E.	Equation (63)	Exp.	F.E.
$T = 5$ N	11.3	8	8	0.14	0.12	0.12
$T = 20$ N	16.0	11	9	0.20	0.14	0.16

Table 1. Number of corner wrinkles, n, and their maximum amplitude, A, under symmetric loading.

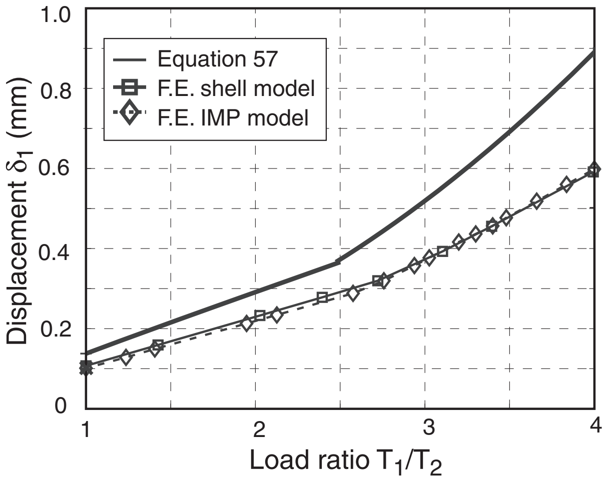

Figure 18. Relationship between corner displacement and load ratio, for asymmetric loading of square membrane.

The number of wrinkles predicted by Equation (60) is typically a 40% overestimate of the number observed in the experiments, whereas the simulation results match the experiments much more closely. It is not surprising that the analytically predicted number of wrinkles should be in excess of the actual number, since we have assumed a uniform fan of wrinkles whereas in reality there are no wrinkles along the edges Wong and Pellegrino [2006a, Figure 9].

The predicted wrinkle amplitudes are also overestimates, by 15% to 40%, due to the fact that in a real membrane a significant amount of out-of-plane displacement associated with wrinkling takes place along the edges of the region.

Next, we consider the same membrane and, while keeping two of the corner forces constant at $T_2 = 5$ N, we increase the other two forces, T_1, until the ratio between T_1 and T_2 becomes 4. For this case we will focus on the relationship between corner displacement and load ratio, and on the diagonal wrinkle.

Figure 18 shows a plot of Equation (53) for the diagonal displacement of the most heavily loaded corners vs. the ratio T_1/T_2, plus two sets of reference results, obtained from two different finite-element models [Wong and Pellegrino 2006b] which have given substantially identical results. An alternative, and simpler, prediction, could be obtained from Equation (30), however we have already seen for the case of symmetric loading that the predictions from this equation are poor.

The main observation from Figure 18 is that the reference response shows an approximately bilinear variation of δ_1, with softening by about 30% at $T_1/T_2 \approx 2.7$. This decrease in stiffness coincides with the formation of a large diagonal

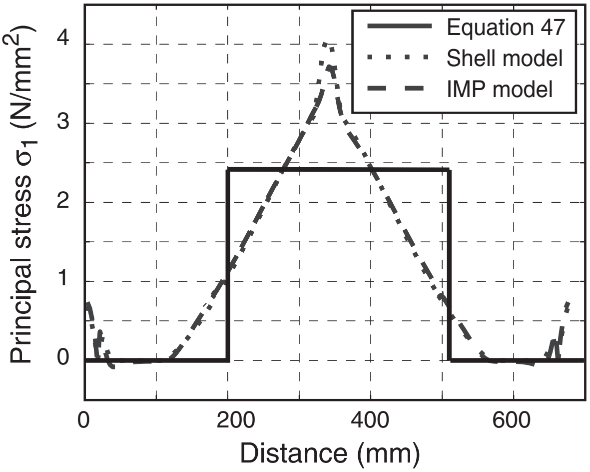

Figure 19. Distribution of midsurface principal stress along a diagonal, for $T_1/T_2 = 4$.

wrinkle. The response predicted by Equation (53) follows the same general trends as the reference solution, but the value of T_1/T_2 at which the slope changes is underestimated by about 10% and the predicted slopes are over-estimated by about 10% and 60%, respectively before and after the slope transition.

Incidentally, the initial mismatch between the two solutions, at $T_1/T_2 = 1$, is largely due to fact that the finite-element models include the corner tabs that were used in our experiments [Wong and Pellegrino 2006a].

It is interesting to compare the distribution of the midsurface, major principal stress along a diagonal, shown in Figure 19. The variation of σ_1 derived from the variable-angle wedge field is a square wave, whereas the finite-element simulations show an almost triangular wave. The stress increases near the corners; also note that the assumed stress field underestimates the peak stress by about 60%.

Finally, Table 2 compares our analytical predictions of the diagonal wrinkle details when $T_1/T_2 = 4$, for two different membrane thicknesses, $t = 0.025$ mm and $t = 0.050$ mm. Experimental results from [Wong and Pellegrino 2006a] and finite-element simulation results from [Wong and Pellegrino 2006b] are provided for comparison.

Regarding the half-wavelength presented in Table 2, our predictions for the thinner membrane practically coincide with the experimental measurements and the FE simulations. For the thicker membrane, Equation (69) over-estimates λ by about 15%.

Regarding the wrinkle amplitude, it can be predicted in two different ways. The most direct method is to follow a fully analytically approach, and hence to estimate

	λ (mm)			A (mm)			
t (mm)	Eq. (69)	Exp.	F.E.[a]	Eq. (70)+(53)	Eq. (70)+F.E.[b]	Exp.	F.E.[b]
0.025	24.6	25.4	22.3	3.55	2.8	1.89	2.02
0.050	41.3	33.9	35.6	3.25	2.1	1.81	1.63

Table 2. Half-wavelength, λ, and amplitude, A, of diagonal wrinkle for $T_1/T_2 = 4$. [a] shell model. [b] IMP model.

δ_1 and δ_2 from Equation (53), and substitute their values into Equation (70). Alternatively, one can estimate δ_1 and δ_2 with a finite-element stress analysis that uses no-compression elements, such as the IMP model used in [Wong and Pellegrino 2006b]. The corresponding results are presented in columns 5 and 6 of Table 2.

The fully analytical estimates are up to 88% higher than the experimental measurements. However, the error decreases, to 48% and 16%, respectively for the thinner and thicker membranes, when Equation (70) is combined with the finite-element estimates.

7. Discussion and conclusions

This paper has presented a general analytical framework for thinking about the location and pattern of wrinkles in thin membranes, and for making preliminary estimates of their wavelength and amplitude.

The key ideas in the analytical model that has been proposed are as follows. First, the wrinkled region and the direction of the wrinkles can be determined from a two-dimensional stress field that admits no compressive stress anywhere, satisfies equilibrium, and provides a reasonably close (upper) bound to the actual complementary strain energy of the membrane. Second, the wavelength of the wrinkles can be estimated by considering a (small) compressive buckling stress in the direction transverse to the wrinkles, and by ensuring that this stress component and the longitudinal stress (given by the two-dimensional stress field) are in equilibrium in the out-of-plane direction, say, at the centre of the wrinkles. Third, the amplitude of the wrinkles is determined by matching the sum of the material strain and geometric strain due to wrinkling, in the direction transverse to the wrinkles, to the boundary conditions imposed by the nonwrinkled region.

This analytical model has been applied to two different problems, a rectangular membrane under simple shear and a square membrane loaded at the corners.

In the first problem, the wrinkles are essentially uniform and the stress field is known. Our model predicts the wavelength and the wrinkle amplitude to be respectively *inversely proportional* and *directly proportional* to the fourth root of the shear angle; see Equations (14) and (22). Both values are *directly proportional* to the square root of the height and thickness of the membrane, and both are independent of the Young's modulus.

In the second problem two wrinkling regimes have been identified. The first is characterised by relatively uniform, small, radial corner wrinkles and occurs for load ratios smaller than $1/(\sqrt{2}-1)$. The number of radial wrinkles is proportional to the fourth root of the radius of the wrinkled region and the corner forces; see Equation (60). The amplitude of these wrinkles is inversely proportional to this number and directly proportional to the square root of the radius of the wrinkled region and to the corner force; see Equation (63). Here the radius of the wrinkled region is proportional to the radius of the uniaxially stressed wedge field (Equation (65)).

The second regime occurs for load ratios larger than $1/(\sqrt{2}-1)$, and is characterised by a large diagonal wrinkle, plus small radial wrinkles at all four corners. The variation of the width and amplitude of this wrinkle are more complex — see Equations (69) and (70) — since the geometric parameters of the stress field are dependent on the load ratio, through Equations (47), (50), and (52).

Acknowledgements

The authors thank Professor C. R. Calladine, FRS, Dr. K. Belvin and Professor K. C. Park for useful discussions and suggestions. Helpful suggestions by an anonymous reviewer are gratefully acknowledged. Financial support from NASA Langley Research Center (research grant NAG-1-02009, technical monitor Dr. K. Belvin) and the Cambridge Commonwealth Trust is gratefully acknowledged.

References

[Calladine 1983] C. R. Calladine, *Theory of shell structures*, Cambridge University Press, 1983.

[Cerda and Mahadevan 2003] E. Cerda and L. Mahadevan, "Geometry and physics of wrinkling", *Phys. Rev. Let.* **90**:7 (2003).

[Epstein 2003] M. Epstein, "Differential equation for the amplitude of wrinkles", *AIAA J.* **41** (2003), 327–329.

[Epstein and Forcinito 2001] M. Epstein and M. A. Forcinito, "Anisotropic membrane wrinkling: theory and analysis", *Int. J. Solids Struct.* **38** (2001), 5253–5272.

[Haseganu and Steigmann 1994] E. M. Haseganu and D. J. Steigmann, "Analysis of partly wrinkled membranes by the method of dynamic relaxation", *Comput. Mech.* **14** (1994), 596–614.

[Ligaro and Valvo 2000] S. Ligaro and P. S. Valvo, "Stress distribution around discontinuities in soft elastic membranes", in *Computational methods for shell and spatial structures* (Chania, Crete, 2000), edited by M. Papadrakakis et al., IASS-IACM, 2000.

[Lin and Mote 1996] C. C. Lin and C. D. Mote, "The wrinkling of rectangular webs under nonlinearly distributed edge loading", *J. Appl. Mech.* **63** (1996), 655–659.

[Mansfield 1968] E. H. Mansfield (editor), *Tension field theory a new approach which shows its duality with inextensional theory*, 12th Int. Congress Applied Mechanics, 1968.

[Mansfield 1970] E. H. Mansfield, “Load transfer via a wrinkled membrane”, *Proc. Royal Soc. London A* **316** (1970), 269–289.

[Mansfield 1981] E. H. Mansfield, “Gravity-induced wrinkle lines in vertical membranes”, *Proc. Royal Soc. London A* **375** (1981), 307–325.

[Mansfield 1989] E. H. Mansfield, *The bending and stretching of plates*, 2nd ed., Cambridge University Press, 1989.

[Murphey et al. 2002] T. Murphey, D. Murphy, M. M. Mikulas, and A. L. Adler, “A method to quantify the thrust degradation effects of structural wrinkles in solar sails”, in *43rd AIAA/ASME/ASCE/AHS Structures, Structural Dynamics, and Materials Conference* (Denver, CO, 2002), 2002. AIAA-2002-1560.

[Pipkin 1986] A. C. Pipkin, “The relaxed energy density for isotropic elastic membranes”, *IMA J. Appl. Math.* **36** (1986), 85–99.

[Reissner 1938] E. Reissner, “On tension field theory”, pp. 88–92 in *Proceedings 5th International Congress of Applied Mechanics*, 1938.

[Rimrott and Cvercko 1986] F. P. J. Rimrott and M. Cvercko, “Wrinkling in thin plates due to in-plane body forces”, pp. 19–48 in *Inelastic behaviour of plates and shells*, edited by L. Bevilacqua et al., Springer, 1986.

[Roddeman et al. 1987] D. G. Roddeman, J. Drukker, C. W. J. Oomens, and J. D. Janssen, “The wrinkling of thin membranes, I: Theory”, *J. Appl. Mech.* (*ASME*) **54** (1987), 884–887.

[Steigmann 1990] D. J. Steigmann, “Tension field theory”, *Proc. Royal Soc. London A* **429** (1990), 141–173.

[Stein and Hedgepeth 1961] M. Stein and J. M. Hedgepeth, “Analysis of partly wrinkled membranes”, NASA Langley Research Center, NASA TN D-813, 1961, Available at http://hdl.handle.net/2002/11964.

[Timoshenko and Goodier 1970] S. P. Timoshenko and J. N. Goodier, *Theory of elasticity*, 3rd ed., McGraw-Hill, New York, 1970.

[Wagner 1929] H. Wagner, “Flat sheet metal girder with very thin metal web”, *Zeitschrift für Flugtechnik Motorluftschiffahrt* **20** (1929), 200–207, 227–233, 256–262, 279–284.

[Wong and Pellegrino 2002] Y. W. Wong and S. Pellegrino, “Amplitude of wrinkles in thin membrane”, pp. 257–270 in *New approaches to structural mechanics, shells and biological structures*, edited by H. Drew and S. Pellegrino, Kluwer, 2002.

[Wong and Pellegrino 2006a] Y. W. Wong and S. Pellegrino, “Wrinkled membranes I: experiments”, *J. Mech. Materials Struct.* **1** (2006), 3–25.

[Wong and Pellegrino 2006b] Y. W. Wong and S. Pellegrino, “Wrinkled membranes III: numerical simulations”, *J. Mech. Materials Struct.* **1** (2006), 63–95.

[Wong et al. 2003] Y. W. Wong, S. Pellegrino, and K. C. Park, “Prediction of wrinkle amplitudes in square solar sails”, in *44th AIAA/ASME/ASCE/AHS/ASC Structures, Structural Dynamics, and Materials Conference and Exhibit*, 2003. AIAA-2003-1980.

[Wu 1978] C. H. Wu, “Nonlinear wrinkling of nonlinear membranes of revolution”, *J. Appl. Mech.* **45** (September 1978), 533–538.

[Wu and Canfield 1981] C. H. Wu and T. R. Canfield, “Wrinkling in finite plane-stress theory”, *Quarterly Journal of Mechanics and Applied Mathematics* **39**:2 (1981), 179–199.

Received 3 Mar 2005. Revised 10 Oct 2005.

Y. WESLEY WONG: wesleywong@cantab.net

SERGIO PELLEGRINO: pellegrino@eng.cam.ac.uk
Department of Engineering, University of Cambridge, Trumpington Street, Cambridge, CB2 1PZ, United Kingdom

JOURNAL OF MECHANICS OF MATERIALS AND STRUCTURES
Vol. 1, No. 1, 2006

WRINKLED MEMBRANES
PART III: NUMERICAL SIMULATIONS

Y. WESLEY WONG AND SERGIO PELLEGRINO

This is the third and final part of a study of wrinkles in thin membrane structures. High-fidelity, geometrically nonlinear finite element models of membrane structures, based on thin-shell elements, are used to simulate the onset and growth of wrinkles. The simulations are carried out with the ABAQUS finite element package. The accuracy of the results is demonstrated by computing the characteristics of the wrinkles in two specific membrane structures that were investigated experimentally and analytically in the first two papers in this series.

1. Introduction

This is the third and final part of a study of wrinkles in thin membrane structures. High-fidelity, geometrically nonlinear finite element models of membrane structures, based on thin-shell elements, are used to simulate the formation and growth of wrinkles.

Previous numerical studies of wrinkled membranes have largely focussed on determining the region(s) affected by wrinkles and the direction of the wrinkles. It is now possible to compute the actual shape and size of the wrinkles in structures of realistic shape and size. Here we present a general procedure for carrying out such simulations using the commercially available finite element package ABAQUS [ABAQUS 2001]. The effectiveness of the proposed procedure is demonstrated by computing the wrinkle details of two particular membrane structures, which we had investigated in detail, both experimentally and analytically [Wong and Pellegrino 2006a; 2006b]. It is shown that the accuracy of the wrinkles computed in this way is such that the numerical simulation can now be seen as a replacement for physical experimentation, although the computer run times are currently still impractically long for the present procedure to be adopted as a design tool. A significant, immediate benefit of the present work is that one can probe the simulation results in order to gain additional insights into the characteristics of wrinkles and their evolution under varying loads or boundary conditions.

Keywords: post-buckling behaviour, mode jumping, thin shell finite elements, membrane structures, wrinkling.

The layout of the paper is as follows. The next section presents a brief review of previous numerical studies of membrane wrinkling, including a few, recent studies that have adopted shell-based models of the membrane.

Section 3 sets out the proposed finite element procedure. The membrane is represented with a fine mesh of thin-shell elements; first it is lightly prestressed, then a buckling analysis is done to determine a number of incipient buckling modes, which are then seeded as initial imperfections for the main, geometrically nonlinear wrinkling analysis. An alternative model is presented in Section 4. Here the structure is represented by membrane elements and an essentially two-dimensional no-compression elastic solution is sought by means of an iterative procedure that alters the effective Poisson's ratio in order to eliminate any compressive stresses (solutions obtained from this membrane model were used as a reference in [Wong and Pellegrino 2006b], to compare with the analytical solutions presented there).

Section 5 presents a study of a rectangular membrane in simple shear. First, the sensitivity of the wrinkle details to the magnitude of the seeded imperfections, the type of finite elements and the mesh density used for the simulation are investigated. Next, the overall response of the membrane is studied, including the characteristics of the wrinkles. Finally, the way the wrinkles change with the shear displacement is investigated, and it is found that the number of wrinkles changes suddenly, both when decreasing or decreasing the old displacement. The mechanism through which new wrinkles are created, or wrinkles disappear, is explained.

Section 6 presents a study of a square membrane that is pulled at the corners. This problem is representative of currently proposed applications of membranes in future spacecraft structures, and has already been examined from an experimental and analytical viewpoint in the previous two papers in this series. Here the finite element simulation is shown to capture both of the wrinkling regimes that had been observed in the experiments, and details of the corresponding stress distributions are also obtained.

Section 7 discusses the outcomes of the present study and concludes the paper.

2. Review of previous numerical studies

The vast majority of all previous numerical solutions of wrinkled membranes have adopted a purely in-plane model of the structure, hence assuming that bending stresses are negligibly small. This approach will be reviewed first. It can accurately predict the stress distribution in the membrane, including wrinkled regions, and also the extent of these regions, but it provides no information on wrinkle details. An alternative approach is to model the membrane as a thin shell; recent work along these lines will be reviewed in the latter part of this section.

2.1. ***Models using membrane elements.*** The first finite element solution to incorporate wrinkling theory was the *Iterative Materials Properties* model (IMP) developed in [Miller and Hedgepeth 1982; Miller et al. 1985]. It is based on the observation that if during a simulation a membrane element is deemed to be wrinkled, the geometric strain in the direction perpendicular to the direction of the wrinkles, due to out-of-plane deformation of the material, can be modelled by introducing a variable effective Poisson's ratio for the element.

Hence, instead of using the standard "taut" modulus matrix, based on Hooke's law for plane stress and given by

$$D_t = \frac{E}{1-\nu^2}\begin{bmatrix} 1 & \nu & 0 \\ \nu & 1 & 0 \\ 0 & 0 & \frac{1}{2}(1-\nu) \end{bmatrix}.$$

Miller et al. used the "wrinkled" modulus matrix

$$D_w = \frac{E}{4}\begin{bmatrix} 2(1+P) & 0 & Q \\ 0 & 2(1-P) & Q \\ Q & Q & 1 \end{bmatrix},$$

where $P = (\epsilon_x - \epsilon_y)/(\epsilon_1 - \epsilon_2)$ and $Q = \gamma_{xy}/(\epsilon_1 - \epsilon_2)$; ϵ_x, ϵ_y, γ_{xy} are the engineering components of plane strain; ϵ_1, ϵ_2 are the major and minor principal strains ($\epsilon_1 \geq \epsilon_2$); and the directions 1 and 2 are parallel and perpendicular to the wrinkles, respectively. For later on, note that σ_1, σ_2 are the major and minor principal stresses ($\sigma_1 \geq \sigma_2$).

Adler [2000] implemented this model as a user-defined material (UMAT) subroutine in the ABAQUS finite element package [ABAQUS 2001]. At any stage of a standard ABAQUS iteration Adler's IMP subroutine begins by calculating the principal strain and stresses at any point using D_t, initially assuming the element to be taut, and then checks:

- If $\sigma_2 \geq 0$, the element is taut and so no change is needed;
- If $\sigma_2 < 0$ and $\epsilon_1 \leq 0$, the element is slack and so all stress components are zero;
- If $\sigma_2 < 0$ and $\epsilon_1 > 0$, the element is wrinkled, so the stress components are recomputed using D_w.

This is known as the *combined wrinkling criterion*, as a combined stress/strain condition has to be satisfied for a wrinkle to exist. Wrinkling criteria based purely on stress or strain have potential shortcomings and are less accurate [Kang and Im 1997; Liu et al. 2001].

Successful predictions of the shape and pattern of the wrinkled regions in a square membrane subjected to point loads, and also in inflated balloons of different shapes were obtained by Adler [2000]. The main problem was that the solution tended to diverge in the presence of many slack regions.

Johnston [2002] used the same approach to analyse the static and dynamic behaviour of the sunshield for a space telescope. This sunshield consists of several reflective foils which wrinkle extensively.

An alternate tension field model was developed by Liu et al. [1998] and incorporated into the nonlinear finite element code TENSION6. The main difference between this method and IMP is that, instead of modifying the material properties iteratively, the user preselects a so-called penalty tension field parameter to provide a small amount of stiffness in the direction transverse to the wrinkles. This helps to overcome the numerical singularities associated with vanishingly small diagonal terms in the tangent stiffness matrix. Liu et al. [1998] carried out a simulation of the deployment of a parachute. Modelling issues, including the selection of the penalty term, influence of the order of integration and local remeshing in the wrinkled regions are all discussed in this paper.

Liu et al. [2000] combined the approach of their earlier paper with the semianalytical determination of the impending buckling mode by Lin and Mote [1996]. The resulting two-level analysis is able to determine both the extent of the wrinkled regions, by determining the stress field with TENSION6, and the wrinkle wavelength and amplitude, by applying Lin and Mote's eigenvalue analysis to determine the number of wrinkles. The wrinkle amplitude is then determined through an argument essentially equivalent to that put forward in [Wong and Pellegrino 2006b, Section 4]. It is implicitly assumed that the number of wrinkles will not vary once the wrinkles have started to form (which is not correct), and that the wrinkled region can be assumed to behave as a simply supported rectangular plate. Liu et al. [2000] have shown this approach to provide reasonably accurate results for a square membrane subjected to a specific combination of tension and shear.

Several iterative schemes that use no-compression material models have been proposed. In their simplest form, these schemes begin by assuming that the behaviour of the membrane is linear elastic. Then, any compressive principal stresses are set to zero and the associated stiffness matrix coefficients are also set to zero. The principal stresses are recalculated at every iteration, to avoid history dependency in the results. An early study of airbag inflation based on this approach [Contri and Schrefler 1988] set a sample problem that many others have subsequently tackled. An analogous approach was attempted by the present authors, using the `*NO COMPRESSION` option in ABAQUS, but poor convergence was observed.

Finally, a number of membrane finite elements that incorporate wrinkling within their formulation have been derived from a continuum mechanics approach. The methods proposed range from using a modified deformation tensor [Roddeman et al. 1987], to a geometrically modified [Nakashino and Natori 2005] or energetically modified [Haseganu and Steigmann 1994; Barsotti and Ligaro 2000] stress-strain tensor.

2.2. ***Models using shell elements.*** Tomita and Shindo [1988] were the first to make use of a three-dimensional shell description of a wrinkled membrane, in a study of the residual wrinkles in a thin metallic plate that has been pulled diagonally. This paper started with an analysis of the onset of wrinkling, which was assumed to be the outcome of a bifurcation from plane deformation to out-of-plane deformation of the plate. The plate was initially represented by a mesh of thin-plate elements, including the effects of material nonlinearity, but the growth of the wrinkles was then traced by switching the model to isoparametric shell elements.

The last five years have seen regular use of the ABAQUS package, and recently also of ANSYS [ANSYS 2000], to simulate the onset of wrinkling in a tensioned strip [Friedl et al. 2000] and the growth of wrinkles. Three approaches to the simulation of wrinkle growth have been proposed, differing in the way the out-of-plane deformation is triggered at the beginning of a geometrically nonlinear analysis. In [Wong and Pellegrino 2002a] and [Wong et al. 2003] we started by extracting a set of eigenvalues/eigenvectors of the tangent stiffness matrix of the structure. Instead, Leifer and Belvin [2003] applied a set of equal and opposite, small magnitude forces perpendicular to the membrane and with a resultant of zero. Finally, Tessler et al. [2003; 2004] and Papa and Pellegrino [2005] imposed randomly distributed, out-of-plane imperfections, of similar magnitudes to those imposed in [Wong and Pellegrino 2002a].

The choice of finite elements and the type of analysis procedure are essentially equivalent in the three simulation techniques (the details are explained in Sections 3 and 5), so the key difference between the first approach and the other two is the additional burden of the initial eigenvalue/eigenvector extraction. In the present study it was found that this additional computation requires only a small fraction of the total simulation time, hence this burden is not significant. The three approaches have been tested on similar problems and found to work equally well for a membrane under shear, where the wrinkles are relatively uniform. For a membrane under equal corner loads the agreement between experiments and results from eigenvector-based perturbations, presented in this paper, is better than the latest results with random imperfections; see Tessler et al. [2005, Figure 5].

3. Three-dimensional finite element models

The bending stiffness of a membrane, although small, plays a key role in determining the shape and amplitude of the wrinkles. Therefore, it is essential that it should be included in any models that aim to capture this kind of detail. Two options are available, first to model the membrane with thin-plate elements and second to use thin-shell elements. Since the first option would only work for flat or nearly flat membranes, the second option has been pursued.

ABAQUS offers several shell elements, and preliminary runs were carried out with 3-node triangular and 4-node quadrilateral general purpose elements with full integration (S3, S4); these elements have six degrees of freedom at each node. 4-node and 9-node reduced integration, thin-shell elements (S4R5, S9R5), with five degrees of freedom per node, were also investigated. ABAQUS also provides other shell elements which are mainly suited for thick shell problems. This is a different class of problem and no detailed investigation of these elements was carried out.

The S3 element uses constant bending curvature and membrane strain approximations; therefore a very fine mesh is required to capture the bending deformation due to wrinkling. Note that the fineness of the discretisation that is required is related to the expected wrinkling wavelength. The formulation of element S4 is similar to S3 for bending, but the in-plane strain field has been enhanced to eliminate shear locking effects. Both S4R5 and S9R5 are thin shell elements with three in-plane translations and two in-plane rotation components. They use reduced integration with hourglass control to avoid shear locking. Both elements can model thin shells fairly accurately and S4R5 was chosen since it is computationally more economical. A detailed comparison of the performance of different shell elements in the analysis of a shear membrane will be presented in Section 5.1.2.

After defining the finite element mesh, type of elements, and material properties, a wrinkling analysis employing thin shell elements is typically performed in three stages, as follows.

3.1. ***Initial conditions.*** The initial stage of the analysis applies a small uniform prestress to the membrane, to stabilize it. Several strategies can be used to apply this initial prestress. One technique is to prescribe a set of edge displacements, corresponding to the level of prestress required. This technique is particularly useful for setting up the true stress state of a membrane structure, e.g. to reproduce the conditions that may exist at the beginning of a test. However, if a uniform stress state is required instead, e.g. to avoid initial numerical singularities, this simpler prestress can be obtained more readily by prescribing a set of initial stresses using the *INITIAL CONDITIONS, TYPE=STRESS parameter in ABAQUS. In the latter case, only membrane forces, bending moment and twisting moments can be specified for shell elements.

After applying the initial prestress, a static, geometrically nonlinear equilibrium check (*STATIC, NLGEOM) is performed. This check induces a small re-distribution of the state of prestress, together with small in-plane displacements.

3.2. ***Eigenvalue/eigenvector extraction.*** The next step of the analysis determines the buckling mode-shapes of a lightly prestressed membrane. These modes are then used as small, initial imperfections that trigger the formation of wrinkles in the subsequent, geometrically nonlinear simulation.

An eigenvalue buckling analysis (*BUCKLE) is used to obtain the possible wrinkling modes of the membrane subjected to its actual boundary conditions and loading. The loading is typically defined in terms of a set of applied forces or displacements at the edge of the membrane, and has to represent the loads on the real structure. It is important that both the initial stresses and displacements from the previous stage of the analysis, as well as those due to the applied load, should be included in the calculation of the tangent stiffness matrix; ABAQUS performs these calculations by default. The eigenvalues and eigenvectors of the tangent stiffness matrix correspond to the load magnitudes and shapes of the possible wrinkling modes of the membrane. Two solvers are available in ABAQUS to extract the eigenvalues, namely subspace iteration and the Lanczos method. The default, subspace iteration method is generally quicker when only a few (typically, less than 20) eigenmodes are needed.

After computing the buckling mode-shapes, a linear combination of all, or some selected eigenmodes is introduced into the structure as a geometrical imperfection. In standard buckling analysis of imperfection-sensitive structures, the imperfections that are seeded in the structure are normally obtained as linear combinations of the eigenvectors corresponding to the lowest eigenvalues. However, the main objective of the present study is not finding the lowest eigenvalue, corresponding to the load which would cause the first wrinkle to form. The first wrinkle forms almost as soon as the load is applied, but we are interested in following the evolution of this first wrinkle, leading to the formation of a second one, and so on until a large number of wrinkles have formed. It is generally best to introduce in the membrane a rather general kind of imperfection, e.g. one obtained as the combination of many eigenvectors. In cases where some features of the final wrinkling pattern are known, introducing in the imperfection mode shape eigenmodes that resemble this pattern, as well as several other eigenmodes, generally increases the speed of convergence during the initial stages of the simulation.

Once a set of eigenmodes has been chosen, geometrical imperfections are introduced in the form of out-of-plane deformations of the membrane, using the *IMPERFECTION directive:

$$\Delta z = \Sigma_i w_i \phi_i ,$$

where w_i is the i-th eigenmode and ϕ_i is a scaling factor whose magnitude is chosen as a proportion of the thickness of the membrane. Values between 1% and 100%

of the thickness have been used, and the sensitivity of the predicted response to different ϕ_i's has been determined, see Section 5.1.1.

3.3. ***Simulation of wrinkle growth.*** A geometrically nonlinear (*NLGEOM) incremental analysis is carried out under edge displacement incrementation, using the Newton–Raphson solution method. Since the equilibrium path of a wrinkled membrane includes many unstable branches, each corresponding to a localised snap-through due to the formation of an additional wrinkle, the only type of solution algorithm able in theory to compute the full response of the structure is an arc-length solution. The full response of the structure cannot be computed by increasing monotonically a single displacement parameter, but all attempts to use the arc-length solution method in ABAQUS (*RIKS) were unsuccessful, possibly because wrinkling is a highly localised type of instability. Hence, monotonic displacement incrementation was the only viable option.

A very effective way of addressing the numerical singularities associated with an instability is to switch from a quasi-static simulation to a transient dynamic analysis. Thus, one would simulate the actual dynamic response of the structure as it snaps, in order to compute the first static equilibrium state after snapping has occurred. This idea can be straightforwardly implemented in ABAQUS using the STABILIZE function. However, instead of computing the actual dynamics of the snap, when an instability is detected ABAQUS automatically introduces pseudo-inertia and pseudo-viscous forces at all nodes, and switches from a solution of the actual stiffness equations to a solution of a set of pseudo-equations-of-motion.

The default fictitious viscous forces are calculated on the basis of the model's response in the first increment of the analysis step, by assuming that the energy dissipated is a prescribed fraction of the strain energy during the first step. This fraction is called *damping intensity*, or *stabilise factor*, in ABAQUS and has a default value of 2×10^{-4}. To achieve good accuracy, it is generally desirable to set this parameter to the lowest possible value for which convergence can still be achieved.

The flowchart in Figure 1 summarises the complete simulation procedure.

4. Two-dimensional finite-element models

In addition to the model presented in the previous section, that has been used very extensively for the work presented in this paper, a number of comparative two-dimensional analyses were also carried out. In these analyses the structure was modelled with a mesh of membrane finite elements, typically 3-node triangular or 4-node quadrilateral full/reduced integration general purpose elements (M3D3, M3D4, M3D4R). As well as the standard linear-elastic material model, a wrinkled

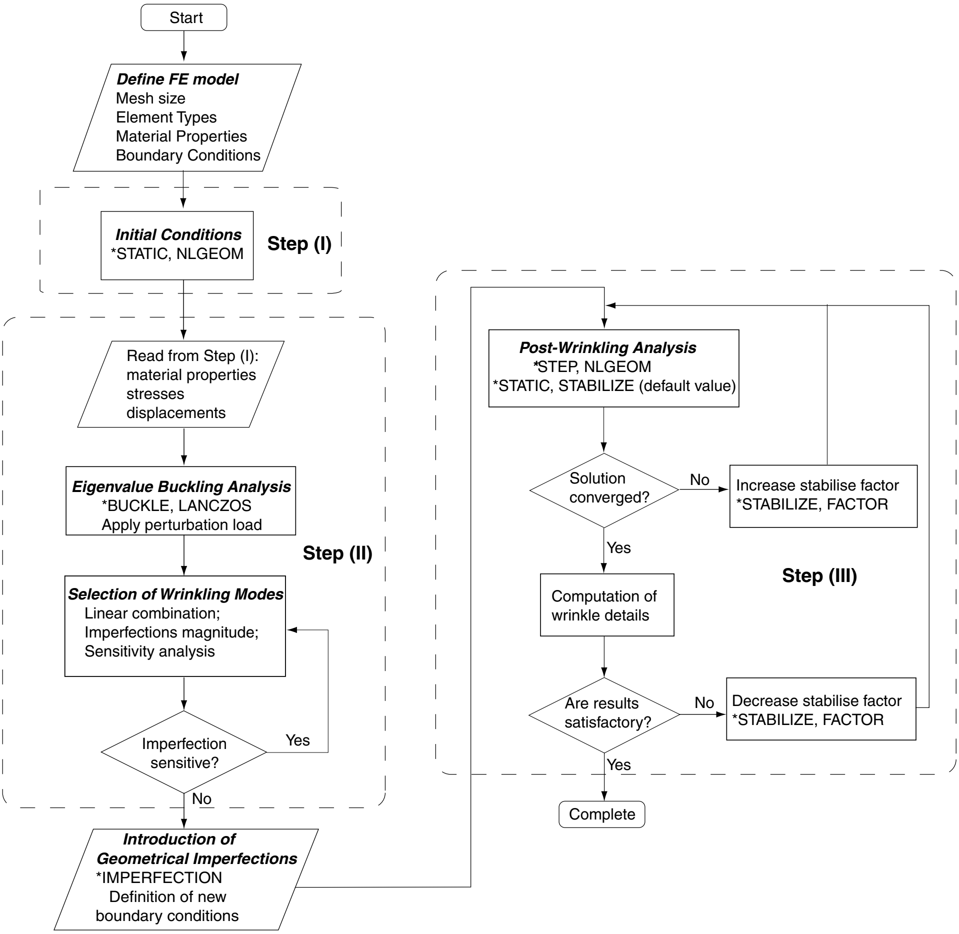

Figure 1. Flowchart for wrinkling analysis using thin shell model.

material definition was implemented through the user-defined material subroutine (UMAT) developed by Adler [2000].

The analysis procedure for the membrane model was similar to that presented in Section 3 for the shell model, but there is no eigenvalue/eigenvector extraction. After setting up the FE model of the structure, using membrane elements, an additional parameter is provided after the *MATERIAL, ELASTIC option USER=IMP.

The model was set up either in two dimensions, by constraining all out-of-plane degrees of freedom, in which case no initial prestress was needed, or in three dimensions, and in this case a small initial prestress was used to numerically stabilise the model, as for the thin-shell model.

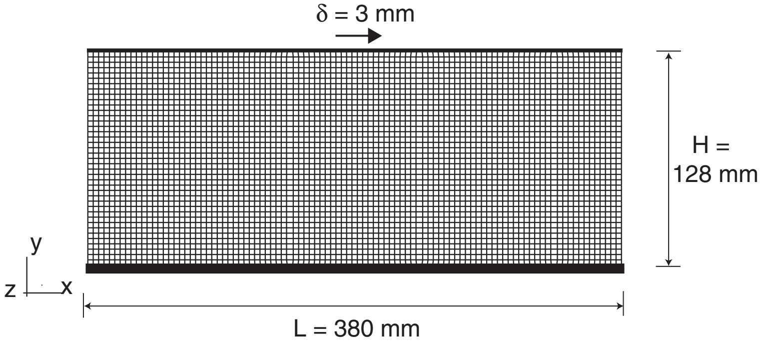

Figure 2. Finite element mesh for membrane in shear.

5. Membrane in simple shear

This section presents a study of the formation and growth of wrinkles in an initially flat and stress-free, linear-elastic rectangular membrane subject to simple shear. The dimensions of the membrane are shown in Figure 2, and the material properties are listed in Table 1.

Figure 2 shows the finite element mesh used for a preliminary analysis that was carried out. It consists of 3960 four-noded quadrilateral S4R5 thin-shell elements; each element has an aspect ratio of approximately one. The analysis started with a relatively fine mesh, in order to properly resolve the wrinkles. The element size was initially set to be smaller than the wrinkle half-wavelength, which in the present problem can be estimated from [Wong and Pellegrino 2006b, Eq. (14)]. Also shown in the figure is the final horizontal shear displacement, $\delta = 3$ mm, of the upper edge of the membrane.

Using the *BOUNDARY, ENCASTRE option, The bottom edge of the membrane was fully constrained. This was the only boundary condition assigned in the model history definition, and so it remained active through all analysis steps. The other boundary conditions were modified during the analysis, as explained in the next section.

Thickness, t (μm)	25
Young's Modulus, E (N/mm^2)	3500
Poisson's ratio, ν	0.31
Density, ρ (kg/mm^3)	1.5×10^{-6}

Table 1. Kapton® membrane properties

The upper edge of the membrane was connected to a series of B21 beam elements, with a 15 mm wide by 30 mm deep rectangular section, $E = 215000$ N/mm^2 and $\nu = 0.35$, modelling the sliding element of the experimental rig used in [Wong and Pellegrino 2006a]. The beam elements were connected to the nodes along the upper edge of the membrane using the multi-point constraint option *MPC, TIE.

5.1. ***Simulation details.*** Each simulation consisted of three steps, as follows.

The first step consisted in pretensioning the membrane by moving the upper edge by 0.5 mm, in the y-direction. Then, a geometrically nonlinear equilibrium check was performed. The geometric stiffness provided by the prestress has the effect of increasing the out-of-plane stiffness of the thin membrane. Only translation in the y-direction was allowed for the two side edges, and all six degrees of freedom of the bottom edge were completely constrained.

In the second step, an eigenvalue buckling analysis was carried out with a prescribed horizontal displacement of 3 mm at the upper edge. The model boundary conditions were modified by using the *BOUNDARY, OP=MOD option. This has the effect of moving the upper edge nodes in the horizontal x-direction by the prescribed displacement. All degrees of freedom of the nodes along the two side edges were completely free, to simulate the actual situation in the experimental model.

Earlier analyses had shown that the eigenmodes corresponding to eigenvalues smaller than 0.2 correspond to local deformation modes of the membrane (note that this particular value of the smallest eigenvalue depends on the initial prestress applied in the first step), and hence are of limited interest for the wrinkling analysis. Therefore, the Lanczos solver in ABAQUS was set to produce only eigenmodes whose eigenvalues are greater than 0.2. The first four symmetric modes are presented in Figure 3. Note that all of these modes closely resemble the expected wrinkled pattern, i.e., the parallelogram of wrinkles observed experimentally in [Wong and Pellegrino 2006a] and also predicted analytically in [Wong and Pellegrino 2006b]. Also note that all four modes have approximately the same wavelength. The chosen geometrical imperfections were then seeded onto the pristine mesh using the *IMPERFECTION command.

The third and final step consisted of two substeps. First, the initial pretensioning step was repeated, as described earlier, but this time with the upper edge only displaced by 0.05 mm to give an initial prestress of approximately 1.5 N/mm^2. Note that, although in the first step a much higher prestress had been used, in order to avoid the presence of many localised modes in the eigenvalue buckling analysis step, here a smaller prestress is sufficient to provide a small, initial out-of-plane stiffness to the membrane, but without affecting the final results. Then, in the second substep the upper edge was moved horizontally by 3 mm while all other

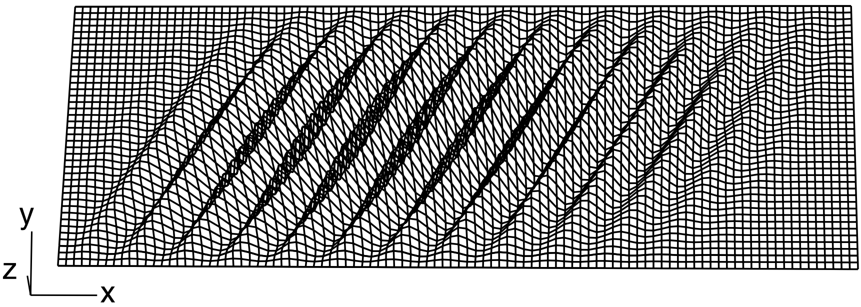

Mode 1: Eigenvalue = 0.20423

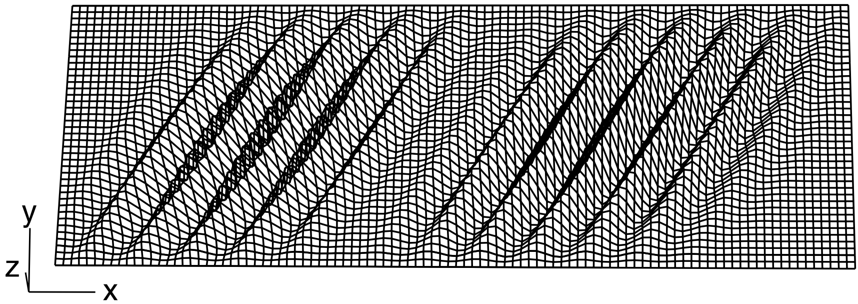

Mode 2: Eigenvalue = 0.20428

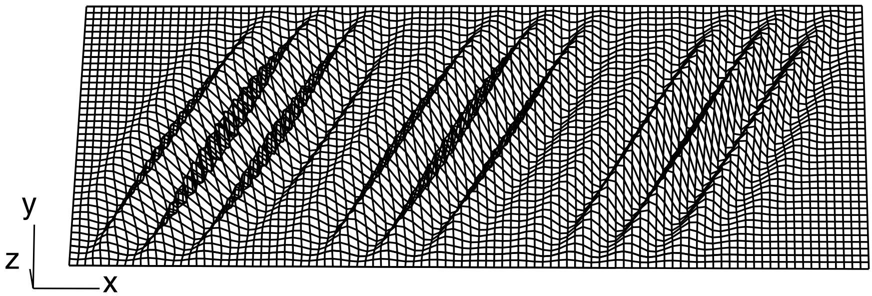

Mode 3: Eigenvalue = 0.20437

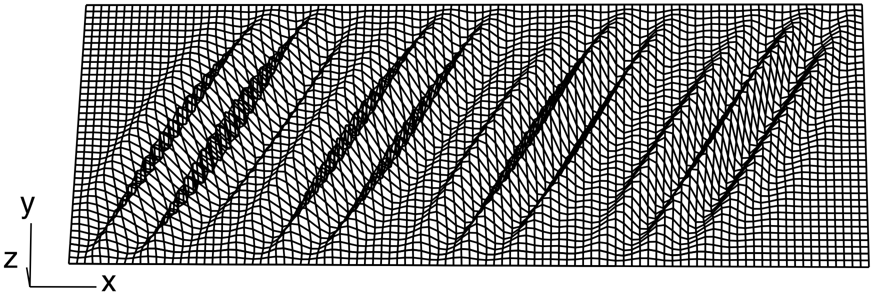

Mode 4 : Eigenvalue = 0.20449

Figure 3. First four eigenmodes with eigenvalue > 0.2, for membrane is shear.

degrees of freedom were constrained. All translational degrees of freedom of the side edges were left free, but the rotations were constrained to aid convergence.

The STABILIZE function was activated for this substep. The parameter that controls the amount of numerical damping has the default value 2×10^{-4}. This parameter was adjusted almost continuously, according to the level of difficulty of converging to a solution, by using the *RESTART option. This approach allows the numerical damping to be made very small, to minimise the deviation between the computed equilibrium path and the actual path, and to be increased only when necessary. The smallest factor used in the rectangular membrane simulations was 1×10^{-8} (*STABILIZE, FACTOR = 1E-8) .

5.1.1. *Initial imperfections.* Many different combinations of eigenmodes and scaling factors were considered to test the sensitivity of the results of the detailed wrinkling analysis. For each set, a complete wrinkling simulation was carried out and the maximum and minimum out-of-plane displacements, $w_{\max}$ and $w_{\min}$, were computed. A set of sample results are shown in Table 2.

Note that the maximum displacements remain practically unchanged when the magnitude of the imperfections is increased by a factor of 10. Also note that the particular displacements listed in the table correspond to the largest two wrinkles, on either side of the membrane, but the smaller wrinkles between these large ones were also found to have the same amplitude and wavelength, regardless of the size of imperfection.

It was thus concluded that the particular magnitude of the chosen imperfection is not critical. It was decided to use a "standard" imperfection consisting of the first four eigenmodes corresponding to eigenvalues greater than 0.2, normalised to a unit length by ABAQUS, each multiplied by a scaling factor $\phi_i = 0.125t$.

5.1.2. *Comparison of different elements.* After selecting a standard set of imperfections on the basis of a mesh of S4R5 thin shell elements, as described in Section 5.1.1, a detailed study of the performance of different elements was carried out.

Table 3 lists the number of wrinkles n (see Section 5.3), the wrinkle wavelength 2λ, the amplitude A, and the total simulation time for each type of element.

$\phi_1, \ldots, \phi_4$	$w_{\max}$ (mm)	$w_{\min}$ (mm)
$0.025t$	1.12	-1.49
$0.125t$	1.09	-1.49
$0.250t$	1.14	-1.51

Table 2. Sensitivity of membrane in shear to imperfection magnitudes

Element	S3	S4	S4R5	S9R5	M3D4
n	13	11	16	16	9
2λ (mm)	28.6	33.9	21.2	23.0	42.3
A (mm)	0.651	0.999	0.432	0.453	0.83
CPU (s)	31869	5714	10192	79419	791

Table 3. Number of wrinkles, wavelength, amplitude and total simulation time for different element types, for membrane in shear.

The most important parameter is the total number of wrinkles, since it can be readily compared to the experimental observations. In [Wong and Pellegrino 2006a] we observed 19 wrinkles when a 3 mm displacement was imposed on a 25 mm Kapton® film.

Here, elements S3 and S4 predicted 13 and 11 wrinkles, whereas S4R5 and S9R5 both predicted 16 wrinkles. Note that S3 failed to converge with the specified stabilize factor of 1×10^{-8}; the results presented in Table 3 were obtained by specifying a damping factor of 5×10^{-3}. The membrane element M3D4, with a standard linear-elastic material model, predicted only 9 wrinkles.

Hence, elements S4R5 and S9R5 match the experimental results most closely. Since S4R5 is superior in terms of computational efficiency and economy, it was adopted for all the following analyses.

5.1.3. *Sensitivity to mesh density.* The initial mesh, shown in Figure 2, predicted a smaller number of wrinkles than that observed in the experiment. Therefore, two additional mesh sizes were used to investigate the effect of mesh density on the final wrinkled shape.

The two meshes consisted of 6950 and 13134 elements, approximately double and four times the number in the initial mesh. Both of the denser meshes predicted the same number of wrinkles as in the experiment (Table 4), which suggests that the solution becomes mesh-independent after a particular level of refinement.

No. elements	Total dof	No. wrinkles
3960	19800	17
6950	34750	19
13134	65670	19

Table 4. Dependence of number of wrinkles on mesh density.

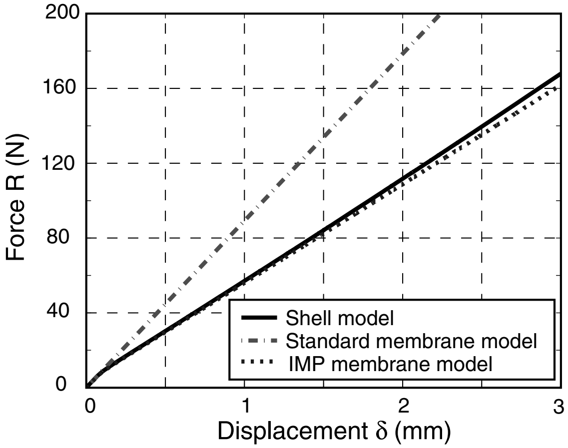

Figure 4. Shear force-displacement relationship, for membrane in shear.

Since the computational time increases roughly proportionally to the number of elements, the mesh with 6950 S4R5 elements was selected. The results presented and discussed from now on are all based on this model.

5.2. ***Global behaviour of wrinkled membrane.*** The overall relationship between the total shear force applied to the membrane and the shear displacement, δ, has been computed using three different models; the results are shown in Figure 4. Both the shell model and the IMP membrane model predict an initial in-plane shear stiffness of 101 N/mm, which quickly decreases by about a third as the wrinkles begin to form. Afterwards, the response is essentially linear. The membrane model with standard, linear-elastic material does not capture the softening associated with the formation of wrinkles (although a certain amount of waviness is created as a result of the initial imperfections).

A vector plot of the midsurface stress distribution (obtained from the shell model) corresponding to the final displacement $\delta = 3$ mm is shown in Figure 5. For each element, the directions and magnitude of the two principal stresses have been plotted, but the major stress, σ_1, is so much larger than the minor stress, σ_2, that only one vector can be seen. The direction of the major principal stress corresponds to the direction of the wrinkles, which are clearly uniform and inclined at 45° in the central part of the membrane. There are two lightly stressed triangular regions near the side edges, and the top right and bottom left corners act as stress risers, with stress concentrations of up to 2.5 times the average stress.

Figure 6 shows the overall, final wrinkle pattern in the membrane. The wrinkles in the central region are at 45° to the edges, but near the pair of corners that move closer together the wrinkles are “pinned” and hence form a kind of fan region.

A deeper understanding of the stress distribution in the wrinkled membrane can be obtained by considering the principal stresses across the midheight section, at $y = 64$ mm, defined by the section line A-A in Figure 6. Figure 7 shows plots of the major and minor principal stresses through the midplane of the membrane for two values of the shear displacement. The plots show that σ_1 increases rapidly, starting from zero at the edges, to an approximately uniform, positive value, whereas σ_2 remains very small. Close inspection shows this value to be always negative and roughly uniform across most of the section.

5.3. ***A closer look.*** The linearity of the overall load-deflection response computed in Section 5.2 hides some interesting instabilities, which become apparent on closer inspection. When the shear displacement is gradually and monotonically increased, the existing set of wrinkles grow in amplitude, then become unstable and give rise to an extra wrinkle, and hence all of the wrinkles suddenly have a smaller wavelength and amplitude, and then the cycle repeats.

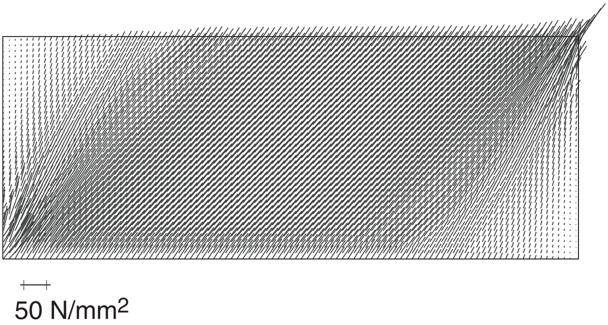

Figure 5. Plot of principal stress directions and magnitudes, for membrane in shear, showing that the major principal stress is (i) uniformly at 45° in the centre region and (ii) about three times larger near the top right and bottom left corners.

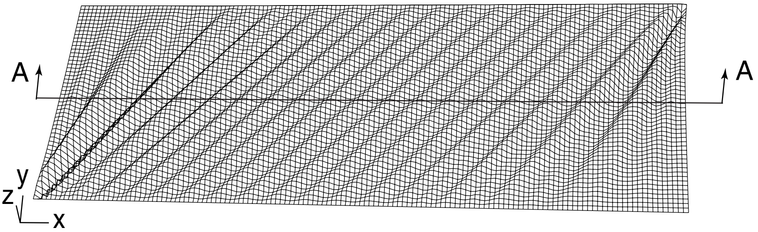

Figure 6. Perspective view of wrinkle pattern, for membrane in shear with $\delta = 3$ mm.

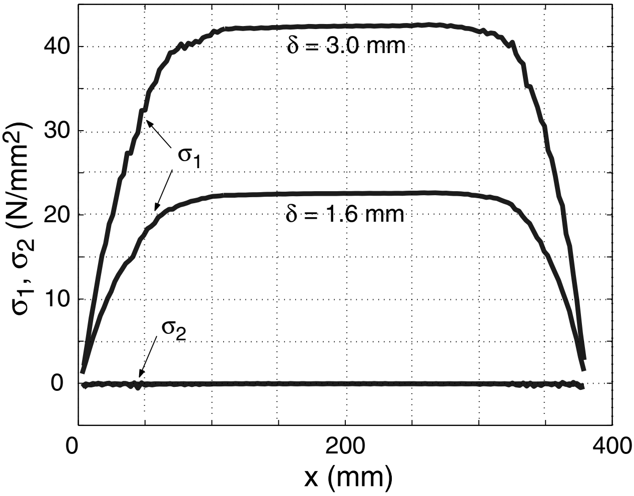

Figure 7. Principal midplane stresses across section A-A of membrane in shear.

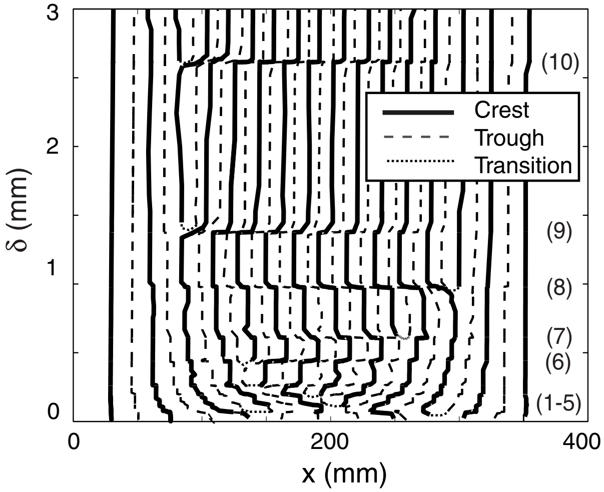

Figure 8. Trajectories of $w_{\max}$ (crest) and $w_{\min}$ (trough), for membrane in shear.

A complete history of how the wrinkle pattern grows is shown in Figure 8. This figure is a plot of δ versus the position of the points of maximum and minimum out-of-plane displacement, i.e. the crests and troughs of the wrinkles, across the midheight section of the membrane.

Note that the solid lines on the two sides of the plot are practically straight and vertical, indicating that the edge wrinkles do not move. Looking further towards the centre of the plot, the first dotted line and the second solid line are continuous, but gently curved outwards. Many other lines contain one or more bifurcation points, which indicate that additional wrinkles are created. The first five bifurcations occur very quickly, at the start of the simulation; afterwards the values of δ associated with each jump can be clearly identified, and are labelled (6)–(10) on the right-hand side of the figure. As the number of wrinkles increases, the membrane becomes more stable and hence a greater increase of δ is required for the next bifurcation to occur.

Because the wrinkles can most easily reorganise themselves in the middle of the membrane, new wrinkles tend to appear close to the edges. The large wrinkles on the sides do not move; they are "pinned" at the corners, as already noted.

Figure 9 shows the different shapes of the midheight section of the membrane, for increasing δ's. The particular shapes shown here were obtained immediately after the bifurcations labelled (2), (4), (6), (7), (9) and (10) in Figure 8. The number of wrinkles, n, defined as the number of crests in each plot, is 9, 11, 13, 14, 16 and 17 respectively. The outermost crest at each side is not counted. Note that the wrinkle amplitude in the central region increases from 0.13 mm to 0.33 mm in these plots, while the wavelength decreases visibly.

5.4. ***Mode jumping.*** The sudden transitions from one wrinkled shape to another, noted in the previous section, were observed experimentally in [Wong and Pellegrino 2006a]. Each change in the number of wrinkles is a mode jump in the post-buckling response of the membrane.

Mode jumping in stiffened panels under compression has been studied in depth by Stein [1959b; 1959a]. A key difference is that, whereas in Stein's work mode-jumping clearly showed in the load-shortening curves for the panels, here the load-deflection curve is linear, as seen in Figure 4. The reason is that each mode-jump is associated with a change of compressive stresses in the membrane, but their magnitude is negligibly small in comparison with the tensile stresses in the membrane.

Mode jumps have been explained in terms of the interaction of the branches of a set of bifurcation points adjacent to the critical load [Riks 1998]. For the present study, the sequence of jumps is seen most clearly in a plot of the *minor* principal stress, σ_2, versus the shear displacement at a representative point of the membrane. For example, Figure 10 shows the stresses at three points near the centre of the membrane. Which particular point is chosen is not significant, but jumps that are associated with an instability that is distant from the chosen point might not show, therefore we have monitored the stress at several points and chosen three after

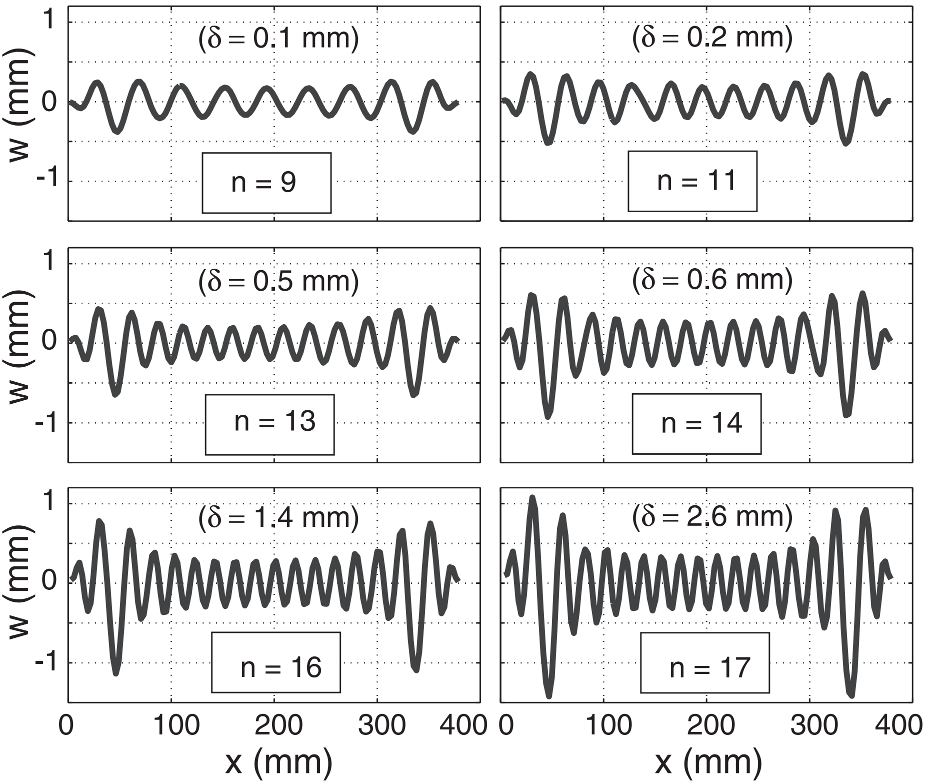

Figure 9. Mid-height cross-sections for different δ's.

completing the analysis. Note that σ_2 is always compressive, and far smaller in magnitude than the tensile stresses plotted in Figure 7.

The stress jumps numbered (1)–(10) in Figure 10 are the same that were investigated in Section 5.3. Jump (1) occurred almost immediately after beginning to increase δ. This jump was facilitated by the initial geometric imperfections. Due to these imperfections, the first jump is directly into a configuration with $n = 7$ wrinkles. This jump is followed in rapid sequence by jumps (2)–(5); and then the membrane settles in a relatively stable configuration. It is interesting to note that, as the membrane becomes more stable, σ_2 remains almost constant between consecutive jumps.

Next, we discuss jump (6) in more detail. Figure 11 shows a sequence of cross-sections of the membrane, corresponding to the 8 points labelled (a-h) on the enlarged part of Figure 7. Figure 11(a-b) shows a 13-wrinkle shape that remains stable until σ_2 has almost reached a peak, at point (c). Here a small asymmetry begins to appear in the cross-sectional plot, which rapidly grows into a new wrinkle (d-e).

Thus, the transition from 13 to 14 wrinkles occurs over a very small increment of δ. Then the new mode becomes stable and the magnitude of σ_2 starts to decrease.

It is also interesting to simulate a loading-unloading cycle. Figure 12 is a plot of the variation of the number of wrinkles when δ is increased from 0 to 3 mm, and then decreased to 0, and finally increased again to 3 mm. Note that during unloading *the wrinkles tend to stay on*, thus the final number of wrinkles does not start decreasing until the shear displacement has been reduced to $\delta = 0.8$ mm. At this point the number of wrinkles suddenly decreases from 17 to 14. Thus, the behaviour upon unloading is different from that upon loading.

During reloading the membrane generally follows the same path as during the initial loading, however the final configuration with 17 wrinkles is achieved slightly earlier this time. This difference may be due to the effect of the geometrical imperfections left in the membrane at the end of the first load cycle, which may have facilitated the formation of the "correct" pattern of wrinkles. Also note that the *stabilise factor* was continuously adjusted during each simulation, and also during load reversal; it is difficult to quantify the effect of this variation.

6. Square membrane under corner loads

This section presents a study of wrinkles in an initially stress free and perfectly flat square membrane, pulled at the four corners by two diagonal pairs of equal

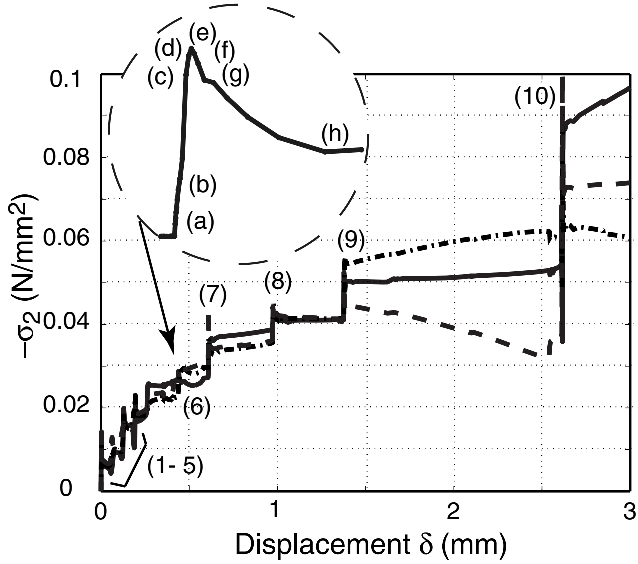

Figure 10. Variation of minor principal stress at three points near centre of membrane under shear.

and opposite forces, T_1 and T_2. Its dimensions are defined in Figure 13 and the material properties are given in Table 1.

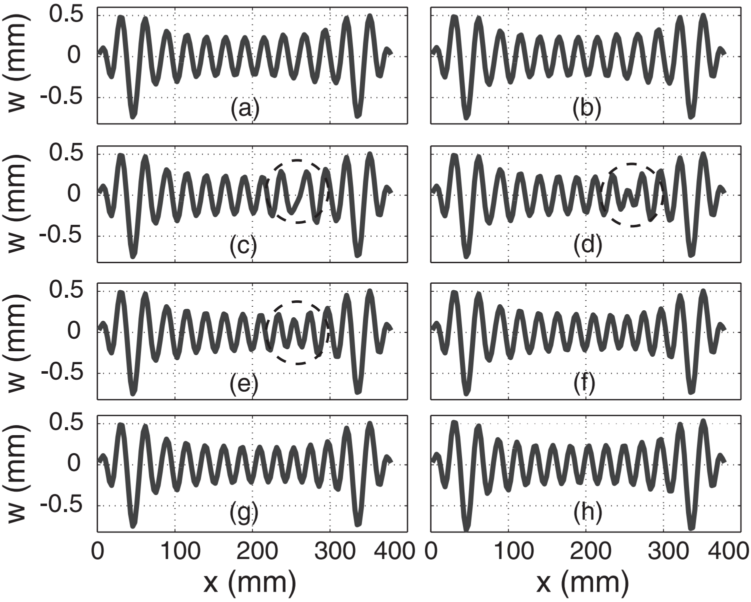

Figure 11. Variation of midheight cross-section during jump (6).

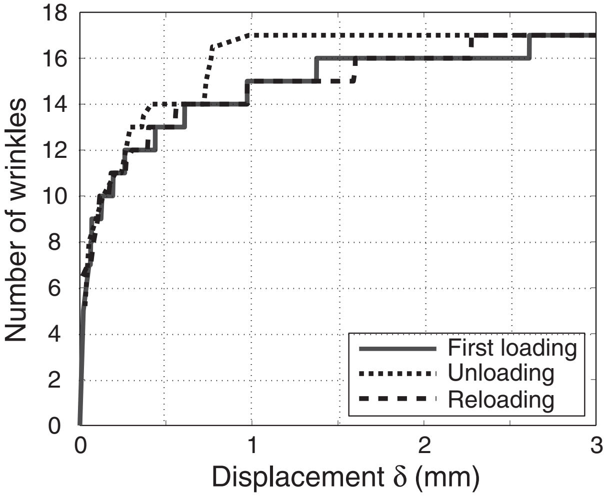

Figure 12. Number of wrinkles during load cycling.

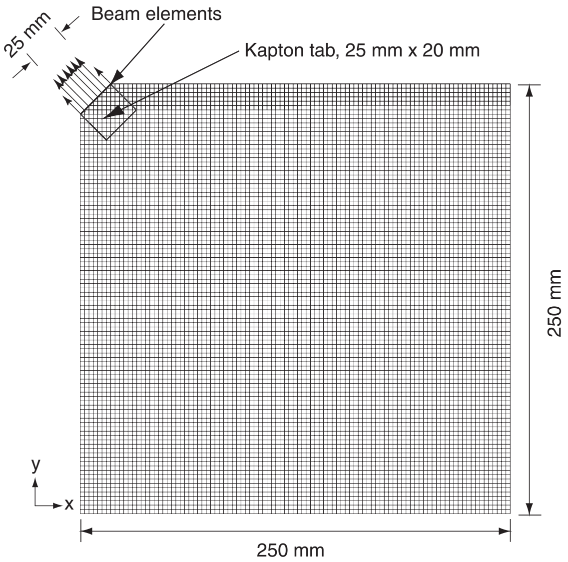

Figure 13. One quarter of the finite element mesh square membrane.

The corners of the square are truncated, to model the actual corners of the experiment in [Wong and Pellegrino 2006a]. They have a width of 25 mm, as shown in Figure 13.

6.1. ***Simulation details.*** The membrane and corner tabs were modelled using S4R5 thin shell elements of different thicknesses. The corner beams were modelled using beam elements with the Circ general beam section. The *MPC, TIE function was used to connect each beam node to the corresponding shell element node. The membrane was constrained in both x and y-directions at the centre node; all four side edges were left free; the z-translations and all rotational degrees of freedom of the corner beam nodes were restrained. The corner loads were distributed uniformly over the nodes of the beams (with only half of the forces applied at the end nodes).

The analysis procedure was essentially identical for all of the simulations. First, a uniform prestress of 0.5 N/mm^2 was applied to provide some initial out-of-plane stiffness to the membrane. This was achieved by using the *INITIAL CONDITION, TYPE=STRESS parameter in ABAQUS. A nonlinear geometry analysis was then carried out, with the *NLGEOM option activated, to check the equilibrium of the system with this initial prestress.

Second, an eigenvalue/eigenvector extraction was carried out. Many global mode-shapes were selected, and were then superposed — each multiplied by the scaling factor $\phi_i = 0.025t$ — and introduced as an initial geometrical imperfection at the start of the final analysis step. A smaller value of ϕ_i was chosen for the square membrane than for the rectangular membrane, because it had been found that this configuration is more sensitive to the magnitude of the initial imperfection, particularly at lower stress levels.

Third, an automatically stabilised nonlinear simulation of wrinkle growth was performed. Because the wrinkle amplitude is initially very small, the increment step was set equal to 0.001 of the total load. The *stabilize factor* was set to 10^{-12}, to minimize the effect of numerical damping on the final solution; this value was found to be sufficient for convergence. Despite the initial symmetry of the perfect structure, note that the imperfections are not symmetric and so the whole structure was analysed.

The loading of the membrane was applied in two steps. The first step involved a symmetric loading, $T_1 = T_2 = 5$ N, applied at all corners. Then, T_2 was maintained constant at 5 N while T_1 was increased up to 20 N, corresponding to a final load ratio of $T_1/T_2 = 4$. The second load step was carried out as a follow-on to the first step. Without changing the boundary conditions, T_1 was increased to 20 N by using the *LOAD, OP=MOD command while keeping T_2 constant at 5 N.

No separate eigenvalue extraction was carried out for the second load case, as it was found that the out-of-plane deformation at the end of the first load step naturally develops into the wrinkled profile for the second step. Also note that the same *stabilize factor* used in the symmetric case was employed. However, it was found that a higher value was required when thinner membranes were analysed.

6.2. ***Wrinkle details.*** Figure 14 shows the deformed shape of the membrane subjected to $T_1 = T_2 = 5$ N. The wrinkle pattern is symmetrical, like the loading, and the wrinkle amplitudes were found to be very small in this case. In the figure, the out-of-plane deformation, in the z-direction, has been magnified 100 times for the wrinkle details to show clearly.

Three asymmetric load cases were then considered: $T_1 = 10, 15, 20$ N, with $T_2 = 5$ N. The shape under the final loading is shown in Figure 15, and it is significantly different from that in Figure 14; a continuous, large diagonal wrinkle goes between the two more heavily loaded corners. In addition to this diagonal wrinkle, fans of small wrinkles can still be seen near the other two corners. The out-of-plane displacements in this plot have been amplified 10 times, for clarity.

The transition from the wrinkled shape shown in Figure 14 to that of Figure 15 is gradual, as can be seen from the contour plots of the out-of-plane displacements for increasing T_1/T_2, shown in Figure 16.

The initial pattern, shown in Figure 16 (top), is almost perfectly symmetric. It consists of four, practically identical fans of 9 wrinkles, one at each corner. Within each fan, each wrinkle subtends approximately the same angle, but the central wrinkles have greater amplitude than the edge ones. Note that the wrinkle heights above and below the membrane are approximately equal.

When T_1 is increased to 10 N, the fans of wrinkles at the top left and bottom right corners become longer and deeper (see second panel in Figure 16), but the number of wrinkles in each fan is still 9. The wrinkle heights above and below the membrane continue to be approximately equal. The wrinkles at the other two corners become smaller in both amplitude and number.

When T_1 is increased to 15 N, the top left and bottom right fans merge and three diagonal wrinkles (down-up-down) go through the middle of the membrane. Note that the maximum wrinkle height above the membrane is now +0.4 mm, but below the membrane it is now −0.25 mm.

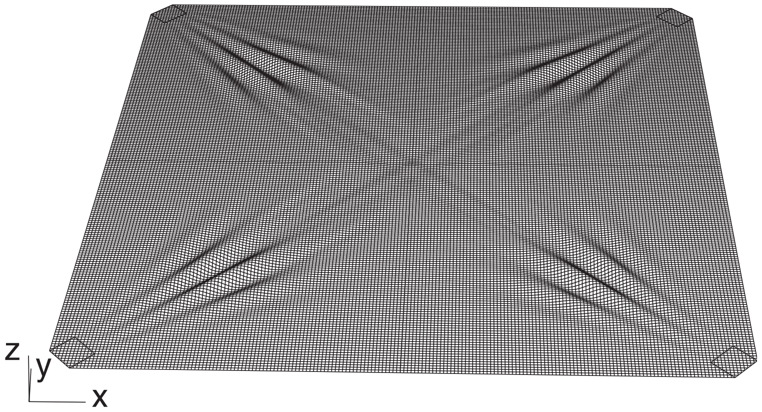

Figure 14. Wrinkled shape for $T_1 = T_2 = 5$ N (amplified 100 times).

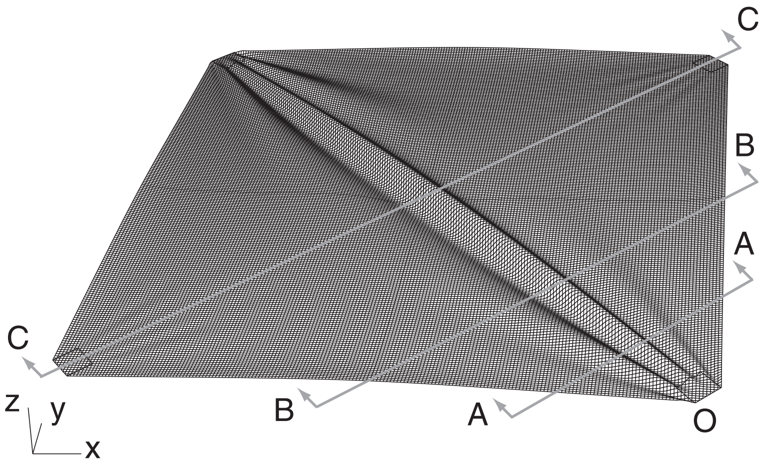

Figure 15. Wrinkled shape for $T_1 = 20$ N and $T_2 = 5$ N (amplified 10 times).

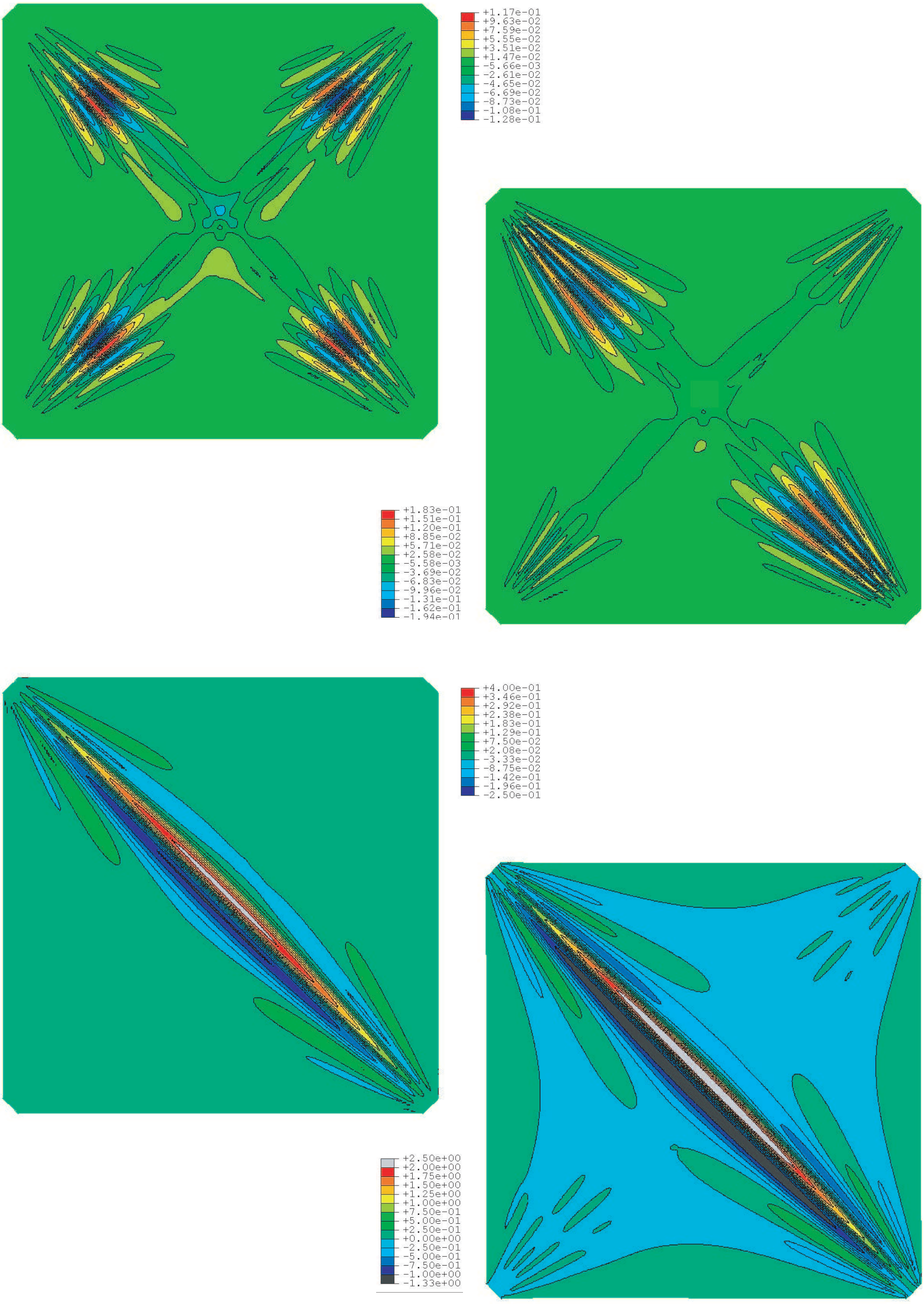

Figure 16. Contours of out-of-plane displacement for $T_2 = 5$ N and (from top to bottom) $T_1 = 5$ N, 10 N, 15 N, 20 N.

Finally, when T_1 is increased to 20 N (bottom panel in Figure 16), the diagonal wrinkles increase in amplitude, approximately five times, while maintaining the down-up-down profile. The wrinkles in the other corners increase in amplitude.

To analyse the final shape of the membrane in more detail, the out-of-plane displacements at three cross-sections (A-A, B-B and C-C in Figure 15) have been plotted in Figure 17. In addition to the three cross-sectional deformation plots obtained from the simulation, the figure shows also the experimental measurements from [Wong and Pellegrino 2006a].

Experiments and simulations match closely in the central region, and particularly the wrinkle wavelengths have been captured accurately. Gravity was included in the numerical simulations, to better capture the deformation of the edges; however, Figure 17(a-b) shows that the simulation still underpredicts the displacements of the edges of the membrane.

6.3. ***Effects of load magnitude on wrinkles.*** This section considers the variation of the wrinkle details with the magnitude of the applied loads. Figure 18(a) compares the cross-section at a distance of 105 mm from point O, which is roughly where the maximum displacements occur, for the case $T_1 = T_2 = 5$ N with the case $T_1 = T_2 = 20$ N. As can be seen, the wrinkle amplitudes increase, but the wavelength does not change.

Figure 18(b) compares the central cross-section, at a distance of 355 mm from point O, for the case $T_1 = 20$ N, $T_2 = 5$ N with the case $T_1 = 40$ N, $T_2 = 10$ N. Note that the wrinkle wavelength decreases when the applied load is increased. Also note that the small downwards wrinkle almost disappears, leaving an almost antisymmetric down-up wrinkle.

6.4. ***Stress distribution.*** Figure 19 shows the distribution of major midplane principal stresses in the membrane, for the four load ratios. The stress limits were set at 6.0 and 0 N/mm^2 in order to better visualize the stress variation. The general trend is that the stress decreases as one moves away from the corners of the membrane. For $T_1/T_2 = 1$ — see Figure 19(a) — the higher stresses are localized near the four corners, but for increasing T_1/T_2 the larger major principal stresses tend to spread along the main diagonal.

Because wrinkling is associated with the existence of (small) compressive stresses, it is instructive to consider also the distribution of the minor principal stresses, shown in Figure 20. The thin-shell model allows these stresses to become negative. For ease of comparison, the maximum and minimum stress limits were set at 1.0 and -2.0 N/mm^2. The key things to note are: (i) for $T_1/T_2 = 1$ — see Figure 20(a) — there are four identical regions of negative stress; (ii) two of these regions become smaller for $T_1/T_2 = 2$ and 3, while the other two regions grow bigger and

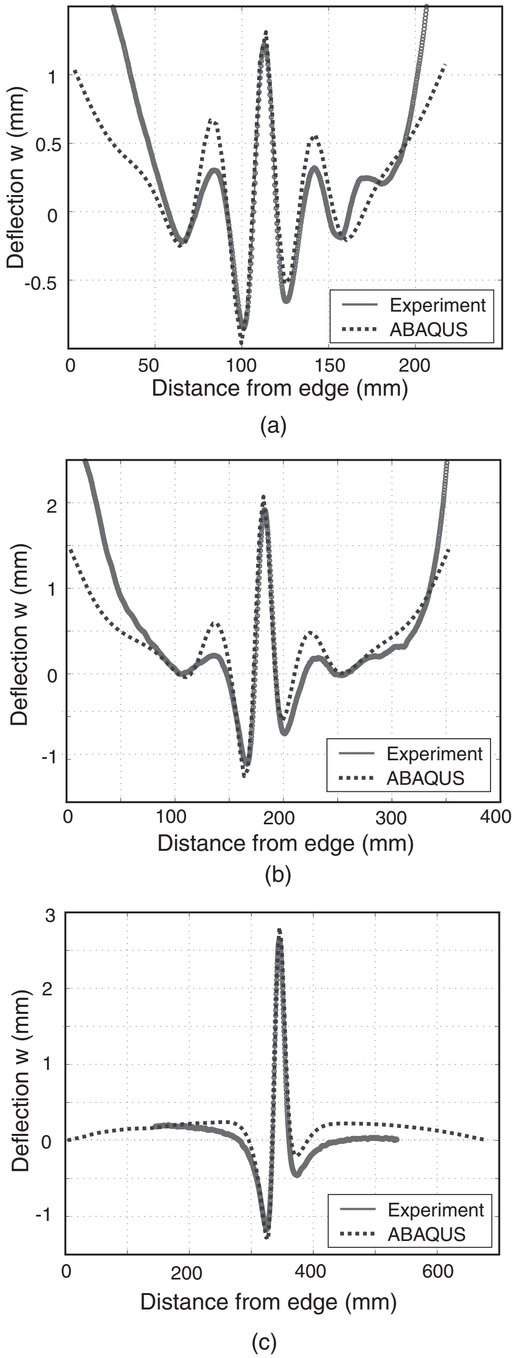

(a)

(b)

(c)

Figure 17. Experimental measurements with ABAQUS results for cross-sections at distances (a) 105 mm, (b) 177 mm, (c) 355 mm from the corner, for $T_1 = 20$ N and $T_1 = 5$ N.

coalesce in Figure 20(c); (iii) for $T_1/T_2 = 4$ the regions of compressive stress near the corners with the smaller loads have grown bigger.

7. Discussion and conclusion

A finite element simulation of wrinkled foils has been carried out with the commercial package ABAQUS, and the accuracy of the resulting wrinkle patterns has been demonstrated for two different problems. A key feature of the present approach is

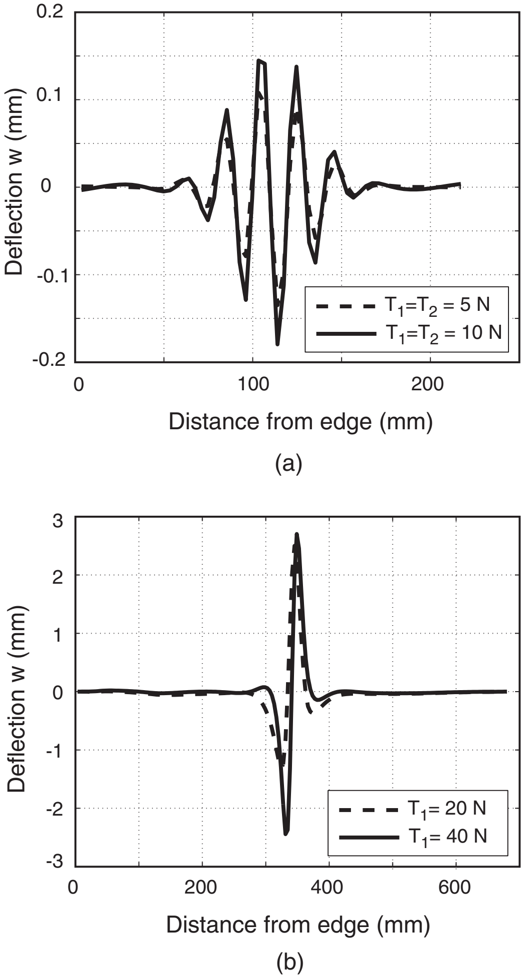

Figure 18. Variation of wrinkle profiles with load; (a) section at 105 mm from corner, for symmetric loads; (b) section at 355 mm from corner, for asymmetric loads with a ratio of 4.

that the geometrical imperfections that are seeded in the initially flat foil were obtained by computing the initial buckling modes of a perfectly flat foil that is lightly prestressed, to avoid highly localised buckling modes. This approach follows established, standard practice for the simulation of the post-buckling behaviour of imperfection-sensitive structures, and it has been shown that the experimentally observed behaviour of the foil is accurately captured.

The reduced integration shell elements available in ABAQUS have been found best suited to handle the combination of in-plane and bending behaviour associated with wrinkling, and element S4R5 was selected for speed of computation and accuracy. A mesh density of about 6 elements over a complete wrinkle wave, of length 2λ, was found sufficient to obtain accurate results. Further details on the analysis

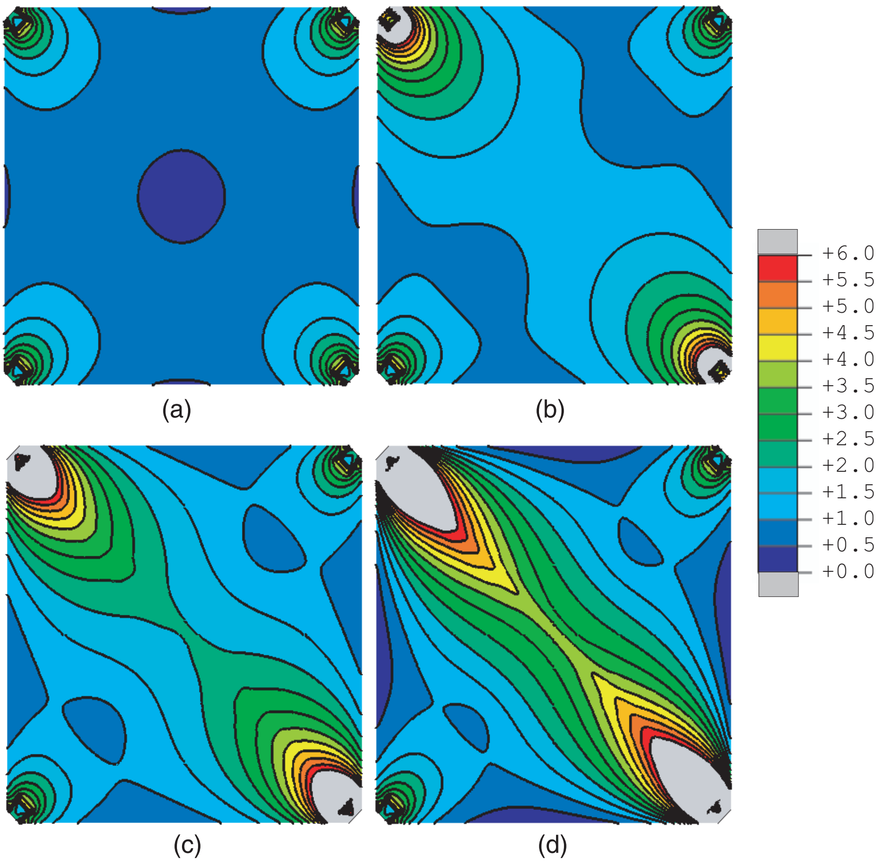

(a) (b)

(c) (d)

Figure 19. Contours of major midplane principal stress (in N/mm^2) obtained from thin-shell model for (a) $T_1 = T_2 = 5$ N; (b) $T_1 = 10$ N, $T_2 = 5$ N; (c) $T_1 = 15$ N, $T_2 = 5$ N; (d) $T_1 = 20$ N, $T_2 = 5$ N.

presented in this paper, including a sample ABAQUS input file, are available in Wong [2003].

In cases where a preliminary analytical estimate of the smallest value of λ is available, this estimate can be used to design a suitable finite element mesh. In other cases, the mesh density has to be refined iteratively until the resulting distribution of wrinkles has converged.

Our predictions are very accurate for the internal region of the foil, but it has been noted that the free edges tend to move about 50% more than predicted by the simulations. This may be due to the initial curling of the edges of Kapton® foil (due to residual stresses resulting from manufacturing), compounded by the fact that the free edges are practically unstressed, and hence "slack". Out-of-plane

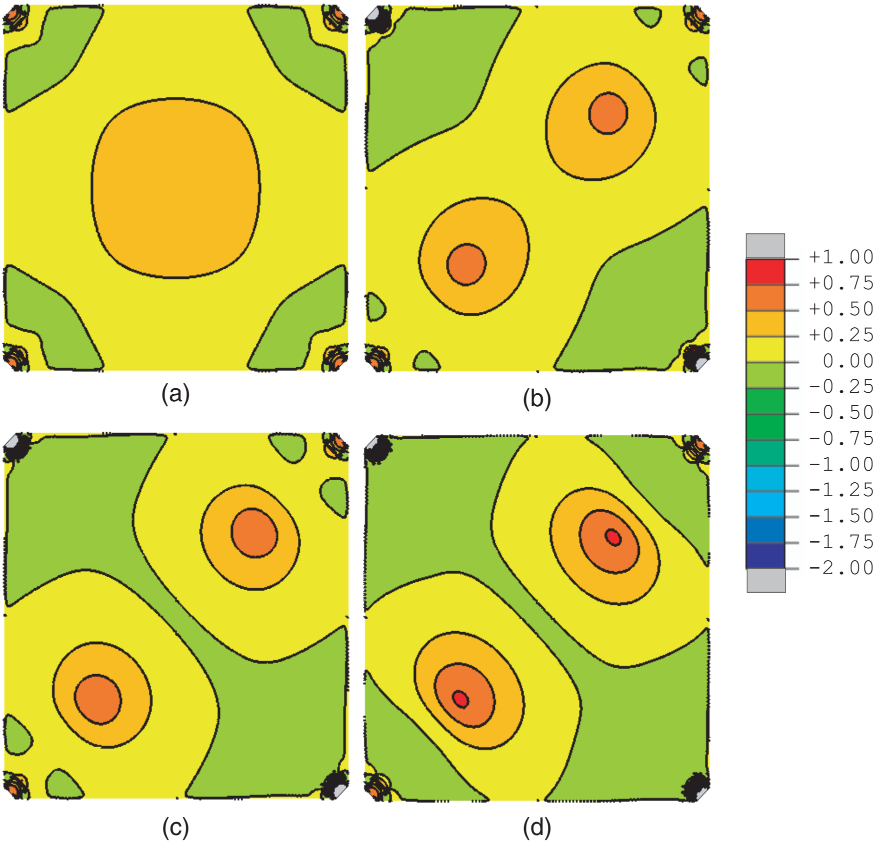

Figure 20. Contours of minor midplane principal stress (in N/mm^2) obtained from thin-shell model for (a) $T_1 = T_2 = 5$ N; (b) $T_1 = 10$ N, $T_2 = 5$ N; (c) $T_1 = 15$ N, $T_2 = 5$ N; (d) $T_1 = 20$ N, $T_2 = 5$ N.

displacements of slack membranes are notoriously ill-conditioned, and computing accurately the shape of a curled free edge would be even more extreme. An analysis specifically focussed on these effects, accompanied by additional experiments, will be required to shed more definitive light on this issue. From a practical standpoint, though, we have noted that edge deformations are often reduced very significantly if the free edges of a foil are cut on a slightly concave curve, instead of straight.

The sudden appearance or disappearance of new wrinkles, accompanied by the rearrangement (and change of wavelength) of the existing wrinkles — which were observed experimentally in [Wong and Pellegrino 2006a] — have been reproduced by our simulations. This behaviour has been understood as a form of mode-jumping, whose suddenness had been established in previous work by Stein [1959b] and Riks [1998]. Our simulations of load-cycling, in Figure 12, have shown that corresponding forward and reverse mode jumps occur at different displacements. This behaviour could be explained in terms of the shape of the equilibrium path of the structure, however, because the present displacement-controlled simulations were not able to trace unstable parts of the equilibrium path, at this stage it cannot be excluded that the behaviour in Figure 12 is an artefact of the type of solution procedure used in the present study.

Finally, it is noted that the present simulations have confirmed the existence of a small, compressive midsurface stress in a wrinkled foil. This was a fundamental assumption for the simple analytical model proposed in [Wong and Pellegrino 2006b].

Acknowledgements

The authors thank Professor C. R. Calladine, FRS, Dr. K. Belvin and Professor K. C. Park for useful discussions and suggestions. Helpful suggestions by two anonymous reviewers are acknowledged. Financial support from NASA Langley Research Center (research grant NAG-1-02009, technical monitor Dr. K. Belvin) and the Cambridge Commonwealth Trust is gratefully acknowledged.

References

[ABAQUS 2001] *ABAQUS theory and user's manual*, Version 6.2, Hibbitt Karlsson Sorensen Inc., Pawtucket, RI, 2001.

[Adler 2000] A. L. Adler, *Finite element approaches for static and dynamic analysis of partially wrinkled membrane structures*, PhD Dissertation, University of Colorado, Boulder, 2000.

[ANSYS 2000] *ANSYS User Manual*, version 5.7, ANSYS, Canonsburg, PA, 2000.

[Barsotti and Ligaro 2000] R. Barsotti and S. S. Ligaro, "An accurate wrinkled membrane model for analysing the post-critical behaviour of stiffened plate-girders", in *IASS-IACM 2000 Computational Methods for Shell and Spatial Structures*, edited by M. Papadrakakis et al., 2000.

[Contri and Schrefler 1988] P. Contri and B. A. Schrefler, “A geometrically nonlinear finite element analysis of wrinkled membrane surfaces by a no-compression material model”, *Comm. Appl. Numer. Methods* **4** (1988), 5–15.

[Friedl et al. 2000] N. Friedl, F. G. Rammerstorfer, and F. D. Fischer, “Buckling of stretched strips”, *Comput. Struct.* **78** (2000), 185–190.

[Haseganu and Steigmann 1994] E. M. Haseganu and D. J. Steigmann, “Analysis of partly wrinkled membranes by the method of dynamic relaxation”, *Comput. Mech.* **14** (1994), 596–614.

[Johnston 2002] J. D. Johnston, “Finite element analysis of wrinkled membrane structures for sunshield applications”, in *43rd AIAA/ASME/ASCE/AHS/ASC Structures, Structures Dynamics and Material Conference and Exhibit* (Denver, CO), 2002. AIAA-2002-1369.

[Kang and Im 1997] S. Kang and S. Im, “Finite element analysis of wrinkling membranes”, *J. Appl. Mech.* **64** (1997), 263–269.

[Leifer and Belvin 2003] J. Leifer and W. K. Belvin, “Prediction of wrinkle amplitudes in thin fil membranes using finite element modeling”, in *44th AIAA/ASME/ASCE/AHS/ASC Structures, Structural Dynamics and Materials Conference* (Norfolk, VA.), 7–10 April 2003 2003. AIAA 2003-1983.

[Lin and Mote 1996] C. C. Lin and C. D. Mote, “The wrinkling of rectangular webs under nonlinearly distributed edge loading”, *J. Appl. Mech.* **63** (1996), 655–659.

[Liu et al. 1998] X. Liu, C. H. Jenkins, and W. W. Schur, “Computational issues in the modelling of wrinkling during parachute deployment”, pp. 239–250 in *IUTAM-IASS Symposium on Deployable Structures: Theory and Application*, edited by S. Pellegrino and S. D. Guest, Kluwer, 1998.

[Liu et al. 2000] X. Liu, C. H. Jenkins, and W. W. Schur, “Fine scale analysis of wrinkled membranes”, *Int. J. Comput. Eng. Sci.* **1** (2000), 281–298.

[Liu et al. 2001] X. Liu, C. H. Jenkins, and W. W. Schur, “Large deflection analysis of pneumatic envelopes using a penalty parameter modified material model”, *Finite Elem. Anal. Des.* **37** (2001), 233–251.

[Miller and Hedgepeth 1982] R. K. Miller and J. M. Hedgepeth, “An algorithm for finite element analysis of partly wrinkled membranes”, *AIAA Journal* **20** (1982), 1761–1763.

[Miller et al. 1985] R. K. Miller, J. M. Hedgepeth, V. I. Weingarten, P. Das, and S. Kahyai, “Finite element analysis of partly wrinkled membranes”, *Comput. Struct.* **20** (1985), 631–639.

[Nakashino and Natori 2005] K. Nakashino and M. C. Natori, “Efficient modification scheme of stress-strain tensor for wrinkled membranes”, *AIAA Journal* **43** (2005), 206–215.

[Papa and Pellegrino 2005] A. Papa and S. Pellegrino, “Mechanics of systematically creased thin-film membrane structures”, in *46th AIAA/ASME/ASCE/AHS/ASC Structures, Structural Dynamics and Materials Conference* (Austin, TX), 2005. AIAA 2005-1975.

[Riks 1998] E. Riks, “Buckling analysis of elastic structures: a computational approach”, *Adv. Appl. Mech.* **34** (1998), 1–76.

[Roddeman et al. 1987] D. G. Roddeman, J. Drukker, C. W. J. Oomens, and J. D. Janssen, “The wrinkling of thin membranes: Part II–Numerical Analysis”, *J. Appl. Mech.* **54** (1987), 888–892.

[Stein 1959a] M. Stein, “Loads and deformations of buckled rectangular plates”, NASA, 1959, Available at http://hdl.handle.net/2002/10499.

[Stein 1959b] M. Stein, “The phenomenon of change of buckling patterns in elastic structures”, NASA, 1959, Available at http://hdl.handle.net/2002/10498.

[Tessler and Sleight 2004] A. Tessler and D. W. Sleight, “Toward effective shell modeling of wrinkled thin-film membranes exhibiting stress concentrations”, in *45th AIAA/ASME/ASCE/AHS/ASC*

Structures, Structural Dynamics and Materials Conference (Palm Springs, CA), 2004. AIAA 2004-1739.

[Tessler et al. 2003] A. Tessler, D. W. Sleight, and J. T. Wang, "Nonlinear shell modeling of thin membranes with emphasis on structural wrinkling", in *44th AIAA/ASME/ASCE/AHS/ASC Structures, Structural Dynamics and Materials Conference* (Norfolk, VA), 2003. AIAA 2003-1931.

[Tessler et al. 2005] A. Tessler, Sleight, D. W., and J. T. Wang, "Effective modeling and nonlinear shell analysis of thin membranes exhibiting structural wrinkling", *J. Spacecraft Rockets* **42**:2 (2005), 287–298.

[Tomita and Shindo 1988] Y. Tomita and A. Shindo, "Onset and growth of wrinkles in thin square plates subjected to diagonal tension", *Int. J. Mech. Sci.* **30** (1988), 921–931.

[Wong 2003] Y. W. Wong, *Wrinkling of thin membranes*, Ph.D. thesis, University of Cambridge, 2003.

[Wong and Pellegrino 2002a] Y. W. Wong and S. Pellegrino, "Computation of wrinkle amplitudes in thin membranes", in *43rd AIAA/ASME/ASCE/AHS/ASC Structures, Structures Dynamics and Material Conference and Exhibit* (Denver, CO), 2002a. AIAA-2002-1369.

[Wong and Pellegrino 2006a] Y. W. Wong and S. Pellegrino, "Wrinkled membranes I: experiments", *J. of Mechanics of Materials and Structures* **1** (2006), 3–25.

[Wong and Pellegrino 2006b] Y. W. Wong and S. Pellegrino, "Wrinkled membranes II: analytical models", *J. of Mechanics of Materials and Structures* **1** (2006), 27–61.

[Wong et al. 2003] Y. W. Wong, S. Pellegrino, and K. C. Park, "Prediction of wrinkle amplitudes in square solar sails", in *44th AIAA/ASME/ASCE/AHS/ASC Structures, Structural Dynamics and Materials Conference and Exhibit*, 2003. AIAA-2003-1980.

Received 3 Mar 2005. Revised 10 Oct 2005.

Y. WESLEY WONG: wesleywong@cantab.net

SERGIO PELLEGRINO: pellegrino@eng.cam.ac.uk
Department of Engineering, University of Cambridge, Trumpington Street, Cambridge, CB2 1PZ, United Kingdom

JOURNAL OF MECHANICS OF MATERIALS AND STRUCTURES
Vol. 1, No. 1, 2006

METAL SANDWICH PLATES WITH POLYMER FOAM-FILLED CORES

A. Vaziri, Z. Xue and J. W. Hutchinson

The role of low-density structural polymeric foams filling the interstices of the cores of metal sandwich plates is studied to ascertain the strengthening of the cores and the enhancement of plate performance under crushing and impulsive loads. Square honeycomb and folded plate steel cores filled with two densities of structural foams are studied. The foam makes direct contributions to core strength and stiffness, but its main contribution is in supplying lateral support to core members thereby enhancing the buckling strength of these members. Performance is assessed at fixed total weight of the sandwich plate such that the weight of the foam is traded against that of the metal. The outcome of the comparative study suggests that plates with foam-filled cores can perform as well, or nearly as well, as plates of the same weight with unfilled cores. The decision on use of foams in the cores is therefore likely to rest on multifunctional advantages such as acoustic and thermal insulation or environmental isolation of core interstices.

1. Introduction

Polymeric foams offer unique structural, thermal and acoustic properties, which make them an excellent choice for many engineering applications [Gibson and Ashby 1997]. Here, we explore another possible application of structural foams: as a filler of the interstices of the cores of metal sandwich plates designed to withstand intense pressure pulses. The main purpose of the filler would be to stabilize core members against buckling, increasing the effective strength of the core. To assess whether structural foam is effective in this application, behaviors of sandwich plates with and without filler, but constrained to have the same total weight, are compared for localized three-point bending loads and for clamped plates subject to uniformly distributed pressure pulses. Attention is directed to two classes of cores: square honeycombs and folded plates (Figure 1).

The background to the present study is the recent discovery that metal sandwich plates can be designed to sustain smaller deflections than monolithic solid plates of the same weight when subject to intense pressure pulses, particularly when the

---

Keywords: polymeric foams, sandwich plates, honeycomb cores, folded plate cores, impulsive loads.

Corresponding author: J. W. Hutchinson.

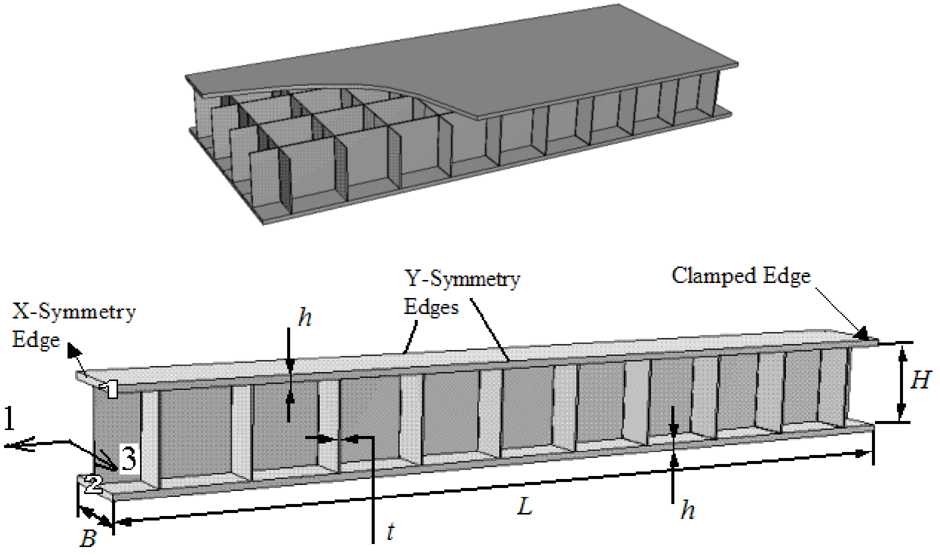

(a) square honeycomb sandwich plate

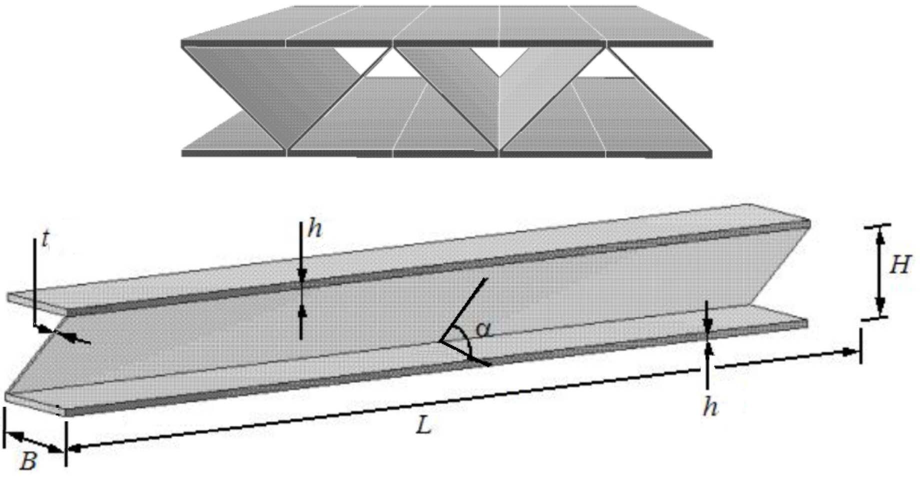

(b) folded sandwich plate

Figure 1: Schematic diagram of sandwich plate core configuration and corresponding computation model of sandwich panel (the polymeric foam components are not shown)

pulse is transmitted through water [Xue and Hutchinson 2003; Xue and Hutchinson 2004a; Xue and Hutchinson 2004b; Hutchinson and Xue 2005]. The core plays a critical role in the performance of the sandwich plate: typically, it must be able to absorb more than one half of the initial kinetic energy imparted to the plate by crushing in the early stages of deformation prior to significant overall bending and stretching without unduly reducing the separation between the face sheets. High crushing strength and energy absorption per unit mass of the core is therefore important. Square honeycomb cores have been shown to be especially effective [Xue and Hutchinson 2004a], and this is one of the core-types considered here. Folded plate cores are more susceptible to buckling under crushing than square honeycombs but are nevertheless effective, and they have manufacturing advantages. In this paper, enhancement of the buckling resistance of the core webs due to lateral support of the foam will be investigated. The tradeoff against such enhancement is the inevitable loss in bending and/or stretching strength accompanying the reduction in metal required to pay for the weight of the foam. The net gain or loss to the overall performance of the plate by incorporating the foam is by no means obvious when the total mass of the plate is constrained to be constant.

The paper begins with the specification of the sandwich plate geometries and material properties in Section 2. The material comprising the sandwich plate core and face sheet is stainless steel (#304). The foam material is a closed-cell PVC foam material with the commercial name *Divinycell*. Two commercially available densities of this polymeric foam are considered, H100 and H200. Details of the continuum constitutive model of the polymeric foam materials are described in Section 2.1. The finite element modeling is described in Section 2.2. A limited investigation of the response of the core to three basic stressing histories (crushing, shear and stretching) is conducted in Section 3 to provide insight into the effect of filling the core interstices with foam. Section 4 presents comparative results, with and without the foam, for wide sandwich plates clamped along opposite edges and subject to a quasi-static load applied by an indenter. Corresponding results for clamped plates subject to a uniformly distributed intense impulse are given in Section 5. Limited results for the plastic energy dissipation history of each component of the empty and foam-filled sandwich plates under impulsive load are presented in Section 6. Conclusions are drawn in Section 7, where topics for further research will also be noted.

2. Specification of sandwich plates and material properties

2.1. ***Sandwich plates.*** Infinite sandwich plates of width $2L$ that are clamped along their edges are considered. Figure 1 shows the periodic units employed in the finite element models of the sandwich plate (the foam is not depicted). Both types of sandwich plates have core height H, core web thickness t, and face sheet thickness h. The square honeycomb core has web spacing B. The folded plate core has an inclination angle α.

Denote the densities of the steel and foam by ρ_s and ρ_f, respectively. The average density of the core, $\bar{\rho}_c$, is

$$\bar{\rho}_c = \upsilon_s \rho_s + \rho_f (1 - \upsilon_s) \tag{1}$$

where υ_s is the volume fraction of the core occupied by steel. Full-scale metal sandwich plates designed to be effective against impulsive loads have cores with a low volume fraction of material, typically with υ_s less than 0.05 [Xue and Hutchinson 2004a]. The mass per area of the sandwich plate, M, including the mass of the foam, is given by

$$M = (2\rho_s h + \bar{\rho}_c H) \tag{2}$$

For the *square honeycomb core:*

$$\upsilon_s = 2\frac{t}{B} - \left(\frac{t}{B}\right)^2 \cong 2\frac{t}{B} \tag{3}$$

With L, M, ρ_s and ρ_f specified, the geometry of the square honey plate is fully determined by the three independent parameters υ_s, H/L and B/L. The trade-off of steel against foam due to filling the interstices of the core with foam when the mass of the core is held fixed can be seen in Figure 2. In that plot, $H_s \equiv \bar{\rho}_c H/\rho_s$ is the thickness of a solid steel sheet with the same mass/area as the core. The volume fraction of steel in the core as a function of H/H_s, $\upsilon_s = (H/H_s - \rho_f/\rho_s)/(1 - \rho_f/\rho_s)$, is shown for the empty core ($\rho_f = 0$) and for the density ratios considered in this paper: H100 ($\rho_f/\rho_s = 0.0125$) and H200 ($\rho_f/\rho_s = 0.025$). For the full-scale plates considered in this paper, typically, $H/H_s \cong 25$ such that the empty core has $\upsilon_s \cong 0.04$, while the equal weight core filled with H200 foam has only about half the amount of steel. Of course, steel can be traded from the face sheets as well as from the core.

For the *folded sandwich core:*

$$\upsilon_s = \frac{t/H}{t/H + \cos\alpha} \tag{4}$$

In this case, with L, M, ρ_s and ρ_f specified, the three independent variables employed to determine the geometry of the folded sandwich plate are: υ_s, H/L and α.

2.2. ***Material specifications.*** The core and face sheets of the sandwich plates are taken to be 304 stainless steel with density $\rho_s = 8000\,\text{kg/m}^3$. A piecewise function

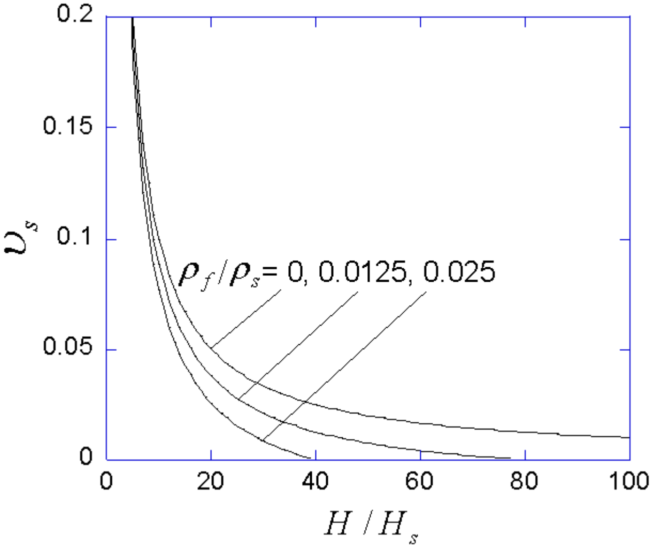

Figure 2: Volume fraction of steel versus normalized core thickness

has been fit to the true stress-log strain tensile behavior of the material giving

$$\sigma = \begin{cases} E_s\varepsilon & \varepsilon \le \sigma_{Ys}/E_s \\ \sigma_{Ys}(E_s\varepsilon/\sigma_{Ys})^N & \varepsilon > \sigma_{Ys}/E_s \end{cases} \tag{5}$$

with Young's modulus $E_s = 200\,\text{GPa}$; Poisson's ratio $\nu = 0.3$; tensile yield strength $\sigma_{Ys} = 205\,\text{MPa}$; strain hardening exponent $N = 0.17$ [Boyer and Gall 1985]. The shear modulus and initial shear strength are $G_s = E_s/[2(1+\nu)] = 76.92\,\text{GPa}$ and $\tau_{Ys} = \sigma_{Ys}/\sqrt{3} = 118.35\,\text{MPa}$. Strain-rate sensitivity of the steel is not taken into account. Classical flow theory based on the Mises yield surface and isotropic hardening is employed in the simulations. The steel is assumed sufficiently ductile to sustain large strains without fracture.

The constitutive model adopted for the foams is that developed for polymeric foams by [Zhang et al. 1997; Zhang et al. 1998] and available as a constitutive option in ABAQUS [ABAQUS 2001]. The model is an isotropic, dilatational plasticity relation. The specific form employed here models the inelastic deformation as perfectly plastic with three inputs: the yield stress in uniaxial compression, σ_c^0, the yield stress in hydrostatic compression, p_c^0, and the yield stress in hydrostatic tension, p_t^0. An ellipsoidal yield surface (see Figure 3) is specified by

$$\hat{\sigma} = \sigma_c^0 \tag{6}$$

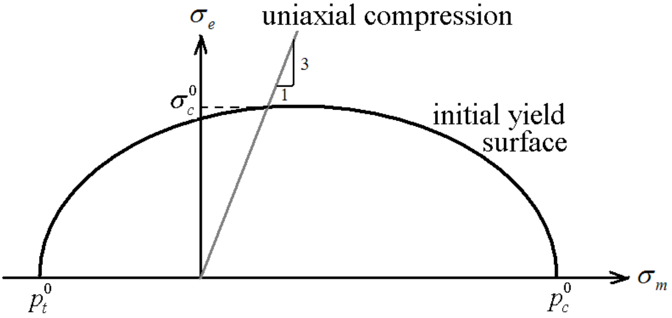

Figure 3: Initial yield surface for the continuum constitutive model of polymeric foam material

with $\hat{\sigma}$ as the *equivalent stress*, defined by

$$\hat{\sigma} \equiv \chi + \left[\chi^2 - 6\sigma_m \chi + \frac{\alpha^2 \sigma_m^2 + \sigma_e^2}{1 + (\alpha/3)^2} \right]^{1/2} \tag{7}$$

Here, $\sigma_e = \sqrt{3 s_{ij} s_{ij}/2}$ is the conventional effective stress with s_{ij} as the stress deviator, $\sigma_m = \sigma_{kk}/3$ is the mean stress,

$$\chi \equiv \frac{\alpha^2}{6\left[1 + (\alpha/3)^2\right]} (\sigma_c^0 - \sigma_t^0) \tag{8}$$

and the yield surface shape factor is

$$\alpha \equiv \frac{3\sigma_c^0/p_c^0}{\sqrt{(3p_t^0/p_c^0 + \sigma_c^0/p_c^0)(3 - \sigma_c^0/p_c^0)}} \tag{9}$$

Non-associative flow is assumed such that $\dot{\varepsilon}_{ij}^p \propto \partial G/\partial \sigma_{ij}$ with flow potential [Zhang et al. 1997; Zhang et al. 1998],

$$G = (\sigma_e^2 + 9\sigma_m^2/2)^{1/2} \tag{10}$$

Under uniaxial stressing, the model predicts that transverse plastic strains vanish, in approximate agreement with experimental findings of [Deshpande and Fleck 2001].

The formulation can incorporate strain hardening and, in particular, the substantial increase in flow stress associated with densification at large plastic compaction can be included. However, in the present application the strains are never large enough to cause significant strengthening due to densification, and the assumption of elastic-perfectly plastic behavior realistically captures the plateau-like response

Table 1: Mechanical properties of PVC polymeric foam

Foam	Young's modulus, E_f (MPa)	Poisson's ratio	Initial uniaxial compressive yield stress, σ_c^0 (MPa)	Initial hydrostatic compressive yield stress, p_c^0 (MPa)	Hydrostatic tensile yield stress, p_t^0 (MPa)
H100	105	0.2	1.1	1.0	1.8
H200	293	0.33	3.0	2.8	4.0

of the foam in the intermediate strain range. The formulation can also incorporate strain-rate dependence of the foam. Tests [Deshpande and Fleck 2001] in the range of strain-rates from $10^{-3}\,\mathrm{s}^{-1}$ to $10\,\mathrm{s}^{-1}$ reveal only a moderately weak rate dependence, which will be neglected in this first study.

Compression tests on the foam reveal some anisotropy with the yield strength typically about 20% higher in the rise direction of the foam than in transverse directions [Abot et al. 2002; Fleck and Sridhar 2002]. The isotropic model used here neglects this anisotropy; the uniaxial yield stress, σ_c^0, is associated with the direction perpendicular to the rise direction. The parameters characterizing the foam are presented in Table 1. The values for σ_c^0 and Young's modulus in Table 1 are taken from data in [Deshpande and Fleck 2001] and [Fleck and Sridhar 2002] and are lower than the values suggested by the manufacturer of the polymeric foams [DIAB 2005].

2.3. ***Finite element model and specification of the plates.*** The finite element models were developed using ABAQUS/CAE software. All components (face sheets, core webs and polymeric foam components) were fully meshed with three-dimensional elements. Eight-node brick elements were employed with reduced integration. The loading was taken to be independent of the coordinate in the long direction, and thus it was possible to analyze the three-dimensional unit of the plate that repeats periodically along its length as shown in Figure 1. Periodic boundary conditions were applied at each end of the repeating unit in the long direction, symmetry about the centerline was invoked, and clamped conditions were imposed along the two sides, corresponding to face sheets welded to rigid walls. Core webs were taken as welded to the face sheets. The commercial code, ABAQUS Explicit [ABAQUS 2001], was utilized to perform most of the calculations, both dynamic and quasi-static.

Full-scale plates are considered in this paper whose half-width, L, is on the order of a meter. Steel sandwich plates with empty, square honeycomb cores optimized against intense impulsive loads to have the minimum weight typically have a normalized core thickness $H/L \cong 0.3$ [Hutchinson and Xue 2005]. However, plates with $H/L = 0.1$ perform almost as well as the thicker optimal plates, and, because thinner cores are preferable in many applications, all the examples considered in this paper have $H/L = 0.1$. These optimal and near-optimal full-scale plates typically have between $1/5$ and $1/3$ of the their total mass in the core, corresponding to a volume fraction of core material in the range $0.02 < \upsilon_s < 0.05$. Several sets of calculations will be performed to explore the role of filling the core interstices with foam: (i) basic core responses to crush, shear and stretch; (ii) plate response to quasi-static load; and (iii) plate response to impulsive load.

3. Responses of empty and foam-filled cores subject to basic loading histories

The unit cells corresponding to core geometries of square honeycomb and folded plates are given in Figs. 4a and 4b, respectively, along with the coordinate system. To reveal the effect of filling the core interstices with foam, overall stress-strain curves of the core are computed using for three basic loading histories: core compression, in-plane tension and out-of-plane shear. These are the three most important loading histories for many applications.

The unit cells of Figure 4 are used in these finite element computations. In the compression and shear loadings, rigid plates are bonded to top and bottom surfaces of the unit cell to simulate the behavior of the core attached to the face sheets. The bottom plate is fixed and the top face is displaced. Periodicity is exploited, and periodic boundary conditions are imposed on the unit cell consistent with each loading. Thus, for example, in core compression of the square honeycomb the shear tractions on the web edges in Figure 4a are zero while the in-plane edge displacement parallel to the web is constrained to be zero, simulating overall uniaxial straining as constrained by the faces. For shear loading, there is no net force in the direction perpendicular to the faces. For the folded plate cell in Figure 4b, the length, ℓ, of the unit is a parameter that must be varied to determine the critical buckling mode. The loading referred to as in-plane tension is in reality overall tension subject to zero in-plane straining in the transverse direction consistent with stretching of the infinitely long plate clamped on its sides. For this loading, the edges of the web aligned with the direction of loading are displaced relative to one another uniformly while the edges of the transverse webs are constrained so they undergo no in-plane displacement parallel to the web. Shear tractions vanish on all the edges, and zero traction on the top and bottom edges is enforced in the direction perpendicular to the faces. Further details are described for the analogous calculations for empty cores in [Xue and Hutchinson 2004b]. In the finite element models of foam-filled cores, the displacements of the steel core and polymeric

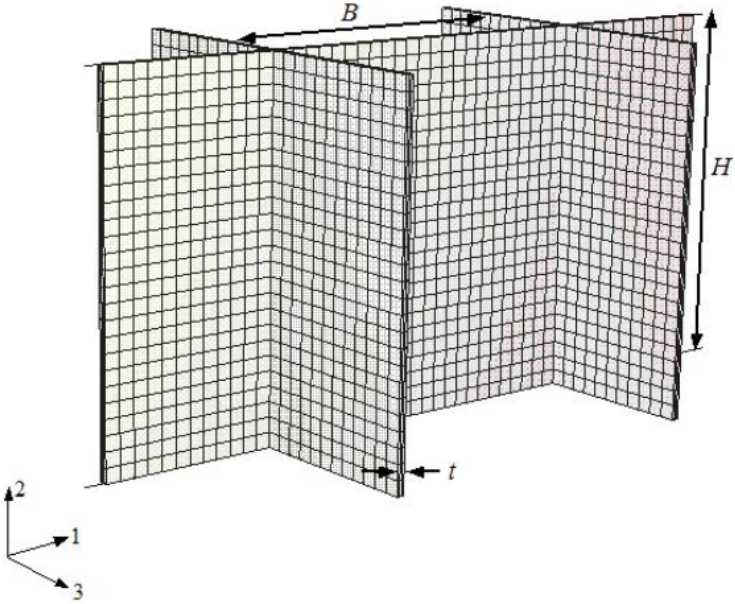

(a) Square honeycomb core geometry

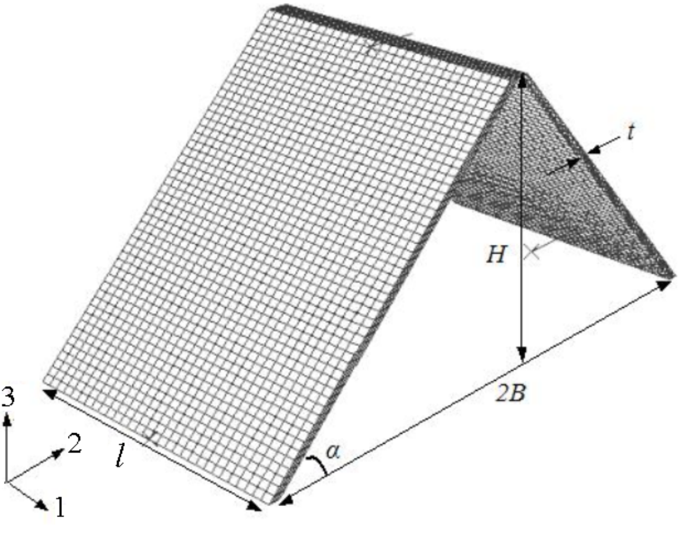

(b) Folded core geometry

Figure 4: Finite element model of a unit core cell

foam coincide at nodal points on shared interfaces. When analyzed with implicit methods, the problems addressed in this paper have very low rates of convergence, because of the complexity of the geometry and the extreme variation of the material behavior. For this reason, ABAQUS Explicit [ABAQUS 2001] is utilized to simulate each simple stress history of empty and foam-filled cores. The analyses are performed under a sufficiently low rate of loading such that inertial effects are very small and the response is essentially quasi-static. Further discussion on this topic is presented in Section 4. The detailed analysis of the "micro" behavior of the core accounts for finite rotations and large plastic strains and it captures features such as plastic buckling and local necking of the core webs (square honeycomb) or core plate (folded sandwich).

3.1. ***Square honeycomb core.*** The overall stress-strain responses for the three basic loading histories are shown (Fig. 5) for a square honeycomb core with $H/B = 1$ and $t/B = 0.02$, corresponding to a volume fraction of steel, $\upsilon_s = 0.04$, whether empty or filled. The foam constitutes *additional* mass in this plot. The dimensions of the core are such that yielding occurs prior to elastic buckling, and plastic buckling is the source of nonlinear deformation for crushing and shearing. The stresses are defined as true stresses. The overall stresses, $\bar{\sigma}_{ij}$, are normalized by their initial yield values for the empty core given later. Because of its relevance to core crush, the compression history is determined to larger strains than in-plane tension and out-of-plane shear. Representative web buckling deflections are included in Figure 5 for compression and shear.

Estimates of the elastic stiffness and initial yield strength of the core based on simple strength of materials formulas are informative as to the role of the foam. For the square honeycomb, estimates of the overall elastic moduli associated with uniaxial stressing in the three directions of orthotropy and out-of-plane shearing are

$$\begin{aligned} E_{22} &\approx \upsilon_s E_s + (1-\upsilon_s)E_f \\ E_{11} = E_{33} &\approx \frac{1}{2}\upsilon_s E_s + (1-\frac{1}{2}\upsilon_s)E_f \\ G_{12} = G_{23} &\approx \frac{1}{2}\upsilon_s G_s + (1-\frac{1}{2}\upsilon_s)G_f \end{aligned} \tag{11}$$

with no accounting for constraint from the faces. The associated average density of the core, $\bar{\rho}_c$, is given by (1). For a typical core with $\upsilon_s = 0.04$, filling with H100 foam increases $\bar{\rho}_c$ by 30%, E_{22} by 1%, and E_{22} and G_{12} by 2%. The corresponding increases for H200 foam are roughly 60%, 3% and 6%. Obviously, the purpose of filling the core with foam is *not* to increase the overall elastic stiffness—employing the additional mass, as steel would be far more effective.

The effect of filling the core with foam on plastic yielding of the core *in the absence of buckling* is more significant than its effect on elastic stiffness. Two

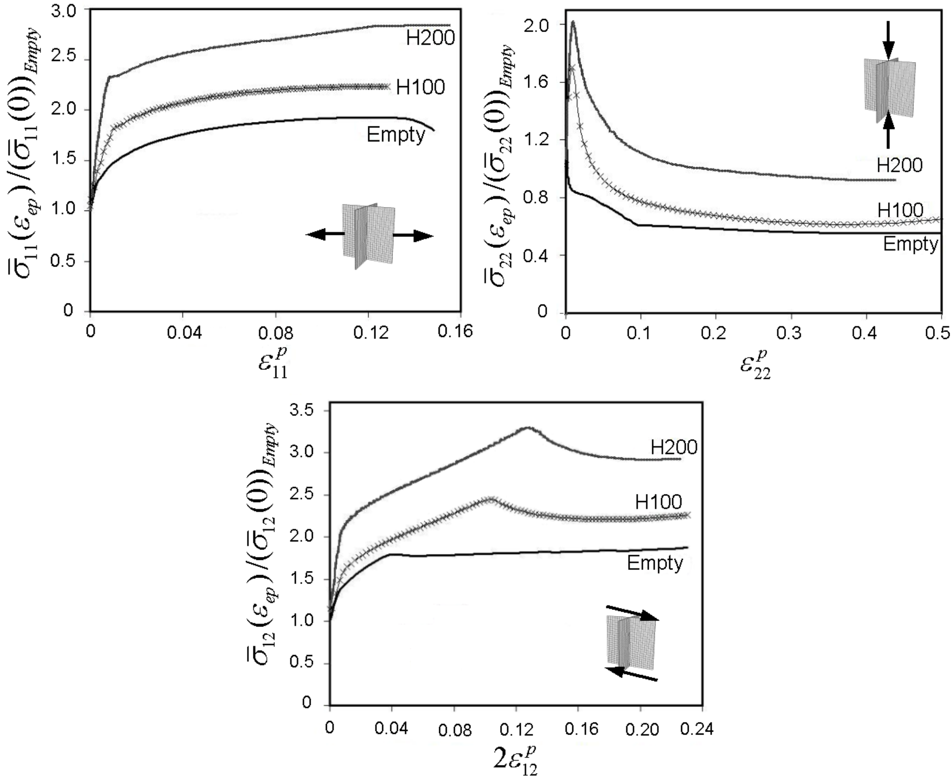

(a) Normalized true stress-true plastic strain relationships for each of the three basic histories for the square honeycomb core with $H/B = 1$ and $t/B = 0.02$ corresponding to $\upsilon_s = 0.04$ (ε_{ij}^p is the true plastic strain associated with the loading).

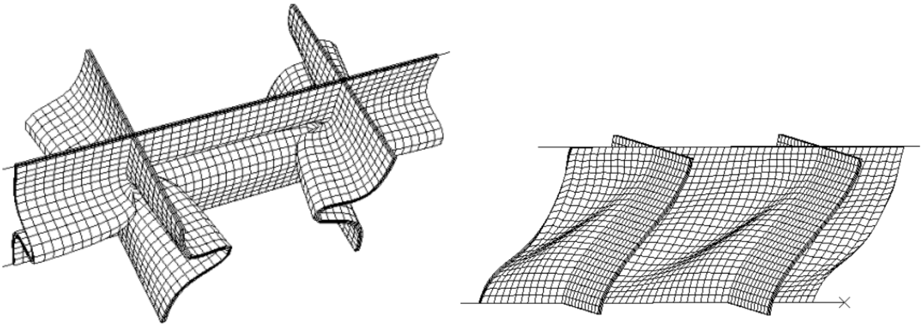

(b) Deformed configuration of the mesh showing compressive buckling of the web for empty square honeycomb core

(c) Deformed configuration of the mesh showing shear buckling of the web for empty square honeycomb core

Figure 5

sets of estimates are given of the overall yield stress for uniaxial stressing in the directions of orthotropy (again with no constraint of the faces) and out-of-plane shearing: (i) the average stress at the strain when the steel yields and (ii) the average stress at the strain when the foam yields[1]. In uniaxial stressing, the steel yields at a strain of 0.1%, while the foams yield at a strain of about 1%. At the strain the steel yields:

$$\begin{aligned}
&\bar{\sigma}_{22}(0) \approx \upsilon_s \sigma_{Ys} + (1-\upsilon_s)(\sigma_{Ys}/E_s)E_f \\
&\bar{\sigma}_{11}(0) = \bar{\sigma}_{33}(0) \approx \frac{1}{2}\upsilon_s \sigma_{Ys} + (1-\frac{1}{2}\upsilon_s)(\sigma_{Ys}/E_s)E_f \\
&\bar{\sigma}_{12}(0) = \bar{\sigma}_{23}(0) \approx \frac{1}{2}\upsilon_s \tau_{Ys} + (1-\frac{1}{2}\upsilon_s)(\tau_{Ys}/G_s)G_f
\end{aligned} \tag{12}$$

Adding foam only increases the initial yield stresses by a few percent. The effect of the foam on the stress at the strain that the foam yields is more significant:

$$\begin{aligned}
&\bar{\sigma}_{22} \approx \upsilon_s \sigma_{Ys} + (1-\upsilon_s)\sigma_{Yf} \\
&\bar{\sigma}_{11} = \bar{\sigma}_{33} \approx \frac{1}{2}\upsilon_s \sigma_{Ys} + (1-\frac{1}{2}\upsilon_s)\sigma_{Yf} \\
&\bar{\sigma}_{12} = \bar{\sigma}_{23} \approx \frac{1}{2}\upsilon_s \tau_{Ys} + (1-\frac{1}{2}\upsilon_s)\tau_{Yf}
\end{aligned} \tag{13}$$

where the yield stresses of the foam are given in Table 1. Strictly, σ_{Ys} and τ_{Ys} should be identified with the corresponding yield strains of the foam, but the increase in stress in the steel above its initial yield due strain hardening at strains on the order of 1% is not large. The elevation in $\bar{\sigma}_{22}$ due to the H100 foam is almost 15% while that for the H200 foam is almost 40%. These increases are still only about half what would be achieved if extra mass were used to increase the steel in the webs. However, for in-plane stressing and out-of-plane shearing, H100 foam gives rise to an 30% increase in the overall yield stresses, while H200 foam increases them by about 80%. These increases are comparable to what would be achieved by increasing the steel in the webs rather filling with foam.

The effects noted above are clearly evident in the overall stress-strain curves in Figure 5. In these plots, each overall stress is normalized by the associated initial yield stress of empty core, $\bar{\sigma}_{ij}(0)_{empty}$, given by (12). First, consider in-plane tension in Figure 5. The overall strain range plotted is too small for necking to begin in the webs. The foam has almost no effect on first yield as expected from the results quoted above. However, the overall stress increases sharply for

---

[1] As in the case of overall elastic stiffness, these are based on elementary estimates from the strength of materials. They ignore, for example, lateral stresses that develop in uniaxial stressing due to difference in the Poisson ratios of the steel and the foam. Nevertheless, the simplicity of the formulas nicely reveals the role of the foam, and the formulas are sufficiently accurate for present purposes.

strains less than about 1% due to the fact that the foam is still elastic. The abrupt change in slope at a strain of about 1% denotes the point where the foam yields; the associated stress is given approximately by (13). For even larger strains, the increases in stress are due to strain hardening of the steel. The behavior in out-of-plane shear in Figure 5 is similar to that described for in-plane tension prior to web buckling which causes the drop in overall stress. Addition of the foam significantly delays the strain at which shear buckling occurs due to its constraint on the lateral deflection of the webs. The consequent effect is the significant increase in the overall flow strength of the core in shear. The foam also delays buckling of the webs in the compressive loading in Figure 5, although buckling occurs at much smaller plastic strains in compression. (The dimensions of the empty core are such that plastic yielding and elastic buckling are almost coincident in compression.) In the post-buckling range, foam helps to stabilize the webs resulting in higher overall stress. It remains to be seen in Section 4, whether the strengthening by the foam observed in Figure 5 will persist when foam is added with a corresponding reduction in steel.

3.2. ***Folded plate core.*** The folded plate core has full orthotropic anisotropy. In particular, the in-plane stretching stiffness and strength of the empty core are substantial in the 1-direction but negligible in the 3-direction. The core plate has core height H, core plate thickness t, and core inclination angle α. The width of the unit cell (Fig. 1b) is

$$B = t/\sin\alpha + H/\tan\alpha. \tag{14}$$

The volume fraction of the core occupied by steel, υ_s, and the relative density of the core, $\bar{\rho}_c$, can be obtained from (4) and (1), respectively.

In the calculations, two core geometries are considered: (a) $\alpha = 45°$ with $t/H = 0.0144$, corresponding to $B/H \approx 1.021$ and $\upsilon_s = 0.02$, and (b) $\alpha = 45°$ with $t/H = 0.0295$, corresponding to $B/H \approx 1.042$ and $\upsilon_s = 0.04$. In out-of-plane compression with no foam, core (a) buckles elastically prior to yielding, while core (b) yields plastically prior to buckling.

Simple estimates for the overall elastic moduli are

$$\begin{aligned}
E_{11} &\approx \upsilon_s E_s + (1-\upsilon_s)E_f\\
E_{22} &= \upsilon_s E_s \sin^4\alpha + (1-\upsilon_s)E_f\\
E_{33} &= (1-\upsilon_s)E_f\\
G_{12} &\approx \upsilon_s G_s \sin^2\alpha + (1-\upsilon_s)G_f\\
G_{23} &\approx \frac{1}{4}\upsilon_s E_s \sin^2 2\alpha + (1-\upsilon_s)G_f\\
G_{13} &\approx \frac{1}{2}\upsilon_s G_s \sin 2\alpha + (1-\upsilon_s)G_f
\end{aligned} \tag{15}$$

Terms of relative order t_c/H_c have been neglected. The overall stresses at which the steel yields (assuming no buckling of the webs) are,

$$\begin{aligned}
\bar{\sigma}_{11}(0) &\approx \sigma_{Ys}\left[\upsilon_s + (1-\upsilon_s)E_f/E_s\right] \\
\bar{\sigma}_{22}(0) &= \sigma_{Ys}\left[\upsilon_s \sin^2\alpha + (1-\upsilon_s)E_f/E_s\right] \\
\bar{\sigma}_{12}(0) &= \tau_{Ys}\left[\upsilon_s \sin\alpha + (1-\upsilon_s)G_f/G_s\right] \\
\bar{\sigma}_{23}(0) &= \tau_{Ys}\left[\upsilon_s \sin 2\alpha/2 + (1-\upsilon_s)G_f/G_s\right] \\
\bar{\sigma}_{13}(0) &= \tau_{Ys}\left[\upsilon_s \cos\alpha + (1-\upsilon_s)G_f/G_s\right]
\end{aligned} \tag{16}$$

The corresponding results for the overall stresses at the strain when the foam yields are

$$\begin{aligned}
\bar{\sigma}_{11} &\approx \upsilon_s\sigma_{Ys} + (1-\upsilon_s)\sigma_{Yf} \\
\bar{\sigma}_{22} &= \upsilon_s \sin^2\alpha\, \sigma_{Ys} + (1-\upsilon_s)\sigma_{Yf} \\
\bar{\sigma}_{12} &= \upsilon_s \sin\alpha\, \tau_{Ys} + (1-\upsilon_s)\tau_{Yf} \\
\bar{\sigma}_{23} &= \upsilon_s \sin 2\alpha\, \tau_{Ys}/2 + (1-\upsilon_s)\tau_{Yf} \\
\bar{\sigma}_{13} &= \upsilon_s \cos\alpha\, \tau_{Ys} + (1-\upsilon_s)\tau_{Yf} \\
\bar{\sigma}_{33} &= (1-\upsilon_s)\sigma_{Yf}
\end{aligned} \tag{17}$$

The basic stress histories for the folded plate core were computed by imposing periodicity conditions on the segment ends. The overall stress-strain curves for the three basic histories, each normalized by the associated initial yield stress of empty core, $\bar{\sigma}_{ij}(0)_{empty}$, are plotted in Figure 6 for the cores with $\upsilon_s = 0.02$ and in Figure 7 for $\upsilon_s = 0.04$. The response for shear, $\bar{\sigma}_{12}$, subsequent to buckling depends on the length of the segment, ℓ; the curves presented in Figs. 6 and 7 have $\ell/H = 1$; this choice ensures that the overall shear at the onset of buckling is only slightly above the critical value.

The webs of the folded plate core with $\upsilon_s = 0.02$ in Figure 6 are sufficiently thin such that elastic buckling occurs prior the plastic yielding of the empty steel core under compression $\bar{\sigma}_{22}$; plastic yielding then occurs immediately after the onset of buckling causing the overall stress to fall dramatically. The role of the foam is substantially increasing the core strength at strains less than about 1%, prior to foam yield, is similar to that described for the square honeycomb core. The effect of the foam on the compressive behavior, $\bar{\sigma}_{22}$, of the core with more steel ($\upsilon_s = 0.04$) in Figure 7 is qualitatively similar in most details. As expected, the strengthening of the foam-filled core relative to the empty core is greatest for the core with the lesser amount of steel.

The effect of the foam on the behaviors under in-plane tension and out-of-plane shear is in accord with the behavior of the square honeycomb cores. In the two

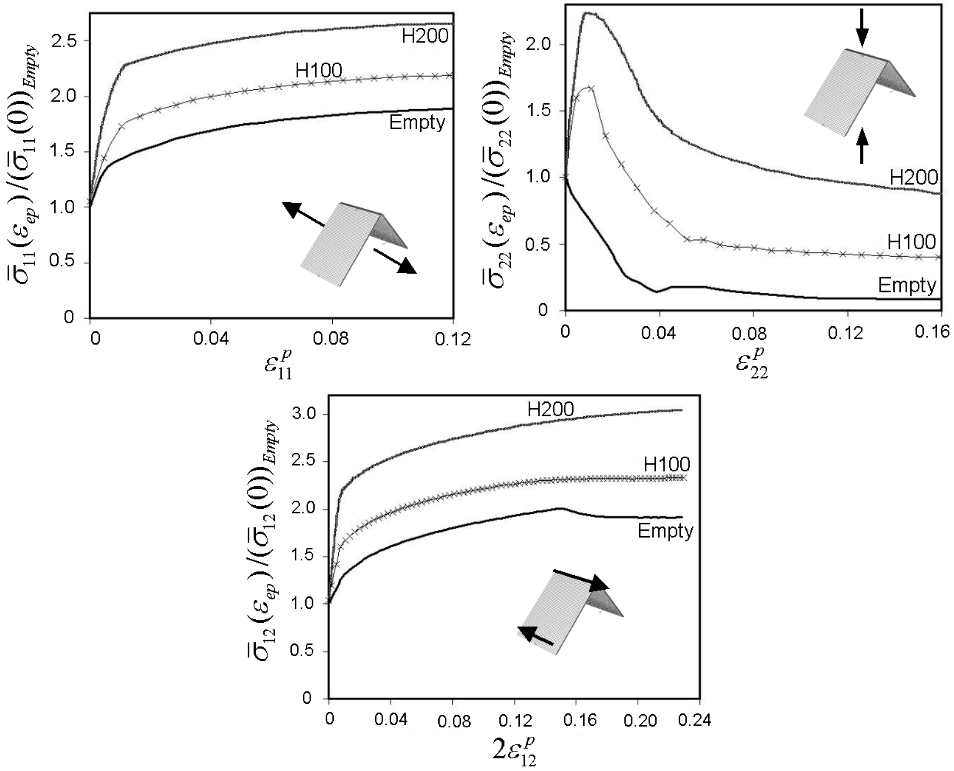

Figure 6: Normalized true stress-true plastic strain relationships for each of the three basic histories for the folded core with $\alpha = 45°$, $t/H = 0.0144$, corresponding to $\upsilon_s = 0.02$.

examples in Figs. 6 and 7, the foam effectively suppresses buckling in shear over the range of shear strain shown.

4. Empty and foam-filled sandwich plates under quasi-static loads

The objective of this section is to provide examples illustrating the influence of filling the core interstices on the structural performance of the two types of sandwich plates under conditions when the loading is quasi-static. Infinitely long plates of width $2L$, clamped along both sides, are subject to normal loads that are independent of the coordinate parallel to the sides. Both punch loads (see Figs. 8 and 9) and uniform pressure loads have been considered. However, because the findings related to the influence of the foam are similar for the two loading cases, only results for the punch load will be presented. Periodicity of the solution in the coordinate parallel to the edges permits analysis of sections of the plates shown in

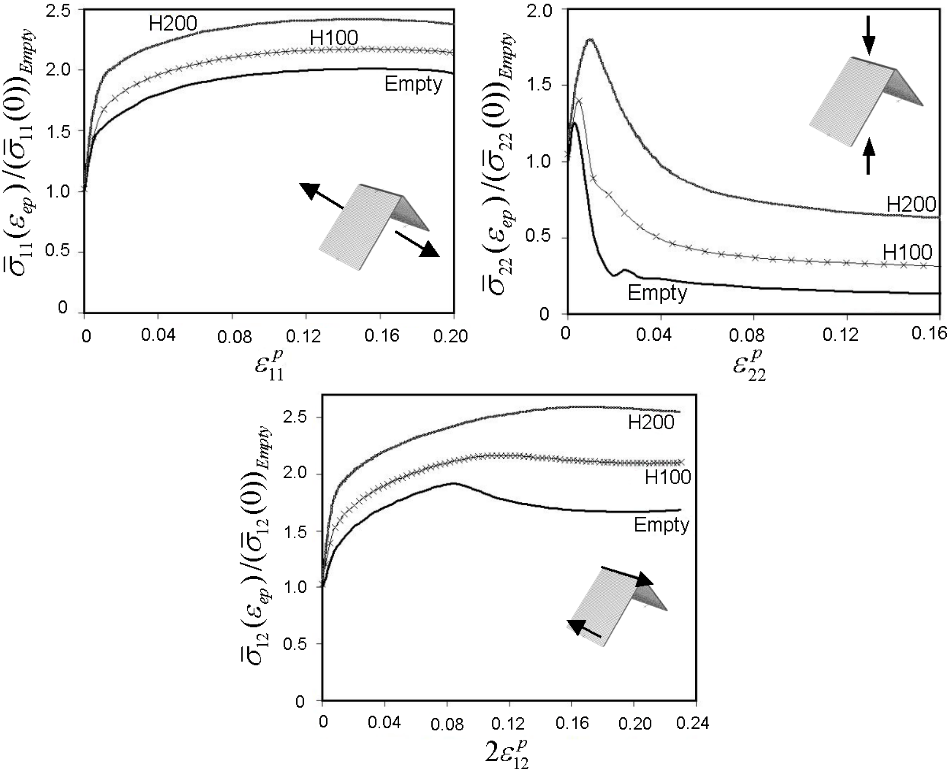

Figure 7: Normalized true stress-true plastic strain relationships for each of the three basic histories for the folded core with $\alpha = 45°$, $t/H = 0.0295$, corresponding to $\upsilon_s = 0.04$.

Figs. 8 and 9. Boundary conditions on the sections are imposed consistent with periodicity and symmetry. The three plates in each of these figures (empty core, core filled with H100, and core filled with H200) all have the same total mass. The amount of steel in the core is also the same for each of these plates; thus, the face sheets of the foam-filled plates have been thinned to offset the mass of the foam. (Alternative accommodation of foam mass by reducing the steel in the core will be considered in another example discussed later.)

For the finite element computations, the sections shown in Figs. 8 and 9 are fully meshed using the same types of three-dimensional elements described in Section 3. The computations are again carried out using ABAQUS Explicit with loads increased at a sufficiently low rate such that the response is effectively quasi-static. For the empty square honeycomb sandwich, the response of the sandwich plate so computed is compared with the result of computations performed using

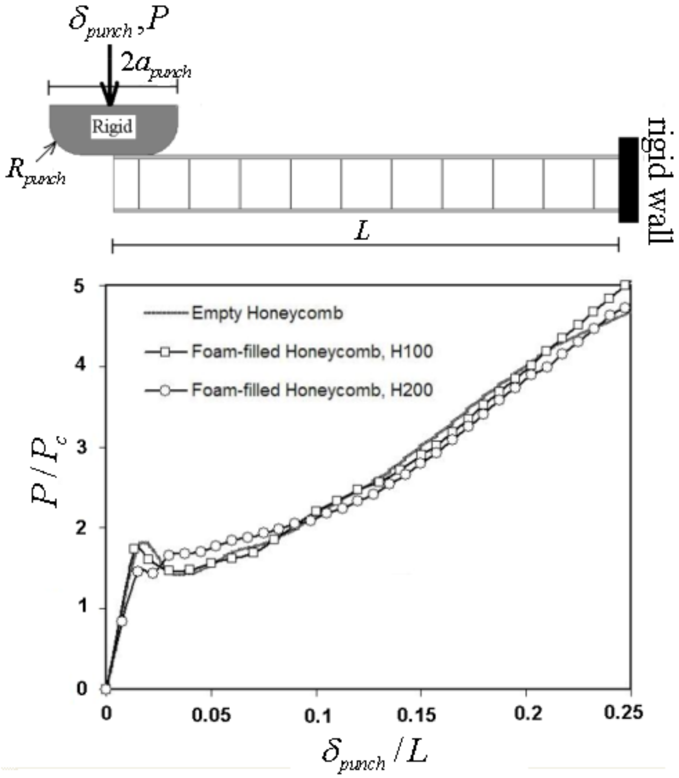

(a) The responses of clamped empty and foam-filled square honeycomb sandwich plates subject to quasi-static punch load

Figure 8
(continued on next page)

ABAQUS Standard [ABAQUS 2001], and good agreement between the two sets of results is revealed. The load/length, P, in Figs. 8 and 9 is normalized by the limit load/length, P_c, for a perfectly plastic empty sandwich plate having limit bending moment/length, $4\sigma_{Ys}h_{face}H$ (based only on contributions from the faces), i.e.

$$P_c = 4\sigma_{Ys}h_{face}H/L \tag{18}$$

The main conclusion that emerges from the results in Figs. 8 and 9 is that there is remarkably little difference between the overall load-deflection behaviors of the sandwich plates with empty cores and that of the plates whose cores are filled with foam. However, there are differences in the details of the deformation. In particular, it can be noted from the deformed configurations shown in the lower

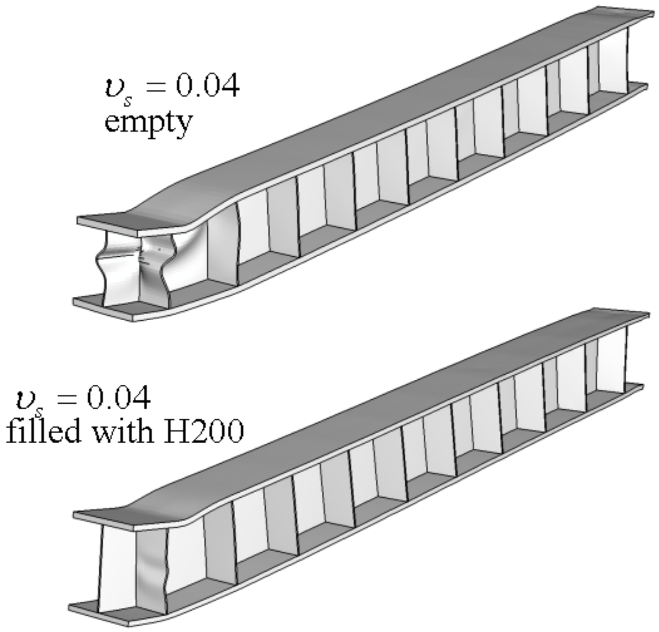

(b) Deformed configuration of the empty and foam-filled square honeycomb sandwich plate at $\delta_{punch}/L = 0.25$ (the polymeric foam components are not shown)

Figure 8 (cont.): The rigid punch is infinite in the direction perpendicular to the cross-section shown and has normalized half-width of $a_{punch}/L = 0.127$ and normalized edge radius of $R_{punch}/a_{punch} = 0.5$. All sandwich plates have $\bar{M}/(\rho_s L) = 0.02$, $H/L = 0.1$ and $B/H = 1$ and $\upsilon_s = 0.04$.

portion of Figs. 8 and 9 that the foam noticeably reduces the buckling deflection of the core webs beneath the indenter.

At low loads, bending dominates the behavior of the plate such that in-plane compressive stresses exist in the top face sheet and in-plane tensile stresses in the bottom face sheet. Plastic yielding begins at $\delta_{Punch}/L \cong 0.01$. Then, as deformation proceeds, the stresses on the top face sheet gradually change from compression to tension signaling the transition to stretching dominated behavior. For the sandwich plate configurations studied here, stretching takes over when δ_{Punch}/L exceeds 0.1. The foam enhances the core crushing strength by providing lateral support of the core webs, and, in this way, it influences the local response of the plate under the punch load. The energy absorbed by plastic deformation by the steel core beneath the indenter is significantly lower for the case of foam-filled sandwich

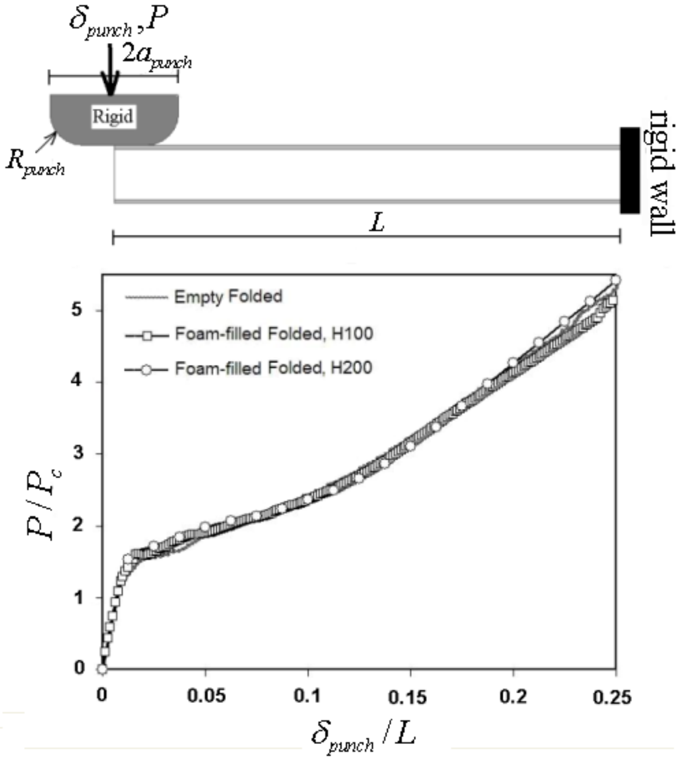

(a) The responses of clamped empty and foam-filled folded sandwich plates subject to quasi-static punch load

Figure 9

(continued on next page)

plates than for the empty core plates because the crushing is much less. In addition, by spreading the deformation more uniformly in the vicinity of the indenter, the foam-filled core may help reduce the tensile strains in the upper face sheet thereby suppressing, or delaying, necking.

5. Empty and foam-filled sandwich plates under impulsive loads

To simulate the response of the plates subject to a uniform air blast, a uniform impulse/area, I (Ns/m^2), is applied to the face sheet towards the blast at time $t = 0$ as a uniform initial velocity, $v = I/\rho_s h_{face}$. The rationale for replacing the pressure pulse by an initial impulse is based on the fact that the response time

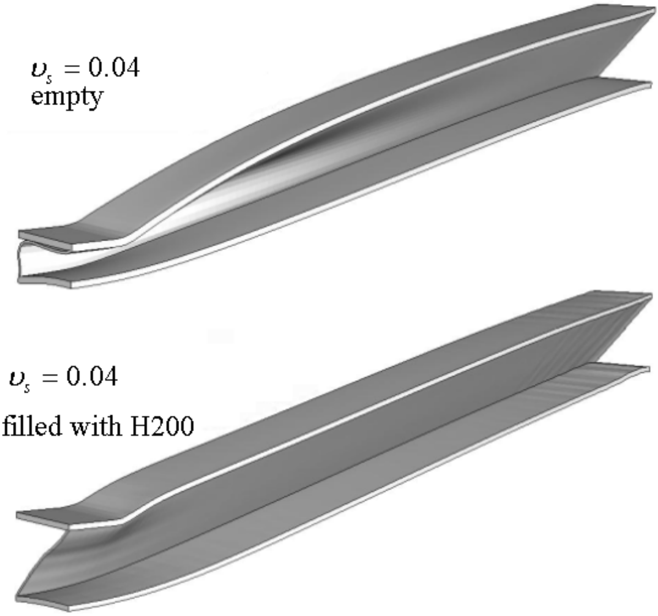

(b) Deformed configuration of the empty and foam-filled sandwich plate at $\delta_{punch}/L = 0.25$ (the polymeric foam components are not shown).

Figure 9 (cont.): The rigid punch is infinite in the direction perpendicular to the cross-section shown and has normalized half-width of $a_{punch}/L = 0.127$ and normalized edge radius of $R_{punch}/a_{punch} = 0.5$. All sandwich plates have $\bar{M}/(\rho_s L) = 0.02,\ \alpha = 45°,\ H/L = 0.1$ and $\upsilon_s = 0.04$.

associated with the overall deflection of the plate is large compared to the period of the pulse [Xue and Hutchinson 2003; Xue and Hutchinson 2004a; Fleck and Deshpande 2004]. For a full-scale plate, the dominant action of the pulse ceases before the face toward the blast has moved only several centimeters.

In this section, the responses of foam-filled square honeycomb and folded plate core sandwich plates under impulsive loads are compared to the corresponding responses of plates with unfilled cores. The plates are similar to those considered in the previous section: infinitely long, of width $2L$, and clamped along their edges. Results for both the deflection of the face sheet toward the blast and the core crushing strain are presented, as are selected results on energy dissipation within the sandwich plate. Define the average crushing strain of the core at the center of the plate by $\bar{\varepsilon}_c = \Delta H/H$, where ΔH is the reduction in core height. Denote the final deflection at the center of the top face sheet by plate by δ. For the plate with the empty square honeycomb core, δ/L and $\bar{\varepsilon}_c$ depend on the following set of dimensionless parameters [Xue and Hutchinson 2004a]:

$$\frac{I}{M\sqrt{\sigma_{Ys}/\rho_s}},\ \frac{M}{\rho_s L},\ \upsilon_s,\ \frac{H}{L},\ \frac{B}{H}$$

plus N and σ_{Ys}/E. For plates with unfilled folded plate cores, normalized maximum deflection and the crushing strain at the center depend on the same list of dimensionless variables with the exception that B/H is replaced by α. In addition, dimensionless time variable governing the time-dependence is $t\big/\big(L/\sqrt{\sigma_{Ys}/\rho_s}\big)$. The computations were carried out using ABAQUS Explicit with the same periodic sections and three-dimensional meshes introduced for the quasi-static loadings.

The effect of the momentum impulse imparted to the top face sheet of the sandwich plates, $I\big/\big(M\sqrt{\sigma_{Ys}/\rho_s}\big)$, on δ/L and $\bar{\varepsilon}_c$ are presented in Figs. 10 and 11. Results for empty cores and foam-filled cores are shown. The plates in these figures all have the same total mass; foam mass is offset by thinning the face sheets, not the core webs. All the sandwich plates have $M/\rho_s L = 0.02$, $\upsilon_s = 0.04$, $H/L = 0.1$. For plates with honeycomb cores in Figure 10, $B/H = 1$, while for plates with folded plate cores in Figure 11, $\alpha = 45°$. The range of normalized impulse plotted covers the full range of realistic deflections. As was the case noted for the quasi-static loadings, there is remarkably little difference in the maximum top face deflection of the two classes of plates between the filled and unfilled cores. Foam reduces the crushing strain of the folded plate core (Figure 11), but this does not translate into a decrease in the overall deflection relative to the plate with the empty core. Inserting foam has little effect on the maximum crushing strain of plates with the square honeycomb cores. This is primarily due to the fact that the webs of the core are stabilized against buckling by their lateral inertia at the high crushing velocities considered here [Vaughn et al. 2005].

In studying the comparative advantages of equal weight filled and unfilled plates, one would obviously want to know whether it is best to offset the weight of the foam by thinning the face sheets or by thinning the core webs, or some combination of the two. We have not carried out a thorough optimization addressing this issue, but we will present one set of computations for the sandwich plates with the square honeycomb cores that provides some insight into the question. The dimensions of the unfilled sandwich plate in Figure 10 were established to be nearly optimal at a normalized impulse level of $I\big/\big(M\sqrt{\sigma_{Ys}/\rho_s}\big) = 0.25$ by [Xue and Hutchinson 2004a]. In particular, the ratio of steel in the core to the total steel in the plate (20%) was found to minimize δ/L at that impulse level for all plates with the same total mass with $B/H = 1$ and $H/L = 0.1$. Moreover, the dependence on B/H and H/L was found to be relatively weak.

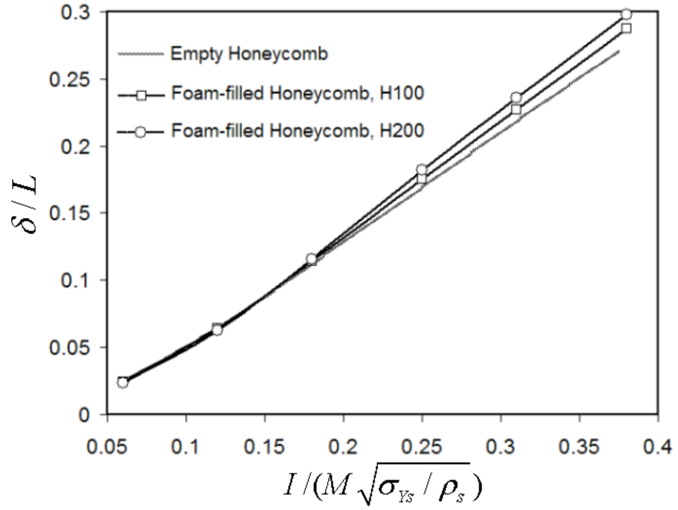

(a) The normalized maximum deflection of the top face sheet δ/L

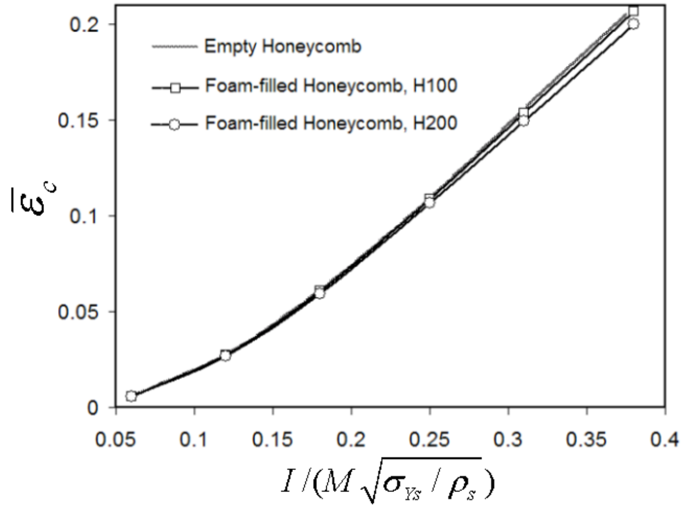

(b) The maximum nominal compressive strain in the core, $\bar{\varepsilon}_c$, of empty and foam-filled square honeycomb sandwich plates versus normalized momentum impulse, $I\big/\left(M\sqrt{\sigma_{Ys}/\rho_s}\right)$.

Figure 10: All sandwich plates have $\bar{M}/(\rho_s L) = 0.02$, $H/L = 0.1$ and $B/H = 1$ and $\upsilon_s = 0.04$.

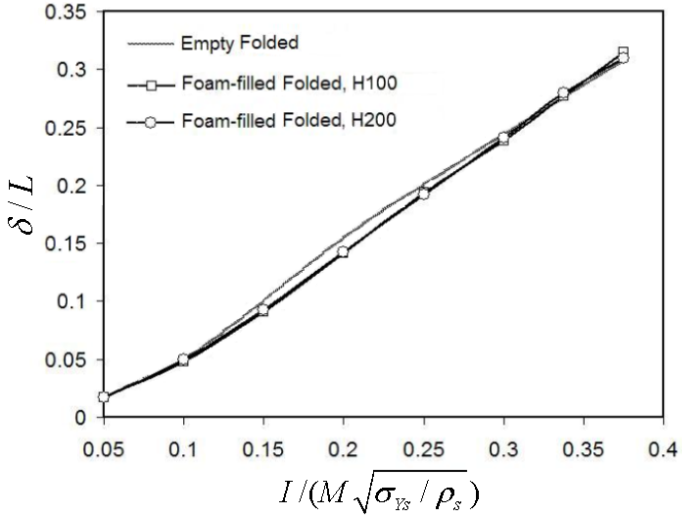

(a) The normalized maximum deflection of the top face sheet δ/L

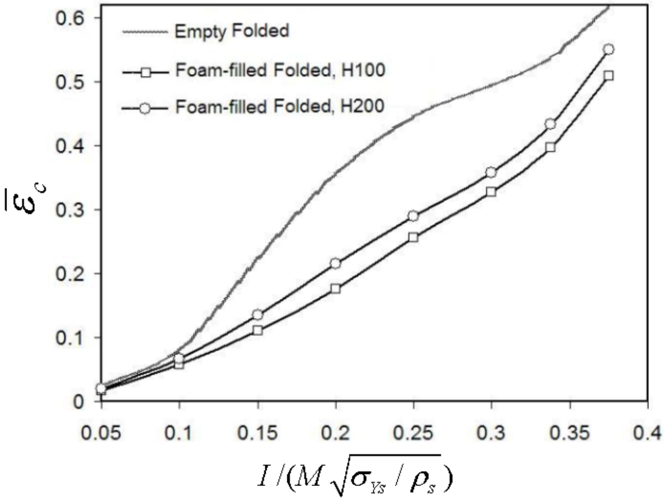

(b) The maximum nominal compressive strain in the core, $\bar{\varepsilon}_C$, of empty and foam-filled sandwich plates versus normalized momentum impulse, $I/\left(M\sqrt{\sigma_{Ys}/\rho_s}\right)$.

Figure 11: All sandwich plates have $\bar{M}/(\rho_s L) = 0.02,\ \alpha = 45°,\ H/L = 0.1$ and $\upsilon_s = 0.04$.

For the sandwich plates with the square honeycomb cores subject to an impulse, $I/\left(M\sqrt{\sigma_{Ys}/\rho_s}\right) = 0.25$, Figure 12 displays the dependence of the normalized maximum deflection, δ/L and the maximum core crushing strain on the volume fraction of steel in the core, υ_s, for unfilled cores and for cores filled with the two densities of foam. The total mass/area of each plate is the same with $M/\rho_s L = 0.02$; the deflection of the solid plate with the same mass/area and subject to the same impulse is included on the abscissa. Reducing ν_s increases the thickness of the faces and vise versa, because the mass of foam in the core varies only slightly over the range plotted of ν_s for each of the two foam-filled sandwiches. Thus, Figure 12 displays the tradeoff between core mass and face sheet mass. While the unfilled sandwich plate has the minimum deflection for cores with steel webs with relative density $\upsilon_s = 0.04$, the best performance from plates with foam-filled cores is achieved with lower relative density of steel—about 0.03 for the H200 foam. For plates with $\upsilon_s \geq 0.02$, the crushing strain is essentially the same for the filled and unfilled plates at the level of impulse imposed, and, moreover, it is less than 20%.

Figure 13 presents the final deformed configuration of the foam-filled square honeycomb sandwich plates (H200 Foam) for three volume fractions of the core occupied by steel, υ_s, under impulse, $I/\left(\bar{M}\sqrt{\sigma_{Ys}/\rho_s}\right) = 0.25$. As in the previous plots, all plates have $\bar{M}/(\rho_s L) = 0.02$, $H/L = 0.1$ and $B/H = 1$. For a low relative density of steel in the core ($\upsilon_s = 0.01$), local plastic buckling of the steel core clearly compromises the performance of the plate such that the crushing strain is almost 30%. For plates with excess steel in the core ($\upsilon_s = 0.08$) and therefore overly thinned face sheets, the top face undergoes extensive plastic bending into the core while the core webs undergo very little deformation. The intermediate case ($\upsilon_s = 0.04$) displays modest amounts of core deformation and face sheet bending. Note that for both $\upsilon_s = 0.04$ and $\upsilon_s = 0.08$, there is very little evidence of core web buckling, even though the core has been crushed to average strains of about 12% and 7%, respectively. These crushing strains are far in excess of the strain at plastic yield (a small fraction of 1%) and, also, well above the quasi-static plastic buckling strain of the webs. The suppression of buckling is due in part to the lateral support of the webs by the foam and the inertial stabilization of the webs under the impulsive loading.

A limited study on the effect of foam densification on the structural performance of square honeycomb sandwich plates filled with polymeric foam H200 under blast load is conducted by fitting a multi-linear line to the response of this material under uniaxial compressive load (see Section 2.2 for more detail). The sandwich plates having $\bar{M}/(\rho_s L) = 0.02$, $H/L = 0.1$ and $B/H = 1$ with various volume fractions of the core occupied by steel, $0 \leq \upsilon_s \leq 0.04$, are analyzed under the initial momentum $I/\left(\bar{M}\sqrt{\sigma_{Ys}/\rho_s}\right) = 0.25$. The result shows that the deformation mechanism of the foam-filled square honeycomb sandwich plates is not significantly affected

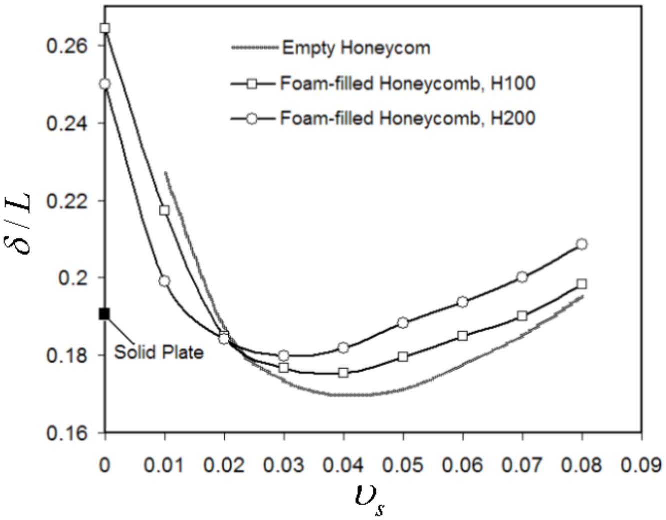

(a) The normalized maximum deflection of the top face sheet δ/L

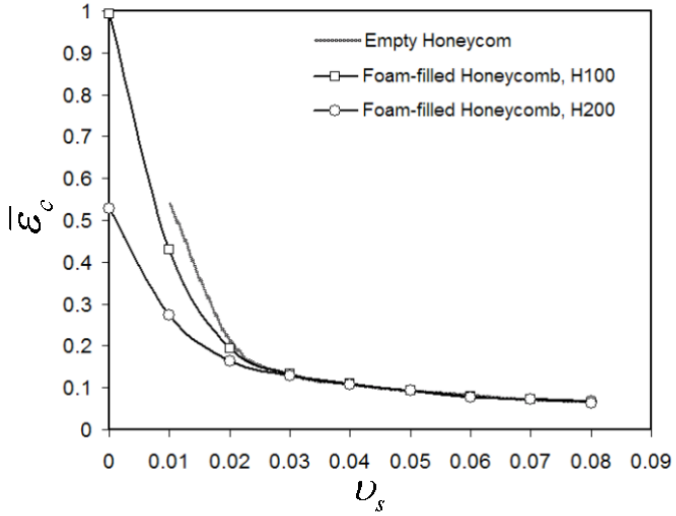

(b) The maximum nominal compressive strain in the core, $\bar{\varepsilon}_c$, of empty and foam-filled square honeycomb sandwich plates versus the volume fraction of the core occupied by steel, υ_s

Figure 12: All sandwich plates have $\bar{M}/(\rho_s L) = 0.02$, $H/L = 0.1$ and $B/H = 1$ and subjected to $I\Big/\left(M\sqrt{\sigma_{Ys}/\rho_s}\right) = 0.25$.

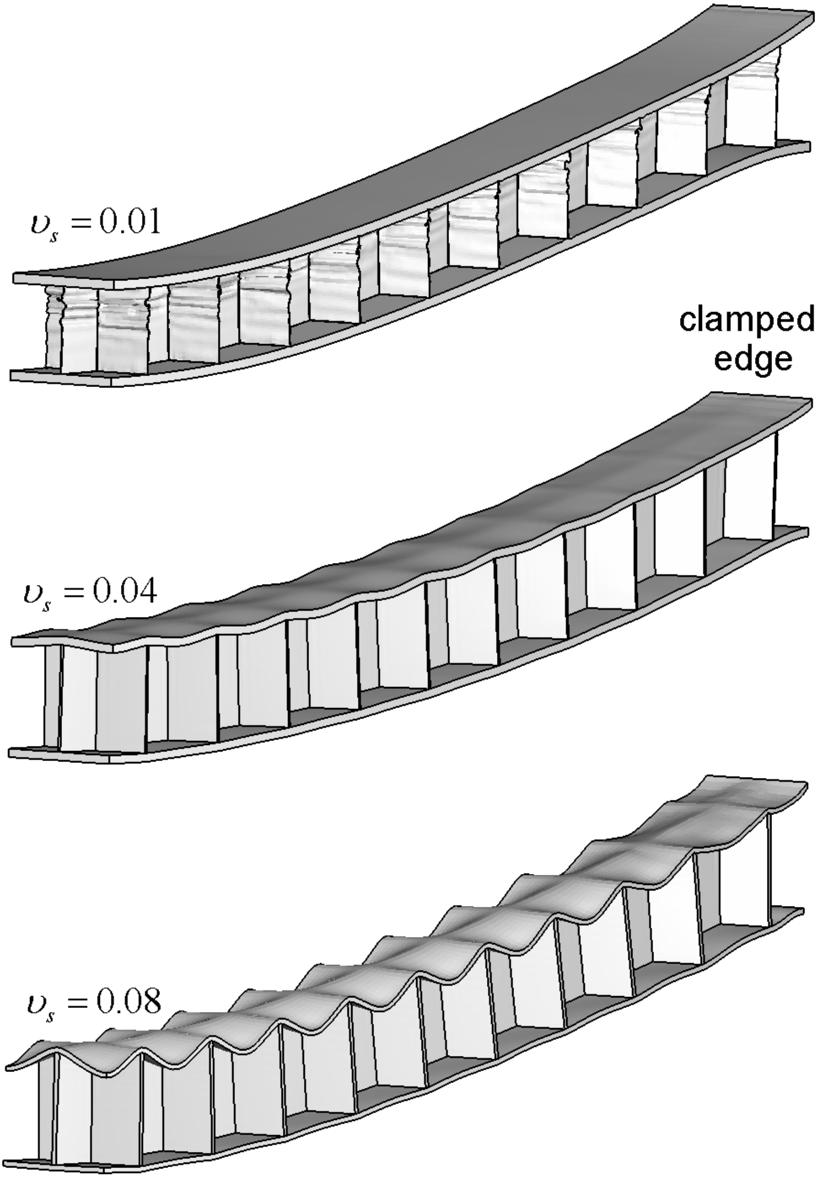

Figure 13: Deformed configurations of the foam-filled square honeycomb sandwich plates (H200 Polymeric Foam) for various volume fraction of the core occupied by steel, υ_s under the normalized momentum impulse $I\big/\big(M\sqrt{\sigma_{Ys}/\rho_s}\big) = 0.25$, at $t\big/\big(\sqrt{\sigma_{Ys}/\rho_s}\big) = 1$. All sandwich plates have $M/(\rho_s L) = 0.02$, $H/L = 0.1$ and $B/H = 1$ (the polymeric foam components are not shown).

by considering the foam densification behavior under uniaxial compression. The maximum effect of accounting for foam densification on the maximum displacement of the top face sheet and maximum nominal compressive strain in the core are $\approx 1.1\%$ and $\approx 6.5\%$, respectively.

6. Plastic energy absorption in foam-filled honeycomb sandwich plates

Insight into the role of the polymer foam is gained by examining the contributions to plastic energy dissipation of each component of the empty and foam-filled (H200 foam) sandwich plates under impulsive load. Figure 14 displays the time history of the plastic dissipation in the core and face sheets along with the total plastic dissipation for the two plates, each of which has $M/\rho_s L = 0.02$, $\upsilon_s = 0.04$, $H/L = 0.1$, $B/H = 1$ and subject to $I\big/\big(\bar{M}\sqrt{\sigma_{Ys}/\rho_s}\big) = 0.25$. The results are plotted in dimensionless form as U_P/KE_0, where KE_0 is the initial kinetic energy imparted to the plate and U_P is the energy dissipated in plastic deformation in the component indicated at time $t\big/\big(L/\sqrt{\sigma_{Ys}/\rho_s}\big)$. The total dissipation is also shown.

For a prescribed initial momentum impulse applied to the top face sheet, I, the initial kinetic energies imparted to the plate is $KE_0 = I^2/(2\rho_s h_{face})$. Thus, the foam-filled plate has to absorb more energy than the unfilled plate since in the example in Figure 14 the face sheets of the filled plate are thinner than those of the unfilled plate (the total mass and the mass of steel in each core is the same for the two plates). The results in Figure 14 show that for both sandwich plates, the earliest stage of deformation with $t\big/\big(L/\sqrt{\sigma_{Ys}/\rho_s}\big) < 0.05$ (Stage II, [Fleck and Deshpande 2004]) consists of the top face sheet flying into, and crushing the core. In this stage, the motion away from the clamped supports is one-dimensional, the bottom face sheet is almost stationary, and very little plastic dissipation occurs in the bottom face sheets. By the end of this stage, the two face sheets are moving with nearly the same velocity. In this stage, the foam contributes significantly to the plastic energy dissipation of the foam-filled sandwich plate core layer by absorbing around 10% of the initial kinetic energy. As a consequence, the energy dissipated in the steel core of the foam-filled sandwich plate is around 10% smaller than that the empty sandwich one. The total plastic energy dissipated in the sandwich plate in stage II is almost the same for both cases ($\approx 60\%$), in close agreement with the simple analysis based on the conservation of momentum between the beginning and end of stage II [Fleck and Deshpande 2004].

Subsequent to stage II, there is essentially no further core compression and the entire sandwich plate undergoes bending followed by in-plane stretching (stage III of [Fleck and Deshpande 2004]. In this stage, the kinetic energy not absorbed in core crush must be absorbed in overall bending and stretching. For both plates,

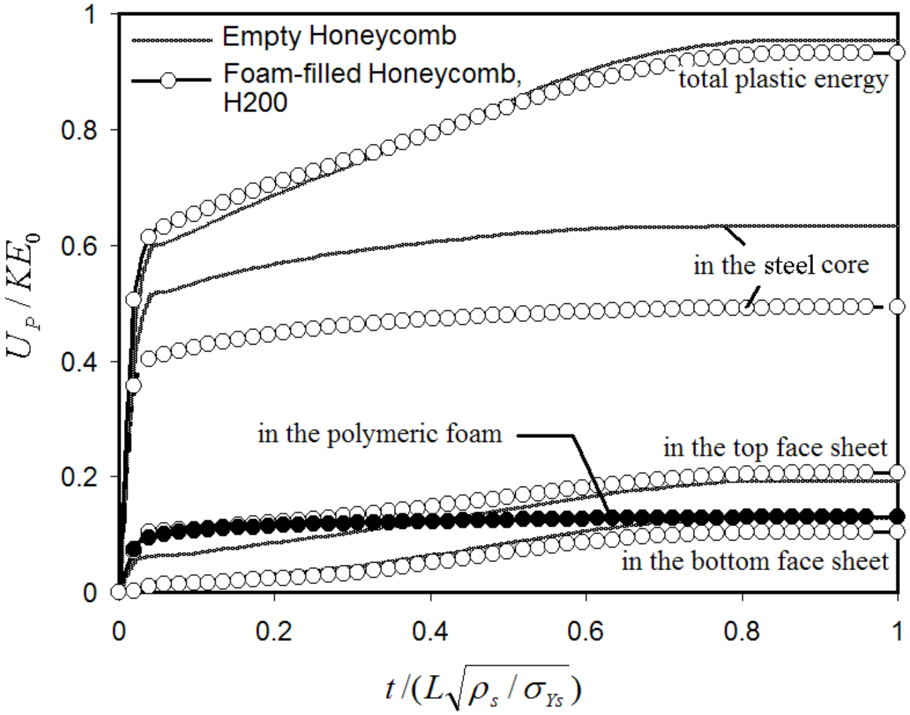

Figure 14: The time history of plastic dissipation in empty and foam-filled square honeycomb sandwich plates (H200 Polymeric Foam) with $M/(\rho_s L) = 0.02$, $\upsilon_s = 0.04$, $H/L = 0.1$ and $B/H = 1$ and subjected to $I/\left(M\sqrt{\sigma_{Ys}/\rho_s}\right) = 0.25$.

almost all the plastic dissipation has occurred by $t/\left(L/\sqrt{\sigma_{Ys}/\rho_s}\right) \approx 0.8$. Subsequently, the plate undergoes elastic vibration, although this is not evident in the plot of plastic energy dissipation. The total plastic energy dissipated in the empty and foam-filled sandwich plates is between 90% and 95% of the initial kinetic energy. The initial kinetic energy is never fully dissipated plastically because of residual elastic stress (the main contribution) and continuing elastic vibratory motion.

The influence of the relative density of the steel in the core, υ_s, on the energy dissipation in sandwich plate components for foam-filled (H200 foam) plates is seen in Figure 15. These plates all have the same total mass ($\bar{M}/(\rho_s L) = 0.02$, $H_c/L = 0.1$, $B/H_c = 0.1$), and thus increases in steel in the core is traded against steel in the faces in the same manner as the examples in Figure 12. The plates are all subject to $I/\left(\bar{M}\sqrt{\sigma_{Ys}/\rho_s}\right) = 0.25$. The maximum plastic energy dissipated corresponds to $\upsilon_s = 0.03$, which is the configuration that experiences the minimum deflection (Figure 12). For the foam-filled plates with $\upsilon_s \geq 0.03$, the steel

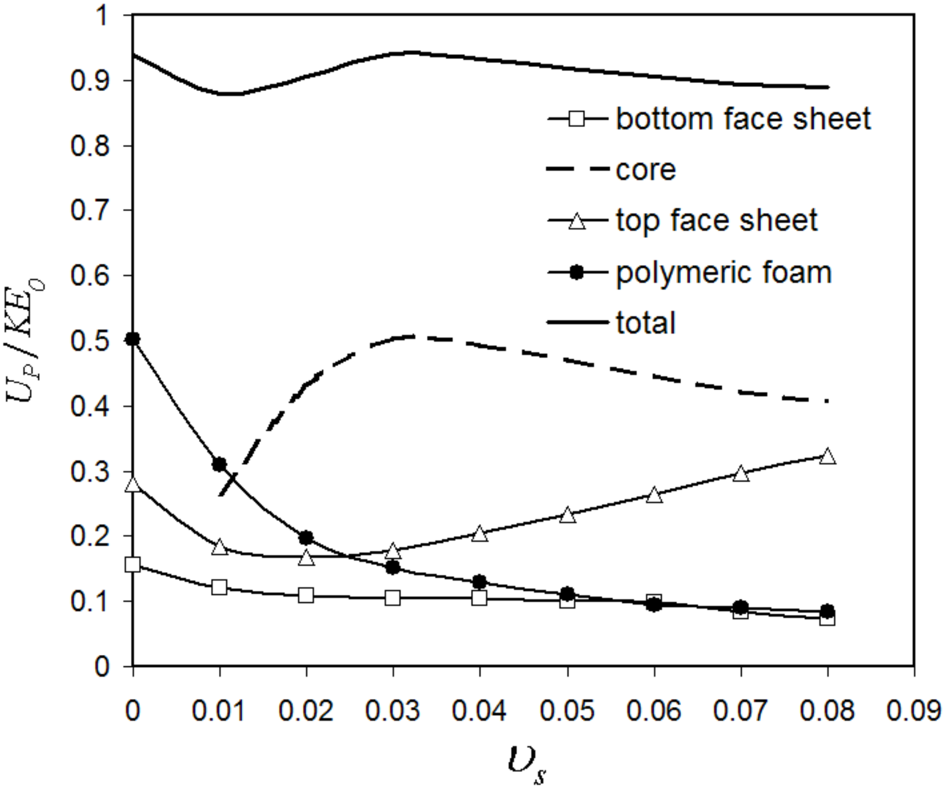

Figure 15: The plastic dissipation in foam-filled square honeycomb sandwich plates (H200 Polymeric Foam) versus the volume fraction of the core occupied by steel, υ_s, at $t\big/\big(L/\sqrt{\sigma_{Ys}/\rho_s}\big) = 1$. All sandwich plates have $M/(\rho_s L) = 0.02$, $H/L = 0.1$, $B/H = 1$ and subjected to $I\big/\big(M\sqrt{\sigma_{Ys}/\rho_s}\big) = 0.25$.

core can withstand the blast load without undergoing a significant plastic buckling (cf. Figure 13). For these sandwich plates, energy dissipation in the core occurs as compressive yielding of the steel core and polymeric foam. However, for smaller volume fractions of the core occupied by steel, $\upsilon_s < 0.03$, the steel webs undergo significant buckling and are unable to absorb energy as effectively as when they do not buckle.

7. Concluding remarks

The examples presented in this paper indicate that sandwich plates with foam-filled square honeycomb cores and folded plate cores exhibit comparable structural performance in resisting deformation to sandwich plates of equal mass with unfilled cores under representative quasi-static and impulsive loads. In other words, while there appears to be no clear advantage to filling the core with foam for structural purposes, there is no evident disadvantage either. Thus, if other compelling reasons to fill core interstices with foam exist, such as environmental protection or soundproofing, the examples here suggest that it should be possible to do this without structural penalty. These conclusions are drawn from the examples in the present study that have been limited to cores with thickness fixed relative to the half-width of the plate at $H/L = 0.1$. Earlier work has shown that this core thickness is associated with plates with near-optimal structural performance against uniformly distributed air and water blasts, although thicker cores can be somewhat more effective. Sandwich plates with foam-filled, thicker cores will have larger fraction of their total mass in foam, and it is not obvious that they will retain the structural performance of their unfilled counter parts. Thus, we emphasize that further study is required if sandwich plates have thickness significantly larger than $H/L = 0.1$.

Acknowledgement

This work has been supported in part by the ONR under grants GG10376-114934 and N00014–02–1–0700 and in part by the Division of Engineering and Applied Sciences, Harvard University.

References

[ABAQUS 2001] *ABAQUS/Explicit user's manual*, Version 6.0, Hibbitt and Karlsson and Sorensen Inc., Pawtucket, RI, 2001.

[Abot et al. 2002] J. L. Abot, I. M. Daniel, and E. E. Gdoutos, "Contact law for composite sandwich beams", *J. Sandw. Struct. Mater.* **4** (2002), 157–173.

[Boyer and Gall 1985] H. E. Boyer and T. L. Gall (editors), *Metals handbook*, desk ed., edited by H. E. Boyer and T. L. Gall, American Society for Metals, 1985.

[Deshpande and Fleck 2001] V. S. Deshpande and N. A. Fleck, "Multi-axial yield behavior of polymer foams", *Acta Mater.* **49** (2001), 1859–1866.

[DIAB 2005] *Divinycell technical data, H Grade*, DIAB International, Sweden, 2005, Available at http://www.diabgroup.com/americas/u_products/u_prods_2.html.

[Fleck and Deshpande 2004] N. A. Fleck and V. S. Deshpande, "The resistance of clamped sandwich beams to shock loading", *J. Appl. Mech.* (*ASME*) **71**:3 (2004), 386–401.

[Fleck and Sridhar 2002] N. A. Fleck and I. Sridhar, "End compression of sandwich columns", *Compos. A: Appl. Sci. Manuf.* **33** (2002), 353–359.

[Gibson and Ashby 1997] L. J. Gibson and M. F. Ashby, *Cellular solids: structures and properties*, 2nd ed., Cambridge University Press, 1997.

[Hutchinson and Xue 2005] J. W. Hutchinson and Z. Xue, "Metal sandwich plates optimized for pressure impulses", *Int. J. Mech. Sci.* **47** (2005), 545–569.

[Vaughn et al. 2005] D. Vaughn, M. Canning, and J. W. Hutchinson, "Coupled plastic wave propagation and column buckling", *J. Appl. Mech.* **72** (2005), 139–146.

[Xue and Hutchinson 2003] Z. Xue and J. W. Hutchinson, "Preliminary assessment of sandwich plates subject to blast loads", *Int. J. Mech. Sci.* **45** (2003), 687–705.

[Xue and Hutchinson 2004a] Z. Xue and J. W. Hutchinson, "A comparative study of impulse-resistant metal sandwich plates", *Int. J. Impact Eng.* **30** (2004), 1283–1305.

[Xue and Hutchinson 2004b] Z. Xue and J. W. Hutchinson, "Constitutive model for quasi-static deformation of metallic sandwich cores", *Int. J. Numer. Methods Eng.* **61** (2004), 2205–2238.

[Zhang et al. 1997] J. Zhang, Z. Lin, A. Wong, N. Kikuchi, V. C. Li, A. F. Yee, and G. S. Nusholtz, "Constitutive modeling and material characterization of polymeric foam", *J. Eng. Mater. Technol. (ASME)* **119** (1997), 284–291.

[Zhang et al. 1998] J. Zhang, N. Kikuchi, V. C. Li, A. F. Yee, and G. S. Nusholtz, "Constitutive modeling of polymeric foam material subjected to dynamic crash loading", *Int. J. Impact Eng.* **21** (1998), 369–386.

Received 9 May 2005. Revised 7 Sep 2005.

A. VAZIRI: `avaziri@deas.harvard.edu`
Division of Engineering and Applied Sciences, Harvard University, Cambridge MA 02138

Z. XUE: `xue@esag.harvard.edu`
Division of Engineering and Applied Sciences, Harvard University, Cambridge MA 02138

J. W. HUTCHINSON: `hutchinson@husm.harvard.edu`
Division of Engineering and Applied Sciences, Harvard University, Cambridge MA 02138

JOURNAL OF MECHANICS OF MATERIALS AND STRUCTURES
Vol. 1, No. 1, 2006

A SEMIANALYTICAL SOLUTION FOR FREE VIBRATION ANALYSIS OF STIFFENED CYLINDRICAL SHELLS

GUANGHUI QING, ZHENYU FENG, YANHONG LIU AND JIAUJUN QIU

Based on a semianalytical solution of the state-vector equations, we propose a novel mathematical model for the free vibration analysis of cylindrical shells with stiffeners and for cylindrical panels with discontinuities in thickness and/or with cutouts. The shell and stiffeners are regarded as three-dimensional elastic bodies, but the same quadrilateral element is used to discretize the shell and stiffeners. The method accounts for the compatibility of displacements and stresses on the interface between layers of the laminated shell and stiffeners, for transverse shear deformation, and of course for the rotational inertia of the shell and stiffeners. To demonstrate the model's excellent predictive abilities, several examples are analyzed numerically.

The model can be easily modified to solve problems of stiffened piezolaminated plates and shells, or plates and shells with patches made of a piezoelectric material.

1. Introduction

A sheet-stiffener combination provides the maximum strength-to-weight ratio for any structure and hence becomes the obvious choice in advanced structures such as pressure vessels, airplanes, submarine hells and missiles. These structures are subject to external dynamic loads. Therefore, prediction of dynamic responses is of considerable interest for engineers.

Stiffened shells or plates can be analyzed by considering equivalent orthotropic systems. This method is mainly applicable only when large numbers of stiffeners are closely and evenly spaced. Another method, treating separately the shell/plate and stiffeners, is more general as it can accommodate any stiffener distribution.

For ring-stiffened or string-stiffened circular cylindrical shells there have been many investigations involving free vibration analysis or dynamic response analysis. Al-Najafi and Warburton [1970], using the finite element method, investigated the

---

Keywords: free vibration, stiffened cylindrical shells, laminated cylindrical shells, semianalytical solution, state-vector equation.

Work supported by Scientific Research Initiation Foundation of CAUC (Grant No. 05QD01S) and the National Natural Science Foundation of China (Grant No. 10072038).

.

natural frequencies and mode shapes of thin circular cylindrical shells with stiffening rings. Wilken and Soedel [1976] employed the receptance method to determine the natural frequencies and mode shapes of circular cylindrical shells stiffened by rings. Stanley and Ganessan [1997] used circular cylindrical shell elements and studied the natural frequencies of stiffened cylindrical shells for short and long shells with clamped-clamped boundary condition. Zhao, Liew, and Ng [Zhao et al. 2002], using an energy approach, investigated the free vibration of stiffened simply supported rotating cross-ply laminated cylindrical shells. Gong and Lam [1998], using layered shell elements for both plate and stiffener in MSC/Patran and LS-DYNA3D, carried out a transient response analysis of a stiffened composite submersible hull. Rikards, Chate, and Ozolinsh [Rikards et al. 2001] developed a triangular finite element method for the study of the free vibrations of stiffened laminated composite shells. Yang and Zhou [1995] used the transfer function method to analyze the free vibration of a ring-stiffened shell. Wang, Swaddiwudhipong and Tian [Wang et al. 1997] investigated the free vibration problem for isotropic cylindrical shells with varying ring-stiffener distribution, using the extended Ritz method. Kim and Lee [2002] analyzed the effects of ring stiffeners on vibration characteristics and transient responses for ring-stiffened composite cylindrical shells subject to step pulse loading. Srinivasan and Krishnan [1989] studied the dynamic response analysis of stiffened conical shell panels. Sinha and Mukhopadhyay [1995] investigated the dynamic response of stiffened plates and shells by the finite element method employing a high-precision arbitrary-shaped triangular shell element in which stiffeners may lie in arbitrary directions within the element. Liao and R. [1994] studied the dynamic stability of laminated composite stiffened or nonstiffened plates and shells due to periodic in-plane forces at boundaries using the finite element method.

The semianalytical method is an important approach in the analysis of multilayered structures with complicated boundary conditions [Zou and Tang 1995b; 1995a; Sheng and Ye 2002b; 2002a; 2003]. The main theory used in these references is state-vector equation theory. Based on the mixed formulation of solid mechanics, we use the finite element approach in the plane and once the transfer matrix of a single layer is obtained, we introduce interface continuity conditions to assemble a global matrix of structures. The advantages of this semianalytical solution method are:

1. The order of the global matrix does not depend on the number of layers, since the matrix is obtained by the multiplication of the transfer matrix of each layer via an interface continuity condition. Hence the three-dimensional problem is transformed into a two-dimensional one.

2. “The varying material and geometric properties along the independent spatial variable are allowed” [Steele and Kim 1992].

3. Anisotropic layered materials can be simply handled [Steele and Kim 1992].

In this paper, a general, novel semianalytical solution for the free vibration analysis of cylindrical shells with different stiffeners and cylindrical panels with discontinuity in the thickness or/and with cutouts is achieved through the separate consideration of the shell and stiffeners. On the basis of the state-vector equation theory, the quadrilateral elemental equation is written in a matrix differential equation of the first order, and the global algebraic equation of the shell and stiffeners are established separately. Transverse shear deformation and rotational inertia are also considered in the model. In Section 3 several numerical examples are analyzed, and the convergence of some of examples is tested.

2. The formulas of the thin shells and stiffened laminated shell

Some typical stiffened circular cylindrical shells are shown in Figures 1–4.

The shells shown in Figures 1 and 2 are commonly called stiffened shells with ring or/and string stiffeners. Those in Figures 3 and 4 are generally called shells with discontinuity in thickness. In fact, all can be regarded as shells with different stiffeners. For example, a laminated shell with discontinuity in thickness, like that of Figure 3, is made up of a laminated circular cylindrical shell and a laminated stiffener, as shown in Figure 5.

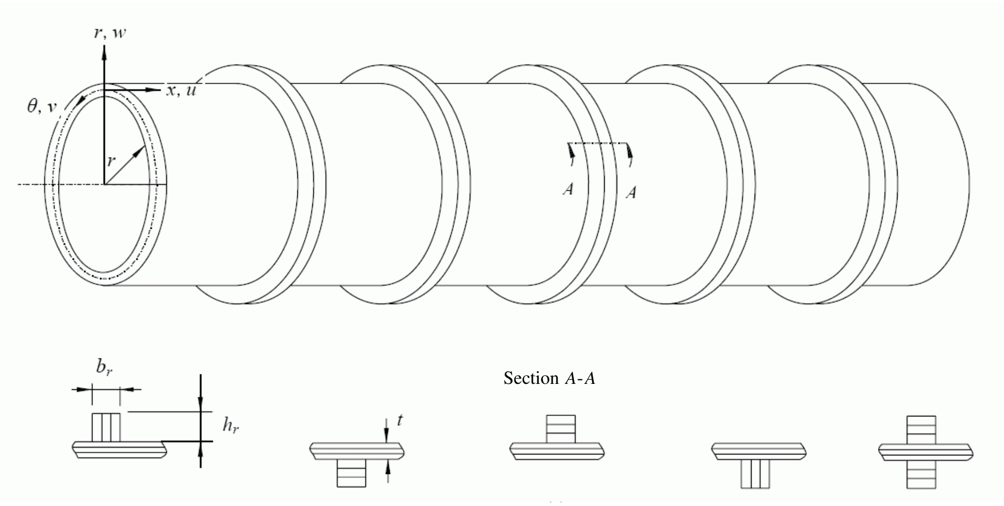

(a) (b) (c) (d) (e)

Figure 1. A laminated shell with ring stiffeners: (a) external type 2; (b) internal type 1; (c) external type 1; (d) internal type 2; and (e) concentric type 1.

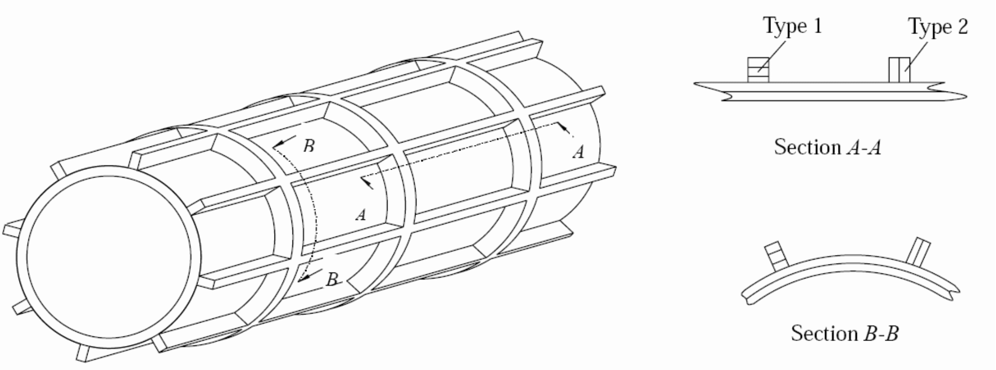

Figure 2. A laminated shell with three rings and eight string stiffeners.

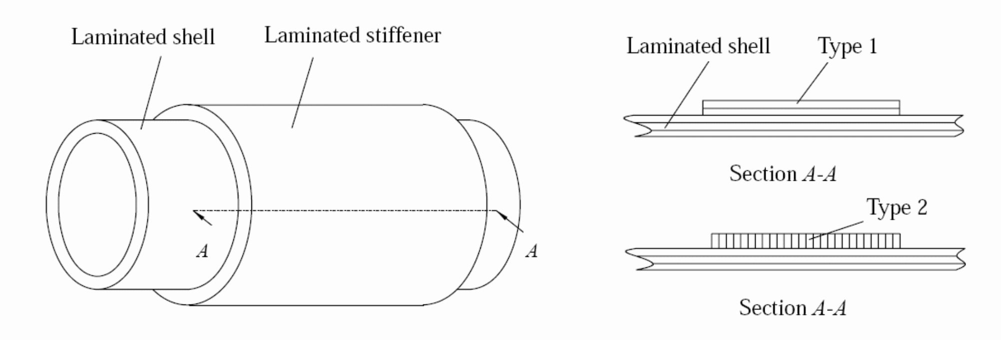

Figure 3. A laminated shell with discontinuity in thickness (one ring stiffener).

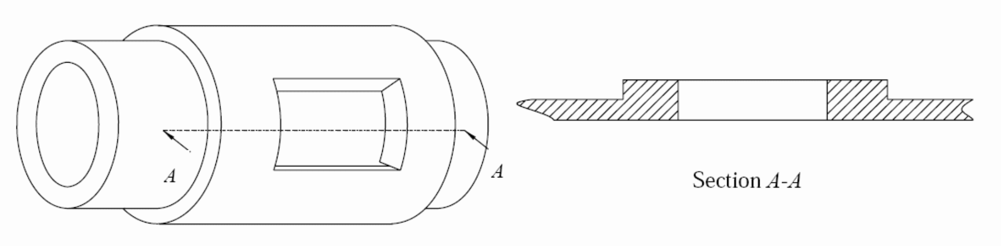

Figure 4. A circular cylindrical shell with a cutout and discontinuity in thickness.

Our laminated shells are considered as n-layered shells (see Figure 1 for the coordinate system). Assuming the material of an arbitrary layer has orthotropic

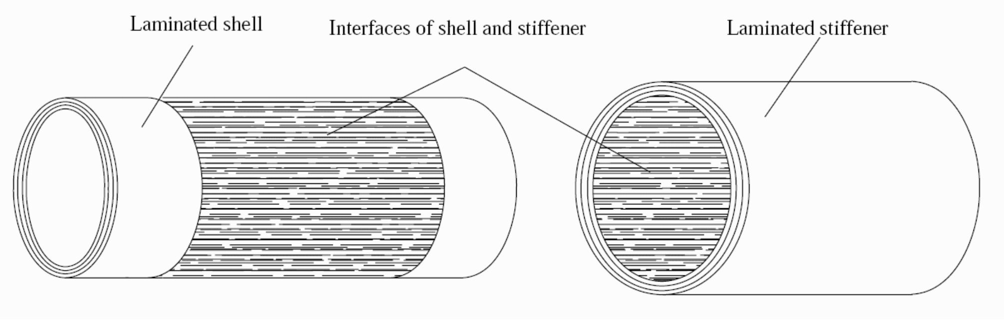

Figure 5. Decomposition of a shell with discontinuity in thickness.

symmetry with respect to the coordinate planes, the stress-displacement relationships can be stated as

$$\begin{pmatrix} \sigma_x \\ \sigma_\theta \\ \sigma_r \\ \tau_{\theta r} \\ \tau_{xr} \\ \tau_{x\theta} \end{pmatrix} = \begin{bmatrix} C_{11} & C_{12} & C_{13} & 0 & 0 & 0 \\ & C_{22} & C_{23} & 0 & 0 & 0 \\ & & C_{33} & 0 & 0 & 0 \\ & & & C_{44} & 0 & 0 \\ & \text{(symm.)} & & & C_{55} & 0 \\ & & & & & C_{66} \end{bmatrix} \begin{pmatrix} \alpha u \\ \beta v/r + w/r \\ \partial w/\partial r \\ \beta w/r + \partial v/\partial r - v/r \\ \alpha w + \partial u/\partial r \\ \beta u/r + \alpha v \end{pmatrix}$$

where σ_x, σ_θ, σ_r, $\tau_{\theta r}$, tau_{xr}, and $\tau_{x\theta}$ are the stress components, the C_{ij} $(i, j = 1, 2, \dots, 6)$ denote the elasticity coefficient of the material, $\alpha = \partial/\partial x$, $\beta = \partial/\partial\theta$, and u, v, w are the displacements in the x, θ and r directions, respectively.

The modified mixed H-R variational principle [Zou and Tang 1995b; 1995a; Steele and Kim 1992] can be expressed as

$$\delta \prod = \delta\Bigl(\iiint_V (\boldsymbol{p}^T \cdot \dot{\boldsymbol{q}} - H)\, r\, dx\, d\theta\, dr \\ - \iint_{S_\sigma} \boldsymbol{q}^T \cdot (\boldsymbol{T} - \overline{\boldsymbol{T}})\, ds_\sigma - \iint_{S_u} \boldsymbol{T}^T \cdot (\boldsymbol{q} - \bar{\boldsymbol{q}})\, ds_u\Bigr), \quad (1)$$

where $\boldsymbol{q} = [u \;\; v \;\; w]^T$, $\boldsymbol{p} = [\tau_{xr} \;\; \tau_{\theta r} \;\; \sigma_r]^T$, $\dot{\boldsymbol{q}} = \partial \boldsymbol{q}/\partial r$, $\boldsymbol{T} = [T_x \; T_\theta \; T_r]^T$, $\overline{\boldsymbol{T}} = [\overline{T}_x \; \overline{T}_\theta \; \overline{T}_r]^T$ represents the stresses acting on the stress boundaries S_σ, and $\bar{\boldsymbol{q}} = [\bar{u} \;\; \bar{v} \;\; \bar{w}]^T$ represents the displacements on the displacement boundaries S_u. The Hamiltonian H can be written (neglecting the body force) as

$$-H = \bigl(C_3 \alpha u + C_4(r^{-1}\beta v + r^{-1}w) - C_5\sigma_r\bigr)(r^{-1}\beta v + r^{-1}w) \\ + \bigl(C_2 \alpha u + C_3(r^{-1}\beta v + r^{-1}w) - C_1\sigma_r\bigr)\alpha u + C_6(r^{-1}\alpha v + r^{-1}u)(\alpha v + r^{-1}\beta u) \\ + \tau_{\theta r}(r^{-1}\beta w - r^{-1}v) + \tau_{xr}\alpha w - 2^{-1}\boldsymbol{\eta}^T \boldsymbol{S} \boldsymbol{\eta} - 2^{-1}\rho(\omega^2 u^2 + \omega^2 v^2 + \omega^2 w^2),$$

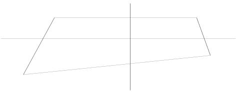

Figure 6. The local coordinate system of a quadrilateral element.

where

$$\boldsymbol{\eta} = \begin{pmatrix} C_2\alpha u + C_3(r^{-1}\beta v + r^{-1}w) - C_1\sigma_r \\ C_3\alpha u + C_4(r^{-1}\beta v + r^{-1}w) - C_5\sigma_r \\ \sigma_r \; \tau_{\theta r} \; \tau_{xr} \; C_6(\alpha v + r^{-1}\beta u) \end{pmatrix},$$

ρ is the mass density, ω is the natural frequency, and

$$\begin{aligned} C_1 &= -C_{13}/C_{33}, & C_4 &= C_{22} - C_{23}^2/C_{33}, & C_7 &= 1/C_{33}, \\ C_2 &= C_{11} - C_{13}^2/C_{33}, & C_5 &= -C_{23}/C_{33}, & C_8 &= 1/C_{55}, \\ C_3 &= C_{12} - C_{13}C_{23}/C_{33}, & C_6 &= C_{66}, & C_9 &= 1/C_{44}. \end{aligned}$$

Using a quadrilateral element with local coordinate system as in Figure 6, the field functions and the shape functions assume the form

$$\begin{gathered} u = [\boldsymbol{N}(x,\theta)]\big(u(r)\big), \qquad v = [\boldsymbol{N}(x,\theta)]\big(v(r)\big), \qquad w = [\boldsymbol{N}(x,\theta)]\big(w(r)\big), \\ \tau_{\theta r} = [\boldsymbol{N}(x,\theta)]\big(\tau_{\theta r}(r)\big), \quad \tau_{xr} = [\boldsymbol{N}(x,\theta)]\big(\tau_{xr}(r)\big), \quad \sigma_r = [\boldsymbol{N}(x,\theta)]\big(\sigma_r(r)\big), \\ \boldsymbol{N}_i(\xi,\eta) = \tfrac{1}{4}(1+\xi_i\xi)(1+\eta_i\eta) \quad \text{for } i = 1,2,3,4, \end{gathered} \tag{2}$$

The x-θ curved surface of a layer is discretized as shown in Figure 7.

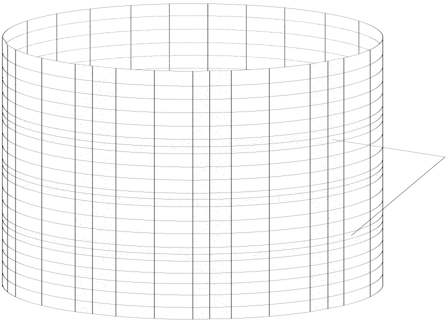

Figure 7. The element meshes of an arbitrary layer of a laminated shell.

Assume the stress boundaries are satisfied ($\boldsymbol{T} = \overline{\boldsymbol{T}}$), and the displacement boundaries of arbitrary layer are satisfied ($\boldsymbol{q} = \bar{\boldsymbol{q}}$). Substituting Equations (2) into (1) and using $\delta \prod = 0$ we obtain the element state-vector equation

$$\boldsymbol{C}^e \frac{d\boldsymbol{H}^e(r)}{dr} = \boldsymbol{K}^e \boldsymbol{H}^e(r). \tag{3}$$

The detailed forms of $\boldsymbol{C}^e$, $\boldsymbol{K}^e$ and $\boldsymbol{H}^e(r)$ in (3) can be found in the Appendix.

The detailed treatments on the various boundary conditions can be found in [Sheng and Ye 2002b].

The standard finite element assemblage process is used. The global state-vector equation for m-th layer takes the form

$$\boldsymbol{C}_m \frac{d\boldsymbol{H}_m(r)}{dr} = \boldsymbol{K}_m \boldsymbol{H}_m(r), \tag{4}$$

with general solution

$$\boldsymbol{H}_m(r_{i,m}) = \boldsymbol{T}_m(h_m)\boldsymbol{H}_m(r_{o,m}), \tag{5}$$

where $\boldsymbol{T}_m(h_m) = e^{\boldsymbol{C}_m \boldsymbol{K}_m \cdot (h_m)}$, $h_m$is the thickness of m-th layer and $h_m = r_{i,m} - r_{o,m}$ is the difference between the inside and outside radii of the m-th layer. When we compute $e^{\boldsymbol{C}_m \boldsymbol{K}_m \cdot h_m}$, the r of each layer in $\boldsymbol{K}_m$ is replaced by $r = (r_{o,m} - r_{i,m})/2$.

The exponential of a matrix can be computed in many ways (approximation theory, differential equations, eigenvalues, characteristic polynomial, and so on). In practice, considerations of stability, efficiency and accuracy make some methods preferable to others, but none is completely satisfactory [Moler and Van Loan 1978]. Hence, the precise integration method [Zhong and Zhu 1996; Zhong 2001] for Equation (4) is employed for the calculations in this paper.

Equation (5) must be satisfied at every layer of our n-layered shell. Based on the compatibility conditions for the displacements and stresses at the interface between two layers, we obtain the recursive formulation

$$\boldsymbol{H}_n(r_{i,n}) = \Big(\prod_{m=1}^{n} \boldsymbol{T}_m\Big)\boldsymbol{H}_1(r_{o,1}), \tag{6}$$

in which $r_{i,n}$, $r_{o,1}$ are the inner and outer radii of the n-layered shell.

Equation (6) expresses the relationship between the physical quantities for the external and internal surface of an n-layered shell. It amounts to a set of linear algebraic equations in terms of node displacements and stresses. In matrix form, this can be written as

$$\begin{pmatrix} \boldsymbol{q}_n(r^s_{i,n}) \\ \boldsymbol{p}_n(r^s_{i,n}) \end{pmatrix} = \begin{bmatrix} \boldsymbol{T}^s_{11} & \boldsymbol{T}^s_{12} \\ \boldsymbol{T}^s_{21} & \boldsymbol{T}^s_{22} \end{bmatrix} \begin{pmatrix} \boldsymbol{q}_1(r^s_{o,1}) \\ \boldsymbol{p}_1(r^s_{o,1}) \end{pmatrix} \tag{7}$$

where the superscript s denotes the laminated shell.

A laminated stiffener is also considered as an l-layered shell, and the element mesh in every layer is assumed to be the same (shaded part of Figure 7). The procedure above for the external and internal stiffeners is repeated, and yields the equations

$$\begin{pmatrix} \boldsymbol{q}_l(r^{es}_{i,l}) \\ \boldsymbol{p}_l(r^{es}_{i,l}) \end{pmatrix} = \begin{bmatrix} \boldsymbol{T}^{es}_{11} & \boldsymbol{T}^{es}_{12} \\ \boldsymbol{T}^{es}_{21} & \boldsymbol{T}^{es}_{22} \end{bmatrix} \begin{pmatrix} \boldsymbol{q}_1(r^{es}_{o,1}) \\ \boldsymbol{p}_1(r^{es}_{o,1}) \end{pmatrix} \tag{8}$$

$$\begin{pmatrix} \boldsymbol{q}_l(r^{is}_{i,l}) \\ \boldsymbol{p}_l(r^{is}_{i,l}) \end{pmatrix} = \begin{bmatrix} \boldsymbol{T}^{is}_{11} & \boldsymbol{T}^{is}_{12} \\ \boldsymbol{T}^{is}_{21} & \boldsymbol{T}^{is}_{22} \end{bmatrix} \begin{pmatrix} \boldsymbol{q}_1(r^{is}_{o,1}) \\ \boldsymbol{p}_1(r^{is}_{o,1}) \end{pmatrix} \tag{9}$$

where superscript es and is denote the external and internal stiffeners, and $r^{es}_{i,l}$, $r^{is}_{i,l}$, $r^{es}_{o,1}$, $r^{is}_{o,1}$ are the inside and outer radius of the external and internal stiffeners.

Noted that the dimensionality of (8) and (9) differs from that of (7).

The displacements and stresses on the interface between shell and stiffeners must be continuous. Uniting (7), (8) and (9) yields

$$\begin{pmatrix} \boldsymbol{q}(r_i) \\ \boldsymbol{p}(r_i) \end{pmatrix} = \begin{bmatrix} \boldsymbol{T}_{11} & \boldsymbol{T}_{12} \\ \boldsymbol{T}_{21} & \boldsymbol{T}_{22} \end{bmatrix} \begin{pmatrix} \boldsymbol{q}(r_o) \\ \boldsymbol{p}(r_o) \end{pmatrix}. \tag{10}$$

We can see that the node number of a layer of a laminated shell determines the number of variables in (10); thus this number of variables has no relationship to the thickness of the shell or the height and number of stiffeners.

Because we are studying natural frequencies, so the external surface and internal surface are traction-free (the stress column vector $\boldsymbol{p}(r_i)$ and $\boldsymbol{p}(r_o)$ are zero), we deduce from (10) that

$$\boldsymbol{T}_{21}\boldsymbol{q}(r_o) = 0.$$

For this to have nontrivial solutions, the determinant of the characteristic matrix must be zero:

$$|\boldsymbol{T}_{21}| = 0.$$

The natural frequencies ω can be obtained from the characteristic polynomial of this last equation through the use of the bisection method [Johnston 1982]. To simplify the analysis and improve the accuracy of the results, dimensionless versions of u, v, w, τ_{xr}, $\tau_{\theta r}$, and σ_r need to be used in the computer program.

3. Numerical examples and discussions

Example 1. As a first test of our method we discuss an example studied experimentally and theoretically by Al-Najafi and Warburton [1970], consisting of a stiffened external steel shell with five identical ring stiffeners (Figure 1). The dimensions of the shell are: inside diameter $d = 0.2158\,\mathrm{m}$; length $l = 0.4572\,\mathrm{m}$; thickness $t = 0.00386\,\mathrm{m}$; breadth of rings $b_r = 0.00635\,\mathrm{m}$; height of rings $h_r = 0.00635\,\mathrm{m}$, 0.01778m , 0.0254 m. There are six bays of equal length. Material properties: Young's modulus $E = 204.0\,\text{GPa}$; shear modulus $G = 79.0\,\text{GPa}$; density $\rho = 7840\,\text{kg}\,\text{m}^{-3}$.

Because compatible finite elements in the x-θ plane are used, the natural frequencies should converge the the values of the mathematical model monotonically as the number of elements in the discretization is increased. The results, listed in Table 1, show that reasonable convergence has been achieved with relatively small

Mesh : layers ($k \times m : n$)		Mode number							
		F-F (Free ends)				S-S (Simply supported ends)			
Shell	Stiffeners	1	2	3	4	1	2	3	4
$h_r = 0.00635$ m									
23×36:1	1×36:1	322.2	338.3	889.5	948.2	840.5	1103.2	1734.7	1808.5
35×45:1	1×45:1	317.2	333.5	867.2	925.5	834.2	1089.6	1719.0	1789.8
47×60:1	2×60:2	314.6	331.9	859.1	920.0	831.8	1074.3	1697.0	1780.7
58×72:1	2×72:2	313.2	330.8	856.4	918.4	831.1	1069.7	1694.9	1776.3
		(2,2)	(2,1)	(3,2)	(3,1)	(2,1)	(3,1)	(3,2)	(0,1)
Experimental		323	342	865	928	809	1065	1658	/
Finite element		317	340	861	926	834	1065	1699	/
$h_r = 0.01778$ m									
23×36:1	1×36:2	636.6	752.9	1506.3	1533.3	1030.9	1640.2	2096.5	2340.7
35×45:1	1×45:3	621.7	733.4	1474.0	1502.9	1017.1	1625.4	2073.4	2313.3
47×60:1	2×60:4	618.9	726.1	1450.5	1480.7	1012.2	1608.9	2040.2	2292.1
58×72:1	2×72:4	618.5	723.4	1443.0	1464.1	1011.4	1602.9	2055.3	2284.2
		(2,2)	(2,1)	(3,2)	(3,1)	(2,1)	(0,1)	(3,1)	(2,2)
Experimental		626	743	1437	1468	996	/	2017	2277
Finite element		626	746	1438	1465	1031	/	2060	2390
$h_r = 0.0254$ m									
23×36:1	1×36:3	830.9	1002.7	1705.0	1703.2	1214.2	1491.4	2296.6	2601.8
35×45:1	1×45:4	815.5	974.7	1677.1	1672.7	1193.1	1485.4	2273.6	2582.7
47×60:1	2×60:5	806.4	963.6	1640.8	1645.4	1191.2	1482.3	2264.2	2564.5
58×72:1	2×72:5	803.5	971.0	1634.9	1639.2	1189.5	1481.3	2259.4	2546.7
		(2,2)	(2,1)	(3,1)	(3,2)	(2,1)	(0,1)	(2,2)	(3,1)
Experimental		814	982	1627	1632	1187	/	2082	2522
Finite element		822	997	1629	1636	1223	/	2279	2607

Table 1. Convergence of natural frequencies (Hz) for steel external shell with 5 ring stiffeners (Example 1). Rows "Experimental" and "Finite element" are from [Al-Najafi and Warburton 1970].

decrements in the four frequencies, never as much as 1%, between corresponding values for the 47 × 60 and 58 × 72 meshes (both one layer).

Figure 8 gives the four mode shapes for Example 1 with simply supported ends. We see that the effect of the stiffening rings on the mode shape increases as h_r increases.

Example 2. In this example (Figure 9) the shell has two identical face layers with thicknesses t_e and t_i, and a core layer of thickness t_c. All three layers have the material properties corresponding to aragonite crystals, which have stiffness ratios

$$\begin{aligned} C_{22}/C_{11} &= 0.543103, & C_{12}/C_{11} &= 0.23319, \\ C_{23}/C_{11} &= 0.098276, & C_{44}/C_{11} &= 0.26681, \\ C_{33}/C_{11} &= 0.530172, & C_{55}/C_{11} &= 0.159914, \\ C_{13}/C_{11} &= 0.010776, & C_{66}/C_{11} &= 0.262931. \end{aligned}$$

We assume $C_{11} = 150\,\text{GPa}$ and $\rho = 1600\,\text{kg/m}^3$ for the two face layers and $C_{11} = 75\,\text{GPa}$ and $\rho = 800\,\text{kg/m}^3$ for the core layer of the laminated shell. We take the material properties of stiffeners to be the same as those of the face layers. The convergence of the first four natural frequencies is listed in Table 2.

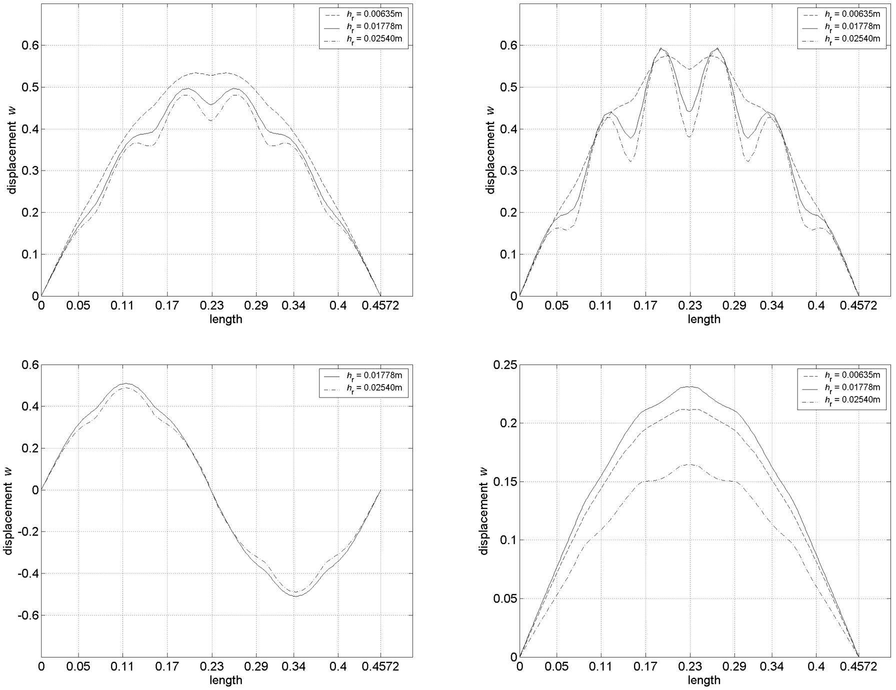

Figure 8. Four mode shapes for Example 1. Clockwise from top left: (2, 1), (3, 1), (0, 1), (2, 2).

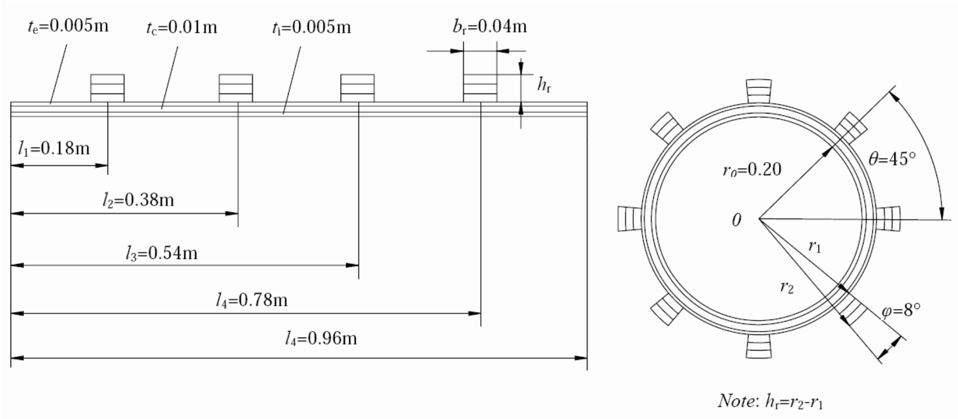

Note: $h_r = r_2 - r_1$

Figure 9. Dimensions of stiffened laminated shell with ring and string stiffeners (Example 2).

Mesh : layers ($k \times m : n$)			Mode number			
Shell	Rings	Strings	1	2	3	4
$h_r = 0.002$ m						
19×32:4	1×32:4	19×1:4	1075.8	1286.6	1856.5	1965.4
29×40:4	1×40:4	29×1:4	1059.5	1282.3	1826.9	1936.1
38×56:4	2×56:4	38×2:4	1050.0	1281.5	1815.6	1924.9
48×72:4	2×72:4	48×2:4	1046.2	1277.4	1808.9	1912.9
58×80:4	2×80:4	58×2:4	1045.1	1276.1	1805.5	1901.7
			(2,1)	(0,1)	(2,2)	(3,1)
$h_r = 0.004$ m						
19×32:4	1×32:8	19×1:8	1156.9	1251.7	1650.8	2072.7
29×40:4	1×40:8	29×1:8	1148.5	1240.7	1638.5	2034.2
38×56:4	2×56:8	38×2:8	1144.7	1231.7	1632.1	2015.3
48×72:4	2×72:8	48×2:8	1143.2	1224.9	1630.3	2005.0
58×80:4	2×80:8	58×2:8	1142.5	1222.8	1629.5	2001.5
			(0,1)	(2,1)	torsion motion	(2,2)
$h_r = 0.006$ m						
19×32:4	1×32:12	19×1:12	1155.4	1483.2	2132.8	2242.7
29×40:4	1×40:12	29×1:12	1146.5	1463.4	2117.6	2216.8
38×56:4	2×56:12	38×2:12	1141.6	1445.8	2104.0	2191.4
48×72:4	2×72:12	48×2:12	1139.8	1438.3	2099.1	2180.6
58×80:4	2×80:12	58×2:12	1138.8	1435.9	2097.2	2176.6
			(0,1)	(2,1)	(0,2)	(2,2)

Table 2. Convergence of natural frequencies (Hz) for a laminated stiffened shell with ring and string stiffeners (Example 2).

Example 3. Strictly speaking, to apply the theory in this paper, we must require the cross-section of the string to be a partial annulus (Figure 10, left). If the cross-section of the string is a rectangle, we can transform the rectangular cross-section of the string into a partial annulus (Figure 10, right). The following example, taken from [Stanley and Ganessan 1997], proves the method feasible. The shell has inside diameter $d = 0.2\,\mathrm{m}$, thickness $t = 0.002\,\mathrm{m}$ and length $l = 0.4\,\mathrm{m}$; the strings have breadth $b_s = 0.004\,\mathrm{m}$ and height $h_s = 0.004\,\mathrm{m}$. The numerical results and comparison are listed in Table 3.

Replacing the rectangular cross-section of the string by a partial annulus, as in the figure, increases the distance between the center of the cross-section and the coordinate origin. Hence, the results obtained by the present method are larger than those of the reference data [Stanley and Ganessan 1997]. It can be seen in Table 3 that the error increases with the mode order; this may be because the effect of distance on the natural frequencies is more prominent for higher modes.

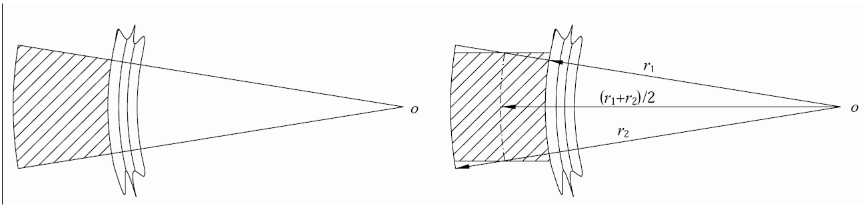

Figure 10. Cross-section of string (Example 3): left, partial annulus; right, switching from a rectangle to a partial annulus.

Mesh : layers		Mode number					
Shell	Strings	1	2	3	4	5	6
4 strings							
58×72:1	58×2:2	915.8 (4,1)	947.6 (3,1)	1227.9 (5,1)	1446.3 (2,1)	1563.5 (4,2)	1591.5 (5,2)
Experimental		914.1	944.9	1214	1432	1547	1571
Relative error		0.19%	0.50%	1.14%	1.00%	1.07%	1.30%
12 strings							
58×72:1	58×2:2	884.6 (4,1)	918.6 (3,1)	1179.5 (5,1)	1397.1 (2,1)	1511.2 (4,2)	1550.4 (5,2)
Experimental		881.7	913.6	1167	1380	1501	1529
Relative error		0.56%	0.55%	1.07%	1.24%	0.68%	1.40%

Table 3. Comparison of natural frequencies (Hz) for steel shell stiffened with strings and clamped at the edges (Example 3). "Experimental" refers to values from [Stanley and Ganessan 1997].

Example 4. Consider a 90° cylindrical panel with discontinuity in the thickness and one cutout (Figure 11). The material parameters for the external layer (ring stiffener) and the shell are the same as for the core layer and external layer, respectively, in Example 1. Two transversal cross-sections are shown; the method applies directly to the first, consisting only of partial annuli, but the idea of Example 3 is suitable here, allowing us to reduce the case of second cross-section to that of the first. The first six natural frequencies are given in Table 4.

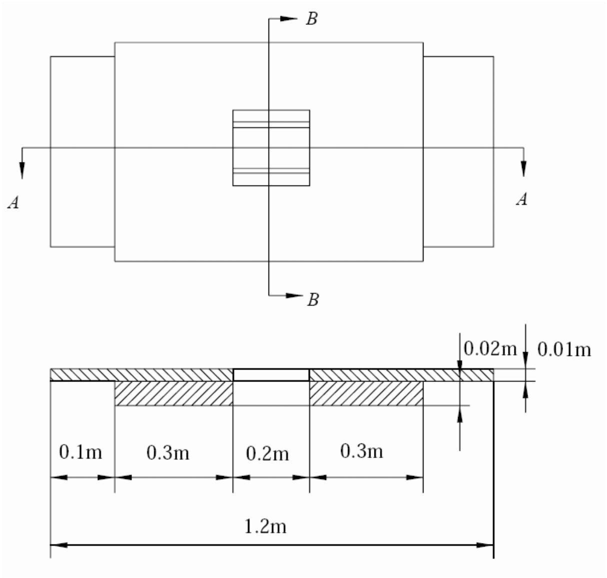

Section A-A

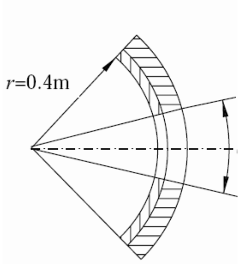

Section B-B (radial)

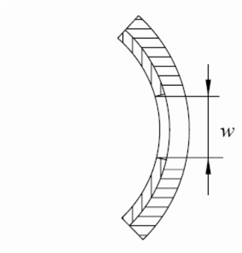

Section B-B (rectangular)

Figure 11. A 90° cylindrical panel with a cutout and discontinuity in thickness (Example 4).

Mesh : layers		Mode number					
Shell	Ring	1	2	3	4	5	6
4 strings							
12×12:1	10×12:2	1387.5	1630.7	2046.4	2071.0	2315.5	2375.1
24×24:1	20×24:2	1305.3	1519.7	1928.1	1943.4	2135.4	2192.7
36×36:1	30×36:2	1301.0	1515.5	1921.8	1936.1	2111.4	2175.3
48×48:1	40×48:2	1285.0	1497.6	1901.0	1909.1	2085.2	2154.5
60×60:1	50×60:2	1281.6	1489.7	1889.1	1904.1	2070.3	2139.7
72×72:1	50×60:2	1280.8	1488.8	1887.4	1902.2	2067.4	2136.2

Table 4. Natural frequencies (Hz) for cylindrical panel with discontinuity in thickness and clamped at all edges (Example 4).

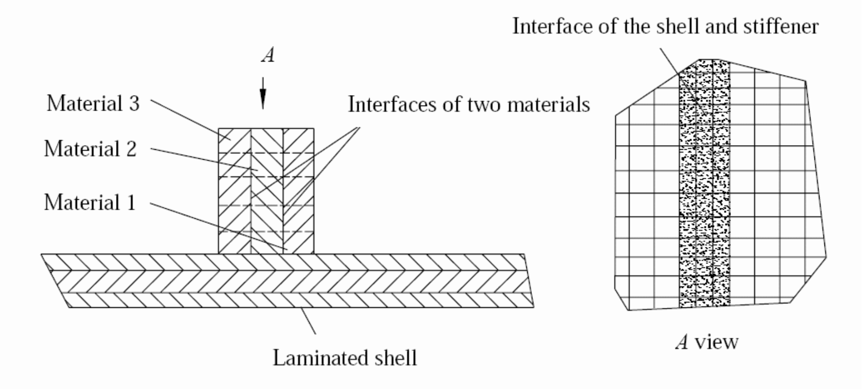

Figure 12. Type 2 stiffener.

In each of these examples, we have considered type 1 stiffeners and the material was the same over the cross-section of the stiffener. However, even if there are two or more materials in the cross-section of the stiffener, the method is also suitable without additional equations. This is because Equation (8) is used to handle the laminated shell that the material of every layer can be different.

If we are dealing with a type 2 stiffener (Figure 2), we can regard it as a layered shell (Figure 12), but there may be two or more materials in a layer. This situation is similar to the type 1 stiffener; the major difference is that we must pay attention to the interfaces of different materials when we discretize each layer of the stiffener. One element cannot include more than one material.

4. Conclusions

This paper introduces a general, novel mathematical model for the free vibration analysis of some stiffened cylindrical shells. In this model the shell and the stiffeners are discretized by the same quadrilateral element. The linear algebraic equations of the shell and stiffeners are established separately. The compatibility of displacements and stresses on the interface between the shell and the stiffeners is maintained. Numerical examples show that the current approach has excellent predictive ability. Some specific features of the model are:

(1) The three-dimensional free vibration problem of stiffened laminated shells is transformed into a two-dimensional one.

(2) The number of variables included in the global linear equation of the stiffened shell has no relationship with the number of layers of the shell and stiffeners. Hence, the number of variables is greatly reduced.

(3) Transverse shear deformation and rotational inertia are taken into account.

If a similar modified H-R mixed variational principle for piezoelectric materials and the corresponding discrete state-vector equation are established, the dynamic behavior of piezoelectric plates with piezoelectric patches [Lee and Saravanos 1997; Lin et al. 1996] and of cylindrical shells with piezoelectric rings or/and strings can be analyzed directly using the present approach.

Acknowledgment

The authors thank the reviewers for their valuable comments.

Appendix: Expressions for $\boldsymbol{C}^e$, $\boldsymbol{K}^e$, $\boldsymbol{H}^e$ in Equation (3)

We have $\boldsymbol{C}^e = \left(\iint \boldsymbol{N}^T \boldsymbol{N} \bar{r}\,|\boldsymbol{J}|\,d\xi\,d\eta\right)\boldsymbol{I}$, where $\boldsymbol{I}$ is the 6×6 unit matrix, $\bar{r}$ is the average of the inside radius r_i and the outside radius r_o of an element, and

$$\boldsymbol{J} = \begin{bmatrix} \sum_{i=1}^{4} \frac{\partial \boldsymbol{N}_i}{\partial \xi} x_i & \sum_{i=1}^{4} \frac{\partial \boldsymbol{N}_i}{\partial \xi} \theta_i \\ \sum_{i=1}^{4} \frac{\partial \boldsymbol{N}_i}{\partial \eta} x_i & \sum_{i=1}^{4} \frac{\partial \boldsymbol{N}_i}{\partial \eta} \theta_i \end{bmatrix}.$$

Further,

$$\boldsymbol{H}^e(r) = \begin{bmatrix} u^e(r) & v^e(r) & w^e(r) & \tau^e_{xr}(r) & \tau^e_{\theta r}(r) & \sigma^e_r(r) \end{bmatrix}^T$$

and

$$\boldsymbol{K}^e = \iint \begin{bmatrix} \boldsymbol{A}^e & \boldsymbol{B}^e \\ \boldsymbol{C}^e & \boldsymbol{D}^e \end{bmatrix} \bar{r}\,|\boldsymbol{J}|\,d\xi\,d\eta,$$

where, setting $\nu = \boldsymbol{N}^T\boldsymbol{N}$, $\lambda = \boldsymbol{N}^T\alpha\boldsymbol{N}$ and $\mu = \boldsymbol{N}^T\beta\boldsymbol{N}$, the matrix entries are

$$\boldsymbol{A}^e = \begin{bmatrix} 0 & 0 & -\lambda \\ 0 & r^{-1}\nu & -r^{-1}\mu \\ C_1\alpha\nu & C_5 r^{-1}\beta\nu & C_5 r^{-1}\nu \end{bmatrix},$$

$$\boldsymbol{B}^e = \begin{bmatrix} C_8\nu & 0 & 0 \\ 0 & C_9\nu & 0 \\ 0 & 0 & C_7\nu \end{bmatrix},$$

$$\boldsymbol{C}^e = \begin{bmatrix} -\rho\omega^2\nu + C_2\alpha\lambda + C_6 r^{-2}\beta\mu & C_3 r^{-1}\alpha\mu + C_6 r^{-1}\beta\lambda & C_3 r^{-1}\alpha\nu \\ C_3 r^{-1}\beta\lambda + C_6 r^{-1}\alpha\mu & -\rho\omega^2\nu + \alpha\lambda + C_6 r^{-2}\beta\mu & C_4 r^{-2}\beta\nu \\ C_3 r^{-1}\lambda & C_4 r^{-2}\mu & -\rho\omega^2\nu + C_4 r^{-2}\mu \end{bmatrix},$$

$$\boldsymbol{D}^e = \begin{bmatrix} -r^{-1}\nu & 0 & -C_1\lambda \\ 0 & -2r^{-1}\nu & -C_5 r^{-1}\mu \\ \alpha\nu & r^{-1}\beta\nu & -(C_5+1)\,r^{-1}\nu \end{bmatrix}.$$

References

[Al-Najafi and Warburton 1970] A. M. Al-Najafi and G. B. Warburton, "Free vibration of ring-stiffened cylindrical shells", *J. Sound Vib.* **13** (1970), 9–25.

[Gong and Lam 1998] S. W. Gong and K. Y. Lam, "Transient response of stiffened composite submersible hull subjected to underwater explosive shock", *Compos. Struct.* **41** (1998), 27–37.

[Johnston 1982] R. L. Johnston, *Numerical methods*, Wiley, New York, 1982.

[Kim and Lee 2002] Y. W. Kim and Y. S. Lee, "Transient analysis of ring-stiffened composite cylindrical shells with both edges clamped", *J. Sound Vib.* **252** (2002), 1–17.

[Lee and Saravanos 1997] H. J. Lee and D. A. Saravanos, "Generalized finite element formulation for smart multilayered thermal piezoelectric composite plates", *Int. J. Solids Struct.* **34**:26 (1997), 3355–3371.

[Liao and R. 1994] C. L. Liao and C. C. R., "Dynamic stability of stiffened laminated composite plates and shells subjected to in-plane pulsating forces", *J. Sound Vib.* **174**:3 (1994), 335–351.

[Lin et al. 1996] C. C. Lin, C. Y. Hsu, and H. N. Huang, "Finite element analysis on deflection control of plates with piezoelectric actuators", *Compos. Struct.* **35**:4 (1996), 423–433.

[Moler and Van Loan 1978] C. Moler and C. Van Loan, "Nineteen dubious ways to compute the exponential of a matrix", *SIAM Review* **20**:4 (1978), 801–836.

[Rikards et al. 2001] R. Rikards, A. Chate, and O. Ozolinsh, "Analysis for buckling and vibrations of composite stiffened shells and plates", *Compos. Struct.* **51**:4 (2001), 361–370.

[Sheng and Ye 2002a] H. Y. Sheng and J. Q. Ye, "A semi-analytical finite element for laminated composite plates", *Compos. Struct.* **57** (2002), 117–123.

[Sheng and Ye 2002b] H. Y. Sheng and J. Q. Ye, "A state space finite element for laminated composite plates", *Comput. Methods Appl. Mech. Eng.* **191**:37 (2002), 4259–4276.

[Sheng and Ye 2003] H. Y. Sheng and J. Q. Ye, "A three-dimensional state space finite element solution for laminated composite cylindrical shells", *Comput. Methods Appl. Mech. Eng.* **192**:22 (2003), 2441–2459.

[Sinha and Mukhopadhyay 1995] G. Sinha and M. Mukhopadhyay, "Transient dynamic response of arbitrary stiffened shells by the finite element method", *J. Vib. Acoustics* **117**:1 (1995), 11–16.

[Srinivasan and Krishnan 1989] R. S. Srinivasan and P. A. Krishnan, "Dynamic analysis of stiffened conical shell panels", *Comput. Struct* **33**:3 (1989), 831–837.

[Stanley and Ganessan 1997] A. J. Stanley and N. Ganessan, "Free vibration characteristics of stiffened cylindrical shells", *Comput. Struct.* **65**:1 (1997), 33–45.

[Steele and Kim 1992] C. R. Steele and Y. Y. Kim, "Modified mixed variational principle and the state-vector equation for elastic bodies and shells of revolution", *J. App. Mech. (ASME)* **59**:3 (1992), 587–595.

[Wang et al. 1997] M. Wang, S. Swaddiwudhipong, and J. Tian, "Ritz method for vibration analysis of cylindrical shells with ring stiffeners", *J. Engineer. Mech.* **123**:2 (1997), 134–142.

[Wilken and Soedel 1976] I. D. Wilken and W. Soedel, "The receptance method applied to ring-stiffened cylindrical shells: analysis of modal characteristics", *J. Sound Vib.* **44**:4 (1976), 563–576.

[Yang and Zhou 1995] B. Yang and J. Zhou, "Analysis of ring-stiffened cylindrical shells", *J. Appl. Mech.* **62**:4 (1995), 1005–1014.

[Zhao et al. 2002] X. Zhao, K. M. Liew, and T. Y. Ng, "Vibrations of rotating cross-ply laminated circular cylindrical shells with stringer and rings stiffeners", *Intl. J. Solids Struct.* **39**:2 (2002), 529–545.

[Zhong 2001] W. X. Zhong, "Combined method for the solution of asymmetric Riccati differential equation", *Comput. methods appl. mech. eng.* **191**:1 (2001), 93–102.

[Zhong and Zhu 1996] W. X. Zhong and J. P. Zhu, "Precise time integration for the matrix Riccati differential equation", *J. Numer. Methods Comput. Appl.* **17**:1 (1996), 26–35. In Chinese; translation in *Chinese J. Numer. Math. Appl.* **18**:4, (1996), 47–57. MR 97f:65047

[Zou and Tang 1995a] G. P. Zou and L. M. Tang, "A semi-analytical solution for laminated composite plates in Hamilton system", *Comput. Methods Appl. Mech. Eng.* **128**:3 (1995), 395–404.

[Zou and Tang 1995b] G. P. Zou and L. M. Tang, "A semi-analytical solution for thermal stress analysis of laminated composite plates in the Hamiltonian system", *Comput. Struct.* **55**:1 (1995), 113–118.

Received 24 Sep 2005. Revised 10 Dec 2005.

GUANGHUI QING: `qingluke@126.com`
Aeronautical Mechanics and Avionics Engineering College, Civil Aviation University of China, Tianjin 300300, People's Republic of China

ZHENYU FENG: *Aeronautical Mechanics and Avionics Engineering College, Civil Aviation University of China, Tianjin 300300, People's Republic of China*

YANHONG LIU: *Aeronautical Mechanics and Avionics Engineering College, Civil Aviation University of China, Tianjin 300300, People's Republic of China*

JIAUJUN QIU: *Department of Mechanics and Engineering Measurement, School of Mechanical Engineering, Tianjin University, Tianjin 300072, People's Republic of China*

JOURNAL OF MECHANICS OF MATERIALS AND STRUCTURES
Vol. 1, No. 1, 2006

APPROXIMATE ANALYSIS OF INTERACTION OF CLOSELY SPACED CRACKS

LI YIN-PING AND YANG CHUN-HE

An approximate method of stress analysis in elastic solids with multiple cracks is proposed to improve the accuracy of the Kachanov method in analyzing closely spaced cracks. Classical Kachanov method assumed that traction in each crack can be represented as the sum of a uniform component and a nonuniform one, and that the interaction among the cracks is only due to the uniform components. The assumptions simplify considerably the mathematics. However, they may not be valid when the cracks are very close and overlap along the direction of load, because each crack may be embedded in the stress-amplifying region as well as the stress-shielding region of the other cracks at this time. To improve the accuracy of the Kachanov method, a new asymptotic method, in which the influence on a crack of the quadratic parabola pseudotractions (QPPTs) rather than the average ones on the other crack are taken into account, is proposed. Applications to the problem of three collinear cracks and two offset parallel closely spaced cracks are considered to validate the accuracy of the new method.

1. Introduction

As one of the key factors in determining the component life of a structure, the interaction effect among cracks has received significant attention in recent years. Various methods [Sneddon and Lowengrub 1969; Erdogan 1983; Chen 1984a; 1984b, Horii and Nemat-Nasser 1985b; Chudnovsky et al. 1987a; 1987b; Kachanov 1987; Lam and Phua 1991; Kachanov 1992; Chen 1995; Basista and Gross 2000; Gorbatikh and Kachanov 2000; Wang et al. 2000; Li et al. 2003] have been developed for the analyses. As the boundary conditions can be more readily defined for traction free cracks, crack interaction problems were formulated in terms of the interaction tractions rather than in terms of the displacement discontinuities. Based on the stress superposition technique, Kachanov [1987] proposed a simple method for calculation of stress intensity factors (SIFs) and effective elastic properties of solids with multiple cracks. The solution can also be used to construct the stress and displacement fields in the solid [Kachanov 1987; Gorbatikh and Kachanov

---

Keywords: crack interaction, stress intensity factor, multiple cracks, quadratic parabola pseudotraction.

2000]. Combining the Kachanov method with the sliding crack model of brittle deformation, Basista and Gross [2000] extended the method to two-dimensional crack interaction problems under overall compression.

In Kachanov's stress superposition method, the key assumption is that the traction in a crack is composed of a uniform and a nonuniform component. The magnitude of each component is computed under the assumed condition that the resultant force of the nonuniform component is zero. The influence of the nonuniform component on crack interaction is ignored. Therefore, the accuracy of the Kachanov method depends on the configuration of crack distribution, and especially on crack spacing [Kachanov 1992; Wang et al. 2000; Kachanov 2003; Li et al. 2003].

To avoid the limitation of the Kachanov method in analyzing closely spaced cracks, Li et al. [2003] proposed a new approximate method for the analysis of cracked solids. The linearly varying component of traction rather than the uniform one is taken into account. It is shown that the accuracy of the modified method is better than Kachanov's. Recently, Kachanov [2003] gave a short overview of various approaches to crack interaction problems in which solutions for closely spaced cracks were discussed. It's pointed out that in 2-D problems of closely spaced cracks the accuracy of Kachanov's method — and even the method of [Li et al. 2003] — may not be sufficient. For example, the problem of two closely spaced cracks overlapping along the direction of load can not be accurately analyzed using such methods. This problem is of great interest because of its relevance to propagation and coalescence of two close cracks [Horii and Nemat-Nasser 1985a; Wang et al. 1996; Li et al. 2003].

One of the original objectives of the Kachanov method is to analyze the meso-damage of solids with multiple cracks first, and then to compute the macro response of the solids. The propagation and coalescence of cracks are not considered. But the accuracy of the Kachanov method and even the linear approximate method are not satisfactory for closely spaced and overlapping cracks in solids, such as the cracks in rock-like materials under compression, in which the propagation and coalescence of cracks have to be taken into account. To improve the accuracy, a new approximate method, in which the influence of the quadratic parabola pseudo-tractions (DPPTs) of cracks on other cracks, is proposed in this paper. It's shown that DPPTs are able to describe adequately the interaction among closely spaced cracks. Numerical examples of the interactions of three collinear cracks and a pair of offset parallel cracks are analyzed in detail to assess the accuracy of the proposed method.

2. The generalised Kachanov method

Consider an infinite xy-plane containing N cracks (Figure 1) under remote stresses σ^{∞}. It is equivalent to the problem of N cracks with tractions

$$-n_i \cdot \sigma^{\infty} \quad (i = 1, 2, \ldots, N).$$

The equivalent one can be further decomposed to N sub-problems with only one crack each, on which the tractions $t_i = \{p_{ni} \;\; p_{ti}\}^T$ are acting, where p_{ni} and p_{ti} are the normal and tangential components of the tractions t_i. The tractions t_i are the summation of the initial tractions $-n_i \cdot \sigma^{\infty}$ and the additional interaction tractions induced by other cracks. We also have

$$\mathbf{t}_i = -\mathbf{n}_i \cdot \sigma^{\infty} + \sum_{j \neq i} \Delta \mathbf{t}_{ji}, \tag{1}$$

where $\Delta \mathbf{t}_{ji}$ is the additional traction on the i-th crack due to the presence of the j-th crack. The key point is how to solve the unknown additional tractions adequately. The Kachanov method [1987] decomposes the unknown tractions into two parts, an average traction and a higher-order one, and only the influence of the average one is considered, while that of the higher-order one is ignored. In the modified method [Li et al. 2003], the linearly varying traction, instead of a uniform one, is used in an effort to improve the accuracy. However, both methods may be erroneous when applied to a problem where cracks are closely spaced and overlapping. Therefore, a modified method considering the influence of QPPTs is carried out in the next section.

3. The quadratic parabola pseudotraction method

First, one only considers the contribution to the other cracks of the tractions

$$t_i^{(0)} = \left\{ \, p_{ni}^{(0)} \;\; p_{ti}^{(0)} \, \right\} = -n_i \cdot \sigma^{\infty}$$

(the subscript 'n' denotes 'normal to crack line' and 't' means 'tangential to crack line') without regard to the additional tractions:

$$\mathbf{t}_i^{(1)} = \left\{ \, p_{ni}^{(1)} \;\; p_{ti}^{(1)} \, \right\}^T = -n_i \cdot \sigma^{\infty} + \sum_{j=1, j \neq i}^{N} \Delta t_{ji}^{(1)} \quad (i = 1, 2, \ldots, N), \tag{2}$$

where

$$\Delta \mathbf{t}_{ji}^{(1)} (i, j = 1, 2, \ldots, N)$$

is the additional traction acting on the i-th crack due to the traction

$$\mathbf{t}_j^{(0)} = -\mathbf{n}_j \cdot \sigma^{\infty}$$

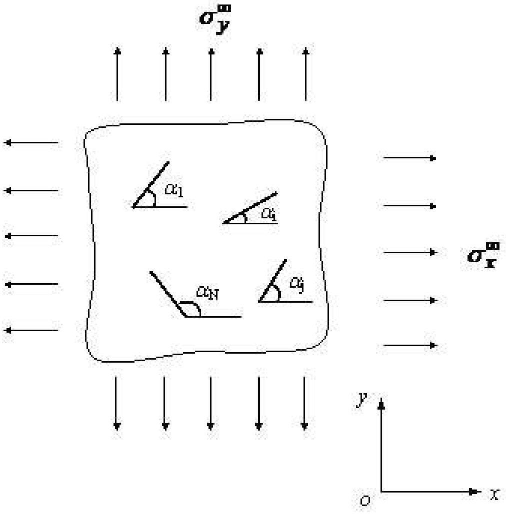

Figure 1. An infinite plane containing N cracks

on the j-th crack. This additional traction can be obtained from the elemental solutions of elastic mechanics [Sneddon and Lowengrub 1969]:

$$t_i^{(1)} = \begin{Bmatrix} p_{ni}^{(1)} \\ p_{ti}^{(1)} \end{Bmatrix} = \begin{Bmatrix} p_{ni}^{(0)} \\ p_{ti}^{(0)} \end{Bmatrix} + \sum_{j=1, j\neq i}^{N} \begin{bmatrix} f_{ji}^{nn} & f_{ji}^{tn} \\ f_{ji}^{nt} & f_{ji}^{tt} \end{bmatrix} \begin{Bmatrix} p_{nj}^{(0)} \\ p_{tj}^{(0)} \end{Bmatrix} \tag{3}$$

$(i = 1, 2, \dots, N)$, where f_{ji}^{rs} $(i, j = 1, 2, \dots, N;\ j \neq i;\ r, s = n, t)$ are those solutions. The explicit forms for f_{ji}^{rs} are given in the Appendix. In fact, the solutions above are only first-order approximations because the contributions of the additional items are ignored.

When considering further the influences of quadratic parabola pseudotractions (QPPTs), it is assumed that the unknown tractions $t_i^{(2)} = \{p_n i^{(2)}\ p_{ti}^{(2)}\}^T$ can be decomposed into

$$\mathbf{t}_i^{(2)} = \tilde{\mathbf{t}}_i^{(2)} + \Delta\mathbf{t}_i^{(2)} = -\mathbf{n}_i \cdot \sigma^\infty + \sum_{j=1, j\neq i}^{N} \Delta\mathbf{t}_{ji}^{(2)} \quad (i = 1, 2, \dots, N), \tag{4}$$

where $\tilde{\mathbf{t}}_i^{(2)}$ are QPPTs. Its normal and tangential components are respectively

$$\tilde{\mathbf{t}}_i^{(2)} = \begin{Bmatrix} \tilde{p}_{ni}^{(2)} \\ \tilde{p}_{ti}^{(2)} \end{Bmatrix} = \begin{Bmatrix} \langle p_{ni}^{(2)} \rangle \bigl(1 + T_{ni1}\xi_i + T_{ni2}(\xi_i^2 - \frac{1}{3} l_i^2)\bigr) \\ \langle p_{ti}^{(2)} \rangle \bigl(1 + T_{ti1}\xi_i + T_{ti2}(\xi_i^2 - \frac{1}{3} l_i^2)\bigr) \end{Bmatrix} \tag{5}$$

$(i = 1, 2, \dots, N)$. In these equations, $\xi_i \in (-l_i\ l_i)$ denotes the coordinate of a point in the i-th crack line with half-length l_i, and T_{ni1}, T_{ni2}, T_{ti1} and T_{ti2} are the dimensionless coefficients of tractions distributions. In (4), the item $\Delta t_{ji}^{(2)}$ is the additional tractions on the i-th crack due to the tractions $t_j^{(2)}$ of the j-th crack, and $\Delta t_i^{(2)}$ denotes the higher-order items of tractions. Averaging (4) and (5) along the crack line, one can know the averages of the higher-order tractions are zero, that is

$$\langle \mathbf{t}_i^{(2)} \rangle = \langle \tilde{\mathbf{t}}_i^{(2)} \rangle = \left\{ \begin{matrix} \langle p_{ni}^{(2)} \rangle \\ \langle p_{ti}^{(2)} \rangle \end{matrix} \right\} = \left\{ \begin{matrix} \langle \tilde{p}_{ni}^{(2)} \rangle \\ \langle \tilde{p}_{ti}^{(2)} \rangle \end{matrix} \right\} \langle \Delta \mathbf{t}_i^{(2)} \rangle = 0, \tag{6}$$

$(i = 1, 2, \dots, N)$.

Assume that the additional tractions

$$\Delta t_{ji}^{(2)}$$

of the i-th crack are contributed by the tractions $\tilde{t}_j^{(2)}$ of the j-th crack, while the higher-order tractions

$$\Delta t_i^{(2)}$$

are ignored. Clearly, if the tractions $\tilde{t}_i^{(2)}$ were known, the

$$\Delta t_{ji}^{(2)}$$

could be determined. However, the average tractions as well as the dimensionless coefficients T_{ni1}, T_{ni2}, T_{ti1} and T_{ti2} are unknown so far. So, it is reasonable to assume that these coefficients can be estimated by the known tractions

$$t_i^{(1)} = \left\{ \; p_{ni}^{(1)} \quad p_{ti}^{(1)} \; \right\}^T$$

to be

$$\begin{aligned} T_{ni1} &= \frac{p_{ni}^{(1)}(l_i) - p_{ni}^{(1)}(-l_i)}{2l_i \langle p_{ni}^{(1)} \rangle}, \\ T_{ni2} &= \frac{p_{ni}^{(1)}(l_i) + p_{ni}^{(1)}(-l_i) - 2p_{ni}^{(1)}(0)}{2l_i^2 \langle p_{ni}^{(1)} \rangle} \quad (i = 1, 2, \dots, N), \end{aligned} \tag{7}$$

where the $\langle p_{ni}^{(1)} \rangle$ are the average normal tractions, which can be obtained by integration:

$$\langle p_{ni}^{(1)} \rangle = \frac{1}{2l_i} \int_{-l_i}^{l_i} p_{ni}^{(1)}(\xi_i) \, d\xi_i, \tag{8}$$

$(i = 1, 2, \dots, N)$. The tangential coefficients T_{ti1} and T_{ti2} and the average tangential tractions

$$\langle p_{ti}^{(1)} \rangle$$

can be obtained by replacing the subscript n by t in (7) and (8).

Now the expressions of the additional tractions $\Delta t_i^{(2)}$ of the i-th crack due to QPPTs on the other cracks can be given as

$$t_i^{(2)} = \begin{Bmatrix} p_{ni}^{(2)} \\ p_{ti}^{(2)} \end{Bmatrix} = \begin{Bmatrix} p_{ni}^{(0)} \\ p_{ti}^{(0)} \end{Bmatrix} + \sum_{j=1, j\neq i}^{N} \begin{bmatrix} \hat{f}_{ji}^{nn} & \hat{f}_{ji}^{tn} \\ \hat{f}_{ji}^{nt} & \hat{f}_{ji}^{tt} \end{bmatrix} \begin{Bmatrix} p_{nj}^{(2)} \\ p_{tj}^{(2)} \end{Bmatrix} \quad (i = 1, 2, \ldots, N). \tag{9}$$

In (9), the coefficients

$$\hat{f}_{ji}^{rs} \quad (i, j = 1, 2, ..., N;\ j \neq i;\ r, s = n, t)$$

denote the interaction coefficients. For example, $\hat{f}_{ji}^{tn}$ is the normal (n) traction of the i-th crack contributed by the tangential (t) QPPT

$$\left(\left(1 + T_{tj1}\xi_i + T_{tj2}(\xi_j^2 - \tfrac{1}{3}l_j^2)\right) \right)$$

of the j-th crack. The QPPT has a unit mean value along the crack line.

Averaging (9) along the i-th crack line, one gets

$$\begin{Bmatrix} \langle p_{ni}^{(2)} \rangle \\ \langle p_{ti}^{(2)} \rangle \end{Bmatrix} = \begin{Bmatrix} \langle p_{ni}^{(0)} \rangle \\ \langle p_{ti}^{(0)} \rangle \end{Bmatrix} + \sum_{j=1, j\neq i}^{N} \begin{bmatrix} \Lambda_{ji}^{nn} & \Lambda_{ji}^{tn} \\ \Lambda_{ji}^{nt} & \Lambda_{ji}^{tt} \end{bmatrix} \begin{Bmatrix} \langle p_{nj}^{(2)} \rangle \\ \langle p_{tj}^{(2)} \rangle \end{Bmatrix} \tag{10}$$

$(i = 1, 2, \ldots, N)$.

In these equations, the coefficients

$$\Lambda_{ji}^{rs} \quad (i, j = 1, 2, \ldots, N;\ j \neq i;\ r, s = n, t)$$

denote the interaction coefficients. For example, Λ_{ji}^{tn} is the average normal traction of the i-th crack contributed by the tangential QPPT of the j-th crack. The explicit forms for $\hat{f}_{ji}^{rs}$ in (9) and Λ_{ji}^{rs} in (10) are listed in the Appendix.

For each crack, one can establish a set of (10). Therefore, there will be $2N$ equations with $2N$ unknown average tractions

$$\langle p_{ni}^{(2)} \rangle \quad \text{and} \quad \langle p_{ti}^{(2)} \rangle \quad (i = 1, 2, \ldots, N).$$

By solving these equations, one can determine the average tractions.

Once the average tractions are determined, one can then obtain the QPPTs

$$\tilde{t}_i^{(2)}$$

acting on these cracks and calculate the tractions $t_i^{(2)}$ in (4) by the elemental solutions of elastic mechanics. The SIFs of each crack can be computed as follows:

$$\left. \begin{matrix} K_I(\pm l_i) \\ K_{II}(\pm l_i) \end{matrix} \right\} = -\frac{1}{\sqrt{\pi l_i}} \int_{-l_i}^{l_i} \sqrt{\frac{l_i \pm \xi_i}{l_i \mp \xi_i}} \begin{Bmatrix} p_{ni}^{(2)}(\xi_i) \\ p_{ti}^{(2)}(\xi_i) \end{Bmatrix} d\xi_i. \tag{11}$$

In fact, it can be seen from (5) that, if the coefficients T_{ni2} and T_{ti2} are zero, the present formulation is similar to that of the linear approximate method [Li et al. 2003] except that the way to estimate the coefficients T_{ni1} and T_{ti1} is slightly different. Furthermore, if all of the coefficients are assumed to be zero, the present formulation is then identical to the original Kachanov method, in which only the average tractions are considered.

4. Example: three collinear cracks

To evaluate the accuracy of the present method, the problem of three collinear cracks in an infinite medium under a uniform tensile stress normal to the crack line as shown in Figure 2 is taken as a test case here. The present results are compared with those available from the literature [Sih 1965] and those obtained by using the original Kachanov method [1987] and the linear approximate method [Li et al. 2003]. The errors are also listed in the table. It can be seen from Table 1 that very good agreement has been achieved between the present method and the exact solutions. On the other hand, the errors of the Kachanov results at the inner tip are significant when three cracks are closely spaced. In addition, the discrepancies of the SIFs of the outer tips are not as obvious as those of the inner tips.

Though the computational time required to obtain the solutions by the present method is slightly more than with Kachanov's method, the much improved accuracy makes it attractive for the analysis of interaction cracks, especially when those cracks are closely spaced.

It is interesting also to compare the improvement in accuracy of the two modified methods. This comparison will be done in Section 6 after another numerical example for two overlapping cracks is given.

5. A pair of offset parallel cracks

In this section, the same approach is used to analyse a pair of offset parallel cracks. In this case, it is slightly more complicated than in the case of collinear cracks, but one can still obtain the interaction factors by integrating the equations given in the Appendix. Having Λ_{ij}^{rs} determined, one can obtain the Kachanov tractions and the improved tractions accordingly. To investigate the influence of the distance between the two overlapping cracks, two parameters are employed: h/a and a/b, as shown in Figures 3 and 4.

The exact solutions, the present solutions and the Kachanov solutions are given together in Figures 3 and 4. Note that K_0 is the stress intensity factor for an isolated crack under normal remote stress and is given by $K_0 = \sigma\sqrt{\pi a}$. It is obvious that the results of the proposed method are in good agreement with those of Rooke and Cartwright [1976] even when the two cracks overlap $(0.5 < h/a < 1.0)$. When

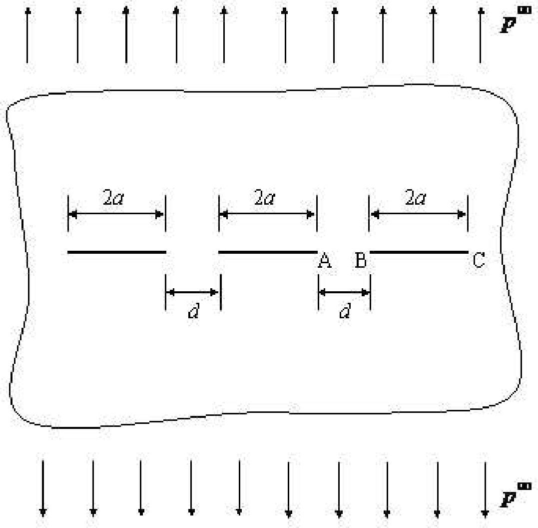

Figure 2. Three collinear cracks.

the two cracks are remotely spaced (e.g., $h/a = 1.0$) or not overlapping ($a/b < 0.5$), the Kachanov solutions are good approximations. However, the Kachanov solutions become increasingly more erroneous as the two cracks get closer (e. g., $h/a = 0.5, 0.1$) and overlapping ($0.5 < h/a < 1.0$) along the load direction. In addition, the discrepancies of the SIFs of the inner tips are more remarkable than those of the outer tips.

So far, there are three Kachanov-type methods for interaction of multiple cracks. An interesting question is when and why it is worth using the present method instead of the linear one [Li et al. 2003] and Kachanov's. Therefore, comparison of this QPPTs method with the other two Kachanov-type methods and also other polynomial approximation techniques is given in next section.

6. Comparison with other techniques

First, we compare the original Kachanov method with its two modifications. The essential difference among the three lies in that they use approximate polynomial functions of different orders — $p = 0$, 1, and 2.

The results of the three methods in Table 1 indicate that the linear method ($p = 1$) and the present quadratic method ($p = 2$) yield smaller errors than does the Kachanov method ($p = 0$). One can conclude that a higher-degree method gives better results than a lower one, though the present method does not generate as

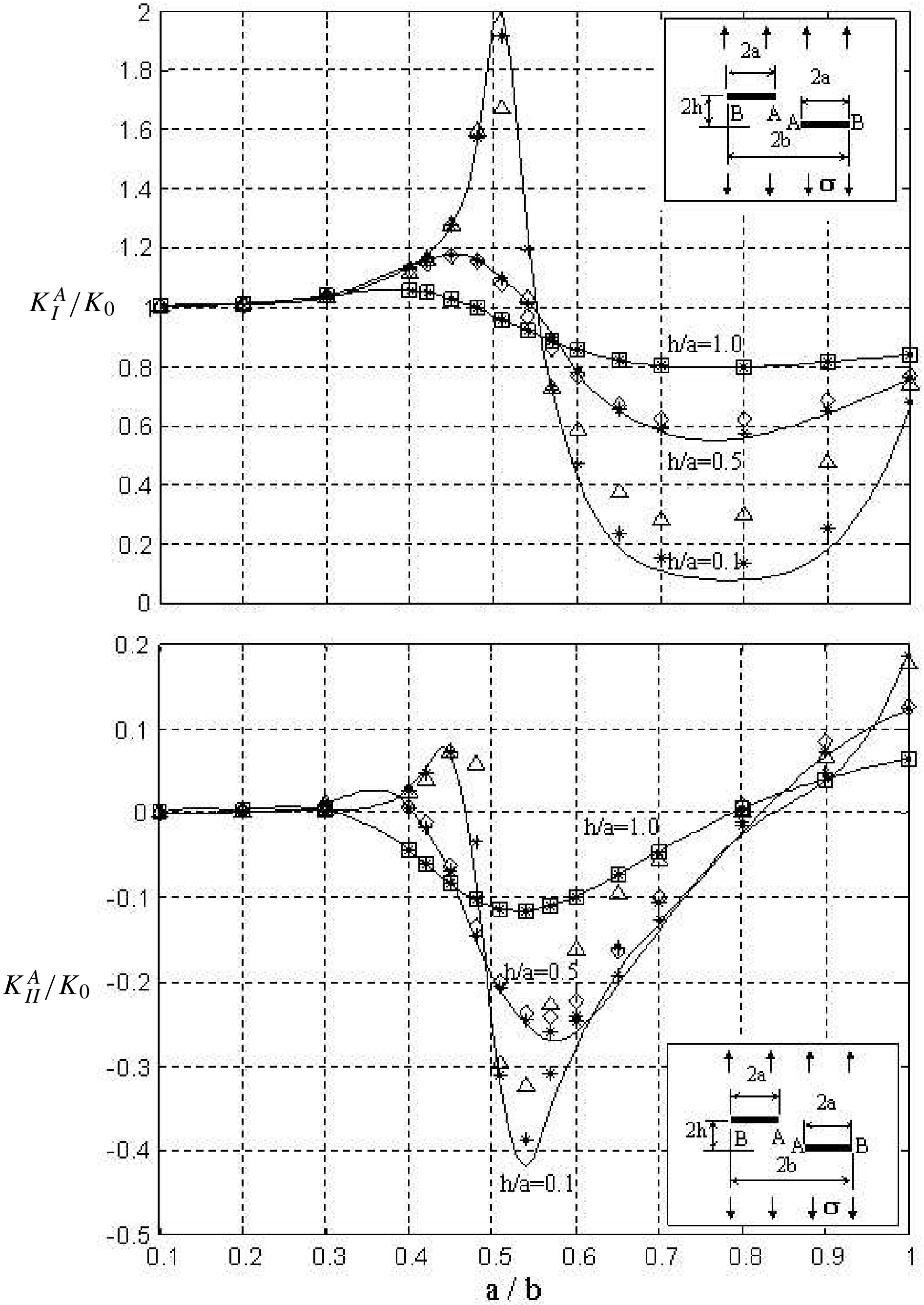

Figure 3. A pair of offset parallel cracks, Tip A. Code: solid line, Rooke and Cartwright [1976]; $*$, present method with $h/a = 0.1$, 0.5, 1.0; $\triangle$, Kachanov method with $h/a = 0.1$; $\diamond$, Kachanov method with $h/a = 0.5$; $\square$, Kachanov method with $h/a = 1.0$.

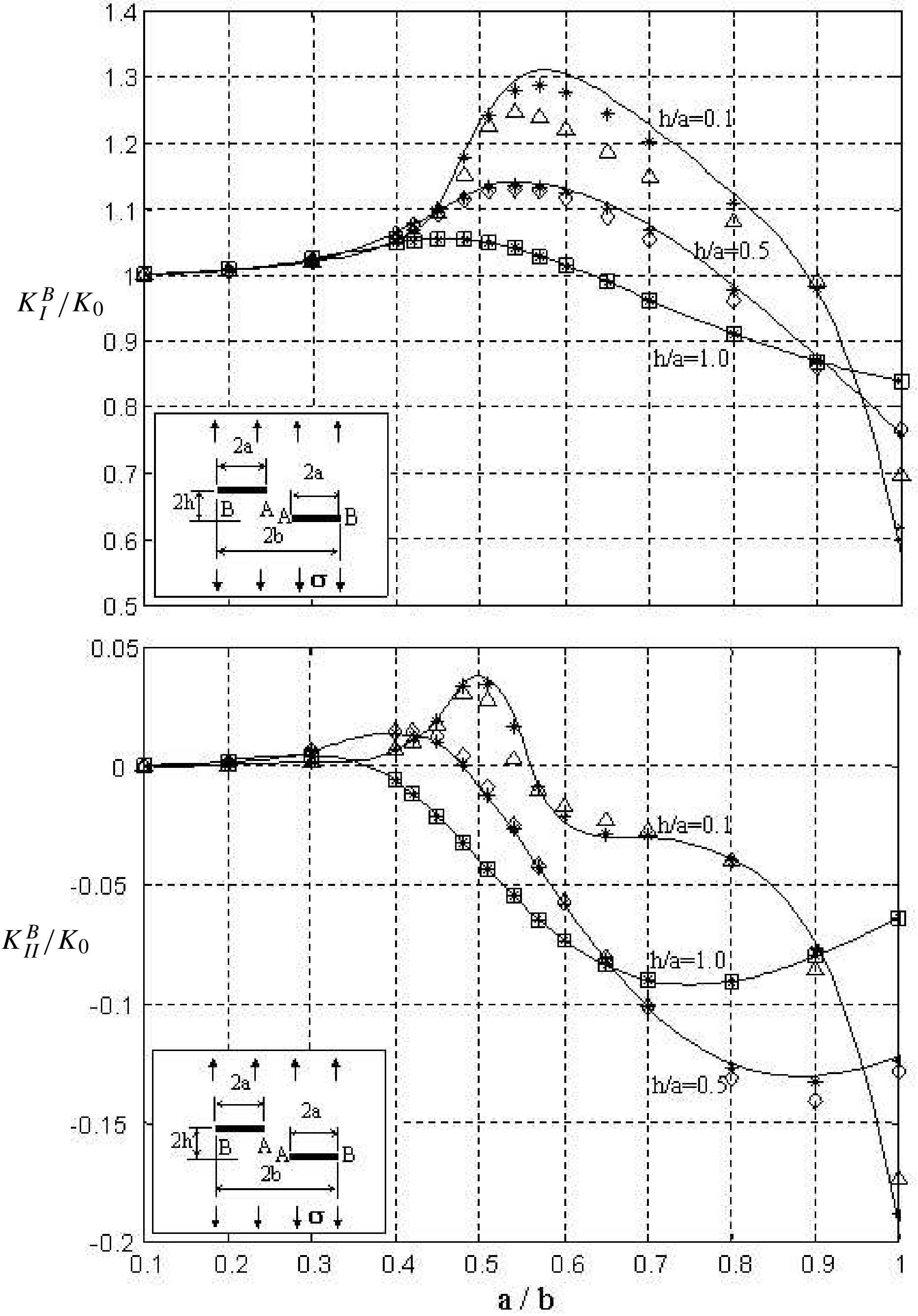

Figure 4. A pair of offset parallel cracks, Tip B. Code: solid line, Rooke and Cartwright [1976]; ∗, present method with $h/a = 0.1$, 0.5, 1.0; △, Kachanov method with $h/a = 0.1$; ◇, Kachanov method with $h/a = 0.5$; □, Kachanov method with $h/a = 1.0$.

		$d/a \rightarrow$	1.0	0.5	0.2	0.1	0.05
K_I/K_0	Tip A	Exact*	1.1674	1.3214	1.6542	2.0325	2.5537
		Kachanov method	1.1669 0.04%	1.3179 0.26%	1.6309 1.4%	1.9601 3.6%	2.3657 7.4%
		Linear method	1.1672 0.02%	1.3210 0.03%	1.6649 0.65%	2.0591 1.3%	2.6252 2.8%
		Present method	1.1673 0.01%	1.3211 0.02%	1.6604 0.37%	2.0453 0.6%	2.5825 1.1%
	Tip B	Exact	1.1387	1.2836	1.6119	1.9923	2.5185
		Kachanov method	1.1382 0.04%	1.2797 0.30%	1.5877 1.5%	1.9086 4.2%	2.3095 8.3%
		Linear method	1.1384 0.03%	1.2833 0.02%	1.6202 0.51%	2.0262 1.7%	2.5941 3.0%
		Present method	1.1385 0.02%	1.2834 0.02%	1.6201 0.50%	2.0093 0.8%	2.5563 1.5%
	Tip C	Exact	1.0687	1.1103	1.1714	1.2167	1.2587
		Kachanov method	1.0686 0.00%	1.1081 0.20%	1.1667 0.40%	1.2094 0.60%	1.2486 0.80%
		Linear method	1.0686 0.00%	1.1101 0.02%	1.1741 0.23%	1.2224 0.47%	1.2637 0.40%
		Present method	1.0686 0.00%	1.1102 0.01%	1.1728 0.12%	1.2195 0.23%	1.2617 0.24%

Table 1. Results for three collinear cracks (after Sih [1965]).

much of an improvement over the linear one as the latter does over the original. For example, comparing the results for the closest cracks ($d/a = 0.05$) at crack Tip B, the errors are 8.3% for the Kachanov method, 3.0% for the linear method and 1.5% for the present method.

One can compare in succession the results of the three methods for the offset cracks case. In fact, to avoid confusion, the results from [Li et al. 2003] for the same example are not shown in Figures 3 and 4. Therefore, here, the SIFs of the inner tips for the closer case ($h/a = 0.2$) not shown in the figures are listed in Table 2 for comparison of the results of the three methods. From Table 2 and Figures 3 and 4, one can see that the discrepancies of the Kachanov solutions become increasingly more serious as the two cracks get closer and overlap along the loading direction.

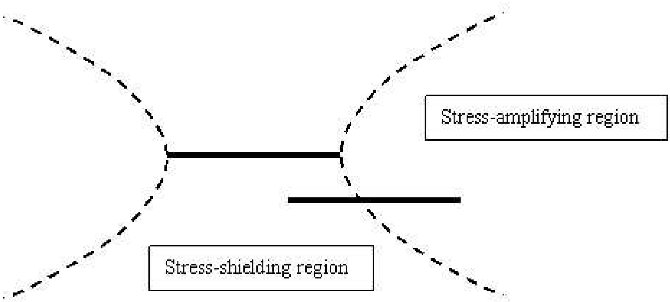

Figure 5. Stress-amplifying region and stress-shielding region of a crack.

The maximal error reaches 30%. By comparison with the Kachanov method, the linear method generates better results with errors below 14.5%. For the same case, the present method yields practically imperceptible errors of only 4% or less. The accuracy of the results is adequate for the analysis of propagation and coalescence of several cracks (see Section 1).

One can examine this phenomenon as illustrated in Figure 5. For the problem of closely spaced cracks overlapping along the loading direction, each crack is embedded in the stress-amplifying region as well as in the stress-shielding region of the other one. The pseudotractions acting on cracks may vary intensely, in which case the use of constant or linearly varying approximation for the tractions would result in significant errors in the SIFs. Then it is reasonable that a higher-order approximation would yield a remarkable improvement in accuracy.

Therefore, we suggest that: for the problems of remotely-spaced cracks, the three Kachanov-type methods all can generate satisfactory results for SIFs; the most simple Kachanov method is preferred; for the problems of cracks closely spaced but not overlapping each other, the linear method is adequate for analysis; for the problem of cracks closely spaced and overlapping each other, the present method instead of the other two methods should be chosen.

These Kachanov-type methods can be considered as further developments of the ideas from [Chen 1984a; Horii and Nemat-Nasser 1985b; Chudnovsky et al. 1987a; 1987b], where tractions on individual cracks were interrelated by self-consistence conditions. Kachanov [1987] compared his method with previous works in detail, so only some statements are repeated here. In [Horii and Nemat-Nasser 1985b; Chudnovsky et al. 1987a; 1987b], Taylor or Chebyshev polynomials centered at the crack center were applied to the configuration “crack-microcrack array” and to the general 2-D crack array. Horii and Nemat-Nasser [1985b] considered the test problem of two collinear cracks. They found that the degree of the approximating polynomials increases rapidly as the spacing between cracks becomes smaller. The

$a/b \rightarrow$	0.1	0.2	0.4	0.48	0.54	0.60	0.70	0.80	0.90
Exact*	1.0017	1.0093	1.1611	1.6988	1.0805	0.5791	0.3023	0.2987	0.4312
Kachanov method	1.0011 0.00%	1.0085 0.10%	1.1260 3.0%	1.4640 13.8%	1.0663 1.3%	0.6438 11.2%	0.3641 20.4%	0.3890 30.0%	0.5502 27.6%
Linear method	1.0016 0.01%	1.0090 0.03%	1.1499 0.97%	1.6049 5.5%	1.0743 0.58%	0.6024 4.0%	0.3295 9.0%	0.3420 14.5%	0.4883 13.3%
Present method	1.0016 0.01%	1.0091 0.02%	1.1558 0.45%	1.6612 2.2%	1.0770 0.33%	0.5895 1.8%	0.3116 3.1%	0.3104 3.9%	0.4479 3.9%

Table 2. K_I^A/K_0 for two offset parallel cracks $h/a = 0.2$ (after Rooke and Cartwright [1976]).

closest distance considered is $1/4$ of the crack length ($1/10$ otherwise in the present work); at this distance the polynomials' degree is 28. At distances one order of magnitude smaller than the crack length, the polynomial's degree in their method can be expected to be several times higher. Kachanov [1987] also pointed out that in the Chebyshev polynomial technique, as with the Taylor polynomial technique, convergence gets increasingly difficult as the spacings between cracks become smaller. At a close distance (1/10 of the crack length), Chebyshev polynomials of the sixth degree yield a 10.7% error in SIFs, while the Kachanov method yields only a 1.5% error.

Note also that the technique of polynomial approximation [Chen 1984a] is based on complex variable representations and is not, therefore, easily extensible to 3-D configurations. The main drawback of the polynomial technique — a large number of polynomial coefficients (rapidly increasing as spacings between cracks become smaller) — will, however, become much more severe in the 3-D problems.

The key idea of Kachanov-type methods — to neglect the impact on a given crack of higher-order traction nonuniformities — is reminiscent of Saint-Venant's principle of elasticity and may be interpreted as a Saint-Venant-type principle for solids with cracks. Moreover, since the SIFs are given by integrals of tractions, the effect of higher-order nonuniformities is neglected not in the pointwise sense but in a milder, integral sense. This may explain why further refinements of the original Kachanov method work well for closely spaced cracks.

7. Conclusions

To improve the accuracy of the Kachanov method in analyzing closely spaced and overlapping cracks, a QPPT method for the analysis of solids with multiple

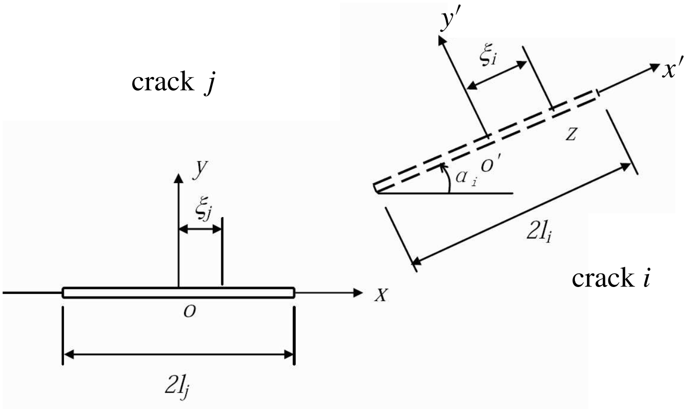

Figure 6. Cracks i and j.

cracks is proposed. The pseudotraction in a crack is decomposed into a quadratic-varying component and a higher-order one. The higher-order component has a zero average. It is further assumed that the interaction effects among the cracks are only due to the quadratic-varying component. Mathematical relations for the tractions in the cracks are derived and the solutions are obtained for various cases. It is shown through two numerical examples that the results of the method are in close agreement with the exact solutions, even when closely spaced cracks overlap along the direction of loading.

Appendix: The interaction coefficients

Consider two cracks i and j as shown in Figure 6; the interaction coefficients in Equations (3), (9) and (10) can be obtained thus [Chen 1984a; Cheung et al. 1992]:

$$f_{ij}^{nn} - \mathbf{i} f_{ij}^{tn} = \int_{-l_j}^{l_j} (\bar{f}_{ij}^{nn} - \mathbf{i} \bar{f}_{ij}^{tn})\, d\xi_j,$$

$$f_{ij}^{tn} - \mathbf{i} f_{ij}^{tt} = \int_{-l_j}^{l_j} (\bar{f}_{ij}^{tn} - \mathbf{i} \bar{f}_{ij}^{tt})\, d\xi_j,$$

$$\hat{f}_{ij}^{nn} - \mathbf{i} \hat{f}_{ij}^{tn} = \int_{-l_j}^{l_j} (\bar{f}_{ij}^{nn} - \mathbf{i} \bar{f}_{ij}^{tn})\big(1 + T_{nj1}\xi_j + T_{nj2}(\xi_j^2 - \tfrac{1}{3} l_j^2)\big)\, d\xi_j,$$

$$\hat{f}_{ij}^{tn} - \mathbf{i} \hat{f}_{ij}^{tt} = \int_{-l_j}^{l_j} (\bar{f}_{ij}^{tn} - \mathbf{i} \bar{f}_{ij}^{tt})\big(1 + T_{tj1}\xi_j + T_{tj2}(\xi_j^2 - \tfrac{1}{3} l_j^2)\big)\, d\xi_j,$$

$$\Lambda_{ij}^{rs} = \frac{1}{2a_i} \int_{-a_i}^{a_i} f_{ij}^{rs}\, d\xi_i \quad (r, s = n, t),$$

where

$$\bar{f}_{ij}^{nn} - \mathbf{i}\bar{f}_{ij}^{tn} = \frac{\sqrt{l_j^2 - \xi_j^2}}{2\pi}\bigl(G(z) + \overline{G(z)} + e^{-2\mathbf{i}\alpha_i}(z - \bar{z})\overline{G'(z)}\bigr),$$

$$\bar{f}_{ij}^{tn} - \mathbf{i}\bar{f}_{ij}^{tt} = -\frac{\sqrt{l_j^2 - \xi_j^2}}{2\pi i}\bigl(\overline{G(z)}(1 - 2e^{-2\mathbf{i}\alpha_i}) - G(z) + e^{-2\mathbf{i}\alpha_i}(z - \bar{z})\overline{G'(z)}\bigr);$$

here $z = z(\xi_i)$ is the complex coordinate in the xy coordinate system of the point $(\xi_i, 0)$ in crack i and

$$G(z) = \frac{1}{(z - \xi_j)\sqrt{z^2 - l_j^2}}, \qquad G'(z) = \frac{l_j^2 + \xi_j z - 2z^2}{(z - \xi_j)^2\bigl(\sqrt{z^2 - l_j^2}\bigr)^3}.$$

Acknowledgements

The author acknowledges the financial support from National Natural Science Foundation of China (50374064, 50334060) and the Project of National Basic Research Program of China (2002CB412704). The helpful suggestions of the anonymous reviewer and discussions with Doctor Q. D. Yang and Mr. X. Y. Wu are also gratefully acknowledged.

References

[Basista and Gross 2000] M. Basista and D. Gross, "A note on crack interactions under compression", *Int. J. Fract.* **102**:3 (2000), L67–L72.

[Chen 1984a] Y. Z. Chen, "Multiple crack problems of antiplane elasticity in an infinite body", *Eng. Fract. Mech.* **20**:5–6 (1984), 767–775.

[Chen 1984b] Y. Z. Chen, "Solutions of multiple crack problems of a circular plate or an infinite plate containing a circular hole by using Fredholm integral equation approach", *Int. J. Fract.* **25**:3 (1984), 155–168.

[Chen 1995] Y. Z. Chen, "A survey of new integral equations in plane elasticity crack problem", *Eng. Fract. Mech.* **51**:1 (1995), 97–134.

[Cheung et al. 1992] Y. K. Cheung, C. W. Woo, and Y. H. Wang, "A general method for multiple crack problems in a finite plate", *Comput. Mech.* **10**:5 (1992), 335–343.

[Chudnovsky et al. 1987a] A. Chudnovsky, A. Dolgopolsky, and M. Kachanov, "Elastic interaction of a crack with a microcrack array, I", *Int. J. Solids Struct.* **23**:1 (1987), 1–10.

[Chudnovsky et al. 1987b] A. Chudnovsky, A. Dolgopolsky, and M. Kachanov, "Elastic interaction of a crack with a microcrack array, II", *Int. J. Solids Struct.* **23**:1 (1987), 11–21.

[Erdogan 1983] F. Erdogan, "Stress intensity factors", *J. Appl. Mech.* (*ASME*) **50** (1983), 992–1002.

[Gorbatikh and Kachanov 2000] L. Gorbatikh and M. Kachanov, "A simple technique for constructing the full stress and displacement fields in elastic plates with multiple cracks", *Eng. Fract. Mech.* **66**:1 (2000), 51–63.

[Horii and Nemat-Nasser 1985a] H. Horii and S. Nemat-Nasser, "Compression-induced microcrack growth in brittle solids: axial splitting and shear failure", *J. Geophys. Res.* **90**:B4 (1985), 3105–3125.

[Horii and Nemat-Nasser 1985b] H. Horii and S. Nemat-Nasser, "Elastic fields of interacting inhomogeneities", *Int. J. Solids Struct.* **21**:7 (1985), 731–745.

[Kachanov 1987] M. Kachanov, "Elastic solids with many cracks: A simple method of analysis", *Int. J. Solids Struct.* **23**:1 (1987), 23–43.

[Kachanov 1992] M. Kachanov, "Effective elastic properties of cracked solids: critical review of some basic concepts", *Appl. Mech. Rev.* **45** (1992), 304–335.

[Kachanov 2003] M. Kachanov, "On the problems of crack interactions and crack coalescence", *Int. J. Fract.* **120**:3 (2003), 537–543.

[Lam and Phua 1991] K. Y. Lam and S. P. Phua, "Multiple crack interaction and its effect on stress intensity factor", *Eng. Fract. Mech.* **40**:3 (1991), 585–592.

[Li et al. 2003] Y. P. Li, L. G. Tham, Y. H. Wang, and Y. Tsui, "A modified Kachanov method for analysis of solids with multiple cracks", *Eng. Fract. Mech.* **70**:9 (2003), 1115–1129.

[Rooke and Cartwright 1976] D. P. Rooke and D. J. Cartwright, *Compendium of stress intensity factors*, Her Majesty's Stationery Office, London, 1976.

[Sih 1965] G. C. Sih, "Boundary problems for longitudinal shear cracks", pp. 117–130 in *Proceedings, Second Conference on Theoretical and Applied Mechanics* (Atlanta, 1964), Pergamon, New York, 1965.

[Sneddon and Lowengrub 1969] I. N. Sneddon and M. Lowengrub, *Crack problems in the classical theory of elasticity*, Wiley, New York, 1969.

[Wang et al. 1996] Y. Z. Wang, J. D. Atkinson, R. Akid, and N. Parkins, "Crack interaction, coalescence and mixed mode fracture mechanics", *Fatigue Fract. Eng. Mater. Struct.* **19**:1 (1996), 51–63.

[Wang et al. 2000] J. Wang, J. Fang, and B. L. Karihaloo, "Asymptotics of multiple crack interactions and prediction of effective modulus", *Int. J. Solids Struct.* **37**:31 (2000), 4261–4273.

Received 22 Sep 2005. Revised 11 Dec 2005.

LI YIN-PING: `ypli@whrsm.ac.cn`
Institute of Rock and Soil Mechanics, Chinese Academy of Science, Wuhan 430071, China

YANG CHUN-HE: *Institute of Rock and Soil Mechanics, Chinese Academy of Science, Wuhan 430071, China*

JOURNAL OF MECHANICS OF MATERIALS AND STRUCTURES
Vol. 1, No. 1, 2006

THE DETERMINATION OF FREQUENCIES OF LAMINATED CONICAL SHELLS VIA THE DISCRETE SINGULAR CONVOLUTION METHOD

ÖMER CIVALEK

The discrete singular convolution (DSC) algorithm for determining the frequencies of the free vibration of laminated conical shells is developed by using a numerical solution of the governing differential equations of motion based on Love's first approximation thin shell theory. By applying the discrete singular convolution method, the free vibration equations of motion of the composite laminated conical shell are transformed to a set of algebraic equations. Convergence and comparison studies are carried out to check the validity and accuracy of the DSC method.

1. Introduction

Because of the practical importance of the free vibration analysis of the composite laminated conical shell in structural, aerospace, nuclear, petrochemical, submarine hulls, and mechanical applications, a few investigators have made efforts to deal with free vibration analysis of this type of structures. Unsymmetric free vibrations of orthotropic sandwich shells of revolution has been made by Bacon and Bert [1967]. Siu and Bert [1970] analyzed the free vibration of isotropic and orthotropic conical shells by using the Rayleigh–Ritz technique. Irie et al. [1982; 1984] developed a transfer-matrix approach for free vibration of conical shells with constant and variable thickness. Using the finite element method, Sivadas and Ganesan [1992] analyzed the free vibration of conical shells with uniform thickness. Yang [1974] adopted the integration method in the vibration analysis of orthotropic conical shells. Tong [1993b; 1993a], and Tong and Wang [1992] examined the vibration and buckling analysis of isotropic, orthotropic and laminated conical shells by the power series expansion method. More recent papers [Shu 1996b; 1996a; Hua 2000; Hua and Lam 2000; Lam and Hua 1997] have used the differential quadrature method to study the free vibration of orthotropic and laminated rotating conical shells. Liew et al. [1995] also studied the effects of initial twist and thickness variation on the vibration behavior of shallow conical shells. Lim and Kitipornchai [1999] have investigated the effects of subtended and

---

Keywords: conical shells, discrete singular convolution, laminated composite, frequencies.

vertex angles on the free vibration of open conical shell. Some selected works in this topic includes [Liew et al. 2005; Liew and Lim 1994; Lim et al. 1997; 1998; Lim and Liew 1995; Leissa 1973; Soedel 1996; Civalek 1998; 2004; 2005; Civalek and Ülker 2005]. More detailed information can be found in [Chang 1981] and [Kapania 1989].

The focus in this work is on the application of the DSC method to the differential equation, which governs the free vibration analysis of laminated conical shells. The governing differential equations of vibration of the shell are formulated using Love's first approximation classical thin shell theory [Love 1888]. In this study, the DSC method was used for spatial discretization of the differential equations governing the problem. In the author's knowledge, it is the first time the discrete singular convolution algorithm has been successfully applied to laminated conical shell problem for vibration analysis.

2. Governing equations

A typical laminated conical shell is given as shown in Figure 1. The cone semivertex angle, thickness of the shell, and cone length are denoted by α, h and L. R_1 and R_2 are the radii of the cone at its small and large edges. The conical shell is

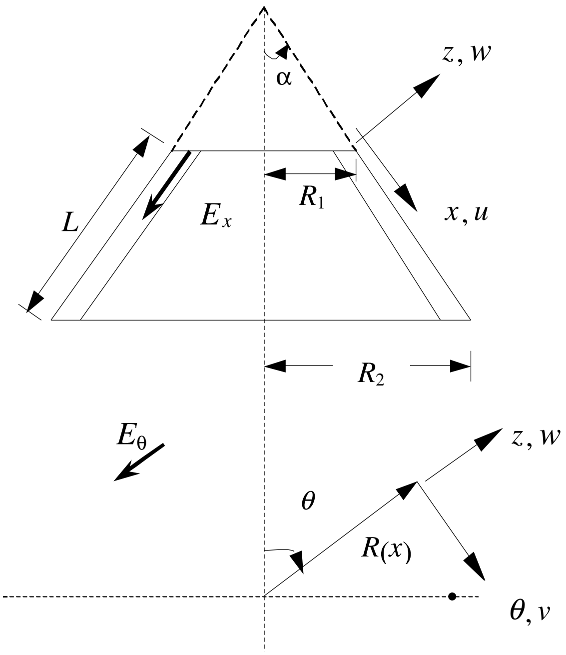

Figure 1. Geometry and notation of laminated conical shell.

referred to a coordinate system (x, θ, z) as shown in Figure 1. The components of the deformation of the conical shell with references to this given coordinate system are denoted by u, v, w in the x, θ and z directions, respectively. E_x and E_θ denote the elastic moduli respectively in the meridional x and circumferential θ directons. The equilibrium equation of motion in terms of the force and moment resultants can be written as in [Tong 1993b]:

$$\frac{\partial N_x}{\partial x} + \frac{1}{R(x)}\frac{\partial N_{x\theta}}{\partial \theta} + \frac{\sin\alpha}{R(x)}(N_x - N_\theta) = \rho h \frac{\partial^2 u}{\partial t^2}, \tag{1}$$

$$\frac{\partial N_{x\theta}}{\partial x} + \frac{1}{R(x)}\frac{\partial N_\theta}{\partial \theta} + \frac{\cos\alpha}{R(x)}\frac{\partial M_{x\theta}}{\partial x} + \frac{\cos^2\alpha}{R^2(x)}\frac{\partial M_\theta}{\partial \theta} + 2\frac{\sin\alpha}{R(x)}N_{x\theta} = \rho h \frac{\partial^2 v}{\partial t^2}, \tag{2}$$

$$\frac{\partial^2 M_x}{\partial x^2} + \frac{2}{R(x)}\frac{\partial^2 M_{x\theta}}{\partial\theta\,\partial x} + \frac{1}{R^2(x)}\frac{\partial^2 M_\theta}{\partial \theta^2} + \frac{2\sin\alpha}{R(x)}\frac{\partial M_x}{\partial x} - \frac{1}{R(x)}\Big(\sin\alpha\frac{\partial M_\theta}{\partial x} + \cos\alpha N_\theta\Big) = \rho h \frac{\partial^2 w}{\partial t^2}, \tag{3}$$

where

$$R(x) = R_1 + x\sin\alpha, \tag{4}$$

$$\rho_a(x,\theta) = \frac{1}{h}\int_{-h/2}^{h/2} \rho(x,\theta,z)\,dz. \tag{5}$$

Here ρ is the density and ρ_a the linear density. The moment resultants and in-surface force are

$$N = (N_x,\, N_\theta,\, N_{x\theta})^T = \int_{-h/2}^{h/2} (\sigma_x, \sigma_\theta, \sigma_{x\theta})^T\,dz, \tag{6}$$

$$M = (M_x, M_\theta, M_{x\theta})^T = \int_{-h/2}^{h/2} (\sigma_x, \sigma_\theta, \sigma_{x\theta})^T z\,dz, \tag{7}$$

where $(\sigma)^T = \{\sigma_x, \sigma_\theta, \sigma_{x\theta}\}$ is the stress vector. The stress vector of the k-th layer for laminated composite conical shells in which each layer is orthotropic is

$$\{\sigma_k\} = [Q^*_{ij}]\{\varepsilon^*_k\}, \tag{8}$$

where $\{\varepsilon^*_k\}^T = \{\varepsilon_x, \varepsilon_\theta, \varepsilon_{x\theta}\}$ is the strain vector. Based on Love's first approximation theory, the strain components of this vector are defined as linear functions of the normal (thickness) coordinate z:

$$\varepsilon_x = \varepsilon_1 + z\kappa_1, \quad \varepsilon_\theta = \varepsilon_2 + z\kappa_2, \quad \varepsilon_{x\theta} = \gamma + 2z\tau \tag{9}$$

where $\{\varepsilon\}^T = \{\varepsilon_1, \varepsilon_2, \gamma\}$ and $\{\kappa\}^T = \{\kappa_1, \kappa_2, 2\tau\}$ are the strain and curvature vectors of the reference surface. They are defined by

$$\varepsilon_1 = \frac{\partial u}{\partial x}, \quad \varepsilon_2 = \frac{1}{R(x)}\frac{\partial v}{\partial \theta} + \frac{u \sin\alpha}{R(x)} + \frac{w \cos\alpha}{R(x)}, \quad \gamma = \frac{1}{R(x)}\frac{\partial u}{\partial \theta} + \frac{\partial v}{\partial x} - \frac{v \sin\alpha}{R(x)}$$

$$\kappa_1 = -\frac{\partial^2 w}{\partial x^2}, \quad \kappa_2 = -\frac{1}{R^2(x)}\frac{\partial^2 w}{\partial \theta^2} + \frac{\cos\alpha}{R^2(x)}\frac{\partial v}{\partial \theta} - \frac{\sin\alpha}{R(x)}\frac{\partial w}{\partial x},$$

$$\tau = -\frac{1}{R(x)}\frac{\partial^2 w}{\partial x \partial \theta} + \frac{\sin\alpha}{R^2(x)}\frac{\partial w}{\partial \theta} + \frac{\cos\alpha}{R(x)}\frac{\partial v}{\partial x} - \frac{v \sin\alpha \cos\alpha}{R^2(x)}. \tag{10}$$

For a thin and generally orthotropic layer, the stresses defined in Equation (8) are given by

$$\begin{Bmatrix} \sigma_x \\ \sigma_\theta \\ \sigma_{x\theta} \end{Bmatrix} = \begin{bmatrix} Q^*_{11} & Q^*_{12} & Q^*_{16} \\ Q^*_{12} & Q^*_{22} & Q^*_{26} \\ Q^*_{16} & Q^*_{26} & Q^*_{66} \end{bmatrix} \begin{Bmatrix} \varepsilon_x \\ \varepsilon_\theta \\ \varepsilon_{\theta x} \end{Bmatrix}, \tag{11}$$

where the transformed reduced stiffness matrix of the k-th layer is defined by

$$[Q^*_k] = [T][Q_k][T]^{-1} \tag{12}$$

and where

$$[T] = \begin{bmatrix} \cos^2\varphi & \sin^2\varphi & 2\sin\varphi\cos\varphi \\ \sin^2\varphi & \cos^2\varphi & -2\sin\varphi\cos\varphi \\ -\sin\varphi\cos\varphi & \sin\varphi\cos\varphi & \cos^2\varphi - \sin^2\varphi \end{bmatrix} \tag{13}$$

in which $[T]$ is the transformation matrix between the material principal coordinate of the k-th layer and the geometric coordinate of the laminated composite conical shell; φ is the angle between these two coordinate directions. The force and moment resultants are given in terms of displacements u, v and w by

$$\begin{Bmatrix} N_x \\ N_\theta \\ N_{x\theta} \\ M_x \\ M_\theta \\ M_{x\theta} \end{Bmatrix} = \begin{bmatrix} c_{11} & c_{12} & c_{13} \\ c_{21} & c_{22} & c_{23} \\ c_{31} & c_{32} & c_{33} \\ c_{41} & c_{42} & c_{43} \\ c_{51} & c_{52} & c_{53} \\ c_{61} & c_{62} & c_{63} \end{bmatrix} \begin{Bmatrix} u \\ v \\ w \end{Bmatrix}, \tag{14}$$

where

$$\begin{gathered}
c_{i1} = A_{i1}\frac{\partial}{\partial x} + A_{i2}\frac{\sin\alpha}{R(x)}, \quad c_{i2} = \frac{A_{i2}}{R(x)}\frac{\partial}{\partial\theta}, \\
c_{i3} = -A_{i2}\frac{\cos\alpha}{R(x)} - B_{1i}\frac{\partial^2}{\partial x^2} - B_{i2}\frac{\sin\alpha}{R(x)}\frac{\partial}{\partial x} - \frac{B_{i2}}{R^2(x)}\frac{\partial^2}{\partial\theta^2}, \\
c_{31} = \frac{A_{66}}{R(x)}\frac{\partial}{\partial\theta}, \quad c_{32} = A_{66}\left(\frac{\partial}{\partial x} - \frac{\sin\alpha}{R(x)}\right), \quad c_{33} = -B_{66}\frac{\partial}{\partial x}\left(\frac{1}{R(x)}\frac{\partial}{\partial\theta}\right) \\
c_{ji} = B_{1i}\frac{\partial}{\partial x} + \frac{B_{i2}\sin\alpha}{R(x)}, \quad c_{j2} = \frac{B_{i2}}{R(x)}\frac{\partial}{\partial\theta}, \\
c_{j3} = -D_{1i}\frac{\partial^2}{\partial x^2} - D_{i2}\frac{\sin\alpha}{R(x)}\frac{\partial}{\partial x} - \frac{D_{i2}}{R^2(x)}\frac{\partial^2}{\partial\theta^2} - B_{i2}\frac{\cos\alpha}{R(x)}, \\
c_{61} = \frac{B_{66}}{R(x)}\frac{\partial}{\partial\theta}, \quad c_{62} = B_{66}\left(\frac{\partial}{\partial x} - \frac{\sin\alpha}{R(x)}\right), \quad c_{63} = -2D_{66}\frac{\partial}{\partial x}\left(\frac{1}{R(x)}\frac{\partial}{\partial\theta}\right).
\end{gathered} \tag{15}$$

Here $i = 1, 2$ and $j = 3 + i$. the tensors A_{ij}, B_{ij} and D_{ij} represent the extensional, coupling and bending stiffnesses and are calculated from the equations

$$(A_{ij}, B_{ij}, D_{ij}) = \int_{-h/2}^{h/2} Q^*_{ij}(1, z, z^2)\, dz. \tag{16}$$

For an arbitrarily laminated composite shell, these stiffnesses can be given as

$$\begin{gathered}
(A_{ij}) = \sum_{k=1}^{N_L} Q^{(k)}_{ij}(h_k - h_{k-1}), \quad (B_{ij}) = \frac{1}{2}\sum_{k=1}^{N_L} Q^{(k)}_{ij}(h_k^2 - h_{k-1}^2), \\
(D_{ij}) = \frac{1}{3}\sum_{k=1}^{N_L} Q^{(k)}_{ij}(h_k^3 - h_{k-1}^3),
\end{gathered} \tag{17}$$

where N_L is the number of total layers of the laminated conical shell, $Q^{(k)}_{ij}$ is the element of the transformed reduced stiffness matrix for the k-th layer, and h_k and h_{k-1} denote distances from the shell reference surface to the outer and inner surfaces of the k-th layer. Substituting Equation (14) into Equations (1)–(3), we obtain the governing equations for the linear free vibration analysis of composite laminated conical shells:

$$L_{11}u + L_{12}v + L_{13}w = \rho h\frac{\partial^2 u}{\partial t^2}, \tag{18a}$$

$$L_{21}u + L_{22}v + L_{23}w = \rho h\frac{\partial^2 v}{\partial t^2}, \tag{18b}$$

$$L_{31}u + L_{32}v + L_{33}w = \rho h\frac{\partial^2 w}{\partial t^2}, \tag{18c}$$

where

$$L_{11} = A_{11}\frac{\partial^2}{\partial x^2} + A_{11}\frac{\sin\alpha}{R(x)}\frac{\partial}{\partial x} - A_{22}\frac{\sin^2\alpha}{R^2(x)} + \frac{A_{66}}{R^2(x)}\frac{\partial^2}{\partial\theta^2}, \tag{19}$$

$$\begin{aligned} L_{12} = {} & \frac{(A_{12}+A_{66})}{R(x)}\frac{\partial^2}{\partial x\partial\theta} - \frac{(A_{22}+A_{66})\sin\alpha}{R^2(x)}\frac{\partial}{\partial\theta} \\ & + \frac{(B_{12}+2B_{66})\cos\alpha}{R^2(x)}\frac{\partial^2}{\partial x\partial\theta} + \frac{(B_{12}+B_{22}+2B_{66})\sin\alpha\cos\alpha}{R(x)}\frac{\partial}{\partial\theta}, \end{aligned} \tag{20}$$

$$\begin{aligned} L_{13} = {} & A_{12}\frac{\cos\alpha}{R(x)}\frac{\partial}{\partial x} - A_{22}\frac{\sin\alpha\cos\alpha}{R^2(x)} - B_{11}\frac{\partial^3}{\partial x^3} - \frac{(B_{12}{+}2B_{66})\cos\alpha}{R^2(x)}\frac{\partial^3}{\partial x\partial\theta^2} \\ & - B_{11}\frac{\sin\alpha}{R(x)}\frac{\partial^2}{\partial x^2} + \frac{(B_{12}+B_{22}+2B_{66})\sin\alpha}{R^2(x)}\frac{\partial^2}{\partial\theta^2} + B_{22}\frac{\sin^2\alpha}{R^2(x)}\frac{\partial}{\partial x}, \end{aligned} \tag{21}$$

$$\begin{aligned} L_{21} = {} & \frac{(A_{12}+A_{66})}{R(x)}\frac{\partial^2}{\partial x\partial\theta} + \frac{(A_{22}+A_{66})\sin\alpha}{R^2(x)}\frac{\partial}{\partial\theta} + \\ & + \frac{(B_{12}+B_{66})\cos\alpha}{R^2(x)}\frac{\partial^2}{\partial x\partial\theta} + \frac{(B_{22}-B_{66})\sin\alpha\cos\alpha}{R^3(x)}\frac{\partial}{\partial\theta}, \end{aligned} \tag{22}$$

$$\begin{aligned} L_{22} = {} & A_{66}\left(\frac{\partial^2}{\partial x^2} + \frac{\sin\alpha}{R(x)}\frac{\partial}{\partial x} - \frac{\sin^2\alpha}{R^2(x)}\right) + \left(\frac{A_{22}}{R^2(x)} + 2B_{22}\frac{\cos\alpha}{R^3(x)} + \frac{D_{22}\cos^2\alpha}{R^4(x)}\right)\frac{\partial^2}{\partial\theta^2} \\ & + 2\frac{D_{66}\cos^2\alpha}{R^2(x)}\left(\frac{\partial^2}{\partial x^2} - \frac{2\sin\alpha}{R(x)}\frac{\partial}{\partial x} + \frac{2\sin^2\alpha}{R^2(x)}\right) \\ & + \frac{B_{66}\cos\alpha}{R(x)}\left(3\frac{\partial^2}{\partial x^2} - \frac{\sin\alpha}{R(x)}\frac{\partial}{\partial x} + \frac{\sin^2\alpha}{R^2(x)}\right), \end{aligned} \tag{23}$$

$$\begin{aligned} L_{23} = {} & \left(\frac{A_{22}\cos\alpha}{R^2(x)} + \frac{B_{22}\cos\alpha}{R^3(x)} - \frac{4D_{66}\cos\alpha\sin^2\alpha}{R^4(x)}\right)\frac{\partial}{\partial\theta} \\ & - \left(\frac{B_{22}}{R^3(x)} + \frac{D_{22}\cos\alpha}{R^4(x)}\right)\frac{\partial^3}{\partial\theta^3} - \left(\frac{B_{22}}{R^2(x)} + \frac{(D_{22}-4D_{66})\sin\alpha\cos\alpha}{R^3(x)}\right)\frac{\partial^2}{\partial x\partial\theta} \\ & - \left(\frac{(B_{12}+2B_{66})}{R(x)} + \frac{(D_{12}+2D_{66})\cos\alpha}{R^2(x)}\right)\frac{\partial^3}{\partial x^2\partial\theta}, \end{aligned} \tag{24}$$

$$\begin{aligned} L_{31} = {} & -A_{12}\frac{\cos\alpha}{R(x)}\frac{\partial}{\partial x} - A_{22}\frac{\sin\alpha\cos\alpha}{R^2(x)} + B_{11}\frac{\partial^3}{\partial x^3} + \frac{(B_{12}+2B_{66})}{R^2(x)}\frac{\partial^3}{\partial x\partial\theta^2} \\ & - \frac{2B_{11}\sin\alpha}{R(x)}\frac{\partial^2}{\partial x^2} + \frac{B_{22}\sin^2\alpha}{R^2(x)}\frac{\partial}{\partial x} + \frac{(B_{22}-2B_{66})\sin\alpha}{R^3(x)}\frac{\partial^2}{\partial\theta^2} + \frac{B_{22}\sin^3\alpha}{R^3(x)}, \end{aligned} \tag{25}$$

$$
\begin{aligned}
L_{32} = {} & -\left(A_{22}\frac{\cos\alpha}{R^2(x)} - \frac{B_{22}\cos^2\alpha - (B_{22}+2B_{66})\sin^2\alpha}{R^3(x)}\right)\frac{\partial}{\partial\theta} \\
& + \left(-\frac{(2D_{12}+2D_{22}+8D_{66})\cos\alpha\sin^2\alpha}{R^4(x)}\right)\frac{\partial}{\partial\theta} + \left(\frac{B_{22}}{R^3(x)} + \frac{D_{22}\cos\alpha}{R^4(x)}\right)\frac{\partial^3}{\partial\theta^3} \\
& + \left(\frac{(B_{12}+2B_{66})}{R(x)} + \frac{(D_{12}+4D_{66})\cos\alpha}{R^2(x)}\right)\frac{\partial^3}{\partial x^2\partial\theta} \\
& + \left(\frac{(B_{22}+2B_{66})\sin\alpha}{R^2(x)} + \frac{(D_{22}+2D_{12}+8D_{66})\sin\alpha\cos\alpha}{R^3(x)}\right)\frac{\partial^2}{\partial x\partial\theta},
\end{aligned}
\tag{26}
$$

$$
\begin{aligned}
L_{33} = {} & -A_{22}\frac{\cos^2\alpha}{R^2(x)} - \frac{2B_{12}\cos\alpha}{R(x)}\frac{\partial^2}{\partial x^2} + \frac{2B_{22}\cos\alpha}{R^3(x)}\frac{\partial^2}{\partial\theta^2} + \frac{B_{22}\cos\alpha\sin^2\alpha}{R^3(x)} \\
& + D_{11}\frac{\partial^4}{\partial x^4} - \frac{2(D_{12}+2D_{66})}{R^2(x)}\frac{\partial^4}{\partial x^2\partial\theta^2} - \frac{D_{22}}{R^4(x)}\frac{\partial^4}{\partial\theta^4} \\
& - \frac{2D_{11}\sin\alpha}{R(x)}\frac{\partial^3}{\partial x^3} + \frac{2(D_{12}+4D_{66})\sin\alpha}{R^3(x)}\frac{\partial^3}{\partial x\partial\theta^2} + \frac{D_{22}\sin^2\alpha}{R^2(x)}\frac{\partial^2}{\partial x^2} \\
& - \frac{2(D_{12}+D_{22}+4D_{66})\sin^2\alpha}{R^4(x)}\frac{\partial^2}{\partial\theta^2} - \frac{D_{22}\sin^3\alpha}{R^3(x)}\frac{\partial}{\partial x}.
\end{aligned}
\tag{27}
$$

The displacement terms are

$$
\begin{gathered}
u = U(x)\cos(n\theta)\cos(\omega t), \qquad v = V(x)\sin(n\theta)\cos(\omega t), \\
w = W(x)\cos(n\theta)\cos(\omega t).
\end{gathered}
\tag{28}
$$

Substituting these equations into (18), we can write the governing equations as

$$
\begin{aligned}
& G_{111}U + G_{112}\frac{\partial U}{\partial x} + G_{113}\frac{\partial^2 U}{\partial x^2} + G_{121}V + G_{122}\frac{\partial V}{\partial x} \\
& \qquad + G_{131}W + G_{132}\frac{\partial W}{\partial x} + G_{133}\frac{\partial^2 W}{\partial x^2} + G_{134}\frac{\partial^3 W}{\partial x^3} = -\rho h\omega^2 U,
\end{aligned}
\tag{29}
$$

$$
\begin{aligned}
& G_{211}U + G_{212}\frac{\partial U}{\partial x} + G_{221}V + G_{222}\frac{\partial V}{\partial x} + G_{223}\frac{\partial^2 V}{\partial x^2} \\
& \qquad + G_{231}W + G_{232}\frac{\partial W}{\partial x} = -\rho h\omega^2 V,
\end{aligned}
\tag{30}
$$

$$
\begin{aligned}
& G_{311}U + G_{312}\frac{\partial U}{\partial x} + G_{313}\frac{\partial^2 U}{\partial x^2} + G_{314}\frac{\partial^3 U}{\partial x^3} + G_{321}V + G_{322}\frac{\partial V}{\partial x} + G_{323}\frac{\partial^2 V}{\partial x^2} \\
& \quad + G_{331}W + G_{332}\frac{\partial W}{\partial x} + G_{333}\frac{\partial^2 W}{\partial x^2} + G_{334}\frac{\partial^3 W}{\partial x^3} + G_{335}\frac{\partial^4 W}{\partial x^4} = -\rho h\omega^2 W,
\end{aligned}
\tag{31}
$$

where G_{ijk} are the related coefficients, found in [Tong 1993b; Shu 1996b]. In this study, the following two type main boundary conditions are considered. These are defined as follows:

Simply supported edge (S):

$$V = 0,\ W = 0,\ N_x = 0,\ M_x = 0 \tag{32a}$$

Clamped edge (C):

$$U = 0,\ V = 0,\ W = 0 \text{ and } \partial W/\partial x = 0 \tag{32b}$$

3. Discrete singular convolution (DSC)

The discrete singular convolution (DSC) algorithm was introduced by Wei [1999]. He and coworkers [Wei 1999; 2001a; 2001b; Wei et al. 2002a; 2002b] first applied the DSC algorithm to solve solid and fluid mechanics problems. Zhao et al. [2002] analyzed the high frequency vibration of plates and plate vibration under irregular internal support using the DSC algorithm. Numerical solution of unsteady incompressible flows using DSC is given in [Wan et al. 2002]. More recently, Lim et al. [2005a; 2005b] presented the DSC–Ritz method for the free vibration analysis of Kirchhoff and Mindlin plates and thick shallow shells.

These studies indicates that the DSC algorithm work very well for the vibration analysis of plates, especially for high-frequency analysis of rectangular plates. It also suggests that the DSC algorithm has the accuracy of global methods and the flexibility of local methods for solving differential equations in applied mechanics. The mathematical foundation of the DSC algorithm is the theory of distributions and wavelet analysis. Consider a distribution T and let $\eta(t)$ be an element of the space of test functions. A singular convolution can be defined by

$$F(t) = (T * \eta)(t) = \int_{-\infty}^{\infty} T(t - x)\eta(x)\, dx, \tag{33}$$

where $T(t - x)$ is a singular kernel. The DSC algorithm can be realized using many approximation kernels. It has been shown that for many problems, the regularized Shannon kernel (RSK) is very efficient. This kernel is given by

$$\delta_{\Delta,\sigma}(x - x_k) = \frac{\sin\big((\pi/\Delta)(x - x_k)\big)}{(\pi/\Delta)(x - x_k)} \exp\left(-\frac{(x - x_k)^2}{2\sigma^2}\right); \quad \sigma > 0 \tag{34}$$

(see [Wei 1999]), where $\Delta = \pi/(N - 1)$ is the grid spacing and N is the number of grid points. The parameter σ determines the width of the Gaussian envelope and often varies in association with the grid spacing, i.e., $\sigma = rh$. Here r is a parameter chosen in computation. It is also known that the truncation error is very small due to the use of the Gaussian regularizer. The formulation in (34) is practical and has an essentially compact support for numerical interpolation. With a sufficiently smooth approximation, it is more effective to consider a discrete singular convolution

$$F_\alpha(t) = \sum_k T_\alpha(t - x_k) f(x_k) \tag{35}$$

where $F_\alpha(t)$ is an approximation to $F(t)$ and $\{x_k\}$ is an appropriate set of discrete points on which the DSC of (33) is well defined. Note that the original test function $\eta(x)$ has been replaced by $f(x)$. This new discrete expression is suitable for computer realization. The mathematical property or requirement of $f(x)$ is determined by the approximate kernel T_α. In the DSC method, the function $f(x)$ and its derivatives with respect to the x coordinate at a grid point x_i are approximated by a linear sum of discrete values $f(x_k)$ in a narrow bandwidth $[x-x_M,\ x+x_M]$. This can be expressed as

$$\left.\frac{d^n f(x)}{dx^n}\right|_{x=x_i} = f^{(n)}(x) \approx \sum_{k=-M}^{M} \delta_{\Delta,\sigma}^{(n)}(x_i - x_k) f(x_k); \quad (n = 0, 1, 2, \ldots), \tag{36}$$

where superscript n denotes the n-th derivative with respect to x. The x_k is a set of discrete sampling points centred around the point x, σ is a regularization parameter, Δ is the grid spacing, and $2M+1$ is the computational bandwidth, which is usually smaller than the size of the computational domain. The higher-order derivative terms $\delta_{\Delta,\sigma}^{(n)}(x - x_k)$ in (34) are given by

$$\delta_{\Delta,\sigma}^{(n)}(x - x_k) = \left(\frac{d}{dx}\right)^n \left[\delta_{\Delta,\sigma}(x - x_k)\right], \tag{37}$$

where the differentiation can be carried out analytically. For example, the second derivative at $x = x_i$ of the DSC kernel is

$$\delta_{\Delta,\sigma}^{(2)}(x - x_j) = \left.\frac{d^2}{dx^2}\left[\delta_{\Delta,\sigma}(x - x_j)\right]\right|_{x=x_i} \tag{38}$$

The discretized form of (6) can then be expressed as

$$f^{(2)}(x) = \left.\frac{d^2 f}{dx^2}\right|_{x=x_i} \approx \sum_{k=-M}^{M} \delta_{\Delta,\sigma}^{(2)}(k\Delta x_N) f_{i+k,j} \tag{39}$$

When the regularized Shannon's delta kernel (RSDK) is used, the detailed expressions for $\delta_{\Delta,\sigma}(x)$, $\delta_{\Delta,\sigma}^{(1)}(x)$, $\delta_{\Delta,\sigma}^{(2)}(x)$, $\delta_{\Delta,\sigma}^{(3)}(x)$ and $\delta_{\Delta,\sigma}^{(4)}(x)$ can be easily obtained for $x \neq x_k$; they are listed in the Appendix. Note that the differentiation matrix in (39) is in general banded. This is a great advantage in large scale computations. Consider a one dimensional, n-th order DSC kernel of delta type:

$$\delta_{\sigma,\Delta}^{(n)}(x - x_k), \quad n = 0, 1, 2, \ldots. \tag{40}$$

Here $\delta^{(0)}_{\sigma,\Delta}(x-x_k)=\delta_{\sigma,\Delta}(x-x_k)$ is the DSC kernel of (36). These derivatives can be regarded as high pass filters. The filters corresponding to the derivatives of Shannon's kernel decay slowly as x increases, whereas the regularized filters are Schwarz class functions and have controlled residual amplitudes at large x values. In the Fourier representation, the derivatives of Shannon's kernel are discontinuous at certain points. In contrast, the derivatives of regularized kernels are all continuous and can be made very close to those of Shannon's if desired. The differential part of the operator on the coordinate grid is then represented by functional derivatives

$$D=\sum_{n=1} d_n(x)\frac{d^n}{dx^n}\to\sum_{n=1} d_n(x_m)\delta^{(n)}_{\alpha,\sigma}(x_m-x_k) \tag{41}$$

(see [Wei et al. 2002a]), where $d_n(x)$ is a coefficient and $\delta^{(n)}_{\alpha,\sigma}(x_m-x_k)$ is analytically given by

$$\delta^{(n)}_{\alpha,\sigma}(x_m-x_k)=\left(\frac{d}{dx}\right)^n \delta_{\alpha,\sigma}(x_m-x_k)\bigg|_{x=x_m}. \tag{42}$$

Therefore, the discretized forms of Equations (29)–(31) can be expressed as

$$\begin{aligned}G_{111}U_{i,j}&+G_{112}\sum_{k=-M}^{M}\delta^{(1)}_{\Delta,\sigma}(k\Delta x)U_{i+k,j}+G_{113}\sum_{k=-M}^{M}\delta^{(2)}_{\Delta,\sigma}(k\Delta x)U_{i+k,j}\\&+G_{121}V_{i,j}+G_{122}\sum_{k=-M}^{M}\delta^{(1)}_{\Delta,\sigma}(k\Delta x)V_{i,j+k}\\&+G_{131}W_{i,j}+G_{132}\sum_{k=-M}^{M}\delta^{(1)}_{\Delta,\sigma}(k\Delta x)W_{i,j+k}=-\rho h\omega^2U_{i,j},\end{aligned} \tag{43a}$$

$$\begin{aligned}G_{211}U_{i,j}&+G_{212}\sum_{k=-M}^{M}\delta^{(1)}_{\Delta,\sigma}(k\Delta x)U_{i+k,j}\\&+G_{221}V_{i,j}+G_{122}\sum_{k=-M}^{M}\delta^{(1)}_{\Delta,\sigma}(k\Delta x)V_{i,j+k}+G_{223}\sum_{k=-M}^{M}\delta^{(2)}_{\Delta,\sigma}(k\Delta x)V_{i+k,j}\\&+G_{231}W_{i,j}+G_{232}\sum_{k=-M}^{M}\delta^{(1)}_{\Delta,\sigma}(k\Delta x)W_{i,j+k}+G_{233}\sum_{k=-M}^{M}\delta^{(2)}_{\Delta,\sigma}(k\Delta x)W_{i+k,j}\\&=-\rho h\omega^2V_{i,j},\end{aligned} \tag{43b}$$

$$G_{311}U_{i,j} + G_{312}\sum_{k=-M}^{M}\delta^{(1)}_{\Delta,\sigma}(k\Delta x)U_{i+k,j}$$
$$+ G_{321}V_{i,j} + G_{322}\sum_{k=-M}^{M}\delta^{(1)}_{\Delta,\sigma}(k\Delta x)V_{i,j+k} + G_{323}\sum_{k=-M}^{M}\delta^{(2)}_{\Delta,\sigma}(k\Delta x)V_{i+k,j}$$
$$+ G_{331}W_{i,j} + G_{332}\sum_{k=-M}^{M}\delta^{(1)}_{\Delta,\sigma}(k\Delta x)W_{i,j+k} + G_{333}\sum_{k=-M}^{M}\delta^{(2)}_{\Delta,\sigma}(k\Delta x)W_{i+k,j}$$
$$+ G_{334}\sum_{k=-M}^{M}\delta^{(3)}_{\Delta,\sigma}(k\Delta x)W_{i+k,j} + G_{335}\sum_{k=-M}^{M}\delta^{(4)}_{\Delta,\sigma}(k\Delta x)W_{i+k,j}$$
$$= -\rho h\omega^2 W_{i,j}, \quad \text{(43c)}$$

where the $\delta^{(n)}_{\alpha,\sigma}$ are the coefficients of the regularized Shannon kernel, listed in the Appendix. Thus, the governing equations are spatialy discretized by using the DSC algorithm. The DSC form of the boundary conditions can be easily written. For the clamped edge, for example, given as

$$U_{i,j} = 0,\ \ V_{i,j} = 0,\ \ W_{i,j} = 0 \quad \text{and} \quad \sum_{k=-M}^{M}\delta^{(1)}_{\Delta,\sigma}(k\Delta x)W_{i+k,j} = 0. \qquad (44)$$

Wei et al. [2002a] proposed a practical method to treatment of the boundary conditions for DSC. Zhao and Wei [2002] proposed a practical method to incorporate the boundary conditions. More recently, the iteratively matched boundary method has been applied [Zhao et al. 2005; Zhou et al. 2006] to impose the free boundary condiitions for the solid mechanic problem.

By the DSC rule, the governing equations and the corresponding boundary condions can be replaced by a system of simultaneously linear algebraic equations in terms of the displacements at all the sampling points. It is noted that for a well-posed problem the number of equations should be identical to the the number of unknowns. A treatment commonly used in the literature [Shu 1996b; Wu and Wu 2000; Civalek 2004] is applied in this study. The first two governing equations in (43) are applied at interior points ($k = 2, 3, \cdots, M-1$) and third governing equation is applied at the interior points ($k = 3, 4, \cdots, M-2$). By rearranging the DSC form of the governing equations, one has the assembled form of the resulting equations as

$$\big[[G_{dd}]\ \ [G_{db}]\big]\begin{Bmatrix}\{U_d\}\\ \{U_b\}\end{Bmatrix} - \Omega\big[[B_{dd}]\ \ [B_{db}]\big]\begin{Bmatrix}\{U_d\}\\ \{U_b\}\end{Bmatrix}\{0\} \qquad (45)$$

where $\{U_b\}$ represents the unknown boundary grid points values, whereas $\{U_d\}$ represent the domain grid point unknowns. The subscript b represents the degree of freedom on the boundary and subscript d represents the degree of freedom on the domain. Substitung the DSC rule into the boundary conditions at the sampling points at two boundary points leads to

$$\begin{bmatrix}[G_{bd}] & [G_{bb}]\end{bmatrix}\begin{Bmatrix}\{U_d\}\\ \{U_b\}\end{Bmatrix} = \{0\} \tag{46}$$

After rewriting this as $U_b = -G_{bb}^{-1}G_{bd}U_d$ and then substituting the resulting equation into (45), we obtain

$$GU = \Omega BU \tag{47}$$

where $G = G_{dd} - G_{db}G_{bb}^{-1}G_{bd}$, $B = B_{dd} - B_{db}G_{bb}^{-1}G_{bd}$, and U is the displacement vector on the domain. In the above eigenvalue equation, Ω is the nondimensional frequency parameter. In (47), G and B are the matrices derived from the governing equations described by (43) and the boundary conditions considered in (44).

4. Numerical applications

This section presents some numerical results for the free vibration analysis of laminated conical shells. The utility and robustness of the proposed method is illustrated by a number of numerical examples in this section. In order to simplify the presentation, S and C represent simply supported, and clamped supports, respectively. Firstly, the convergence of DSC results is studied. To check whether the purposed formulation and programming are correct, an isotropic conical shell is analysed first. The numerical results are given by the dimensionless frequency parameter Ω, defined by

$$\Omega = R_2\sqrt{\frac{\rho h}{A_{11}}}\omega$$

where ω is referred to as the frequency parameter. The obtained results by DSC are listed in Table 1. This table shows the convergence of computed frequency parameters Ω for an isotropic conical shell with $\theta = 60°$, $L\sin\theta/R_2 = 0.75$ and circumferential wave number $n = 0$. The table also shows results given in [Irie et al. 1984; Tong 1993a; Shu 1996a]. To examine the influence of bandwidth on the accuracy, we choose five values of N (8, 11, 16, 21, 32), with corresponding regularization parameters $\sigma/\Delta = 1.73$, 2.15, 2.46, 2.8 and 3.2, and set $M = N$ with r optimally selected. From Table 1, it is seen that the convergence of DSC results is very good. In comparison with the results in [Irie et al. 1984], DSC results using 16 uniform grid points are very accurate. When the number of grid points is larger than 16, the DSC results are grid-independent. The fundamental frequency param-

	$L\sin\alpha/R_2 = 0.25$				
	$\alpha = 15^\circ$	$\alpha = 30^\circ$	$\alpha = 45^\circ$	$\alpha = 60^\circ$	$\alpha = 75^\circ$
$N = 8$	0.8983	0.9058	0.8204	0.7704	0.6629
$N = 11$	0.8355	0.8901	0.8151	0.7556	0.6447
$N = 16$	0.7851	0.8935	0.8043	0.7357	0.6228
$N = 21$	0.7856	0.8941	0.8047	0.7361	0.6234
$N = 32$	0.7856	0.8941	0.8047	0.7361	0.6234
[Irie et al. 1984]	—	0.8938	0.8041	0.7353	—
[Tong 1993b]	—	0.8938	0.8041	0.7353	—
[Shu and Du 1997]	—	—	—	0.7366	—

Table 1. Frequency parameters of C-S conical shells; $\nu = 0.3$, $h/R_2 = 0.01$, $n = 0$.

eters Ω for an antisymmetric cross-ply laminated circular cylindrical shell with the S-C boundary condition are shown in Table 2. This table shows the fundamental frequency parameters based on classical shell theory (CST) [Shu and Du 1997] and the present DSC formulation. The results in Wu and Lee [2001], obtianed using the differential quadrature method (DQM), are also listed for comparison. Note that

h/R	L/R	Present DST results		CST [Shu and Du 1997]		DQM [Wu and Lee 2001] for $N = 11$	
		max.cplg $N_L = 2$	no cplg $N_L = \infty$	max.cplg $N_L = 2$	no cplg $N_L = \infty$	max.cplg $N_L = 2$	no cplg $N_L = \infty$
0.01	1	0.6585	0.7729	0.6440	0.8044	0.6725	0.8003
	2	0.3802	0.4463	0.3750	0.4545	0.3742	0.4534
	5	0.1849	0.2186	0.1858	0.2193	0.1852	0.2187
	10	0.1014	0.1195	0.1030	0.1223	0.1027	0.1217
	20	0.0477	0.0628	0.0496	0.0641	0.0494	0.0639
0.05	1	1.1406	1.4803	1.3201	1.8327	1.2820	1.6531
	2	0.6228	0.7474	0.6518	0.8146	0.6432	0.7975
	5	0.2785	0.3502	0.2886	0.3615	0.2876	0.3562
	10	0.1663	0.1956	0.1745	0.2021	0.1733	0.2015
	20	0.0771	0.0787	0.0875	0.0886	0.0870	0.0881

Table 2. Fundamental frequency parameters of an antisymmetric cross-ply laminated circular cylindrical shell with the S-C boundary condition ($\nu = 0.3$, $h/R_2 = 0.01$).

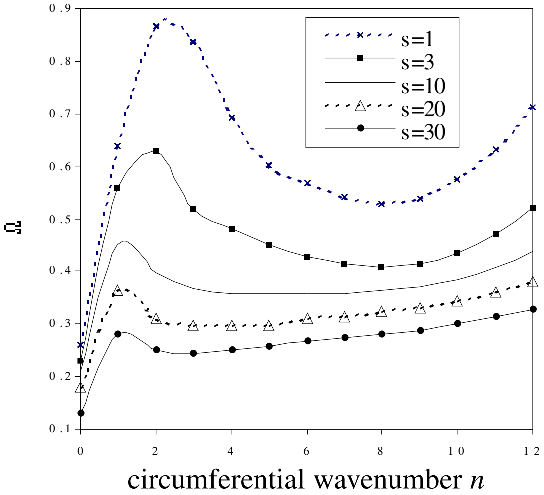

Figure 2. Effect of $s = E_x/E_\theta$ ratio on frequency with the S-S boundary condition for cone angle 15° ($L \sin\alpha/R_2 = 0.25$; $h/R_2 = 0.01$.)

$N = 11$ is sufficient to obtain accurate results. The present numerical solutions are in close agreement with the DQM and CST solutions available in the literature. We also see from Table 2 that the results of two layers ($N_L = 2$) are always less than that of infinite layers ($N_L = \infty$). This suggests that the fundamental frequency parameters decrease as the coupling rigidity terms increase.

Figure 2 shows the frequency parameters of clamped and simply supported orthotropic conical shells for $\mu_{x\phi} = 0.3$, $s = E_x/E_\theta$, $E_x = 2.1 \times 10^6$ and $G_{x\theta} = 807692$. The effects of the ratio s on the values of Ω for $\alpha = 15°$ are displayed. Note that the values of Ω decrease when the ratio s increases. The variation is marginal for larger values of s, irrespective of cone angles. In general, Ω increases considerably with circumferential wave number for larger values of s ($s > 10$).

To examine the influence of h/R_2 on the frequency characteristics for S-S boundary conditions, we plot in Figure 3 the dependence for three different cone angles α (30°, 45°, 60°). With the increase of ratio h/R_2, the frequency parameter Ω increases rapidly. Generally, decreasing the cone angle also decreases the frequency parameter Ω.

Figure 4 shows the effect of h/R_2 on the frequency, and suggests that the frequency parameter increases uniformly with the ratio h/R_2. The C-C conical shell has the highest frequency parameter, followed by C-S and S-C. The S-S conical shell has the lowest frequency parameter.

For the ratio $L/R_2 = 0.5$, Figure 5 highlights the influence of the geometric ratio h/R_2 on the frequency parameter Ω, for four different cone angles α. We see

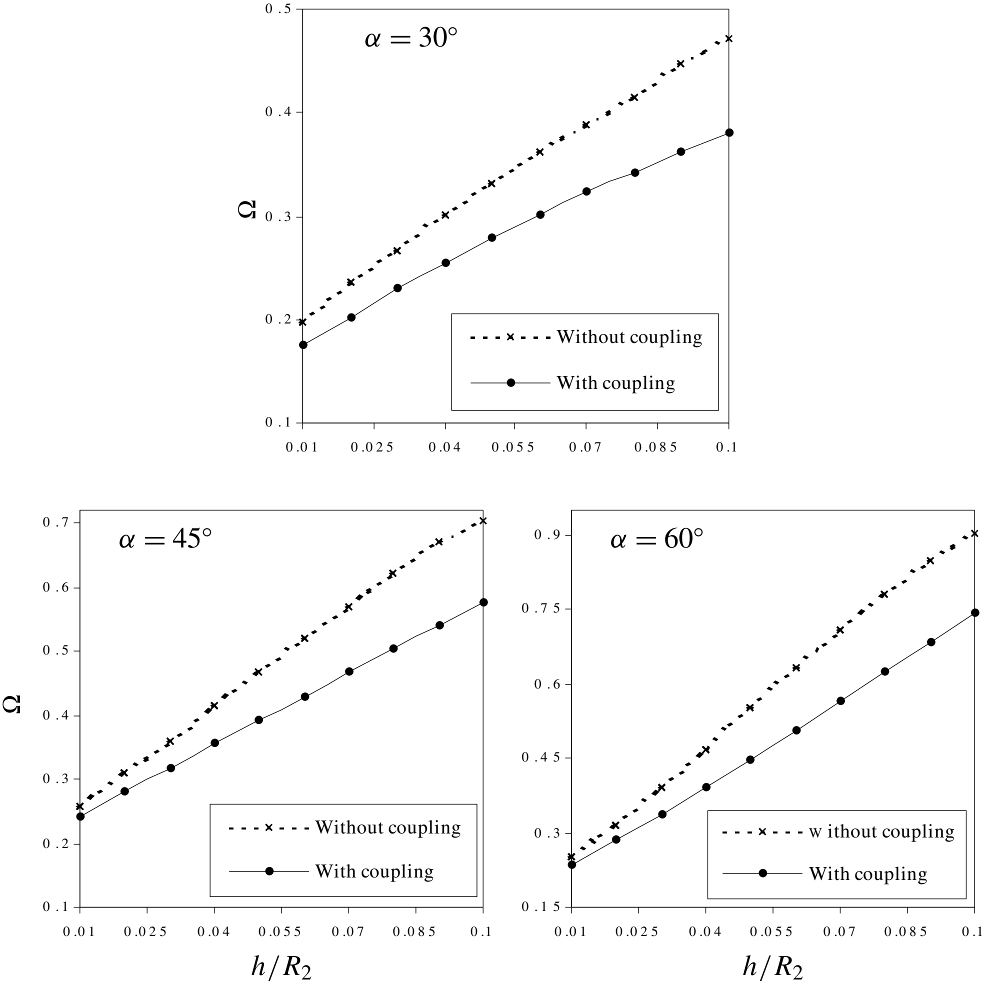

Figure 3. Variation of frequency Ω with geometric ratio h/R_2 for S-S conical shell, for various values of α.

that this influence is significant, that increasing α always increases Ω, and that the influence of the boundary condition on Ω with h/R_2 is significant.

Figure 6 shows the frequency parameters of (0/90/0) laminated conical shells with S-S boundary conditions for the ratio $L/R_1 = 5$. The layer material properties are $\nu_{12} = 0.25$, $\nu_{22} = 0.25$, $E_{11}/E_{22} = 25$, $G_{12}/E_{22} = 0.5$, $G_{22}/E_{22} = 0.2$. These figures show the effects of the ratio h/R_1 on the values of Ω for two types of cone angles, $\alpha = 30°$ and $\alpha = 60°$. The variation is only marginal for larger values of n, irrespective of cone angles. For the cases under consideration, axisymmetric frequencies ($n = 0$) are not the lowest frequencies. The lowest frequencies occur for a higher value of n.

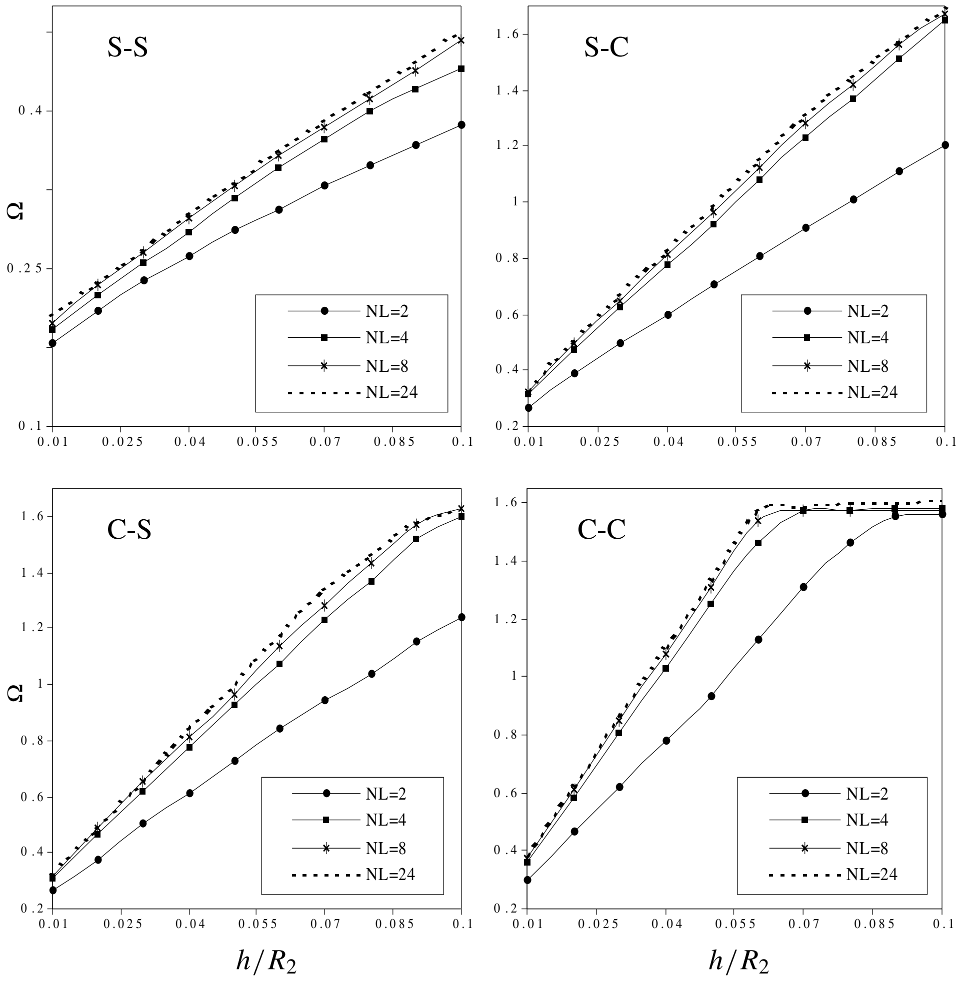

Figure 4. Variation of frequency Ω with geometric ratio h/R_2 for various conical shells ($\alpha = 30°$, $L \sin\alpha/R_2 = 0.25$).

5. Conclusions

In conjunction with the method of DSC, the free vibration of orthotropic laminated conical shells is presented. Convergence tests are performed to validate the proposed approach for handling various combinations of two types of boundary conditions. A number of numerical examples are considered to explore the usefulness and test the accuracy of the present method. Accurate solutions have been presented for the frequencies of orthotropic laminated conical shells. The cone angle α and the $L \sin\alpha/R_2$ ratio has been found to have significant influence on the frequency parameters of the conical shell. The approach has been validated by convergence studies and comparisons with existing results in the literature.

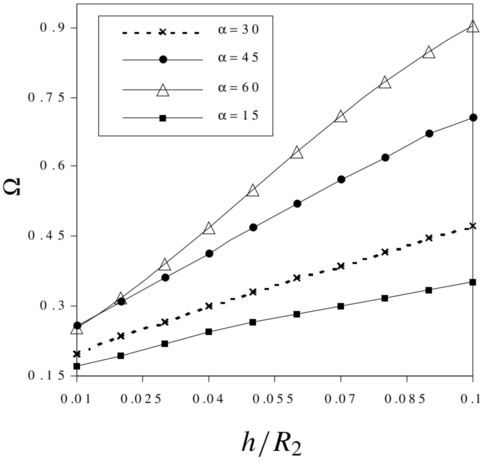

Figure 5. Variation of frequency Ω with geometric ratio h/R_2 for various cone angles of S-S conical shell ($L/R_2 = 0.5$; $h/R_2 = 0.01$; $\nu = 0.3$).

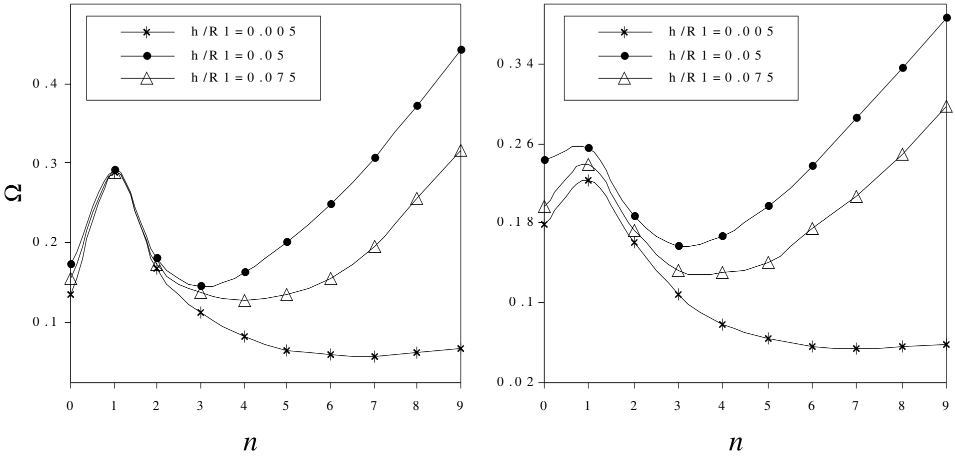

Figure 6. Variation of frequency Ω with value of n for 0/90/0 laminated conical shells with S-S boundary conditions ($L/R_1 = 5$). Left: $\alpha = 30°$. Right: $\alpha = 60°$.

Appendix: The derivatives $\delta^{(n)}_{\Delta,\sigma}$

Here are the first four derivatives of the function $\delta_{\Delta,\sigma}(x)$, needed in Equations (43). For brevity, we set $\xi := x - x_k$, $s = \sin(\pi/\Delta)$, $c = \cos(\pi/\Delta)$.

$$\delta^{(1)}_{\pi/\Delta,\sigma}(x_m - x_k) = e^{-\xi^2/2\sigma^2}\left(c - \frac{\Delta}{\pi}s\left(\frac{1}{\xi} + \frac{\xi}{\sigma^2}\right)\right),$$

$$\delta^{(2)}_{\pi/\Delta,\sigma}(x_m - x_k) = e^{-\xi^2/2\sigma^2}\left(-\frac{\pi}{\Delta}s - \left(\frac{2}{\xi} + \frac{2\xi}{\sigma^2}\right)c + \frac{\Delta}{\pi}\left(\frac{2}{\xi^2} + \frac{1}{\sigma^2} + \frac{\xi^2}{\sigma^4}\right)s\right),$$

$$\begin{aligned}\delta^{(3)}_{\pi/\Delta,\sigma}(x_m - x_k) = e^{-\xi^2/2\sigma^2}\biggl(&-\frac{\pi^2}{\Delta^2}c + \frac{\pi}{\Delta}\left(\frac{3}{\xi} + \frac{3\xi}{\sigma^2}\right)s + \left(\frac{6}{\xi^2} + \frac{3}{\sigma^2} + \frac{3\xi^2}{\sigma^4}\right)c\\ &- \frac{\Delta}{\pi}\left(\frac{6}{\xi^3} + \frac{3}{\xi\sigma^2} + \frac{\xi^3}{\sigma^4}\right)s\biggr),\end{aligned}$$

$$\begin{aligned}\delta^{(4)}_{\pi/\Delta,\sigma}(x_m - x_k) = e^{-\xi^2/2\sigma^2}\biggl(&\frac{\pi^3}{\Delta^3}s + \frac{\pi^2}{\Delta^2}\left(\frac{4}{\xi} + \frac{4\xi}{\sigma^2}\right)c - \frac{\pi}{\Delta}\left(\frac{12}{\xi^2} + \frac{6}{\sigma^2} + \frac{6\xi^2}{\sigma^4}\right)s\\ &-\left(\frac{24}{\xi^3} + \frac{12}{\xi\sigma^2} + \frac{4\xi^3}{\sigma^6}\right)c + \frac{\Delta}{\pi}\left(\frac{24}{\xi^4} + \frac{12}{\xi^2\sigma^2} + \frac{3}{\sigma^4} - \frac{2\xi^2}{\sigma^6} + \frac{\xi^4}{\sigma^8}\right)s\biggr).\end{aligned}$$

Acknowledgements

The financial support of the Scientific Research Projects Unit of Akdeniz University is gratefully acknowledged.

References

[Bacon and Bert 1967] M. Bacon and C. W. Bert, "Unsymmetric free vibrations of orthotropic sandwich shells of revolution", *AIAA J.* **5**:3 (1967), 413–417.

[Chang 1981] C. H. Chang, "Vibration of conical shells", *Shock Vib. Dig.* **13**:1 (1981), 9–17.

[Civalek 1998] Ö. Civalek, "Finite-element analyses of plates and shells", Fırat University, Elazığ, 1998. In Turkish.

[Civalek 2004] Ö. Civalek, *Geometrically non-linear static and dynamic analysis of plates and shells resting on elastic foundation by the method of polynomial differential quadrature (PDQ)*, Ph.D. thesis, Fırat University, Elazığ, 2004. In Turkish.

[Civalek 2005] Ö. Civalek, "Geometrically nonlinear dynamic analysis of doubly curved isotropic shells resting on elastic foundation by a combination of HDQ–FD methods", *Int. J. Pressure Vessels Piping* **82**:6 (2005), 470–479.

[Civalek and Ülker 2005] Ö. Civalek and M. Ülker, "HDQ–FD integrated methodology for nonlinear static and dynamic response of doubly curved shallow shells", *Int. J. Struct. Engin. Mech.* **19**:5 (2005), 535–550.

[Hua 2000] L. Hua, "Frequency characteristics of a rotating truncated circular layered conical shell", *Compos. Struct.* **50**:1 (2000), 59–68.

[Hua and Lam 2000] L. Hua and K. Y. Lam, "The generalized differential quadrature method for frequency analysis of a rotating conical shell with initial pressure", *Int. J. Numer. Meth. Eng.* **48**:12 (2000), 1703–1722.

[Irie et al. 1982] T. Irie, G. Yamada, and Y. Kaneko, "Free vibration of a conical shell with variable thickness", *J. Sound Vib.* **82**:1 (1982), 83–94.

[Irie et al. 1984] T. Irie, G. Yamada, and K. Tanaka, "Natural frequencies of truncated conical shells", *J. Sound Vib.* **92**:3 (1984), 447–453.

[Kapania 1989] R. K. Kapania, "A review on the analysis of laminated shells", *J. Pressure Vessel Technol. (ASME)* **111** (1989), 88–96.

[Lam and Hua 1997] K. Y. Lam and L. Hua, "Vibration analysis of a rotating truncated circular conical shell", *Int. J. Solids Struct.* **34**:17 (1997), 2183–2197.

[Leissa 1973] A. W. Leissa, "Vibration of shells", NASA, 1973.

[Liew and Lim 1994] K. M. Liew and C. W. Lim, "Vibratory characteristics of cantilevered rectangular shallow shells of variable thickness", *AIAA J.* **32**:2 (1994), 387–396.

[Liew et al. 1995] K. M. Liew, M. K. Lim, C. W. Lim, D. B. Li, and Y. R. Zhang, "Effects of initial twist and thickness variation on the vibration behaviour of shallow conical shells", *J. Sound Vib.* **180**:2 (1995), 271–296.

[Liew et al. 2005] K. M. Liew, T. Y. Ng, and X. Zhao, "Free vibration analysis of conical shells via the element-free kp-Ritz method", *J. Sound Vib.* **281**:3–5 (2005), 627–645.

[Lim and Kitipornchai 1999] C. W. Lim and S. Kitipornchai, "Effects of subtended and vertex angles on the free vibration of open conical shell panels: a conical co-ordinate approach", *J. Sound Vib.* **219**:5 (1999), 813–835.

[Lim and Liew 1995] C. W. Lim and K. M. Liew, "Vibratory behaviour of shallow conical shells by a global Ritz formulation", *Eng. Struct.* **17**:1 (1995), 63–70.

[Lim et al. 1997] C. W. Lim, K. M. Liew, and S. Kitipornchai, "Free vibration of pretwisted, cantilevered composite shallow conical shells", *AIAA J.* **35**:2 (1997), 327–333.

[Lim et al. 1998] C. W. Lim, K. M. Liew, and S. Kitipornchai, "Vibration of cantilevered laminated composite shallow conical shells", *Int. J. Solids Struct.* **35**:15 (1998), 1695–1707.

[Lim et al. 2005a] C. W. Lim, Z. R. Li, and G. W. Wei, "DSC–Ritz method for high-mode frequency analysis of thick shallow shells", *Int. J. Numer. Meth. Eng.* **62**:2 (2005), 205–232.

[Lim et al. 2005b] C. W. Lim, Z. R. Li, Y. Xiang, G. W. Wei, and C. Wang, "On the missing modes when using the exact frequency relationship between Kirchhoff and Mindlin plates", *Adv. Vib. Eng.* **4** (2005), 221–248.

[Love 1888] A. E. H. Love, "On the small free vibrations and deformations of thin elastic shells", *Philos. T. Roy. Soc. A* **179A** (1888), 491–546.

[Shu 1996a] C. Shu, "An efficient approach for free vibration analysis of conical shells", *Int. J. Mech. Sci.* **38**:8–9 (1996), 935–949.

[Shu 1996b] C. Shu, "Free vibration analysis of composite laminated conical shells by generalized differential quadrature", *J. Sound Vib.* **194**:4 (1996), 587–604.

[Shu and Du 1997] C. Shu and H. Du, "Free vibration analysis of laminated composite cylindrical shells by DQM", *Compos. B: Eng.* **28**:3 (1997), 267–274.

[Siu and Bert 1970] C. C. Siu and C. W. Bert, "Free vibrational analysis of sandwich conical shells with free edges", *J. Acoust. Soc. Am.* **47**:3B (1970), 943–945.

[Sivadas and Ganesan 1992] K. R. Sivadas and N. Ganesan, "Vibration analysis of thick composite clamped conical shells of varying thickness", *J. Sound Vib.* **152**:1 (1992), 27–37.

[Soedel 1996] W. Soedel, *Vibrations of shells and plates*, 2nd ed., Marcel Dekker, New York, 1996.

[Tong 1993a] L. Tong, "Free vibration of composite laminated conical shells", *Int. J. Mech. Sci.* **35**:1 (1993), 47–61.

[Tong 1993b] L. Tong, "Free vibration of orthotropic conical shells", *Int. J. Eng. Sci.* **31**:5 (1993), 719–733.

[Tong and Wang 1992] L. Tong and T. K. Wang, "Simple solutions for buckling of laminated conical shells", *Int. J. Mech. Sci.* **34**:2 (1992), 93–111.

[Wan et al. 2002] D. C. Wan, Y. C. Zhou, and G. W. Wei, "Numerical solution of incompressible flows by discrete singular convolution", *Int. J. Numer. Meth. Fl.* **38**:8 (2002), 789–810.

[Wei 1999] G. W. Wei, "Discrete singular convolution for the solution of the Fokker–Planck equation", *J. Chem. Phys.* **110**:18 (1999), 8930–8942.

[Wei 2001a] G. W. Wei, "A new algorithm for solving some mechanical problems", *Comput. Methods Appl. Mech. Eng.* **190**:15–17 (2001), 2017–2030.

[Wei 2001b] G. W. Wei, "Vibration analysis by discrete singular convolution", *J. Sound Vib.* **244**:3 (2001), 535–553.

[Wei et al. 2002a] G. W. Wei, Y. B. Zhao, and Y. Xiang, "Discrete singular convolution and its application to the analysis of plates with internal supports. Part 1: Theory and algorithm", *Int. J. Numer. Meth. Eng.* **55**:8 (2002), 913–946.

[Wei et al. 2002b] G. W. Wei, Y. B. Zhao, and Y. Xiang, "A novel approach for the analysis of high-frequency vibrations", *J. Sound Vib.* **257**:2 (2002), 207–246.

[Wu and Lee 2001] C. P. Wu and C. Y. Lee, "Differential quadrature solution for the free vibration analysis of laminated conical shells with variable stiffness", *Int. J. Mech. Sci.* **43**:8 (2001), 1853–1869.

[Wu and Wu 2000] C. P. Wu and C. H. Wu, "Asymptotic differential quadrature solutions for the free vibration of laminated conical shells", *Comput. Mech.* **25**:4 (2000), 346–357.

[Yang 1974] C. C. Yang, "On vibrations of orthotropic conical shells", *J. Sound Vib.* **34** (1974), 552–555.

[Zhao and Wei 2002] Y. B. Zhao and G. W. Wei, "DSC analysis of rectangular plates with non-uniform boundary conditions", *J. Sound Vib.* **255**:2 (2002), 203–228.

[Zhao et al. 2002] Y. B. Zhao, G. W. Wei, and Y. Xiang, "Discrete singular convolution for the prediction of high frequency vibration of plates", *Int. J. Solids Struct.* **39**:1 (2002), 65–88.

[Zhao et al. 2005] S. Zhao, G. W. Wei, and Y. Xiang, "DSC analysis of free-edged beams by an iteratively matched boundary method", *J. Sound Vib.* **284**:1–2 (2005), 487–493.

[Zhou et al. 2006] Y. C. Zhou, S. Zhao, M. Feig, and G. W. Wei, "High order matched interface and boundary method for elliptic equations with discontinuous coefficients and singular sources", *J. Comput. Phys.* **213**:1 (2006), 1–30.

Received 29 Sep 2005. Revised 28 Nov 2005.

ÖMER CIVALEK: `civalek@yahoo.com`
Akdeniz Üniversitesi, Mühendislik Fakültesi, İnşaat Mühendisliği Bölümü, 07200 Antalya, Turkiye

JOURNAL OF MECHANICS OF MATERIALS AND STRUCTURES
Vol. 1, No. 1, 2006

YIELD FUNCTIONS AND PLASTIC POTENTIALS FOR BCC METALS AND POSSIBLY OTHER MATERIALS

RICHARD M. CHRISTENSEN

Yield functions and plastic potentials are expressed in terms of the invariants of the stress tensor for polycrystalline metals and other isotropic materials. The plastic volume change data of Richmond is used to evaluate the embedded materials properties for some bcc metals and one polymer. A general form for the plastic potential is found that is intended to represent and cover a wide range of materials types.

1. Introduction

The present work is concerned with the yield functions describing the departure from ideal, linear elastic conditions, and with the plastic potentials which are used to describe the ensuing plastic flow which occurs after the yield functions have been traversed. The definitive theoretical work in this area was formalized by Hill in his early and insightful book [1950] and his many later contributions such as [Hill 1959; 1968a; 1968b; Hill and Rice 1972]. The definitive experimental work was given by Richmond and colleagues (to be cited later), based mainly upon body centered cubic (bcc) metals. The present work follows the lead of these two valuable sources. In the intervening time, most efforts to use yield functions and plastic potentials have proceeded by taking whatever forms were expedient for the particular application of immediate interest. A main objective here is to deduce general representations for yield functions and plastic potentials that have a minimum number of embedded parameters (properties) in order to have the most reasonably useful forms for application to a wide range of full density materials. The resulting forms will be evaluated for various materials types. We begin with the consideration of very ductile metals.

Face centered cubic (fcc) metals provide the backbone of ideal elastic-plastic behavior. Such metals as copper, nickel, aluminum, silver, gold and lead constitute the basis for ideal plastic flow, whether that flow be described at the dislocation level or the continuum level using so-called J_2 plasticity theory. The first significant evidence for the nonideal behavior not adequately described by J_2 theory is the class of bcc metals: chromium, molybdenum, tantalum, tungsten, vanadium, iron

---

Keywords: yield functions, plastic potentials, BCC Metals.

and most steels. These bcc metals provide the perfect test bed for studying the inception of nonideal plastic effects, with the ultimate aim of generalizing beyond this class to much broader classes of materials such as polymers and ceramics.

The present work is at the macroscopic level, but it is helpful to rationalize controlling effects at a more basic level. There are at least two possible sources for the departure of most bcc metals from the ideal behavior exhibited by most fcc metals. One is the far-from-ideal form of grain boundaries on the atomic scale. This state of disorder quite naturally implies a state of nonuniformity and heterogeneity in the strength properties of grain boundaries. The other possible source of nonideal behavior for bcc metals is the fact that the core structure of dislocations spreads over many atomic layers of glide planes [Hirsch 1960; Christian 1983; Vitek 1975]. This fact greatly decreases the mobility of the dislocations, and results in a greater sensitivity to temperature (and pressure) dependent behavior. Other explanations are certainly possible for the nonideal behavior of bcc metals; dislocation dynamics studies related to these matters are rapidly evolving and likely will ultimately provide new insights. Until that time, however, only the two sources just mentioned will be further considered here.

The nonuniformity of strength of grain boundaries in fcc materials is of little importance because the great mobility of the dislocation structures implies that the loads on the grain boundaries are insufficient to cause any disruption of the grain boundary. However, in bcc metals the grain boundaries are much more highly stressed than in fcc metals. Our interest here is with initially isotropic materials, so only polycrystalline aggregates of bcc crystals will be considered. The actual behavior on the grain scale involves variability from grain to grain, and progressive and accumulating degrees of irreversible damage. Because of this variability, the slip on the grain boundaries and the slip systems within the grains may coordinate and interact in some grains. A macroscopic description is necessarily an average over all grains. Probably the grain boundary behavior is much more variable than that of the grain-to-grain form.

The grain failure itself and the grain boundary failure are not necessarily independent and competing physical events. They can be interactive with the grain boundaries, operating to some extent as slip systems in conjunction with those within the crystal. In the macroscopic view, sufficiently general descriptors must be used to cover these possibilities. Even if only shear stresses are needed for the individual crystals, both shear and normal stresses are needed for the grain boundary failure. Macroscopically this then requires both shear and normal stresses.

The behavior of the polycrystalline aggregate thus depends not only upon the shear stress on the slip planes in the individual grains, but also upon normal stresses acting within the grains and upon the grain boundaries. The corresponding macroscopic characteristics involved are the shear stresses and the mean normal stress.

For the failure of isotropic materials, we will then use the invariants that involve the shear stresses and the mean normal stress.

The formal statement of the yield function is given by

$$f(\sigma_{ij}) \leq 1.$$

The plastic potential $G(\sigma_{ij})$ describes the plastic flow through the standard flow form

$$\dot{\varepsilon}_{ij}^{p} = \lambda \frac{\partial G}{\partial \sigma_{ij}}, \tag{1}$$

where the strain is decomposed into elastic and plastic components. The associative form of (1) is that which occurs when the yield function and plastic potential are taken to be identical:

$$G(\sigma_{ij}) = f(\sigma_{ij}).$$

As is well known, this ideal associative form occurs only in the extremely ductile limit for application to most fcc metals.

Some of the complications to be considered in the following work will include the following effects. All materials except the ideal case, show an asymmetry in the uniaxial tensile and compressive yield values, $T \neq C$. Also, all except ideal materials show a pressure dependency. Is one of these effects a fundamental effect and the other a following consequence? An answer to this question will be sought. Since the materials are initially isotropic, most approaches utilize the invariants of the stress tensor, I_1, J_2 and J_3. The first two, I_1 and J_2, are commonly used, but the third invariant, J_3, is sometimes also argued to be important. The present work will seek to clarify the significance or lack thereof of J_3 for use in yield functions and plastic potentials. We also will look for a unifying method by which to treat plastic potentials for materials other than bcc metals. In the present context, the term yield is interpreted to mean the stress value at the point of major deviation from the preceding linear elastic region, not at some hypothetical, initial deviation point, which can be extremely difficult to identify. We begin by considering the three standard invariants.

2. Invariants

Consider the eigenvalue problem used to find the principal values of the stress tensor. The notation will follow that of [Wilson 2002]. The invariants I_1, I_2 and I_3 follow from the characteristic equation

$$\lambda^3 - I_1\lambda^2 + I_2\lambda - I_3 = 0,$$

where

$$\begin{aligned} I_1 &= \sigma_{11}+\sigma_{22}+\sigma_{33}, \\ I_2 &= \sigma_{11}\sigma_{22}+\sigma_{22}\sigma_{33}+\sigma_{33}\sigma_{11}, \\ I_3 &= \sigma_{11}\sigma_{22}\sigma_{33}. \end{aligned}$$

Alternatively, the deviatoric stress is taken as

$$s_{ij} = \sigma_{ij} - \frac{\delta_{ij}}{3}\sigma_{kk}, \tag{2}$$

and the invariants for s_{ij} are given through

$$\lambda^3 + J_1\lambda^2 - J_2\lambda - J_3 = 0,$$

where

$$\begin{aligned} J_1 &= 0, \\ J_2 &= \tfrac{1}{6}\big((\sigma_{11}-\sigma_{22})^2+(\sigma_{22}-\sigma_{33})^2+(\sigma_{33}-\sigma_{11})^2\big), \\ J_3 &= (\sigma_{11}-\sigma_m)(\sigma_{22}-\sigma_m)(\sigma_{33}-\sigma_m), \\ \sigma_m &= \tfrac{1}{3}I_1. \end{aligned} \tag{3}$$

The invariants for σ_{ij} and s_{ij} are related through

$$\begin{aligned} J_2 &= \tfrac{1}{3}I_1^2 - I_2, \\ J_3 &= \tfrac{2}{27}I_1^3 - \tfrac{1}{3}I_1 I_2 + I_3 = -\tfrac{1}{27}I_1^3 + \tfrac{1}{3}I_1 J_2 + I_3. \end{aligned} \tag{4}$$

Using the identities (4) it is completely equivalent to take the three independent invariants as either the grouping I_1, I_2 and I_3 or I_1, J_2 and J_3. It is advantageous to use the latter combination since the two invariants J_2 and J_3 are independent of mean normal stress, which then comes in only through I_1. These invariants will be taken to be those that will be used to specify yield functions for isotropic materials.

Begin by considering yield functions for isotropic materials. The two widely recognized features of nonideal yield behavior are, first, the asymmetry in the uniaxial tensile and compressive yield values T and C, thus $T \leq C$. The other feature is the dependence of the yield function upon mean normal stress, in all cases except the ductile limit described by the Mises form. Consider cases where these two effects are taken to be independent of each other. In particular take cases having $T \neq C$ but no dependence upon mean normal stress.

Consider a possible yield function of the form

$$aJ_2 + bJ_3 \leq 1, \tag{5}$$

which, because of independence of I_1, has no mean normal stress dependence. The yield stress asymmetry $T \neq C$ can however be accommodated by (5). Evaluate a

and b in (5) to give the uniaxial yield values T and C. The form that (5) then takes is

$$3\left(\frac{1+(C/T)^3}{1+C/T}\right)\frac{J_2}{C^2}+\frac{27}{2}\left(\frac{-1+(C/T)^2}{1+T/C}\right)\frac{J_3}{C^3}\leq 1. \tag{6}$$

Now specialize (6) to a biaxial stress state with only principal stresses σ_1 and σ_2 but $\sigma_3=0$. Then

$$J_2=\tfrac{1}{3}(\sigma_1^2-\sigma_1\sigma_2+\sigma_2^2)$$

and

$$J_3=\tfrac{1}{27}(2\sigma_1-\sigma_2)(\sigma_1-2\sigma_2)(\sigma_1+\sigma_2). \tag{7}$$

Take the particular case of $T/C=1/2$, which is well within the range of possibility. Then the yield function (6) becomes

$$\frac{J_2}{C^2}+3\frac{J_3}{C^3}\leq\frac{1}{9}. \tag{8}$$

It can be shown analytically that the yield envelopes in the equation of (8) with (7) are the linear (line) segments as shown in Figure 1, going through the tensile and compressive values along the axes.

As seen from Figure 1 the yield function at $T/C=1/2$ has a strongly nonconvex character. In the limit of $T/C=1$, the yield function is the Mises form with a

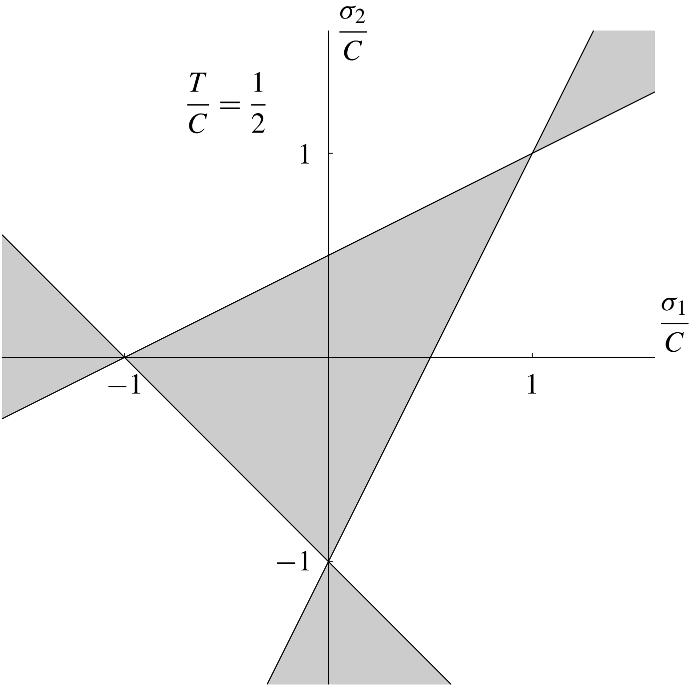

Figure 1. J_2-J_3 yield criterion, Equation (6).

completely convex character. But as the value of T/C diminishes, a nonconvex form develops, becoming that of Figure 1 at $T/C = 1/2$. The yield form shown in Figure 1 is also physically unrealistic in other respects. It predicts unlimited yield strength in a state of equibiaxial tension, as well as other nonrealistic features.

Continuing the examination of yield forms which have the strength asymmetry characteristic but no dependence upon mean normal stress leads to forms such as

$$aJ_2^{1/2} + bJ_3^{1/3} \leq 1, \quad aJ_2 + bJ_3^{1/3} \leq 1, \quad aJ_2^{3/2} + bJ_3 \leq 1.$$

All of these cases were been examined (together with Dr. A. Arsenlis) and were found to reveal the emergence of a nonconvex character somewhere in the range $1/2 \leq T/C < 1$. The nonconvex character results as the direct consequence of the third invariant J_3.

Now consider the opposite situation, namely, yield functions which have no strength asymmetry but do have a dependence upon mean normal stress. For example, the yield form

$$aI_1^2 + bJ_2 \tag{9}$$

does have a dependence on mean normal stress through I_1^2 but it does not allow $T \neq C$. However, the form (9) must be excluded from consideration because it is independent of whether the mean normal stress is tensile or compressive, which is a known and strong physical effect.

The conclusion from examining these yield function cases, which are somewhat arbitrarily tailored to reflect a particular physical effect, is that this is an unproductive approach. In the next section, in connection with bcc metals data, a more organized approach to yield functions (and plastic potentials) will be taken, one which assures convexity of the related forms, and interrelates the tension-compression asymmetry and the pressure dependence.

3. Polynomial expansion for BCC Metals, $0 \leq \alpha \leq 1$

Both yield functions $f(\sigma_{ij})$ and plastic potentials $G(\sigma_{ij})$ for isotropic materials will now be considered. For either of these, perform a polynomial expansion in the invariants. Take an expansion in the invariants of the stress tensor, giving

$$F(\sigma_{ij}) = a_1 I_1 + a_2 I_1^2 + a_3 J_2 + a_4 I_1^3 + a_5 I_1 J_2 + a_6 J_3 + \cdots, \tag{10}$$

where $F()$ represents either $f()$ or $G()$.

Rewrite this form explicitly designating the different possible levels of truncation through third degree terms

$$F = a_1 I_1 \Big|_{\text{1st degree}} + a_2 I_1^2 + a_3 J_2 \Big|_{\text{2nd degree}} + a_4 I_1^3 + a_5 I_1 J_2 + a_6 J_3 \Big|_{\text{3rd degree}} \tag{11}$$

At the first-degree level there is one parameter to be evaluated, at the second-degree level there are three parameters and at the third degree level there are six parameters. Obviously the first-degree level cannot give the operative physical effects; this leaves either the second degree level or the third-degree level to be examined. It is convenient to rewrite (11) normalized by the modulus E so that the coefficients are in preferred nondimensional form. This gives

$$F = b_1 \frac{I_1}{E} + b_2 \frac{I_1^2}{E^2} + b_3 \frac{J_2}{E^2} + b_4 \frac{I_1^3}{E^3} + b_5 \frac{I_1 J_2}{E^3} + b_6 \frac{J_3}{E^3}. \tag{12}$$

Whatever the level of truncation, the form (12) gives a rationale for neglecting the terms of higher order beyond that level. Obviously the lowest degree level that can adequately reflect the physical effects of interest must be used. The second-degree level will be considered in this work. If it does not successfully capture the requisite physical effects, then the third degree level with six parameters must be considered.

Using the form (11) rather than (12) for convenience, the second degree form is

$$F = a_1 I_1 + a_2 I_1^2 + a_3 J_2. \tag{13}$$

In application to yield functions and plastic potentials, if it is assumed that there can be no plastic response under a state of purely hydrostatic compressive stresses then it can be shown that the coefficient a_2 in (13) must vanish. This condition will be used in this work, leaving (13) as

$$F = a_1 I_1 + a_3 J_2. \tag{14}$$

The form (14) has a considerable history, described in [Christensen 2004].

The form (14) thus excludes the third invariant from participation in the process. It is quite logical that the third invariant not be involved with yielding and plastic flow even though it is involved in the eigenvalue problem of principal stresses. Stress is a 3 × 3 matrix and the characteristic equation necessarily involves the third invariant. In the present approach, there are only two relevant stress states for isotropic materials. These are dilatation and shear, and it is these that are directly involved with the first and second invariants. The third invariant cannot be visualized as a specific and independent stress state having $I_1 = J_2 = 0$. For these reasons the polynomial expansion is truncated at terms of 2^{nd} degree, not bringing in J_3. It may also be noted that the form (14) always produces a convex surface. Finally, since the expansion directly involves the mean normal stress, I_1, it is concluded that the dependence upon mean normal stress is a primary effect, and that the tension compression asymmetry is merely a consequence of that.

As shown in [Christensen 2004] the form (14) as a yield function can be written as

$$\alpha\hat{\sigma}_{kk}+\tfrac{3}{2}(1+\alpha)\hat{s}_{ij}\hat{s}_{ij}\leq 1, \tag{15}$$

where the stress is nondimensionalized by the uniaxial compressive yield strength as

$$\hat{\sigma}_{ij}=\frac{\sigma_{ij}}{\kappa},$$

where

$$\kappa=C$$

and

$$\alpha=\frac{C}{T}-1.$$

It is advantageous to use the nondimensional parameter α, and in this section it will be restricted to cover the range $0\leq\alpha\leq 1$ which does cover most bcc metals. Either of the two properties groupings T and C or α and κ will be used, as appropriate.

Now, using the representation (14) for the plastic potential, G, in flow form (1) gives

$$G=\beta\kappa\sigma_{kk}+\tfrac{3}{2}s_{ij}s_{ij}. \tag{16}$$

The $3/2$ factor in (16) could be absorbed into λ (1) but it is retained here for scaling convenience, and parameter β remains to be determined from data. Comparing (15) and (16) it is seen that the associative form of the plastic potential is given by

$$\beta=\frac{\alpha}{1+\alpha},\qquad\text{(associative)}.$$

The deviatoric term in the yield function can be written in terms of stress components as

$$\hat{s}_{ij}\hat{s}_{ij}=\tfrac{1}{3}\big((\hat{\sigma}_{11}-\hat{\sigma}_{22})^2+(\hat{\sigma}_{22}-\hat{\sigma}_{33})^2+(\hat{\sigma}_{33}-\hat{\sigma}_{11})^2\big)+2(\hat{\sigma}_{12}^2+\hat{\sigma}_{23}^2+\hat{\sigma}_{31}^2). \tag{17}$$

The plastic potential is

$$\begin{aligned}G=\kappa\beta(\sigma_{11}+\sigma_{22}+\sigma_{33})+\tfrac{1}{2}\big((\sigma_{11}-\sigma_{22})^2+(\sigma_{22}-\sigma_{33})^2+(\sigma_{33}-\sigma_{11})^2\big)&\\+3(\sigma_{12}^2+\sigma_{23}^2+\sigma_{31}^2).&\end{aligned} \tag{18}$$

Using the flow rule (1) with (18) gives the plastic strain increments as

$$\begin{aligned}\frac{\dot{\varepsilon}^p_{11}}{\lambda}&=\kappa\beta+2\sigma_{11}-\sigma_{22}-\sigma_{33}, & \frac{\dot{\varepsilon}^p_{22}}{\lambda}&=\kappa\beta-\sigma_{11}+2\sigma_{22}-\sigma_{33}\\ \frac{\dot{\varepsilon}^p_{33}}{\lambda}&=\kappa\beta-\sigma_{11}-\sigma_{22}+2\sigma_{33} & \frac{\dot{\varepsilon}^p_{ij}}{\lambda}&=6\sigma_{ij}\quad\text{for } i\neq j.\end{aligned} \tag{19}$$

The plastic volume change is then given by

$$\dot{\varepsilon}^{p}_{kk} = 3\lambda\kappa\beta. \tag{20}$$

The volume change in states of uniaxial tension and compression will be used to evaluate the parameter β in the plastic potential (18). From the yield function (15) and (17) it is found that for uniaxial tension

$$\hat{\sigma}^{T}_{11} = \frac{1}{1+\alpha}, \tag{21}$$

and for uniaxial compression

$$\hat{\sigma}^{C}_{11} = -1. \tag{22}$$

Using (21) and (22) in the plastic strain expressions (19) and using the volume change form (20) gives the plastic volume change normalized by the plastic strain increment in the stress direction as

$$\frac{\dot{\varepsilon}^{p}_{kk}}{\dot{\varepsilon}^{p}_{11}} = \frac{3}{1+\dfrac{2}{\beta(1+\alpha)}} \qquad \text{(tension)} \tag{23}$$

and

$$\frac{\dot{\varepsilon}^{p}_{kk}}{|\dot{\varepsilon}^{p}_{11}|} = \frac{3}{1-2/\beta} \qquad \text{(compression).} \tag{24}$$

At this point, data can be used to evaluate the parameter β. The carefully prepared and evaluated data of Spitzig, Sober and Richmond [Spitzig et al. 1975] on two formulations of steel will be used. The two materials types give the same results, to within experimental accuracy. Spitzig et. al. expressed the T/C asymmetry through a factor defined as the strength differential (SD). The relation between their strength differential and parameter α defined above is given by

$$\alpha = \frac{\mathrm{SD}}{1-\mathrm{SD}/2}. \tag{25}$$

For the two quenched and tempered (4310 and 4330) steels, the strength differential was determined to be in the range

$$\mathrm{SD} = 0.045 - 0.065.$$

The strength differential of $\mathrm{SD} = 0.05$ will be used giving an α value of

$$\alpha = 0.051.$$

This means that the tensile yield value T was about 5% less than the compressive value C. The experimental value for the plastic volume change normalized by the plastic strain was

$$\frac{\dot{\varepsilon}^p_{kk}}{\dot{\varepsilon}^p_{11}} = 0.005,$$

with the same values for both the tension and compression cases. This very small plastic volume increase is likely due to the generation of vacancies as dislocation lines cross each other [Hull and Bacon 2001].

Using the α value and the above plastic volume change value in either (23) or (24) gives β as

$$\beta = 0.0032.$$

The associative value for β, $\beta = \alpha/(1+\alpha)$, would be given by

$$\beta = 0.049 \qquad \text{(associative)}.$$

Thus the actual material parameter β in (16) is an order of magnitude less than the associative value for it would be in the case of these bcc metals.

The fact that the tensile and compressive plastic volume changes were indistinguishable experimentally is a form of partial verification for the results (23) and (24) in this range of α and β values. [Spitzig et al. 1976] tested several more steel formulations and in all cases but one found results compatible with those just used for these first cases. Their main conclusions were that the associative flow rule is in error by about an order of magnitude for these materials. Their results are also compatible with the general forms of yield functions and plastic potentials considered here, namely (15) and (16). It can be said that these forms appear adequately to describe the plastic behavior for these bcc metals.

The situation as it stands at this point is that the yield function (15) is completely specified by measurements of the uniaxial tensile and compressive yield strengths for each material of interest. The plastic potential is completely specified by the evaluation of the parameter β in (16) for each material of interest. In the next section we consider a more general approach for specifying the plastic potential, possibly applicable to a much broader class of materials than just bcc metals.

4. General materials, $0 \le \alpha \le \infty$

With no certainty of success, we now look for a more general and unifying approach than that of determining parameter β in the plastic potential (16) for each separate material of interest. First some recent results need to be assembled to approach this problem.

Write the yield function (15) in a slightly different form as

$$\frac{\alpha}{1+\alpha}\hat{\sigma}_{kk} + \frac{3}{2}\hat{s}_{ij}\hat{s}_{ij} \le \frac{1}{1+\alpha}, \tag{26}$$

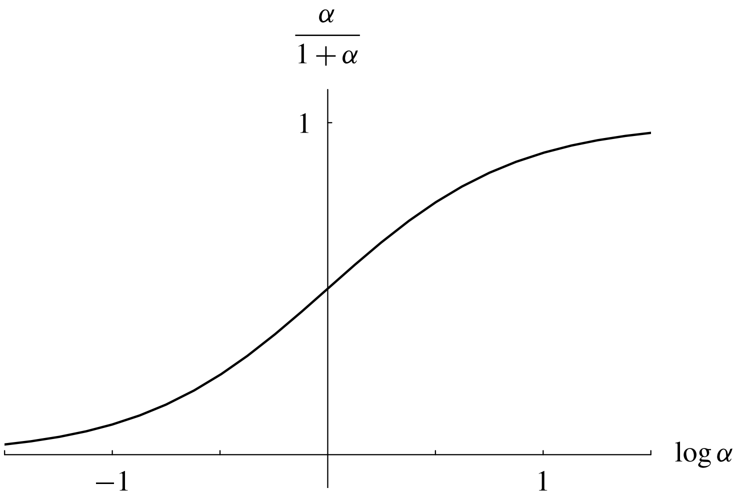

Figure 2. Dilatational term coefficient, Equation (26).

with α now having the full range

$$\alpha = \frac{C}{T} - 1, \qquad 0 \le \alpha \le \infty.$$

The value $\alpha = 0$ is that of the perfectly ductile Mises material. The other limit $\alpha \to \infty$ is the brittle limit, wherein the tensile yield strength is negligible compared with the compressive yield strength. This limiting case still has material integrity as opposed to that of a granular material. Free flowing granular materials as well as porous materials are separate and distinct classes from the macroscopically homogeneous materials considered here.

The coefficient $\alpha/(1+\alpha)$ in (26) has an interesting behavior. It is shown in Figure 2 with a log scale. The log scale is natural to use because α varies from 0 to ∞ and, as with spectra, this properties variation is best viewed through log scales. Note that at $\log\alpha = 0$, $\alpha = 1$ the coefficient shown in Figure 2 undergoes a transition (transition of material type) defined by the point of maximum slope (rate of change) with respect to $\log\alpha$. Thus, the coefficient $\alpha/(1+\alpha)$ in (26) determines the relative weights of the dilatational and distortional terms. Over the range of α, this goes from no dilatational contribution to the yield function up to a fully interactive dilatational contribution. Then there is the transition between these two extremes at $\alpha = 1$ for this contribution of the dilatational term.

Christensen [2004] has examined this yield/failure behavior described above and found that at the transition value of $\alpha = 1$, a Rankine type fracture criterion must come into effect. Thus the yield function (26) must be augmented by the explicit fracture criterion

$$\sigma_1 \le T \qquad \text{if } \alpha \ge 1, \tag{27}$$

where σ_1 is the largest principal stress. The fracture criterion has no effect directly at $\alpha = 1$, but as α is incrementally increased beyond that value, the fracture criterion (27) gains a gradually increasing effect, more limiting than the yield criterion (26) under some conditions. For large values of α the fracture criterion can be very limiting in effect. See [Christensen 2005] for an elaboration.

With the above background, we can now proceed with the plastic potential problem. For the plastic potential form given in (16) the coefficient β controls the relative weight of the dilatational and distortional terms. Take $\beta = \beta(\alpha)$ and note that it is required that

(i) $\beta = 0$ at $\alpha = 0$,

in order to be consistent with Mises behavior at that limit. Now, assume two more conditions on $\beta(\alpha)$ in (16) and its applicability over the full range of α. Take

(ii) $\beta \to A$ as $\alpha \to \infty$,

where A is some nonzero constant, unknown at this point. Finally require that $\beta(\alpha)$ have a transition (point of maximum slope versus $\log \alpha$) at the same value as for the yield function, namely at $\log \alpha = 0,\ \alpha = 1$. Thus

(iii) $\beta(\alpha)$ has transition at $\alpha = 1$.

This requirement ensures compatibility between the transition locations in the yield function and the plastic potential.

A standard form for $\beta(\alpha)$ in the plastic potential (16) would be as an expansion of the type

$$\beta = \sum_{n=1}^{\infty} A_n \left(\frac{\alpha}{1+\alpha} \right)^n .$$

The first term will be explicitly considered here, as a form that directly satisfies conditions (i), (ii) and (iii),

$$\beta = \frac{A\alpha}{1+\alpha}, \tag{28}$$

where A is a constant with respect to α and to be determined. Parameter α is considered to be known from the yield function. Substituting (28) into (16) gives the plastic potential as

$$G = A \left(\frac{\alpha}{1+\alpha} \right) \hat{\sigma}_{kk} + \frac{3}{2} \hat{s}_{ij} \hat{s}_{ij} .$$

Form (28) for the plastic potential in (16) is intimately related to the yield form, being directly proportional to the corresponding coefficient in (26) over the full range of α. The limits on A are

$$0 \le A \le 1,$$

where

$$A = \begin{cases} 0 & \text{for a purely distortional plastic potential,} \\ 1 & \text{for an associative plastic potential.} \end{cases}$$

The constant A is unlikely to be universal, but the form (28) could possibly be useful as an approximation. If so, the form (28) would have considerable utility since β would not have to be re-determined for each different material of interest. The possible validity and usefulness of (28) will now be examined.

With the form (28), the results (23) and (24) on uniaxial tension and compression volume change for the plastic response become

$$\frac{\dot{\varepsilon}^p_{kk}}{\dot{\varepsilon}^p_{11}} = \frac{3A\alpha}{2 + A\alpha} \qquad \text{(tension)} \tag{29}$$

and

$$\frac{\dot{\varepsilon}^p_{kk}}{|\dot{\varepsilon}^p_{11}|} = \frac{3A\alpha}{2(1+\alpha) - A\alpha} \qquad \text{(compression).} \tag{30}$$

The steel testing data of [Spitzig et al. 1975] given in the previous section just after Equation (25) with the values for β and α inserted into (28) give constant A as

$$A = 0.065 = 1/15 \qquad \text{(steel).} \tag{31}$$

This result means that the dilatational contribution to the plastic potential is $1/15$ the size of the dilatational contribution to the yield function at the same value of α.

Next, a very different type of material will be considered. Spitzig and Richmond [1979] performed tests on polyethylene, similar to those described for steel. The strength differential was determined to be

$$\mathrm{SD} = 0.085,$$

giving α as

$$\alpha = 0.089.$$

The plastic volume change was measured in uniaxial compression and tension and was found to be

$$\frac{\dot{\varepsilon}^p_{kk}}{\dot{\varepsilon}^p_{11}} = 0.011.$$

Using these data to evaluate β and A gives

$$\beta = 0.0067,$$

$$A = 0.083 = 1/12 \qquad \text{(polyethylene).}$$

Other testing data on polycarbonate by Spitzig and Richmond [1979] were inconclusive.

Compare the β values for steel and polyethylene of 0.0032 and 0.0067, respectively. These differ by more than a factor of two. However, the corresponding A values of $1/15$ and $1/12$ are much closer together. The β values difference show the two materials to have strongly different behaviors, but the much smaller A value differences shows the form (28) for $\beta(\alpha)$ to have a unifying effect.

The previous two materials examples are of a very ductile type; now an example far removed from this condition will be given, that of cast iron. For grey cast iron the yield values in [Grassi and Cornet 1949; Coffin 1950] give

$$\frac{T}{C} = \frac{1}{3}, \qquad \alpha = 2.$$

Using this value of α in the uniaxial compression result (30) gives

$$\frac{\dot{\varepsilon}_{kk}^{p}}{|\dot{\varepsilon}_{11}^{p}|} = \frac{3A}{3-A} \qquad \text{(compression).} \tag{32}$$

The corresponding result for uniaxial tension is not relevant because it is excluded by the fracture criterion (27) for this value of α. The same situation applies for simple shear stress, at large values of α plastic flow is subsumed by the fracture criterion (27) and brittle behavior.

Unfortunately, there does not appear to be data for the plastic volume change in compression of cast iron of the quality of that of the previous two examples. An alternative approach using plastic Poisson's ratio will be given instead. Plastic Poisson's ratio is defined in the usual way as

$$\upsilon^{p} = -\frac{\dot{\varepsilon}_{22}^{p}}{\dot{\varepsilon}_{11}^{p}}.$$

With $\dot{\varepsilon}_{22}^{p} = \dot{\varepsilon}_{33}^{p}$, this then gives

$$\frac{\dot{\varepsilon}_{kk}^{p}}{|\dot{\varepsilon}_{11}^{p}|} = 1 - 2\upsilon^{p}. \tag{33}$$

Note that $\upsilon^{p} > 1/2$ must occur to have positive plastic volume change in uniaxial compression. The elastic restrictions on Poisson's ratio do not apply here.

Equating the forms in (32) and (33) gives

$$\upsilon^{p} = \frac{1}{2}\left(\frac{3+2A}{3-A}\right), \qquad \alpha = 2. \tag{34}$$

The limits of A give the values for υ^{p} as

$$A = \begin{cases} 0, & \upsilon^{p} = 1/2, \\ 1, & \upsilon^{p} = 5/4. \end{cases}$$

The extremely large value of υ^p at the associative value $A = 1$ is completely unrealistic, again specifying extremely large plastic volume change. The value of A must be small, $A \ll 1$, to avoid this unrealistic behavior.

Poisson's ratio is difficult to measure accurately unless very precise volumetric measurements are done. As a first approximation, it is widely taken that the deformation is plastically not expandable, $\upsilon^p = 1/2$, which we will loosely refer to as incompressible, since that is common terminology. The error or difference for the plastic deformation to be taken as incompressible, when in fact it is slightly expandable, is given by ε as

$$\varepsilon = \frac{\upsilon^p - 1/2}{\upsilon^p}, \tag{35}$$

where υ^p is the actual value. For example, for $\upsilon^p = 0.55$ the error in assuming plastic incompressibility is 9.1%. By this method, taking realistic errors in assuming an incompressible plastic Poisson's ratio to be in the range of 5–10% can then be used to give the value of υ^p from (35). With the υ^p value, the corresponding constant A value follows from (34). The results, for this case of $\alpha = 2$, are

Error	6%	8%	10%
$A =$	$^1/_{16.0}$	$^1/_{11.8}$	$^1/_{9.3}$.

These values of A are in the same range as those found for steels and the one polymer. The corresponding β values are found from (28). For example for $A = 1/14$ and at the value $\alpha = 2$, $\beta = 0.047$. This is over an order of magnitude larger than the value found for steel of $\beta = 0.0032$. Thus the form (28) for β involving A does appear to be reasonable and realistic in going from the extremely small value of α in the ductile range to an order of magnitude larger value of $\alpha = 2$ for cast iron.

Finally, consider the limiting case $\alpha \to \infty$. From (30) it follows that

$$\frac{\dot{\varepsilon}_{kk}^p}{|\dot{\varepsilon}_{11}^p|} = -\frac{3A}{2-A}. \tag{36}$$

Equating (36) and (33) then gives

$$\upsilon^p = \frac{1+A}{2-A}, \qquad \alpha \to \infty. \tag{37}$$

The associative case with $A = 1$ gives $\upsilon^p = 2$, a wholly unrealistic condition. Again, constant A must be small. Following the method just outlined, for a 10% error in assuming υ^p to be incompressible compared with its actual value, (35) and (37), give the corresponding A value as

$$A = \frac{1}{14.0}, \qquad \alpha \to \infty. \tag{38}$$

The plastic potential in (16) has the A value in (28) to be in the general range of an order of magnitude less than one. This then is consistent with bcc behavior and polymer behavior at the ductile end of the α scale and also consistent with the above reasoning for behavior in the brittle range at $\alpha = 2$ and the brittle limit $\alpha \to \infty$.

5. Conclusions

The consequence of this assessment is that the dilatational contribution to the plastic potential (16) is found to be much less influential than the dilatational contribution to the yield function (26) over the full range of each. At first it might be surprising that the dilatational contribution to the plastic potential seems so small, by comparison. The present work suggests, however, that the inverse situation is more understandable; that is, the small dilatational contribution to the plastic potential can be reasoned, but the much stronger dilatational contribution to the yield function is the somewhat surprising effect. The plastic flow, as accessed through the plastic potential, seems quite naturally to be highly influenced by the physical effects of shearing (distortional) motion, indeed, that is the essence of ductile behavior. However, the yield function shows a strong departure from distortionally dominated effects for larger values of α. The source for this effect is the emerging importance of fracture as α increases. In the present context, the yield function (26) undergoes rather drastic changes of shape as α increases — changes necessary to ensure compatibility with the fracture criterion (27), as evidenced by their union at $\alpha = 1$. This emergence of fracture modes greatly cuts down the size of the domain for plastic flow, as α increases.

For the examples considered, the values of constant A in the plastic potential (16) and (28) were found to be in the general range of $1/10$ to $1/20$. We now inquire as to whether there is any special significance to this magnitude of A in the plastic potential. The coefficient $A\alpha/(1+\alpha)$ controls the size and effect of the dilatational term in the plastic potential. This coefficient at the full extent of its range, $\alpha \to \infty$, just becomes coefficient A itself, which is about $1/14$, to take a specific value from the examples considered earlier. Thus at the limit $\alpha \to \infty$ the plastic volume change, (36), at $A = 1/14$ becomes

$$\dot{\varepsilon}_{kk}^{p} = \tfrac{1}{9}|\dot{\varepsilon}_{11}^{p}| = 0.111|\dot{\varepsilon}_{11}^{p}|.$$

The plastic volume change is about 11% of the size of the imposed strain for uniaxial compressive stress, at this limit. This size for the plastic volume change is in the proper range for the effect of dilatancy in highly damaged materials. The dilatancy is most likely due to the nucleation of voids in general and void space at grain boundaries in particular materials of that type. The dilatancy is still a significant and recognizable effect at this size, but it is not at the unrealistically large size predicted by the associative form. Alternatively, if the constant A were yet another order of magnitude smaller than the above value, the predicted dilatancy effect would be much too small to be recognizable or significant. Thus the constant A being about an order of magnitude less than one recovers the proper result for bcc metals approaching the extreme ductile range, $\alpha \to 0$, and it also recovers the proper dilatancy behavior approaching the opposite limit, $\alpha \to \infty$. If a single value for A were to be taken for general applications, the present work suggests it would be about $1/15$ as supported by the data of Richmond and colleagues.

The plastic potential apparently would be of purely distortional form were it not for the proclivity of homogeneous materials to generate voids, requiring the small correction found here. In the very ductile range, such as with most bcc metals, the combination of a small value of α and small A in (28) means that it is justified, and perhaps obvious, to approximate the plastic potential as being purely distortional, even though the yield function may not be taken to be so. For materials with values of α that are not small, the smallness of constant A still provides assurance that the dilatational term in the plastic potential can be neglected in many situations. According to the preceding examples the resulting error would be of the order of constant A. Thus the present work indicates that for most homogeneous and isotropic materials (not just ductile metals) in stress states allowing plastic flow rather than brittle behavior, the plastic potential is quite well represented by the simple distortional form of (16) having $\beta \cong 0$, and as coordinated with the yield function (15) or (26) having interacting distortional and dilatational effects. The competitive fracture mode of failure is controlled by criterion (27). All of these forms are fully specified by two properties: the uniaxial tensile yield (or fracture) strength and the uniaxial compressive yield strength.

Acknowledgements

I wish to thank Dr. A. Arsenlis for many spirited and helpful discussions and Dr. R. Becker for reacquainting me with the fine work of Richmond. Support from the Office of Naval Research is appreciated, Dr. Y. D. S. Rajapakse, Program Manager.

This work was performed under the auspices of the U.S. Department of Energy by the University of California, Lawrence Livermore National Laboratory under Contract No. W–7405–Eng–48.

References

[Christensen 2004] R. M. Christensen, "A two-property yield, failure (fracture) criterion for homogeneous, isotropic materials", *J. Eng. Mater. Technol.* **126**:1 (2004), 45–52.

[Christensen 2005] R. M. Christensen, “Exploration of ductile, brittle failure characteristics through a two-parameter yield/failure criterion”, *Mater. Sci. Eng. A* **394**:1–2 (2005), 417–424.

[Christian 1983] J. W. Christian, “Some surprising features of the plastic deformation of body-centered cubic metals and alloys”, *Metall. Mater. Trans. A* **14A** (1983), 1237–1256.

[Coffin 1950] L. F. Coffin, “The flow and fracture of a brittle material”, *J. Appl. Mech.* **17** (1950), 233–248.

[Grassi and Cornet 1949] R. C. Grassi and I. Cornet, “Fracture of gray cast iron tubes under biaxial stresses”, *J. Appl. Mech.* **16** (1949), 178–182.

[Hill 1950] R. Hill, *The mathematical theory of plasticity*, Oxford Univ. Press, Oxford, UK, 1950.

[Hill 1959] R. Hill, “Some basic principles in the mechanics of solids without a natural time”, *J. Mech. Phys. Solids* **7**:3 (1959), 209–225.

[Hill 1968a] R. Hill, “On constitutive inequalities for simple materials I”, *J. Mech. Phys. Solids* **16**:4 (1968), 229–242.

[Hill 1968b] R. Hill, “On constitutive inequalities for simple materials II”, *J. Mech. Phys. Solids* **16**:5 (1968), 315–322.

[Hill and Rice 1972] R. Hill and J. R. Rice, “Constitutive analysis of elastic-plastic crystals at arbitrary strain”, *J. Mech. Phys. Solids* **20**:6 (1972), 401–413.

[Hirsch 1960] P. B. Hirsch, “Recorded Oral Communication”, in *5th Int. Conf. on Crystallography*, Cambridge, 1960.

[Hull and Bacon 2001] D. Hull and D. J. Bacon, *Introduction to dislocations*, 4th ed., Butterworth–Heinemann, Oxford, 2001.

[Spitzig and Richmond 1979] W. A. Spitzig and O. Richmond, “Effect of hydrostatic pressure on the deformation behavior of polyethylene and polycarbonate in tension and in compression”, *Polym. Eng. Sci.* **19**:16 (1979), 1129–1139.

[Spitzig et al. 1975] W. A. Spitzig, R. J. Sober, and O. Richmond, “Pressure dependence of yielding and associated volume expansion in tempered martensite”, *Acta Metall.* **23**:7 (1975), 885–893.

[Spitzig et al. 1976] W. A. Spitzig, R. J. Sober, and O. Richmond, “The effect of hydrostatic pressure on the deformation behavior of maraging and HY-80 steels and its implications for plasticity theory”, *Metall. Mater. Trans. A* **7A** (1976), 1703–1710.

[Vitek 1975] V. Vitek, “Theory of the core structures of dislocations in body centered cubic metals”, *Crystal Lattice Defects* **5** (1975), 1–34.

[Wilson 2002] C. D. Wilson, “A critical reexamination of classical metal plasticity”, *J. Appl. Mech.* **69**:1 (2002), 63–68.

Received 28 Oct 2005.

RICHARD M. CHRISTENSEN: `christensen6@llnl.gov`, `christensen@stanford.edu`
Lawrence Livermore National Laboratory, P.O. Box 808, L–356, Livermore CA 94550

and

Department of Aeronautics and Astronautics, Stanford University, Stanford, CA 94305

SUBMISSION GUIDELINES

ORIGINALITY

Authors may submit manuscripts in PDF format on-line. Submission of a manuscript acknowledges that the manuscript is *original and has neither previously, nor simultaneously, in whole or in part, been submitted elsewhere.* Information regarding the preparation of manuscripts is provided below. Correspondence by email is requested for convenience and speed. For further information, write to:

Marie-Louise Steele
Division of Mechanics and Computation
Durand Building, Room 262
Stanford University
Stanford CA 94305

LANGUAGE

Manuscripts must be in English. A brief abstract of about 150 words or less must be included. The abstract should be self-contained and not make any reference to the bibliography. Also required are keywords and subject classification for the article, and, for each author, postal address, affiliation (if appropriate), and email address if available. A home-page URL is optional.

FORMAT

Authors are encouraged to use LaTeX and the standard article class, but submissions in other varieties of TeX, and, exceptionally in other formats, are acceptable. Electronic submissions are strongly encouraged in PDF format only; after the refereeing process we will ask you to submit all source material.

REFERENCES

Bibliographical references should be listed alphabetically at the end of the paper and include the title of the article. All references in the bibliography should be cited in the text. The use of BibTeX is preferred but not required. Tags will be converted to the house format (see a current issue for examples), however, in the manuscript, the citation should be by first author's last name and year of publication, e.g. "as shown by Kramer, et al. (1994)". Links will be provided to all literature with known web locations and authors are encoraged to provide their own links on top of the ones provided by the editorial process.

FIGURES

Figures prepared electronically should be submitted in Encapsulated PostScript (EPS) or in a form that can be converted to EPS, such as GnuPlot, Maple, or Mathematica. Many drawing tools such as Adobe Illustrator and Aldus FreeHand can produce EPS output. Figures containing bitmaps should be generated at the highest possible resolution. If there is doubt whether a particular figure is in an acceptable format, the authors should check with production by sending an email to:

production@mathscipub.org

Each figure should be captioned and numbered so that it can float. Small figures occupying no more than three lines of vertical space can be kept in the text ("the curve looks like this:"). It is acceptable to submit a manuscript with all figures at the end, if their placement is specified in the text by means of comments such as "Place Figure 1 here". The same considerations apply to tables.

WHITE SPACE

Forced line breaks or page breaks should not be inserted in the document. There is no point in your trying to optimize line and page breaks in the original manuscript. The manuscript will be reformatted to use the journal's preferred fonts and layout.

PROOFS

Page proofs will be made available to authors (or to the designated corresponding author) at a web site in PDF format. Failure to acknowledge the receipt of proofs or to return corrections within the requested deadline may cause publication to be postponed.

JOURNAL OF
MECHANICS OF MATERIALS AND STRUCTURES

Volume 1 No. 1 January 2006
